# MATHEMATICAL MODELLING OF COMPACTION AND DIAGENESIS IN SEDIMENTARY BASINS

Xin-She Yang

Corpus Christi College

University of Oxford

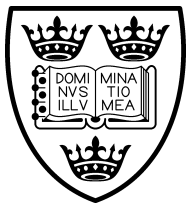


Thesis submitted for the degree of Doctor of Philosophy in the

University of Oxford

Michaelmas Term 1997

## Acknowledgements

First and foremost, I would like to thank my supervisor, Dr Andrew C. Fowler, for his kind supervision, help and encouragement. Not only did he provide me with the fascinating research problems on which to work, but also his direction over the last few years has proven invaluable. I especially thank him for helping me on numerous matters, ranging from the writing of English and read-proof of the manuscripts to finding an academic post, and from supporting me financially to attend international conferences to providing me the opportunity to get some teaching experience.

I am also grateful to my supervisor Dr Andrew C. Fowler and my college tutor Dr Colin McDiarmid for their role in awarding me the 1995 Garside Senior Scholarship. I would like to express my appreciation to Dr Ron Hills for providing me the opportunity to attend the Advanced School and International Conference in Mixed Phase Regions in Edinburgh 1997. I would also like to thank Prof. D L Turcotte and Dr H Ockendon for their kind suggestions and help. I also thank Prof. Desmond McConnell and Dr D. M. Audet for their helpful discussions on the dissolution and precipitation mechanism of diagensis in Chapter 7.

I would like to express my gratitude to Corpus Christi College for the financial support. I would also like to express my gratitude to OCIAM and Mathematical Institute for supporting me to attend the European Study Group in Industrial Mathematics.

I thank the Garside, SBF and SHELL Scholarships for the financial support. Last but not least, I thank my wife for her support throughout my time here.

# Mathematical Modelling of Compaction and Diagenesis in Sedimentary Basins (DPhil Thesis by Xin-She Yang) (**Abstract**)

Sedimentary basins form when water-borne sediments in shallow seas are deposited over periods of millions of years. Sediments compact under their own weight, causing the expulsion of pore water. If this expulsion is sufficiently slow, overpressuring can result, a phenomenon which is of concern in oil drilling operations. The competition between pore water expulsion and burial is complicated by a variety of factors, which include diagenesis (clay dewatering), and different modes (elastic or viscous) of rheological deformation via compaction and pressure solution, which may also include hysteresis in the constitutive behaviours. This thesis is concerned with models which can describe the evolution of porosity and pore pressure in sedimentary basins.

We begin by analysing the simplest case of poroelastic compaction which in a 1-D case results in a nonlinear diffusion equation, controlled principally by a dimensionless parameter $\lambda$, which is the ratio of the hydraulic conductivity to the sedimentation rate. We provide analytic and numerical results for both large and small $\lambda$ in Chapter 3 and Chapter 4. We then put a more realistic rheological relation with hysteresis into the model and investigate its effects during loading and unloading in Chapter 5. A discontinuous porosity profile may occur if the unloaded system is reloaded. We pursue the model further by considering diagenesis as a dehydration model in Chapter 6, then we extend it to a more realistic dissolution-precipitation reaction-transport model in Chapter 7 by including most of the known physics and chemistry derived from experimental studies.

We eventually derive a viscous compaction model for pressure solution in sedimentary basins in Chapter 8, and show how the model suggests radically different behaviours in the distinct limits of slow and fast compaction. When $\lambda \ll 1$, compaction is limited to a basal boundary layer. When $\lambda \gg 1$, compaction occurs throughout the basin, and the basic equilibrium solution near the surface is a near parabolic profile of porosity. But it is only valid to a finite depth where the permeability has decreased sufficiently, and a transition occurs, marking a switch from a normally pressured environment to one with high pore pressures.

# Contents

# Chapter 1

# Introduction

## 1.1 Motivation for Modelling Compaction and Diagenesis

When well-bores are being drilled for oil exploration, drilling mud (a clay suspension in water) is used in the hole to maintain its integrity and safety. The mud density must be sufficient to prevent collapse of the hole, but not so high that hydrofracturing of the surrounding rock occurs. Both these effects depend on the pore fluid pressure in the rock, and drilling problems occur in regions where abnormal pore pressure or *overpressuring* occurs, that is in the regions, normally in the *sedimentary basins* such as the North Sea, where pore pressure increases downward faster than hydrostatic pressure. Such kind of overpressuring can substantially affect oil-drilling rates and even cause serious blowouts during drilling. Therefore, an industrially important objective is to predict overpressuring before drilling and to identify its precursors during drilling. Another related objective is to predict reservoir quality and hydrocarbon migration. An essential step to achieve such objectives is the scientific understanding of their mechanisms and the evolutionary history of post-depositional sediments such as shales.

Shales and other fine-grained compressible rocks are considered to be the source rocks for much petroleum found in sandstones and carbonates. At deposition, sediments such as shales and sands typically have porosities of order $0.5 \sim 0.75$ or $50\% \sim 75\%$ (Lerche, 1990). When sediments are drilled at a depth, say 5000 m,

porosities are typically $0.05 \sim 0.2$ ($5\% \sim 20\%$). Thus an enormous amount of water has escaped from the sediments during their deposition and later evolution. Because of the fluid escape, the grain-to-grain contact pressure must increase to support the overlying sediment weight. Dynamical fluid escape depends lithologically on the permeability behavior of the evolving sediments. As fluid escape proceeds, porosity decreases, so permeability becomes smaller, leading to an ever-increasing delay in extracting the residual fluids. The addition of more overburden sediments is then compensated for by an increase of excess pressure in the retained fluids. Thus overpressure develops from such a *non-equilibrium compaction* environment (Audet and Fowler, 1992). A rapidly accumulating basin is unable to expel pore fluids sufficiently rapidly due to the weight of overburden rock. The development of overpressuring retards compaction, resulting in a higher porosity, a higher permeability and a higher thermal conductivity than are normal for a given depth, which changes the structural and stratigraphic shaping of sedimentary units and provides a potential for hydrocarbon migration.

The compactional fluid escape from the sediments is such a large factor that the movement of subsurface fluids must play a dominant role in any attempt to understand the evolutionary history of geological processes including petroleum formation and migration, generation of overpressuring, cementation and dissolution of sedimentary rocks, fracture formation and dynamical closure, reservoir formation and seals, and the formation of ore deposits. Therefore, the determination of the mechanism of dynamical evolution of fluid escape and the timing of oil and gas migration out of such fine-grained rocks is a major problem. The fundamental understanding of mechanical and physico-chemical properties of these rocks in the earth's crust has important applications in petrology, sedimentology, soil mechanics, oil and gas engineering and other geophysical research areas.

One purpose of compactional and diagenetic modelling on a basinwide scale is to derive an adequate theory to describe the geological processes during compaction, to give a series of evolutionary profiles of porosity versus depth, i.e. *compaction curves*, from which geologists and sedimentologists can better understand the burial and

subsidence histories (Smith 1971). In any attempt to model the dynamic compaction of sediments, the main goals are to reproduce, with acceptable agreement and consistency, four major controls: a) the observed formation thickness, b) the observed porosity as a function of depth, c) the observed fluid pressure as a function of depth, and d) the observed formation permeability as a function of depth (Lerche 1990). These four variables can be calculated in principle from the compaction curves.

The other important purpose of compactional and diagenetic modelling is to contribute to a better understanding of how abnormally high fluid pressures come about and what factors cause these abnormal pressures to persist for many millions of years (Bredehoeft & Hanshaw 1968, Bishop 1979). These high pressures affect seismic interpretation, mud programs during drilling, and drilling safety. Sediment compaction models will be of interest both to the oil industry which always needs better models for clay-shale behaviour and to sedimentologists who are concerned with basin analysis such as *backstripping* and *burial history*.

The thermal history and the generation of hydrocarbon in a sedimentary basin are also closely related to the compaction processes since the thermal conductivity and the diagenesis rates depend on the porosity of sediments. The compaction curves are also a basis for further studies of petroleum migration. Clay diagenesis is a very important process during compacting burial of sediments. Diagenesis is a thermally activated reaction in which, for example, water-rich clay mineral smectite dewaters to illite, releasing "bound interlayer" water into the fluid system and enhancing the development of overpressuring. Such an illitization process is temperature and pressure dependent and is triggered by the catalysis of potassium cations (from K-feldspar).

In addition the major stage of the smectite-to-illite diagenetic reaction often occurs fairly shortly before *oil generation and migration*, indicating close organic-inorganic interactions. In fact, smectite interlayers may not only incorporate large amount of organic products that constitute potential precursors for hydrocarbons, but also act as important water *reservoirs*, that can provide through diagenesis the carrier necessary for hydrocarbon migration (Chamley, 1989). Furthermore, it has been recognised that overpressuring may often be associated with the formation of *seals*, which act

as barriers to pore fluid expulsion (Hunt, 1990). Within the sealed compartment, oil and gas release can build up high pore pressures. The seal formation may in turn be related to *pressure*-enhanced *dissolution* and reprecipitation of clay minerals. All these processes occur in fluid-sediment (water-rock) system, and depend on the operating mechanisms of the fluid-sediment interactions. The main purpose of the diagenetic modelling is obviously to investigate the operating mechanism of diagenesis and reproduce much of the known physics and chemistry of the complex system.

## 1.2 Geological Terminology

The mathematical modelling of compaction and diagenesis is a multi-disciplinary study. It is helpful to review the geological terminology related to the present studies.

*Compaction* is the process of volume reduction via pore-water expulsion within sediments due to the increasing weight of overburden load. The requirement of its occurrence is not only the application of an overburden load but also the expulsion of pore water. The extent of compaction is strongly influenced by burial history and the lithology of sediments. The freshly deposited loosely packed sediments tend to evolve, like an open system, towards a closely packed grain framework during the initial stages of burial compaction and this is accomplished by the processes of grain slippage, rotation, bending and brittle fracturing. Such reorientation processes are collectively referred to as *mechanical compaction* (Kearey & Allen, 1993), which generally takes place in the first 1 - 2 km of burial. After this initial porosity loss, further porosity reduction is accomplished by the process of *chemical compaction* such as pressure solution at grain contacts. It is worth pointing out that *consolidation* is a term often used in geotechnical engineering and implies the reduction of pore space by mechanical loading.

*Diagenesis* generally refers to the sum of all those physical, chemical and biological post-depositional modification/reaction processes prior to the onset of metamorphism. *Metamorphism* is the process of substantial changes to the structure of the sedimentary rock by high temperature and pressures. Diagenesis encompasses

a broad spectrum of modifications to sediments. Despite its geological importance, there is still no universally accepted definition of diagenesis (Rieke & Chilingarian, 1974). There is no current definitive delimitation of diagenesis either with respect to the processes of weathering or metamorphism. In the loosest sense, diagenesis can be considered as everything that contributes to making up a sedimentary rock, from its weathering near the basin surface to its metamorphism during deep burial. The fundamental mechanism behind diagenesis is still less well-documented and there exist large discrepancies between laboratory and field data. Diagenesis is influenced by burial history, temperature, pressure and pore-fluid chemistry. Diagenesis is dynamic as the sedimentary assemblage reacts via the interstitial pore fluids in an attempt to equilibrate with the newly established conditions. At diagenetic temperatures and pressures, it is very common that the kinetics of diagenetic reactions are slow and metastable. Thus, in this sense, diagenesis can be considered simply as low temperature geochemistry.

One of the most important diagenetic processes is the smectite-to-illite transformation during shale diagenesis. Its reaction mechanism is still under discussion though it has received much attention in the last two decades in the literature. One main part of our present work is devoted to the mathematical modelling of this important diagenetic process.

*Smectite* is a family of clay minerals that includes *montmorillonite* and bentonite which is also mainly a kind of montmorillonite-rich clay. The term *illite* is less a name for a definite mineral than a name for a group of substances with composition intermediate between montmorillonite and muscovite. During diagenesis, montmorillonite can release its bounded interlayer-water to form illite which is thermodynamically more stable than montmorillonite.

*Dissolution* is the diagenetic process by which a solid mineral is dissolved by a pore-fluid. There are two fundamental mechanisms for dissolution reactions: *transport-controlled* or *surface-controlled* dissolutions. The former dissolution reaction is controlled by the rate of transport of ions to and away from the reacting surface. This type of dissolution is typical of fast dissolution by strongly concentrated solutions or

of dissolution of highly soluble minerals. In the latter case, dissolution is controlled by the reaction rate at the solid-solution interface, and the reaction is relatively slow. This type of dissolution is typical of many diagenetic dissolution reactions of relatively insoluble minerals in dilute solution with low chemical reactivity.

*Pressure solution/dissolution* is the dissolution process under stress. One of its most common occurrences is during diagenesis. The increasing vertical load leads to dissolution on contact surfaces, and deposition in pore spaces, and thus results in (chemical) compaction. The solubility of minerals increases with increasing effective normal stress at grain contacts. Pressure dissolution at grain contacts is thus a compactional response of the sediments during burial in an attempt to increase the grain contact area so as to distribute the effective stress over a larger surface. Unfortunately, the mechanism and chemistry of the processes are still poorly understood.

*Precipitation* is the deposition process of a mineral from a supersaturated pore-fluid in either solid form by crystallization or as a gel by flocculation resulting in the cementation of the porosity of the host rock. The type of the newly precipitated mineral is determined by the type of chemical species in solution and input rate of dissolved species into the pore-fluids. Precipitation involves two fundamental processes, *nucleation* and *crystal growth*. Nucleation is invariably followed by crystal growth, and the two processes are separated by an energy barrier as a result of the developing interface between the crystal nuclei and the aqueous solution. Once this energy barrier has been surmounted, spontaneous crystal growth, with a net decrease in free energy, will proceed until an equilibrium state is achieved when sufficient material is removed from solution so that supersaturation ceases. Experiments show that both the rate of nucleation and crystal growth depend upon the supersaturation state of the solution. The function of the rate laws is often nonlinear and is poorly understood.

## 1.3 Review of Compaction and Diagenesis Models

Despite the importance of compaction and diagenesis for geological problems, the literature of quantitative modelling is not a huge one though the processes received much attention in the literature. The effect of gravitational compaction was reviewed by Hedberg (1936) who suggested that an interdisciplinary study involving soil mechanics, geochemistry, geophysics and geology is needed for a full understanding of the gravitational compaction process. Later in 1959, Weller reviewed the application of compaction curves in stratigraphy and structural geology. A more comprehensive and detailed review on the subject of compaction of argillaceous sediments was done by Rieke & Chilingarian (1974). Audet & Fowler (1992) presented more recently a short review on models of compaction. Here we only give a very brief review concerning the models of compaction & diagenesis and their developments.

The mathematical model of compaction and consolidation of shale layers is considered as a sediment system consisting of a porous solid phase whose interstitial volume is saturated with pore fluid. Due to the action of gravity and the density difference between the two phases, the solid phase compacts under its own weight by reducing its porosity, thus leading to the expulsion of the pore fluid out of the solid matrix. The earliest model about clay consolidation and compaction was proposed by Gibson(1958) based on the earlier work by Terzaghi (1943). This is a linear compaction model in which it is assumed that the clay permeability and compressibility are constant. Gibson's linear model is sufficiently accurate for modelling thin clay layers often encountered in geotechnical engineering. For thick layers and non-constant permeability , the non-linear model was developed by Gibson, England & Hussey (1967) and by Gibson, Schiffman & Cargill (1981). Applications of Gibson's linear model investigating sedimentary clay layers were by Bredehoeft & Hanshaw(1968) and Hanshaw & Bredehoeft(1968), who modeled diagenesis by considering a layer of source rock which produces pore water, leading to overpressuring under the circumstances of sufficiently low permeability of the sediments surrounding the source layer.

The compaction model of shales was developed by Smith (1971) who derived a non-

linear compaction model which took into account the dependence of permeability on porosity and the dependence of water viscosity on salinity, temperature, and pressure. The problem considered was that of a sediment layer growing linearly in time over an impermeable basin floor. Water was considered to flow upward or downward out of a compacting rock according to Darcy's law until the pore-water pressure within the rock is normal for the depth in question. The conclusion showed that the porosity decreases during compaction until a minimum porosity is obtained which is determined by the difference between total vertical stress (overburden pressure) and pore-water pressure. But Smith's theory is restrictive in application because the compressibility law used by Smith does not include any parameter describing the intrinsic strength of the clay sediments.

The effect and coupling of variation of permeability and temperature with compaction was investigated by Sharp & Domenico (1976) and Sharp (1976) whose results are heuristic, but unfortunately technically incorrect. This mistake was finally corrected by Sharp (1983). Keith & Rimstidt (1985)'s work was similar to the earlier work by Smith but the numerical method they used encountered many difficulties in the convergence of the numerical results. Therefore, the usefulness of their results are restrictive. Bishop (1979) examined a different problem by considering the compaction states of thick abnormally pressured shales. The solution predicted the interesting characteristic of a density inversion near the overburden shale layer interface.

A two-dimensional model was first investigated by Bethke(1985) who investigated the case of the temperature dependence of material properties. Unfortunately, assumptions made in this model are not internally self-consistent, and therefore the validity of the results received severe criticism. Some related extensions were analysed by Bethke & Corbet(1988) including the porosity dependence of permeability and the specific storage. The problem of erosional unloading was treated poroelastically by Neuzil & Polluck (1983). An Athy-type constitutive law was used in most of these earlier models.

Audet & Fowler(1992) formulated a rather general mathematical model for the

non-equilibrium compaction of clay rocks in sedimentary basins. The model generalised those of earlier authors. The simplest assumptions were made concerning the rheology, but diagensis and thermal coupling were neglected. In this case, their model reduced to a generalized consolidation equation, which for the classical Darcy flow is a non-linear diffusion equation for the porosity, with a free boundary. The model was non-dimensionalized and a robust numerical method was used to solve the non-linear diffusion compaction equation. It is interesting that their results only depend on one significant dimensionless parameter, the ratio of the Darcy flow rate to the sedimentation rate. An application of Audet & Fowler's theory with a detailed parameter discussion was made by Audet & McConnell (1992) to investigate the porosity and pore pressure evolution for the one-dimensional case in sedimentary basins. Comparison with earlier works shows that the predictions of their model are consistent with well data, but it still needs further improvement in the constitutive law for the effective stress and for the permeability.

Wangen (1992) studied the pressure and temperature evolution with a model in terms of the void ratio instead of porosity. A new dimensionless parameter is introduced in this model to characterise the temperature evolution. But the coupling between the heat equation and void ratio reduction is a weak one in this model and diagenesis is not considered. Luo & Vasseur (1992) investigated the relative importance of aquathemal pressuring to geopressure development. This study shows that mechanical overloading is the control factor in the development of geopressure but the aquathermal effect is less important. Luo & Vasseur's model and their results are similar to Shi & Wang's model (1986) on pore pressure evolution. Discussion on this problem was presented by Miller & Luk (1993) and Luo & Vasseur (1993).

Diagenesis has been intensively studied in the past two decades, but the attempts of dynamical modelling of the process have been made more recently. Several theoretical and computer models have been built. The first model was developed by Helgeson (1968) to consider water-rock interactions as a system of coupled dissolution and precipitation reactions in which reactions are irreversible and partial equilibrium is assumed. Then modified models were proposed by Wolery (1979). These mod-

els were then written as software packages PATH (Helgeson, 1968) and EQ3/EQ6 (Wolery, 1979) and there are later revised versions. The main objections are that one has to make an *a priori* choice of secondary minerals and little information is provided on the time-scale of the metastable phases. Other theoretical and computer models are the REACTRAN model (Ortoleva, Merini, Moore & Chadam 1987) and the SOLMINEQ.88 model (Perkins, Kharaka, Gunter & DeBraal 1990). Such models predict successive solution compositions and amounts for the dissolved and precipitated minerals as water-rock interaction proceeds. As pointed out by Helgeson (1979) and Steefel & Cappellen (1990), the assumption of partial equilibrium is only justified where the rate of precipitation of a secondary phase is faster then the rate of dissolution. However, the precipitation of the stable insoluble minerals may be slow even on geological time scales. Therefore, more realistic dissolution and precipitation dynamic treatment is essential to diagenetic modelling. Baccar & Fritz (1993) investigated a computational geochemical model of sandstone diagenesis and its effect on porosity evolution. Their results show that diagenesis effects are very important for the evolution of porosity from the point of view of pore fluid chemistry. However, it is still difficult to form a clear mathematical model from the existing work on diagenesis.

Field investigations by Freed & Peacor (1989) in the Gulf Coast and Pearson & Small (1988) in the North Sea reveal that diagenesis occurs mainly at burial depths from 1 to 2 km in the temperature range from 69° C to 116° C. The illitization of smectite with depth in sedimentary basins is observed worldwide and represents one of the fundamental reactions in clastic diagenesis. Abercrombie, Hutcheon, Bloch & Caritat (1994) analysed the data from oceanic and sedimentary basins and suggested that the smectite-illite (S-I) reaction is closely linked to burial parameters such as temperature, time and fluid compositions. In a slow sedimentation environment, the S-I reaction may begin at temperatures as low as about 50° C, and reach completion by about 90° C, while in the rapid sedimentation environment, the S-I reaction may not begin at temperatures as high as about 120° C, and reach near completion by about 150° C.

The S-I reaction has received much attention but the nature of both the il-

lite/smectite (I/S) mixed-layer and the reaction mechanism are still under discussion, and many experiments have been carried out to investigate the kinetic features of the S-I conversion (Eberl & Hower 1976; Huang, Longo & Pevear, 1993; Abercromie, Hutcheon, Bloch & Caritat, 1994). Thermodynamic analysis shows theoretically that quartz and smectite should not coexist at temperatures between 25° and 200°C (Aagaad & Helgeson, 1983). Lasaga (1984) presented the possible range of activation energy variations for a variety of mineral dissolution reactions. Two main mechanisms have been put forward to explain the S-I reaction process. The *transformation* mechanism suggests that the S-I reaction is a transformation process through mixed-layering with (a series of) reordering processes of the intermediate mixed-layer (Hower et al, 1976). An alternative modification is a solid-state transformation mechanism without mixed-layering. The *dissolution-precipitation* mechanism involves the processes of smectite dissolution and illite precipitation without mixed-layering. According to high-resolution electromicroscopic data, the mixed-layering mechanism appears to be questionable (Chamley 1989), but Ahn & Peacor (1986) provide a seemingly convincing example of a smectite-to-illite transformation rather than a neoformation. Although there is no universal consensus, the dissolution-precipitation mechanism is theoretically favoured and is consistent with most experimental studies (Chamley, 1989; Abercromie, Hutcheon, Bloch & Caritat, 1994).

Potassium cation concentration has an important effect on the reaction rate. $K^+$ is mainly supplied by the dissolution of the K-feldspar. The characterization of K-feldspar dissolution rate may be essential for an accurate description of the overall S-I process. Four major zones were recognized in the diagenesis of oceanic sediments. The apparent lag in illite formation (in deeper zones) may reflect the rate at which the S-I reaction proceeds or the availability of potassium for illite formation. The interesting correlation with the sedimentation rate and the appreciable variability of the data clearly need more systematic work on the mathematical modelling of diagenesis and its related consequences.

The use of correct rate laws are essential to the modelling of water-rock interactions. Many experiments have been carried out to study the rate laws. However,

the laboratory data are not directly applicable to field observations. Unfortunately, the discrepancies between field estimates and laboratory measurements of reaction rates can be as large as four orders of magnitude (Swoboda-Colberg & Drever, 1993, Lasaga et al, 1994). One possibility of explaining this big difference is the effect made by coating of mineral surfaces, but this explanation is challenged by the fact that extensive etching is widely observed. The fact that diagenesis, which is still imperfectly understood, largely depends on lithology, fluid pressure, geothermal gradient and pore fluid compositions is one of the main motivations for us to develop a more realistic reaction-transport dissolution-precipitation model in the present work.

In addition, compaction and diagenesis have been treated separately in conventional studies. Most available compaction models studied mechanical compaction neglecting diagenetic reactions, while the geochemical compaction models mainly investigated diagenesis by either prescribing (static) compaction functions or simply neglecting the mechanical compaction.

In summary, the above brief review shows that existing models of compaction and diagenesis processes still need more systematical work. In this thesis, we intend to extend Audet and Fowler's (1992) work in the following ways. Firstly, mechanical compaction (such as overpressuring), diagenetic (smectite-illite) reactions and thermal history can be treated simultaneously in a three-dimensional compacting frame with a more detailed analysis of some one-dimensional cases of geological importance (chapters 2,3 and 4) Secondly, more realistic constitutive models of stress-strain behaviour can be used by employing non-Athy's type laws and introducing the hysteresis during sediment unloading based on experimental data of soils (chapter 5); Thirdly, diagenesis can be treated more properly by using more realistic diagenesis models such as the first-order dehydration model (chapter 6) and dissolution-precipitation model (chapter 7); Fourthly, other related processes such as pressure solution creep and fluid geochemistry can also be included in a unified model by utilizing a viscous compaction creep law similar to a regelative-flow (chapter 8); Finally, further modifications can be developed by considering more realistic basin type and boundary conditions (chapter 9).

# Chapter 2

# Mathematical Model

The general mathematical model of compaction and diagenesis considers the fluid-sediment system as a porous medium consisting of multiple mineral species. The interstitial volume of the porous solid phase is saturated with pore fluid. Due to the action of gravitational overburden load and the density difference between the two phases, the solid phase compacts by reducing its porosity, thus leading to the expulsion of the pore fluid out of the solid matrix. During compaction and continuous burial, the multiple mineral species react and are transported in an evolving pressure and temperature environment with a changing rheology. The fundamental underlying physical laws to be used are the conservation of mass, the conservation of energy, force balance and Darcy's law. The simple assumptions to be made are related to the rheology of the porous medium and the geochemistry of the pore fluid.

## 2.1 Audet & Fowler's Generalised Model for Compaction

The fundamental model given by Audet and Fowler (1992) can be summarised here as follows. Consider a matrix consisting of four interdispersed media: core particles (e.g. quartz), two clay minerals, (hydrated) montmorillonite and (dehydrated) illite, and free pore water. Let the volume fractions of the respective media (coarse, montmorillonite, illite, water) be $\phi_c, \phi_m, \phi_i, \phi_l$, so that

$$\phi_c + \phi_m + \phi_i + \phi_l = 1, \tag{2.1}$$

and suppose that all the solids move with the same averaged velocity $\mathbf{u}^s$, while the pore water has velocity $\mathbf{u}^l$.

**The conservation of mass equations** for the four phases will then be in the form

$$\frac{\partial}{\partial t}(\rho_c\phi_c) + \nabla\cdot(\rho_c\phi_c\mathbf{u}^s) = 0, \tag{2.2}$$

$$\frac{\partial}{\partial t}(\rho_m\phi_m) + \nabla\cdot(\rho_m\phi_m\mathbf{u}^s) = -r_m, \tag{2.3}$$

$$\frac{\partial}{\partial t}(\rho_i\phi_i) + \nabla\cdot(\rho_i\phi_i\mathbf{u}^s) = r_i, \tag{2.4}$$

$$\frac{\partial}{\partial t}(\rho_l\phi_l + \nabla\cdot(\rho_l\phi_l\mathbf{u}^l) = r_w, \tag{2.5}$$

where quartz particles are supposed inert, but clay particles can be transformed by dehydration processes which release bound water. The rate at which montmorillonite is transformed is denoted by $r_m$, and this is balanced by a production of illite at rate $r_i$, and free pore water at the rate $r_w$. In fact, the relation $r_m = r_i + r_w$ clearly results from the total conservation of mass.

Diagenesis takes place when montmorillonite ( clay particles with bound water between the platelets) releases water to the pore space and is transformed to illite. Measured rates of this process in the laboratory (Eberl & Hower 1976) suggest that at elevated temperature, this process will proceed very fast from the geological point of view. On the other hand, observations suggest that diagenesis is initiated relatively suddenly at a temperature $90^0C$ ($T_c$), but then takes place gradually over a depth of several hundred meters, which suggests a time scale of the order of a million years. This is problematic for the concept of diagenesis as a simple reaction. In fact, the mechanism of diagenesis is rather more complicated and is not simply understood. Diagenesis may take place via dissolution of montmorillonite in free pore water and the subsequent precipitation of silica as illite. **Diagenesis** is considered here as a one-step (first order) dehydration process whose validity is discused in more detail later in chapter 7 where a more realistic reaction-transport dissolution-precipitation model will be presented. However, the first-order dehydration model is a good approximation in the sense of describing the extent of progress of the overall smectite-to-illite

transformation without much concern for its detailed geochemical features. Therefore, we represent it schematically as

$$[\text{clay}]\cdot[\text{H}_2\text{O}](\text{montmorillonite})\xrightarrow{\text{k}_\text{r}}[\text{clay}](\text{illite})+\text{n}[\text{H}_2\text{O}](\text{free water}) \tag{2.6}$$

in which we suppose montmorillonite is *clay* with $n$ moles of bound water per mole of clay. From the law of mass action, the prescription of the rates is given by

$$r_m = k_r\rho_m\phi_m,\ r_i = k_r(\frac{M_i}{M_m})\rho_m\phi_m,\ r_w = k_r(\frac{nM_w}{M_m})\rho_m\phi_m, \tag{2.7}$$

where $M_m, M_i, M_w$ are the respective molecular weights with $M_m = M_i + nM_w$. The reaction rate $k_r$ is assumed to follow an Arrhenius law:

$$k_r = A\exp(-\frac{E_a}{RT}), \tag{2.8}$$

where $E_a$ is the activation energy which is about 19.6 kcal/mole (Eberl & Hower 1976) for the dehydration process, but it may vary in the range of 40-80 kJ/mol (Lasaga, 1984). $R$ is the gas constant, $T$ is the absolute temperature, and $A$ is a rate factor. Let $T_0$ be the surface temperature at the top of the basin; for $\Delta T = T - T_0 << T_0$, we have

$$\frac{E_a}{RT} = \frac{E_a}{RT_0}\cdot\frac{T_0}{T_0+\Delta T} \approx \frac{E_a}{RT_0}\cdot(1-\frac{\Delta T}{T_c}). \tag{2.9}$$

Hence, $k_r$ can also be written as

$$k_r = A\text{exp}(-\frac{E_a}{RT}) \approx k_r^0\text{exp}[\frac{E_a}{RT_0^2}(T-T_0)], \tag{2.10}$$

where

$$k_r^0 = A\text{exp}(-\frac{E_a}{RT_0}). \tag{2.11}$$

Denote the heat change per mole during the diagenesis process by $\Delta H$ , and suppose that $r_m$, $r_i$ and $r_w$ depend on the temperature and assume that the temperatures of each phase are equal, then the **energy equation** or **temperature equation** is

$$\begin{aligned}\frac{\partial}{\partial t}\{[\rho_c c_c\phi_c + \rho_m c_m\phi_m + \rho_i c_i\phi_i + \rho_l c_l\phi_l]T\} + \nabla\cdot\{[(\rho_c c_c\phi_c + \rho_m c_m\phi_m + \rho_i c_i\phi_i)\mathbf{u}^s \\ +\rho_l c_l\phi_l\mathbf{u}^l]T\} = \nabla\cdot(K_{th}\nabla T) - r_m\Delta H.\end{aligned} \tag{2.12}$$

Where $c_c$... are the various specific heats, $K_{th}$ is the average thermal conductivity.

According to Fowler (1990), **Darcy's law** takes the form

$$\phi_l(\mathbf{u}^l - \mathbf{u}^s) = -\frac{k}{\mu}(\nabla p^l + \rho_l g\mathbf{j}), \tag{2.13}$$

where $\mathbf{j}$ is the unit vector pointing vertically upwards, $k$ is the matrix permeability, $\mu$ is the liquid viscosity and $p^l$ is the pore pressure.

For a slow flow, the **force balance equation** can be written

$$\boldsymbol{\nabla} \cdot \boldsymbol{\sigma} \ - \rho g\mathbf{j} = 0, \tag{2.14}$$

where $\boldsymbol{\sigma}$ is the total stress and the density $\rho = \rho_s\phi_s + \rho_l\phi_l$ (Drew 1983). By employing the sign convention for stress in fluid dynamics and using Skempton's effective pressure relation (Skempton 1960, see equation (2.18) in next section)

$$-\boldsymbol{\sigma_e} \ = -\boldsymbol{\sigma} \ - (1-a)p^l\boldsymbol{\delta} \ , \tag{2.15}$$

the above force balance equation becomes

$$\nabla \cdot \boldsymbol{\sigma_e} \ - \nabla[(1-a)p^l] - \rho g\mathbf{j} = 0, \tag{2.16}$$

where $\boldsymbol{\sigma_e}$ is the effective stress.

## 2.2 Skempton's Effective Pressure Relation

Terzaghi (1943) was the first to suggest the principle of effective pressure. According to this, the total vertical pressure $P$ at a point in a soil medium consists of two parts. One part is carried by water and is continuous and acts with equal intensity in all direction. This is the *pore water pressure* $p^l$. The other part is the pressure carried by the soil structure and controls the deformation of the soil structure, and is thus called *effective pressure* $p_e$. Terzaghi formulated this concept as

$$p_e = P - p^l, \tag{2.17}$$

which is one of the most important principles of soil mechanics. The modern developments on compressibility of soils, shear strength, and lateral earth pressure on retaining structures are all based on Terzaghi's effective pressure concept. Despite

its importance, the relation (2.17) is only valid for saturated soils (Skempton, 1960; Bear & Bachmat, 1990) . Skempton (1960) extended this relation in a more general way, and expressed it in the form

$$p_e = P - (1 - a)p^l, \tag{2.18}$$

where $a$ is a constant. For soils, it may be in the range of 0.1 to 0.5. At pressures normally encountered in engineering and geological problems, $a$ is very small ($a \ll 1$). Thus, for fully saturated soils, Skempton's equation degenerates into the form of Terzaghi's equation (2.17) for effective pressure. This corresponds to an incompressible and purely cohesive material with $a = 0$.

## 2.3 Constitutive Laws

### 2.3.1 Rheological relation for poroelasticity

The constitutive laws that extend standard linear elasticity to poroelastic materials were originally presented by Biot (1941). The constitutive equations were reformulated by Rice & Cleary (1976) and are most frequently used in the geophysical literature. Kumpel (1991) gives a nice review of the poroelastic parameters, and more recently Wang (1993) reviews the experimental techniques for measuring the static poroelastic moduli and hydrogeologic parameters with particular emphasis on the constants that are useful for solving typical geophysical problems.

Biot's (1941) linear poroelasticity theory of saturated clay proposed an elastic **rheological constitutive relation**

$$\boldsymbol{\sigma_e} = 2G\boldsymbol{\epsilon} - (\frac{2G\nu}{1-2\nu}\nabla \cdot \mathbf{U} - \gamma p^l)\mathbf{I} \tag{2.19}$$

where $\boldsymbol{\epsilon}$ is the strain tensor with $\epsilon_{ij} = \frac{1}{2}(\partial U_i/\partial x_j + \partial U_j/\partial x_i)$, $\mathbf{U}$ is the displacement field, $\mathbf{I}$ is the second order unit tensor and $p_e$ is the effective pressure. $G = E/2(1+\nu), \nu$ are shear modulus and Poisson's ratio respectively, and $E$ is Young's modulus. The constitutive relation for porosity is taken to be

$$\phi_l - \phi_0 = \frac{1}{Q}p^l + \gamma\nabla \cdot \mathbf{U}, \tag{2.20}$$

where $\phi_0$ is the initial porosity before deformation. $Q$ and $\gamma$ are two physical constants. This relation is equivalent to an ordinary elastic medium, with the pressure defined by

$$-\frac{1}{3}\sigma_{ii} = P = \frac{1}{Q}p^l - \frac{2G(1-\nu)}{3(1-2\nu)}\nabla\cdot\mathbf{U}, \tag{2.21}$$

For a saturated clay, Biot suggests $Q=\infty$, $\gamma = 1-a$, hence

$$\phi_l - \phi_0 = \gamma\nabla\cdot\mathbf{U} = -\frac{3\gamma(1-2\nu)}{2G(1-\nu)}p_e. \tag{2.22}$$

Therefore, $p_e = p_e(\phi_l)$ which is an Athy-type law of effective pressure and porosity relation.

For the case of a linear elastic medium, the rheological constitutive relation is simplified as

$$\boldsymbol{\sigma_e} = 2G\epsilon - (p_e + \frac{2}{3}G\nabla\cdot\mathbf{U})\mathbf{I}, \tag{2.23}$$

with a constitutive relation

$$\dot{p}_e = -K_e\nabla\cdot\mathbf{u}^s, \tag{2.24}$$

where $\dot{}$ denotes $d/dt_s = \frac{\partial}{\partial t} + \mathbf{u}^s\cdot\nabla$ and $K_e$ is a constant. To follow $\boldsymbol{\sigma_e}$ with a material element, we have

$$\frac{d\boldsymbol{\sigma_e}}{dt_s} = 2G\dot{\epsilon} - (\dot{p}_e + \frac{2}{3}G\nabla\cdot\mathbf{u^s})\mathbf{I}. \tag{2.25}$$

It is worth pointing out that the rheological equation of state should be objective. That is to say, the rheological relation of stress-strain should be invariant under the coordinate transformation. This is not always guaranteed due to the complexity of the rheological relations (Bird, Armstrong & Hassager 1977). Fortunately, for one-dimensional *irrotational* flow, the equation is invariant and all the different equations in corotional and codeformational frames degenerate into the same form. In the one-dimensional case we will discuss below, we can take this for granted.

For the very simple case of a one-dimensional model, the effective stress tensor is in the form of

$$\boldsymbol{\sigma_e} = \mathrm{diag}(-\sigma_1, -\sigma_1, -\sigma_3). \tag{2.26}$$

By using equation (2.23), we have

$$\sigma_1 = (1 - \frac{2G}{3K_e})p_e \text{ and } \sigma_3 = (1 + \frac{4G}{3K_e})p_e. \tag{2.27}$$

### 2.3.2 Permeability

The permeability, for the convenience of later usage, can be expressed in the normalized form (Smith 1971)

$$k = k_0 \tilde{k}(\phi_l) = k_0 (\frac{\phi_l}{\phi_0})^m, \tag{2.28}$$

where $k_0$ and $\phi_0$ are the permeability and porosity at the top of the basin. $m$ is a positive number which characterizes how quickly the permeability decreases as the porosity is reduced. The unit of permeability is Darcy ($1D = 10^{-12}\mathrm{m}^2$). Typical values of the permeability of clays are in the range of $1.5 \times 10^{-8} \sim 1.5 \times 10^{-3}$ Darcy for the porosity range from 0.33 to 0.8 (Lambe & Whitman 1979).

### 2.3.3 Thermal conductivity

Thermal conductivities of sedimentary rocks vary with porosity. High-porosity unconsolidated rocks have low values of thermal conductivities, while nearly fully compacted sediments with low porosity have high values. To calculate the averaged thermal conductivity $K_{th}$ of a porous medium, we use a rough quasi-empirical relation (Lewis & Rose, 1970)

$$K_{th} = K_0 (\frac{K_l}{K_s})^{\phi_l - \phi_0}, \tag{2.29}$$

where $K_l$ is the thermal conductivity of pore water and $K_s$ the thermal conductivity of sediment matrix. $K_0$ and $\phi_0$ are the thermal conductivity and porosity at the top of the basin.

## 2.4 One-dimensional Model

In order to simplify the following calculations and to compare the results with earlier work, we will consider a one-dimensional compaction model in a basin $b(t) < z < h(t)$ (Fig. 2.1), where $h$ is the ocean floor and $b$ is the basement rock, instead of more general cases in two or three dimensions. This one-dimensional compaction model is applicable to the case in which the basin depth is small compared to its length and width.

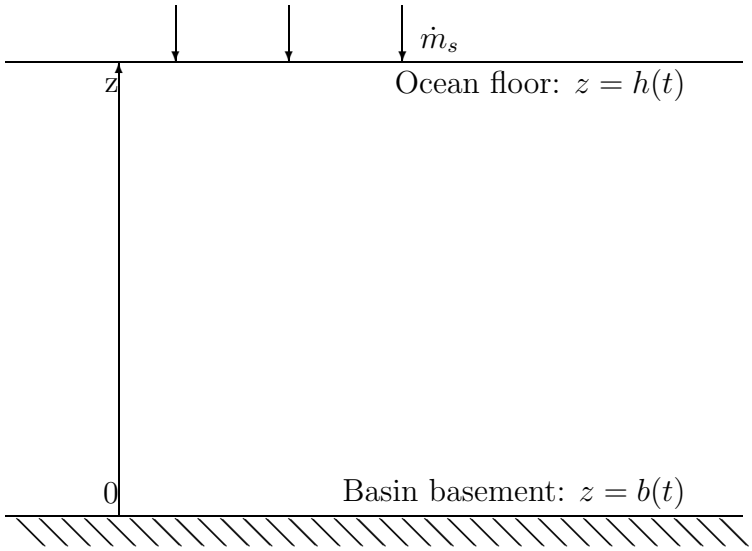


Figure 2.1 One-dimensional compacting sedimentary basin. The coordinate $z$ is directed upwards.

### 2.4.1 1-D governing equations

For convenience in the following discussion, we put $p^l = p$. We will investigate the simplest behaviour of non-linear compaction restricting our attention to the case where the solid species have density $\rho_c = \rho_m = \rho_i = \rho_s$ =constant and specific heat $c_c = c_m = c_i = c_s$ =constant. With these simplifications, we can easily obtain the governing equations from the above section.

*Mass conservation*

$$\frac{\partial \phi_c}{\partial t} + \frac{\partial}{\partial z}(\phi_c u^s) = 0, \tag{2.30}$$

$$\frac{\partial \phi_m}{\partial t} + \frac{\partial}{\partial z}(\phi_m u^s) = -k_r \phi_m, \tag{2.31}$$

$$\frac{\partial \phi_i}{\partial t} + \frac{\partial}{\partial z}(\phi_i u^s) = k_r(\frac{M_i}{M_m})\phi_m, \tag{2.32}$$

$$\frac{\partial \phi_l}{\partial t} + \frac{\partial}{\partial z}(\phi_l u^l) = k_r(\frac{n\rho_s M_w}{\rho_l M_m})\phi_m, \tag{2.33}$$

$$\phi_c + \phi_m + \phi_i + \phi_l = 1, \tag{2.34}$$

*Darcy's law*

$$\phi_l(u^l - u^s) = -\frac{k}{\mu}(\frac{\partial p}{\partial z} + \rho_l g), \tag{2.35}$$

*Energy conservation*

$$\frac{\partial}{\partial t}\{[\rho_s c_s(1-\phi_l)+\rho_l c_l \phi_l]T\}$$
$$+\frac{\partial}{\partial z}\{[\rho_s c_s(1-\phi_l)u^s+\rho_l c_l \phi_l u^l]T\} = \frac{\partial}{\partial z}(K_{th}\frac{\partial T}{\partial z}) - k_r \rho_s \phi_m \Delta H, \tag{2.36}$$

*Force balance*

$$\frac{\partial}{\partial z}[-(1+\frac{4G}{3K_e})p_e - (1-a)p] - [\rho_s(1-\phi_l)+\rho_l\phi_l]g = 0, \tag{2.37}$$

*Constitutive relation*

$$p_e = p_e(\phi_l). \tag{2.38}$$

These are nine equations for nine unknown variables: four for volume fractions $\phi_c$, $\phi_m$, $\phi_i$, $\phi_l$, two for velocities $u^s$, $u^l$, one for temperature $T$, and two for effective pressure $p_e$ and pore water pressure $p$.

In order to get an expression for $u^s$, we add the four equations of mass conservation together and thus have

$$\frac{\partial}{\partial z}[\phi_l u^l + (1-\phi_l)u^s] = k_r(\delta-1)(\frac{nM_w}{M_m})\phi_m \text{ with } \delta = \rho_s/\rho_l. \tag{2.39}$$

By using Darcy's law, the above equation becomes

$$\frac{\partial u^s}{\partial z} = \frac{\partial}{\partial z}[\frac{k}{\mu}(\frac{\partial p}{\partial z}+\rho_l g)] + k_r(\delta-1)(\frac{nM_w}{M_m})\phi_m, \tag{2.40}$$

Integrating $z$ from 0 to $z$, we obtain

$$u^s = \frac{k}{\mu}(\frac{\partial p}{\partial z}+\rho_l g) + (\delta-1)(\frac{nM_w}{M_m})\int_0^z k_r\phi_m dz + \dot{b}(t), \tag{2.41}$$

and

$$\phi_l u^l + (1-\phi_l)u^s = (\delta-1)(\frac{nM_w}{M_m})\int_0^z k_r\phi_m dz + \dot{b}(t). \tag{2.42}$$

### 2.4.2 Boundary conditions

The related boundary conditions for the nine governing equations are as follows. If we take $b(t)$ as a known boundary, but $h(t)$ as unknown, then we still require boundary conditions on $u^l, u^s, p, p_e, T$ for the equations. Obviously, the natural boundary conditions are the following:

boundary conditions at $z = b$:

$$u^s = u^l = \dot{b}; \tag{2.43}$$

a kinematic condition at $z = h$:

$$\dot{h} = \dot{m}_s + u^s, \tag{2.44}$$

where $\dot{m}_s$ is the sedimentation rate at $z = h$. Also at $z = h$,

$$\phi_l = \phi_{l0} = \phi_0, \ (\text{i.e.}, p_e = 0), \ p = p_0 \tag{2.45}$$

and

$$\phi_c = \phi_{c0}, \ \phi_i = \phi_{i0}, \ \phi_m = \phi_{m0}, \tag{2.46}$$

where $p_0$ is the overburden pressure, e.g. due to ocean depth. $\phi_{c0}$, $\phi_{i0}$, $\phi_{m0}$ and $\phi_0$ are the values at the top of basin during sedimentation.

The boundary conditions for the temperature (or energy) equation become

$$T(t = 0, z = h) = T_0 \quad \text{and} \quad \frac{\partial T}{\partial z}(t, z = b) = -\frac{q_0}{K_{th}}, \tag{2.47}$$

where $q_0$ is the heat flux at the bottom of the basin. This corresponds to a constant temperature $T_0$ at the top of the basin and a constant heat flux at the base. Equation (2.44) gives the moving boundary $h(t)$, and therefore we have the number of conditions which the equations require.

## 2.5 Non-dimensionalization

We define a length-scale $d$ by writing

$$(1 + \frac{4G}{3K_e})p_e = (\rho_s - \rho_l)gd\tilde{p}(\phi_l), \tag{2.48}$$

and require that $\tilde{p} = O(1)$. Meanwhile, we scale $z$ with $d$, $u^s$ with $\dot{m}_s$, time $t$ with $d/\dot{m}_s$, pore pressure $p$ with $(\rho_s - \rho_l)gd$, permeability $k$ with $k_0$, heat conductivity $K_{th}$ with $K_0$, temperature $T$ with $q_0 d/K_0$, $k_r$ with $k_r^0$ and $\Delta H$ with $q_0/(\dot{m}_s \rho_s)$; thus we have

$$k = k_0\tilde{k}, \ k_r = k_r^0\bar{k}_r \ \ K_{th} = K_0\hat{K}, \tag{2.49}$$

and

$$T = T_0 + \frac{q_0 d}{K_0}\Theta, \quad \Delta H = \frac{q_0}{\dot{m}_s \rho_s}\overline{\Delta H}. \tag{2.50}$$

The dimensionless form of equations (2.30)-(2.37) is then

*Mass conservation*

$$\frac{\partial \phi_c}{\partial t} + \frac{\partial}{\partial z}(\phi_c u^s) = 0, \tag{2.51}$$

$$\frac{\partial \phi_m}{\partial t} + \frac{\partial}{\partial z}(\phi_m u^s) = -\mathcal{R}\bar{k}_r \phi_m, \tag{2.52}$$

$$\frac{\partial \phi_i}{\partial t} + \frac{\partial}{\partial z}(\phi_i u^s) = \mathcal{R}\bar{k}_r (\frac{M_i}{M_m})\phi_m, \tag{2.53}$$

$$\frac{\partial \phi_l}{\partial t} + \frac{\partial}{\partial z}(\phi_l u^l) = \mathcal{R}\bar{k}_r a_1 \delta \phi_m, \tag{2.54}$$

$$\phi_c + \phi_m + \phi_i + \phi_l = 1, \tag{2.55}$$

*Darcy's law*

$$\phi_l(u^l - u^s) = -\lambda \tilde{k}(\frac{\partial p}{\partial z} + r), \tag{2.56}$$

*Energy conservation*

$$\frac{\partial}{\partial t}\{[\alpha(1-\phi_l) + \phi_l]\Theta\}$$
$$+\frac{\partial}{\partial z}\{[\alpha(1-\phi_l)u^s + \phi_l u^l]\Theta\} = \Lambda \frac{\partial}{\partial z}(\hat{K}\frac{\partial \Theta}{\partial z}) - \Lambda \mathcal{R}\bar{k}_r \phi_m \overline{\Delta H}, \tag{2.57}$$

*Force balance*

$$-\frac{\partial \tilde{p}}{\partial z} - (1-a)\frac{\partial p}{\partial z} - (1+r) + \phi_l = 0 \tag{2.58}$$

where

$$\lambda = \frac{k_0(\rho_s - \rho_l)g}{\mu \dot{m}_s}, \quad r = \frac{\rho_l}{\rho_s - \rho_l}, \tag{2.59}$$

$$\Lambda = \frac{K_0}{\rho_l c_l \dot{m}_s d}, \quad \alpha = \frac{\rho_s c_s}{\rho_l c_l}, \tag{2.60}$$

$$\mathcal{R} = \frac{k_r^0 d}{\dot{m}_s}, \quad a_1 = \frac{n M_w}{M_m}, \quad \delta = \frac{\rho_s}{\rho_l}, \tag{2.61}$$

and define

$$\psi = \int_0^z \bar{k}_r \phi_m dz, \ \text{clearly } \psi = 0 \ \text{ on } \ z = 0. \tag{2.62}$$

For the diagenesis parameter, we have

$$\bar{k}_r = \exp(\beta\Theta) \quad \text{with} \quad \beta = \frac{E_a q_0 d}{R K_0 T_0^2}, \tag{2.63}$$

where $\Theta = (T - T_0)K_0/q_0 d$ is the dimensionless temperature with reference to the surface temperature $T_0$.

The dimensionless expressions for $u^s$ and $u^l$ from (2.41) and (2.42) now become

$$u^s = \lambda\tilde{k}(\frac{\partial p}{\partial z} + r) + (\delta - 1)\delta\mathcal{R}\psi + \dot{b}, \tag{2.64}$$

$$\phi_l u^l + (1 - \phi_l)u^s = (\delta - 1)a_1\mathcal{R}\psi + \dot{b}. \tag{2.65}$$

The *boundary conditions* in the dimensionless form are

$$-\tilde{p}'(\phi_l)\frac{\partial \phi_l}{\partial z} - (1 + ar - \phi_l) = 0 \text{ at } z = b, \tag{2.66}$$

$$\begin{aligned}(1 - a)\dot{h} = (1 - a)\dot{m} - \lambda\tilde{k}[\tilde{p}'(\phi_l)\frac{\partial \phi_l}{\partial z} + (1 + ar - \phi_l)] \\ +(1 - a)(\delta - 1)(\frac{nM_w}{M_m})\mathcal{R}\psi + (1 - a)\dot{b} \text{ at } z = h.\end{aligned} \tag{2.67}$$

$$\phi_l = \phi_0, \quad \phi_c = \phi_{c0}, \ \phi_i = \phi_{i0}, \ \phi_m = \phi_{m0} \quad \text{at } z = h, \tag{2.68}$$

$$\Theta(t = 0, z = h) = 0 \quad \text{and} \quad \frac{\partial \Theta}{\partial z}(t, z = b) = -\frac{1}{\hat{K}}. \tag{2.69}$$

Here, $\dot{m}$ is the dimensionless sedimentation rate which is 1 if it is constant, or $O(1)$ if time-varying.

It is very interesting that the above derived dimensionless *porosity*, *temperature* and *diagenesis* equations are based on eight dimensionless parameters. The five parameters $r$, $\alpha$, $\delta$, $a_1$, $\beta$ are constants to some extent. The other three parameters, namely $\lambda$, $\Lambda$, $\mathcal{R}$, are the governing parameters controlling the whole evolution process. It is worth pointing out that the parameters $r$ and $\delta$ are not independent. $\lambda = k_0(\rho_s - \rho_l)g/\mu\dot{m}_s$, $\Lambda = K_0/\rho_l c_l \dot{m}_s d$ and $\mathcal{R} = k_r^0 d/\dot{m}_s$ are parameters which characterize the porosity, the temperature and diagenesis evolution, respectively. Here $k_0$ is the permeability at the top of the basin, $\mu$ is the viscosity at the top of the basin, $\rho_l$, $c_l$ are density and the heat capacity of fluid (water). The parameter $K_0$ in $\Lambda$ is the bulk heat conductivity of the sediments at the top of the basin.

## 2.6 Determination of Model Parameters

It is useful for the understanding of the solutions to get an estimate for $\lambda$, $\Lambda$ and $\mathcal{R}$ by using values taken from observations. The model parameters are chosen by referring the values given by other authors (Smith 1971, Sharp 1976, Sharp & Domenico 1976,

Eberl & Hower 1976, Bethke & Corbet 1988, Lerche 1990, Audet & Fowler 1992). The values used in the present model are $d \sim 1$ km, $k_0 \sim 1 \times 10^{-18}\,\mathrm{m}^2$, $\rho_s \sim 2.6 \times 10^3$ kg m$^{-3}$, $g \sim 10\,\mathrm{m\,s}^{-2}$, $\rho_l \sim 1 \times 10^3$ kg m$^3$, $\mu \sim 1 \times 10^{-3}$ N s m$^{-2}$, $\dot{m}_s \sim 300\,\mathrm{m\ Ma}^{-1} = 1 \times 10^{-11}$ m s$^{-1}$, $c_s \sim 500$ J Kg$^{-1}$ K$^{-1}$,$c_l \sim 4200\,\mathrm{J\,Kg}^{-1}$ K$^{-1}$, $K_0 \sim 1 \times 1.5$ W $m^{-1}$ $K^{-1}$, $T_0 \sim 280$ K, $T_c \sim 363$ K, $E_a \sim 8.18 \times 10^4$ J mol$^{-1}$ and $k_r^0 \sim 1 \times 10^{-16}$ s$^{-1}$ ; then $\beta \approx 2.3$, $\lambda \approx 1$, $\Lambda \approx 30$ and $\mathcal{R} \approx 0.01$. Therefore, $\lambda = 1$ defines a transition between the fast sedimentation ($\lambda << 1$) and slow sedimentation ($\lambda >> 1$). The parameter $\lambda$ , which is the ratio between the permeability and the sedimentation rate, governs the evolution of the pore pressure and porosity in sedimentary basins. High sedimentation rate may gives rise to excess pressures even in the basins with moderate permeability.

Similarly, the parameter $\Lambda$ also defines a transition. $\Lambda << 1$ shows that the temperature solution is dominated by the constant growth of the basin thickness due to fast sedimentation, while $\Lambda >> 1$ shows that the sedimentation rate has little influence on the temperature solution. The parameter $\mathcal{R}$ characterizes the effect of diagenesis on compaction.

An initial porosity of $\phi_0 = 0.5$ for pore water at the top of the basin has been used by other authors (Smith 1971, Sharp 1976, Bethke & Corbet 1988, Audet & Fowler 1992). Initial porosity 0.2 for montmorillonite, 0 for illite and 0.3 for quartz are used in the following computations.

## 2.7 Overpressure Definition

The hydrostatic pressure at $z$ is defined as

$$p_h = \int_z^{h(t)} \rho_l g dz. \tag{2.70}$$

The overburden pressure at $z$ is defined as

$$P = \int_z^{h(t)} [(1 - \phi_l)\rho_s + \phi_l \rho_l] g dz. \tag{2.71}$$

The excess pore pressure or abnormal overpressure $p_a$ is defined as

$$p_a = p - p_h, \tag{2.72}$$

which is the pressure in excess of the hydrostatic pressure.

By using these definitions and employing the force balance equation ( 2.58), the dimensionless differential forms of the above definitions are

$$-\frac{\partial P}{\partial z} = 1 + r - \phi_l. \tag{2.73}$$

$$-\frac{\partial p_h}{\partial z} = r. \tag{2.74}$$

$$(1-a)\frac{\partial p_a}{\partial z} = -\frac{\partial \tilde{p}}{\partial z} - (1 + ar - \phi_l). \tag{2.75}$$

It can be seen that pressure profiles can be easily calculated from the porosity profile or *compaction curve* of $\phi_l$ versus $z$. Therefore, the main target is to find evolving features of the compaction curves.

# Chapter 3

# Numerical Simulations

## 3.1 A Simple Case

In a moving frame of reference, it is obvious that $\dot{b} = 0$ can be selected, equations (2.52), (2.53), (2.54),(2.56), (2.57) and (2.58) then form a free boundary problem for $\phi_m$, $\phi_i$, $\phi_l$ and $\Theta$, depending essentially on three parameters $\lambda$, $\Lambda$ and $\mathcal{R}$. For simplicity we also take $\overline{\Delta H} = 0$ in these equations. Based on the work of Smith (1971), Sharp (1976) and Audet & Fowler (1992), we adopt the following constitutive functions:

$$\tilde{p} = \ln(\phi_0/\phi_l) - (\phi_0 - \phi_l), \tag{3.1}$$

$$\tilde{k} = (\phi_l/\phi_0)^m, \quad m = 8, \tag{3.2}$$

$$\hat{K} = (K_l/K_s)^{\phi_l - \phi_0}, \quad K_l/K_s = 0.3, \tag{3.3}$$

$$\dot{m} = 1, \quad \bar{k}_r = \exp(\beta\Theta). \tag{3.4}$$

By using these constitutive relations together with the force balance equation, and eliminating $u^s$, $u^l$ and $p$ in equations (2.56), (2.58) and (2.64), we can the obtain coupled non-linear diffusion equations for $\phi_c, \phi_m$, $\phi_l$ and $\Theta$ whose forms are suitable for numerical calculations and asymptotic analysis. These equations are

*Equations for volume fractions*

$$(1-a)\frac{\partial \phi_c}{\partial t} = -\lambda \frac{\partial}{\partial z}\{\tilde{k}\phi_c(1-\phi_l)[\frac{1}{\phi_l}\frac{\partial \phi_l}{\partial z} - (1 + \frac{ar}{1-\phi_l})]\}$$

$$-(1-a)(\delta-1)a_1\mathcal{R}(\psi\frac{\partial\phi_c}{\partial z}+\bar{k}_r\phi_c\phi_m), \tag{3.5}$$

$$(1-a)\frac{\partial\phi_m}{\partial t}=-(1-a)\mathcal{R}\bar{k}_r\phi_m-\lambda\frac{\partial}{\partial z}\{\tilde{k}\phi_m(1-\phi_l)[\frac{1}{\phi_l}\frac{\partial\phi_l}{\partial z}-(1+\frac{ar}{1-\phi_l})]\}$$

$$-(1-a)(\delta-1)a_1\mathcal{R}(\psi\frac{\partial\phi_m}{\partial z}+\bar{k}_r\phi_m^2), \tag{3.6}$$

$$(1-a)\frac{\partial\phi_l}{\partial t}=\lambda\frac{\partial}{\partial z}\{\tilde{k}(1-\phi_l)^2[\frac{1}{\phi_l}\frac{\partial\phi_l}{\partial z}-(1+\frac{ar}{1-\phi_l})]\}$$

$$+(1-a)\mathcal{R}\bar{k}_ra_1\phi_m-(1-a)(\delta-1)a_1\mathcal{R}[\psi\frac{\partial\phi_l}{\partial z}+\bar{k}_r(1-\phi_l)\phi_m], \tag{3.7}$$

*Temperature equation*

$$(1-a)[\alpha(1-\phi_l)+\phi_l]\frac{\partial\Theta}{\partial t}=(1-a)\Lambda\frac{\partial}{\partial z}(\hat{K}\frac{\partial\Theta}{\partial z})-(1-a)R\bar{k}_ra_1(\delta-\alpha)\phi_m\Theta$$

$$-(\delta-1)(1-a)a_1\psi\frac{\partial\Theta}{\partial z}-(\alpha-1)\lambda\tilde{k}(1-\phi_l)^2[\frac{1}{\phi_l}\frac{\partial\phi_l}{\partial z}-(1+\frac{ar}{1-\phi_l})]\frac{\partial\Theta}{\partial z}, \tag{3.8}$$

where

$$\lambda=\frac{k_0(\rho_s-\rho_l)g}{\mu\dot{m}_s},\ \ r=\frac{\rho_l}{\rho_s-\rho_l}, \tag{3.9}$$

$$\Lambda=\frac{K_0}{\rho_lc_l\dot{m}_sd},\ \ \alpha=\frac{\rho_sc_s}{\rho_lc_l}, \tag{3.10}$$

$$\mathcal{R}=\frac{k_r^0d}{\dot{m}_s},\ \ a_1=\frac{nM_w}{M_m},\ \ \delta=\frac{\rho_s}{\rho_l}, \tag{3.11}$$

and

$$\psi=\int_0^z\bar{k}_r\phi_m dz. \tag{3.12}$$

The related *boundary conditions* (2.66)-(2.69) become

$$\frac{\partial\phi_l}{\partial z}-\phi_l-\frac{ar\phi_l}{1-\phi_l}=0,\ \ \frac{\partial\Theta}{\partial z}=-\frac{1}{\hat{K}}\ \text{ at } z=0, \tag{3.13}$$

and

$$\phi_j(t,h(t))=\phi_{j0},\ \ (1-a)\dot{h}=(1-a)\dot{m}+\lambda\tilde{k}(1-\phi_l)[\frac{1}{\phi_l}\frac{\partial\phi_l}{\partial z}-(1+\frac{ar}{1-\phi_l})]$$

$$+(1-a)(\delta-1)a_1\mathcal{R}\psi\ \text{ at } z=h. \tag{3.14}$$

where $\phi_j=\phi_c,\phi_i,\phi_m$, or $\phi_l$; and $\phi_c+\phi_i+\phi_m+\phi_l=1$. The condition $\phi_l(t)=\phi_0$ at $z=h(t)$ is equivalent to $\tilde{p}(t)=0$ (the effective pressrue is zero).

The dimensionless form for the excess pressure (2.75) is then

$$(1-a)\frac{\partial p_a}{\partial z}=(1-\phi_l)(\frac{1}{\phi_l}\frac{\partial\phi_l}{\partial z}-1)-ar, \tag{3.15}$$

with a bounday condition $p_a = 0$ at $z = h(t)$.

It is based on these equations that the moving boundary problem will be solved numerically by using the predictor/corrector implicit finite-difference method presented by Meek & Norbury (1982), which is very robust for the non-linear parabolic equations.

## 3.2 Audet & Fowler's Case

If we set $a = 0$, $\mathcal{R} = 0$ (no diagenesis) and leave out the temperature equation in the previous section, we then get a very special case which was considered by Audet & Fowler (1992). The equation for $\phi_l$ degenerates simply to a general non-linear diffusion equation

$$\frac{\partial \phi_l}{\partial t} = \lambda \frac{\partial}{\partial z}\{\tilde{k}(1-\phi_l)^2[\frac{1}{\phi_l}\frac{\partial \phi_l}{\partial z} - 1]\} \tag{3.16}$$

$$\dot{h} = 1 + \lambda \tilde{k}(1-\phi_l)[\frac{1}{\phi_l}\frac{\partial \phi_l}{\partial z} - 1], \tag{3.17}$$

with boundary conditions

$$\frac{\partial \phi_l}{\partial z} - \phi_l = 0 \text{ at } z = 0, \tag{3.18}$$

$$\phi_l(t, h(t)) = \phi_0 \text{ at } z = h. \tag{3.19}$$

which was discussed in detail by Audet & Fowler (1992).

## 3.3 Finite Difference Approach

In order to solve the highly coupled non-linear equations in this work, an implicit numerical difference method is used (Smith 1985). The essential equations describing for porosity and temperature are of the standard non-linear parabolic form (Meek & Norbury, 1982)

$$u_t = F(x,t,u)u_{xx} + f(x,t,u,u_x). \tag{3.20}$$

The first stage gives $u^{n+1/2}$ as a solution of the following equation

$$\frac{2}{\Delta t}(u_i^{n+1/2} - u_i^n) = (\frac{1}{\Delta x^2})F(x_i, t^{n+1/2}, u_i^n)\delta_x^2 u_i^{n+1/2}$$

$$+f(x_i, t^{n+1/2}, u_i^n, \frac{1}{\Delta x}\delta_x u_i^n), \tag{3.21}$$

where $\delta_x^2 u_i = (u_{i+1} - 2u_i + u_{i-1})$ and $\delta_x u_i = (1/2)(u_{i+1} - u_{i-1})$. The second stage gives $u_i^{n+1}$ as a solution of the following equation

$$\frac{1}{\Delta t}(u_i^{n+1} - u_i^n) = (\frac{1}{2(\Delta x)^2})F(x_i, t^{n+1/2}, u_i^{n+1/2})\delta_x^2(u_i^{n+1} + u_i^n)$$

$$+f(x_i, t^{n+1/2}, \frac{1}{\Delta x}\delta_x u_i^{n+1/2}). \tag{3.22}$$

The convergence is second-order in space for this method, and $O(\Delta t)^{2-\epsilon}$ in time, where $\epsilon$ is a small number less than $1/2$.

The computational convergence of the calculation of this method has been tested by 1) changing the grid number from 5 to 1000 in space and from 10 to 5000 in time, and by 2) comparing with the results of asymptotic results. The changes of grid intervals all result in the same converged results which conform well to the asymptotic solutions. This shows that this method is robust for the solution of the equations encountered in our problems.

## 3.4 Numerical Results

By using the above mentioned implicit numerical method, we can solve the equations numerically for various values of $\lambda$, $\Lambda$, $\mathcal{R}$ and $\beta$. We used a normalized grid parameterized by the fixed domain variable $Z = z/h(t)$. This will make it easy to compare the results of different times and different depths with different values of dimensionless parameters in a fixed frame. This transformation maps the basement of the basin to $Z = 0$ and the basin top to $Z = 1$. The numerical method was first tested in MATLAB and later transformed to FORTRAN codes with double precision. The calculations were mainly implemented for the time evolutions in the range of $t = 0.5 \sim 10$ since the thickness in the range of 0.5km $\sim$ 10km is the one of interest in the petroleum industry and in civil engineering. Preliminary numerical results are presented and explained briefly below.

### 3.4.1 Comparison with Audet & Fowler's results

In Audet & Fowler's case ($a = 0$ and $\mathcal{R} = 0$), we get a moving boounadry problem (3.16) (Section 3.2). Solving this problem with different values of $\lambda$ and time $t$, we have the following numerical results.

**Porosity evolution** with different $\lambda$ values, corresponding to different sedimentation rates, are calculated. The numerical results are shown in Fig. 3.1 for different values of $\lambda = 0.01$, 0.1, 1, 10, 100, at a fixed time $t = 5$.

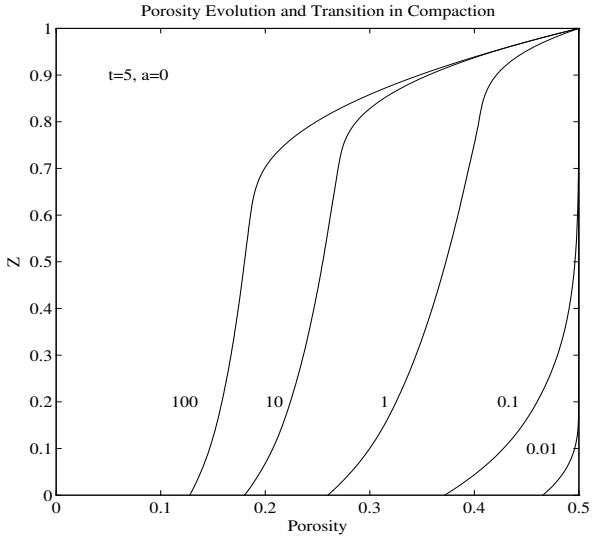


Figure 3.1 Porosity evolution with different values of $\lambda$ or sedimentation rates. $Z$ is scaled height, and the different values of $\lambda$ are given along the curves. This figure shows that porosity evolution is essentially controlled by $\lambda$. A porosity boundary layer develops near the basement in a rapid sedimentation environment ($\lambda = 0.01$) while porosity decreases nearly exponentially in a slow sedimentation environment ($\lambda = 100$).

For the case of $\lambda = 100$ in Fig. 3.2 and $\lambda = 0.01$ in Fig. 3.3, different results for different evolution times are plotted as porosity versus depth. Fig. 3.2 and Fig. 3.3 are essentially the same results as those discussed by Audet & Fowler (1992). It is clearly seen in Fig. 3.2 that there exists a travelling wave solution of porosity $\phi$ for the large $\lambda$ case in the top region where the porosity profile is only a function of depth $z - h(t)$. On the other hand, a boundary layer develops near the basement in Fig. 3.3 for the case of small $\lambda$.

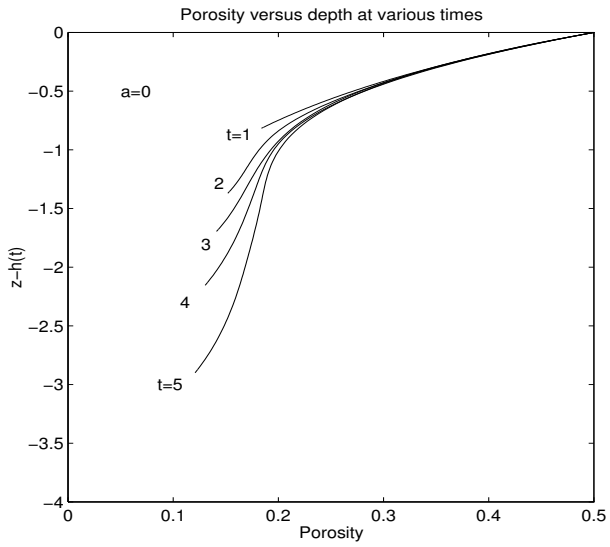


Figure 3.2 Porosity versus depths at various times with a fixed value of $\lambda = 100$. $z - h(t)$ is the depth measured from the basin top.

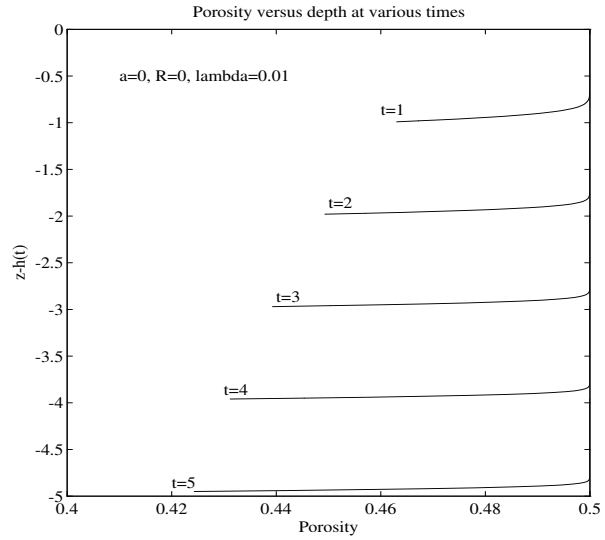


Figure 3.3 Porosity versus depths at various times $t$ for $\lambda = 0.01$. $z - h(t)$ is the depth measured from the basin top.

The results in Fig. 3.1-3.3 show that the parameter $\lambda$ is the most important dimensionless parameter controlling the degree of compaction and overpressure. In the case of high permeability and low sedimentation rate ($\lambda >> 1$), the pore water will leave the sediments at almost the *same* rate as the increase in the overburden load. The sediment column will remain nearly hydrostatic and the compaction will be almost maximal. Thus, porosity decreases nearly exponentially in the top region.

While, in the opposite case, with low permeability and high sedimentation rate ($\lambda << 1$), the water is nearly unable to escape from the sediments at the *same* rate as the increase in the overburden load. Water gets trapped in the pores, water pressure builds up, and the compaction is very small. This results in a porosity boundary layer near the basement.

**Effects of $a$ on porosity** are computed. Fig. 3.4 gives the results of different values of $a = 0, 0.3, 0.6, 0.9$ for the same evolution time $t = 5$ with values of $\lambda = 1$, $\Lambda = 1$ and $\mathcal{R} = 0$. This clearly shows that $a$ has a significant effect on porosity. In the extreme case, $a = 1$, which corresponds to the elastic *perfectly-compacted* rock sediments, the porosity will be zero at all depths.

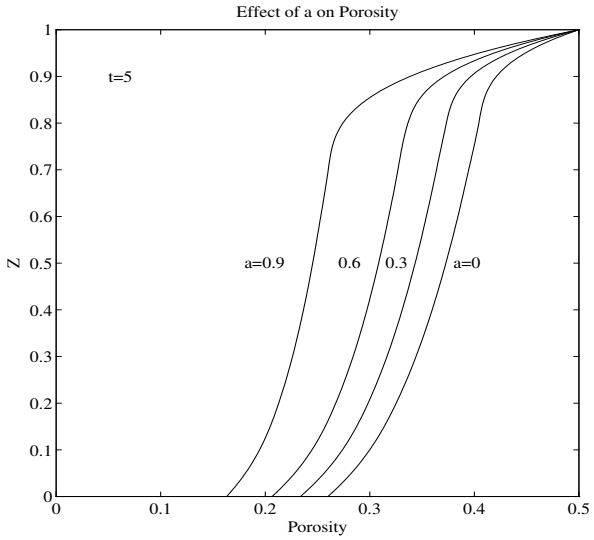


Figure 3.4 Effect of $a$ on porosity for $\lambda = 1$ and $t = 5$. $Z$ is scaled height, and the different values of $a$ are given along the curves. This clearly shows that $a$ has a significant effect on porosity evolution.

**Basin thickness** is calculated for different values of $\lambda = 0.1, 1, 10$ for the case of $t \leq 10$ with all the other values fixed as before.

The results in Fig 3.5 demonstrate that the thickness of the basin for different sedimentation rates is always nearly linear, but the slopes can vary (0.98, 0.68, 0.59 respectively for $\lambda$=0.01, 1, 100).

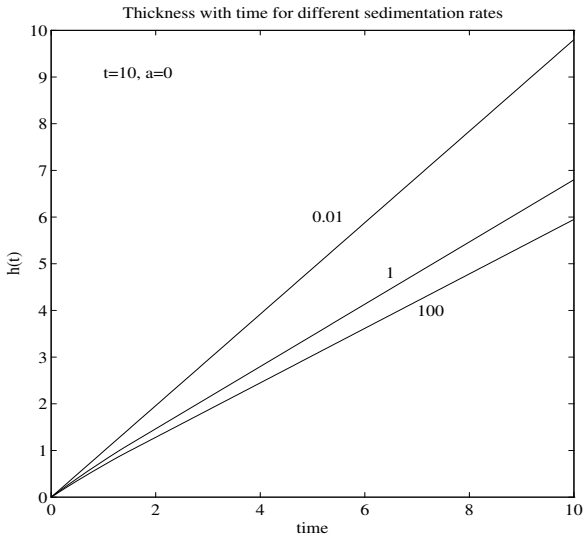


Figure 3.5 Thickness $h(t)$ versus time $t$ at different sedimentation rates ($\lambda = 0.01, 1, 100$), with a initial value of $h(0) = 0$. $h(t)$ increases almost linearly at longer times.

**Subsidence and fluid flow** velocity are presented in Fig. 3.6. The solid velocity at the top of the basin shows the compaction-driven subsidence velocity of the basin top. The fluid velocity $u^l$ and Darcy velocity (dashed curve) shows the compaction-driven fluid flow fields at different depths.

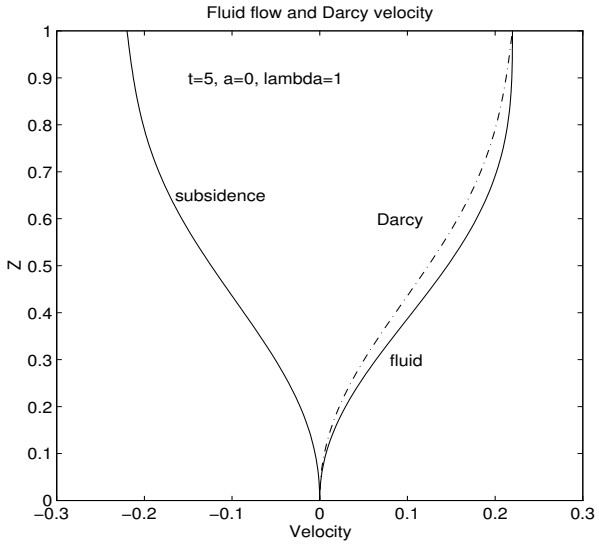


Figure 3.6 Subsidence velocity $u^s$ (solid), fluid velocity $u^l$ (solid) and Darcy velocity $\phi(u^l - u^s)$ (dashed) versus scaled height $Z$ at time $t = 5$ for $\lambda = 1$.

### 3.4.2 The development of excess pressure

The overburden ($P$), hydrostatic ($p_h$) and pore ($p$) pressures are calculated for two cases of $\lambda = 0.01$ and $\lambda = 100$. The results are shown in Fig. 3.7 and Fig. 3.8, respectively.

Figure 3.7 shows that the water is almost unable to escape from the sediments at the *same* rate as the increase in the overburden load in the case of low permeability or high sedimentation rate ($\lambda << 1$). Fluid gets trapped in the pores, pore water pressure builds up, and the compaction is very small. The excess pressure develops proportionally to basin thickness.

Figure 3.8 shows that pore water will leave the sediments at almost the *same* rate as the increase in the overburden load in the case of high permeability or low sedimentation rate ($\lambda >> 1$). The sediment column will remain nearly hydrostatic and the compaction will be almost maximal. Excess pressure does not occur for short times or in the top region but may develop at large times in the lower region.

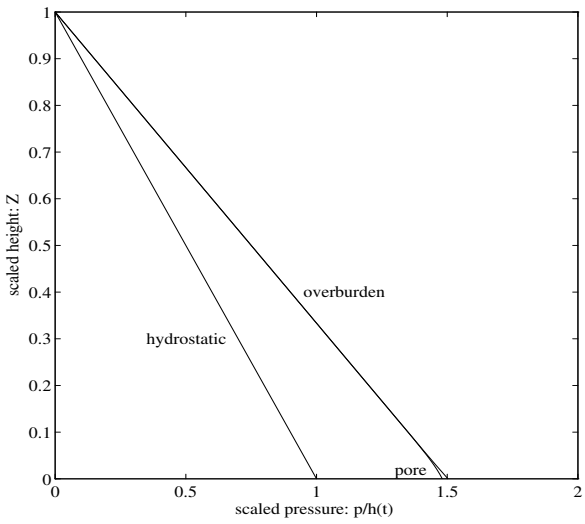


Figure 3.7 Hydrostatic, pore and overburden pressures at $t = 5$ for the case of $\lambda = 0.01$. Because water is almost unable to escape from the sediments at the same rate as the burial, water gets trapped in the pores and pore pressure builds up.

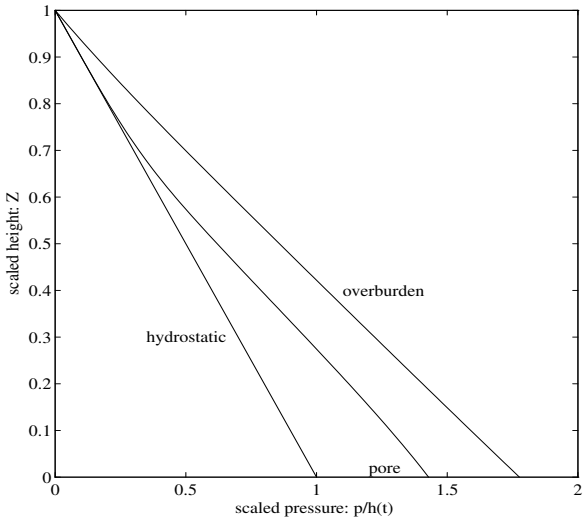


Figure 3.8 Hydrostatic, pore and overburden pressures at $t = 5$ for the case of $\lambda = 100$. Excess pressure does not occur for short times or in the top region but may develop at large times in the lower region.

### 3.4.3 Temperature evolution

For simplicity, we now put $\mathcal{R} = 0$, $a = 0$, $\phi = \phi_l$, then the governing equation for temperature evolution becomes

$$[\alpha(1-\phi)+\phi]\frac{\partial\Theta}{\partial t} = \Lambda\frac{\partial}{\partial z}(\hat{K}\frac{\partial\Theta}{\partial z})$$
$$-(\alpha-1)\lambda\tilde{k}(1-\phi)^2(\frac{1}{\phi}\frac{\partial\phi}{\partial z}-1)\frac{\partial\Theta}{\partial z}, \tag{3.23}$$

with *boundary conditions*

$$\frac{\partial\Theta}{\partial z} = -\frac{1}{\hat{K}} \quad \text{at} \quad z = 0, \tag{3.24}$$

and

$$\Theta = \Theta_0, \;\; \dot{h} = 1 + \lambda\tilde{k}(1-\phi)(\frac{1}{\phi}\frac{\partial\phi}{\partial z}-1)\text{at } z = h. \tag{3.25}$$

This is a moving boundary problem which can be solved numerically.

**Temperature profile** for values $\Lambda = 0.1, 1, 10$ is shown in Fig. 3.9 with other parameters fixed ( $t = 5$, $a = 0$, $\alpha = 0.3, \lambda = 1$, $\mathcal{R} = 0$).

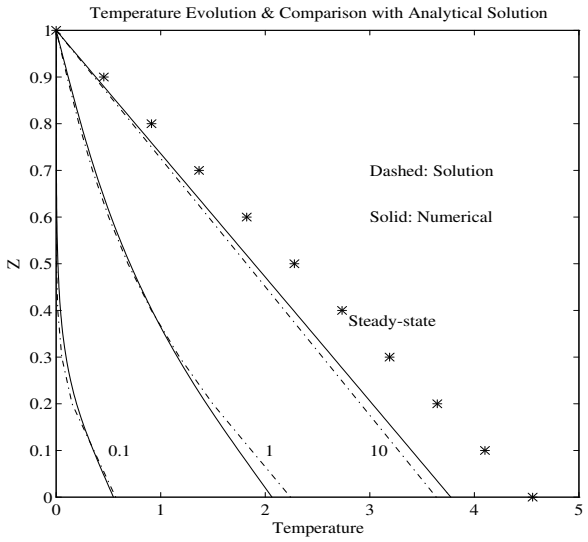


Figure 3.9 Comparison of analytical solutions (dashed) for temperature evolution with numerical results (solid) for different values of $\Lambda = 0.1$, 1, 10. $Z$ is scaled height. The asterisk (*) corresponds to the steady-state solution.

The non-linearity seen in Fig. 3.9 for $\Lambda = 0.1$ is due to the effect of the fast moving boundary and the conductivity function $\hat{K}(\phi_l)$. The calculations show that the heat convection term in equation (3.23) has no significant effect on the temperature evolution. This result is in accordance with other authors (Bethke, 1985, Deming, Nunn & Evans, 1990) who have pointed out that convective heat transfer is less important in the one-dimensional compaction models, but may be important in two- or three-dimensional models with lateral fluid flow.

### 3.4.4 Heat conduction with constantly moving boundary

From the numerical simulations, we see that the heat convection term has no significant effect on the changes of temperature evolutions. This can be understood from the fact that the second term on right hand side of equation (3.23) is equivalent to $(\alpha - 1)(1 - \phi)u^l \partial\Theta/\partial z$. This means that there is no significant difference in the temperature profiles when $\alpha$ changes from 0.3 to 1. The analysis in the next chapter will show that the convective term is $O(\lambda) << 1$ for slow compaction ($\lambda << 1$), while for fast compaction ($\lambda >> 1$), Athy's solution suggests that $\phi_z/\phi \approx 1$, then the convec-

tive term is also small compared to the conduction term. In addition, the numerical results in Section 3.4.1 show that $h(t)$ almost linearly depends time $t$. Therefore, we will mainly concentrate on the solutions of the standard equation of heat conduction with a constantly moving boundary. To approximate this, let $h(t) = Ut$. For $\lambda << 1$, $U \approx 1$; for $\lambda >> 1$ then $U \approx 0.59$. To simplify the analysis, we assume $\alpha = 1$ and $\hat{K}$ =constant, then the temperature equation becomes

$$\frac{\partial \Theta}{\partial t} = \Lambda \hat{K} \frac{\partial^2 \Theta}{\partial z^2} \tag{3.26}$$

with

$$\Theta(t, z = h) = 0 \text{ and } \frac{\partial \Theta}{\partial z}(t, z = 0) = -\frac{1}{\hat{K}}. \tag{3.27}$$

This is a diffusion equation with a specified moving boundary. The solution of this problem can be constructed by employing Green's function method and using the method similar to Gibson's (1958) approach for a consolidation problem with a constantly increasing thickness. We assume the solution of the following form

$$\Theta(z,t) = \frac{2(\Lambda \hat{K} t)^{1/2}}{\hat{K}} \text{ierfc}[\frac{z}{2(\Lambda \hat{K} t)^{1/2}}]$$
$$-\frac{1}{2(\pi \Lambda \hat{K} t)^{1/2}} \int_0^\infty g(\zeta)[\exp(-\frac{(z-\zeta)^2}{4\Lambda \hat{K} t}) - \exp(-\frac{(z+\zeta)^2}{4\Lambda \hat{K} t})]d\zeta, \tag{3.28}$$

where $\text{ierfc}(\zeta) = \frac{1}{\sqrt{\pi}} e^{-\zeta^2} - \zeta \text{erfc}(\zeta)$, and $\text{erfc}(\zeta) = 1 - \frac{2}{\sqrt{\pi}} \int_0^\zeta e^{-\eta^2} d\eta$.

It is easy to check that the above solution satisfies the temperature equation and the boundary condition at $z = 0$. Therefore, we are at liberty to regard $g(\zeta)$ as an arbitrary function which must be chosen to satisfy the upper boundary condition at $z = h(t)$. This requirement is met if $g(\zeta)$ satisfies

$$(4\pi)^{1/2} \Lambda t \text{ ierfc}[\frac{h(t)}{2(\Lambda \hat{K} t)^{1/2}}] \exp(\frac{h^2}{4\Lambda \hat{K} t})$$
$$= \int_0^\infty g(\zeta) \sinh \frac{\zeta h(t)}{2\Lambda \hat{K} t} \cdot \exp(-\frac{h^2 \zeta^2}{4\Lambda \hat{K} t}) d\zeta. \tag{3.29}$$

By substituting $h(t) = Ut$, changing the variable $\zeta^2 = \eta$, $t = 1/4\Lambda \hat{K} \tau$ and using the Laplace integral technique, we obtain

$$g(\zeta) = \frac{(\pi)^{1/2}}{2\hat{K}} \text{cosech} \frac{U\zeta}{2\Lambda \hat{K}}$$

$$\cdot\frac{1}{2\pi i}\int_{Br}\frac{1}{\tau}\text{ierfc}[(\frac{U^2}{16\Lambda^2\tau})^{1/2}]\exp(\frac{U^2}{16\Lambda^2\tau}+\tau\zeta^2)d\tau. \tag{3.30}$$

Substituting this back into the solution, we will have an integral form of the solution. The calculation of the integral is still rather complicated. In order to compare the analytical solution with the numerical results, we can approximate this moving boundary problem as a slab with an increasing thickness with time. By employing the solution for heat conduction of slab with fixed thickness and replacing the thickness by $h(t) = Ut$, we have

$$\Theta(z,t) = (\frac{4\Lambda t}{\hat{K}})^{1/2}\sum_{n=0}^{\infty}(-1)^n\{\text{ierfc}[\frac{2nUt+z}{2(\Lambda\hat{K}t)^{1/2}}] - \text{ierfc}[\frac{(2n+2)Ut-z}{2(\Lambda\hat{K}t)^{1/2}}]\}, \tag{3.31}$$

with

$$0 < z < Ut.$$

This is easy to calculate and the sum of the first several terms gives enough accuracy to compare with the numerical results. Now we consider two special cases.

**Slow conduction ($\Lambda << 1$)**

In this case, only the first term in the terms when $n = 0$ in the above solution is dominant. All the other term vanish very quickly. This corresponds to the semi-infinite space solution for the heat conduction with a constant heat flux at $z = 0$ (Carslaw & Jaeger 1959). That is

$$\Theta(z,t) = (\frac{4\Lambda t}{\hat{K}})^{1/2}\text{ierfc}\frac{z}{2(\Lambda\hat{K}t)^{1/2}}. \tag{3.32}$$

**Fast conduction ($\Lambda >> 1$)**

When $\Lambda >> 1$, the temperature will quickly reach a steady-state. The temperature equation is approximately

$$\frac{\partial^2\Theta}{\partial z^2} = 0, \tag{3.33}$$

with

$$\Theta(t, z = Ut) = 0 \text{ and } \frac{\partial\Theta}{\partial z}(t, z = 0) = -\frac{1}{\hat{K}}. \tag{3.34}$$

The solution for the equation can be easily obtained. We have the steady state solution

$$\Theta(z,t) = \frac{Ut-z}{\hat{K}}. \tag{3.35}$$

The comparison of the above temperature solution is given in Fig. 3.9. The dashed curves are the asymptotic solutions, the asterisk ($*$) corresponds to the data of steady state solution, and the solid lines are the numerical results. It is clearly seen in this figure that they all are consistent.

### 3.4.5 Effect of diagenesis

**Effect of diagenesis** on compaction: illite & montmorillonite fractions in Fig. 3.10 show illite formation and the montmorillonite diagenesis process. Values of $\lambda = 1, \Lambda = 1, \mathcal{R} = 0.01, a = 0.3, n = 10$ and $t = 5$ have been used. The extent and speed of diagenesis essentially depend on the temperature and residence time of diagenetically active temperature. Diagenesis proceeds more efficiently and fully at a higher temperature and deeper burial depth than that at a lower temperature and shallower region.

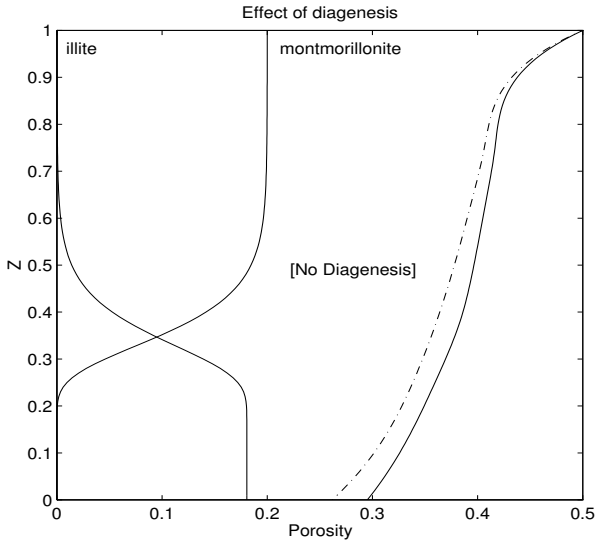


Figure 3.10 Effect of diagenesis on compaction. $Z$ is the scaled height. Dashed curve corresponds to the solution for the case of no diagenesis. Mechanical compaction is clearly the main important factor controlling the porosity evolution while diagenesis is of secondary importance with this choice of parameter values.

This figure presents a more complete and full view of porosity evolution during diagenesis. From this figure, we see that mechanical compaction is the most important

factor controlling the porosity evolution, while diagenesis is also a very important factor, but it is in the secondary position.

In this chapter, we have only provided some numerical results for the cases of geological importance to indicate some features of the compaction and diagenesis processes. A mathematical analysis of the model is the main purpose of the following chapters.

# Chapter 4

# Asymptotic Analysis and Comparison

Despite the importance of compaction, few analytical solutions are available for situations of practical importance. Gibson (1958) obtained a solution in terms of excess pressure with prescribed constant moving boundary. This solution is most commonly used in the literature for linear compaction theory. Audet & Fowler (1992) obtained two asymptotic solutions for the case of $\lambda >> 1$ and $t >> 1$, and for the case of $\lambda << 1$. But these solutions do not fall into the time ranges of geological interest. In fact, the useful solutions for the evolutionary history are those with $t = O(1)$. Hence the main purpose in this chapter is to extend Audet & Fowler's work to the geologically relevant situations of smaller times.

In order to verify the validity of the numerical results, we will use an asymptotic analysis to give an approximate description of the different cases corresponding to different values of the dimensionless parameters and compare the numerical results with the approximate solutions with the same parameters. The analysis is mainly based on the relative size of $\lambda$ and $m$. The analsysis is further elaborated in Fowler & Yang (1997) who investigate slow and fast compaction in sedimentary basins and the related geological significance.

## 4.1 Non-linear Diffusion Equation for Porosity Evolution

We now neglect diagenesis ($\bar{k}_r = 0$ or $\mathcal{R} = 0$) and let $a = 0$, and restrict our attention to a single solid species. Let $\phi = \phi_l$ be the porosity, then the porosity equation (3.16)-(3.19) degenerates into a general non-linear diffusion equation

$$\frac{\partial \phi}{\partial t} = \lambda \frac{\partial}{\partial z}\{\tilde{k}(1-\phi)^2[\frac{1}{\phi}\frac{\partial \phi}{\partial z} - 1]\} \tag{4.1}$$

$$\tilde{k} = (\phi/\phi_0)^m, \;\; m >> 1, \tag{4.2}$$

$$\dot{h} = 1 + \lambda \tilde{k}(1-\phi)[\frac{1}{\phi}\frac{\partial \phi}{\partial z} - 1], \tag{4.3}$$

with boundary conditions

$$\phi_z - \phi = 0 \text{ at } \; z = 0, \tag{4.4}$$

$$\phi = \phi_0 \text{ at } \; z = h. \tag{4.5}$$

This is a non-linear diffusion problem with a free boundary, whose behaviour is essentially controlled by the dimensionless parameter $\lambda$.

## 4.2 Analysis

From the parameter estimation, we understand that values of $\lambda$ will usually lie in the range $10^{-2} - 10^3$. Since $\lambda$ is the controlling parameter which characterises the compaction behaviour, we can therefore expect that $\lambda = 1$ defines a transition between slow sedimentation $\lambda >> 1$ and fast sedimentation $\lambda << 1$, and that the evolution features of fast and slow compaction may be also quite different.

### 4.2.1 Slow compaction ($\lambda << 1$)

For $\lambda << 1$ and $z \sim 1$, the $\phi$ equation implies that $\partial\phi/\partial t \approx 0$, with $\phi[h(t)] = \phi_0$, therefore, $\phi \approx \phi_0$ and $\tilde{k} \approx 1$. The outer solution $\phi \approx \phi_0$ does not satisfy the boundary condition at the base $z = 0$, which implies that there exists a boundary layer near $z = 0$. From the numerical results, and the fact that $\lambda << 1$ corresponds to the fast

sedimentation case, we then can write the $\phi$ equation in the form in terms of rescaled inner variable $\zeta$

$$\frac{\partial \phi}{\partial t} = \frac{\partial^2 \phi}{\partial \zeta^2}, \quad \zeta = \frac{z}{\sqrt{\lambda'}}, \quad \lambda' = \frac{\lambda}{1-a}\frac{(1-\phi_0)^2}{\phi_0}, \tag{4.6}$$

with boundary conditions

$$\frac{\partial \phi}{\partial \zeta} - \sqrt{\lambda'}\phi = 0 \ \text{ on } \ \zeta = 0, \tag{4.7}$$

$$\phi \to \phi_0 \ \text{ as } \ \zeta \to \infty. \tag{4.8}$$

This $\phi$ equation is equivalent to the case of heat conduction in a semi-infinite space with a radiation boundary at $z = 0$ and with a far field matching condition (equivalent to the initial temperature condition). The solution can be easily obtained by the standard Laplace transformation method (Carslaw & Jaeger 1959)

$$\phi = \phi_0 \text{erf}[\frac{z}{(4\lambda' t)^{1/2}}] + \phi_0 e^{z+\lambda' t}\text{erfc}[\frac{z}{(4\lambda' t)^{1/2}} + (\lambda' t)^{1/2}]. \tag{4.9}$$

This solution shows that for the case of $\lambda << 1$, the sedimentation is so fast that the compaction can only develop in a small range near the basin basement with a thickness proportional to $\sqrt{\lambda' t}$. When $a = 0$, we are in the case discussed by Audet & Fowler (1992) with a similarity solution (their equation (5.26)).

Audet & Fowler's solution (5.26) is in fact equivalent to the case of conduction in a semi-infinite space with a constant flux $\phi_z = \phi_0$ at $z = 0$ into the medium with zero 'temperature'. The solution of this case can be expressed exactly as (Carslaw & Jaeger 1959)

$$\phi = \phi_0 - \phi_0\sqrt{4\lambda' t}\ \text{ierfc}(\xi), \quad \xi = \frac{z}{\sqrt{4\lambda' t}} = \frac{z}{2(1-\phi_0)}\sqrt{\frac{\phi_0}{\lambda t}}, \tag{4.10}$$

where

$$\text{ierfc}(\xi) = \frac{1}{\sqrt{\pi}}e^{-\xi^2} - \xi\text{erfc}(\xi). \tag{4.11}$$

This solution is essentially the same solution as equation (5.26) given by Audet & Fowler (1992). Audet & Fowler's solution is only an approximation with a constant flux boundary, which is accurate if $\sqrt{\lambda' t} << 1$. As $\lambda << 1$, we expect that this solution is a good approximation when $t \leq O(1)$. If $t$ is large, then this solution

will break down. But the solution (4.9) will hold uniformly for all time. In fact, if $\sqrt{\lambda' t} << 1$, Both equation (4.9) and Audet & Fowler's equation will approximately predict the same value at $z = 0$ (i.e. $\xi = 0$)

$$\phi(z = 0) \approx \phi_0 - \phi_0 \sqrt{\frac{4\lambda' t}{\pi}}. \tag{4.12}$$

When $\xi$ is large ($\xi \to \infty$), by using the asymptotic expansion of erf($\xi$) (Hinch 1991)

$$\text{erf}(\xi) = 1 - \frac{e^{-\xi^2}}{\xi\sqrt{\pi}}(1 - \frac{1}{2\xi^2} + ...) \quad \text{with} \quad \xi \to \infty, \tag{4.13}$$

and $\xi >> \sqrt{\lambda' t}$, we can write both solutions in the same approximate expression

$$\phi \approx \phi_0 - \phi_0 \frac{\sqrt{4\lambda' t}}{2\xi^2\sqrt{\pi}} e^{-\xi^2}. \tag{4.14}$$

The comparison of the above solution with the numerical results is given in Fig. 4.1. This shows the good agreement between the solution (4.9) and the numerical results. The agreement between Audet & Fowler's solution and the numerical results is almost the same as the solution (4.9) when $t$ is small, but it clearly gets worse when $t$ becomes larger.

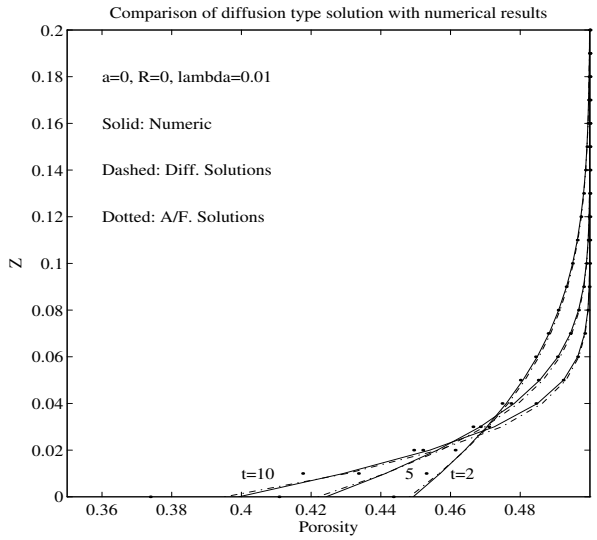


Figure 4.1 Comparison of analytical solutions with numerical results (solid) ($\lambda = 0.01$). The diffusion solution (4.9) (dashed) and Audet & Fowler's solution (dotted) are plotted versus the scaled height $Z$ at different values of time $t$.

The comparison suggests that the mechanism of porosity evolution for the case of $\lambda << 1$ is essentially controlled by the diffusion mechanism. In the present case, the problem is equivalent to the case of heat radiation into a semi-infinite space at $z = 0$.

The overburden, hydrostatic and excess pore pressures satisfy, respectively,

$$-\frac{\partial P}{\partial z} = 1 + r - \phi, \tag{4.15}$$

$$-\frac{\partial p_h}{\partial z} = r, \tag{4.16}$$

$$-\frac{\partial p_a}{\partial z} = (1-\phi)(1-\phi_z/\phi). \tag{4.17}$$

For the case of $\lambda << 1$, we substitute the solution (4.9) into (4.17) and integrate from $h(t)$ to $z$ with a boundary condition $p_a = 0$ at the top $z = h(t)$, to obtain

$$p_a = (1-\phi_0)(h-z) - (1-\phi_0)[\mathrm{erf}(h) - \mathrm{erf}(z)]$$

$$-(1-\phi_0)[\mathrm{erfc}(\frac{h}{\sqrt{4\lambda' t}} + \sqrt{\lambda' t})e^{h+\lambda' t} - \mathrm{erfc}(\frac{z}{\sqrt{4\lambda' t}} + \sqrt{\lambda' t})e^{z+\lambda' t}]. \tag{4.18}$$

This solution gives the leading order solution $p_a \approx (1-\phi_0)(h-z)$. The other terms are only small corrections. The excess pressure develops proportionally to basin thickness.

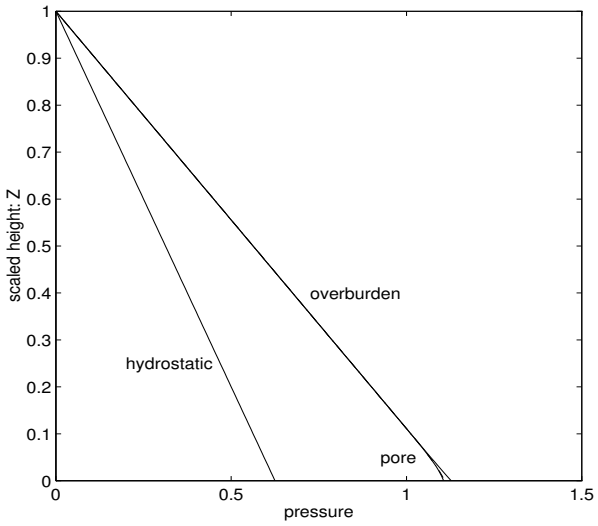


Figure 4.2 Hydrostatic, pore and overburden pressures at $t = 5$ for $\lambda = 0.01$. Solid lines correspond to numerical results, the dashed line is calculated from solution (4.18). The numerical and analytical results are indistinguishable.

The comparison of the above solution with the numerical results is plotted in Fig. 4.2. The pressure is rescaled in such a way that $p_h = r(\approx 0.6)$ at the base. It can be seen that the agreement is very good, and that for $\lambda << 1$, overpressure is essentially proportional to basin thickness.

### 4.2.2 Fast compaction ($\lambda >> 1$)

From the above $\phi$ equation (4.1), it is clearly seen that the control parameter $\lambda$ is always combined with $\tilde{k}$. This suggests that $\lambda\tilde{k} = 1$ will define a transition for the $\phi$ solutions. This condition gives equivalently a critical value of $\phi^*$

$$\phi^* = \phi_0 e^{-\frac{1}{m}\ln\lambda}. \tag{4.19}$$

Thus $\phi > \phi^*$ corresponds to $\lambda\tilde{k} >> 1$ which is the range of $z \sim h(t)$ at the top of the basin, while $\phi < \phi^*$ corresponds to $\lambda\tilde{k} << 1$ which is the range near the bottom of the basin. The features of the solution in these two ranges can be expected to be different. For $t$ less than a critical value $t_0$, there is not enough time for compaction to proceed, then we will have $\phi > \phi^*$ everywhere, so that the low $\lambda\tilde{k}$ regime will only exist for $t > t_0$.

### 4.2.3 Compaction of thin sediment layers ($\phi > \phi^*$ with $t < t_0$)

When $\lambda$ is large, the problem is one of singular perturbation type. We will assume expansions of the form

$$\phi = \phi^{(0)} + \frac{1}{\lambda}\phi^{(1)} + \frac{1}{\lambda^2}\phi^{(2)} + ..., \tag{4.20}$$

$$h = h^{(0)} + \frac{1}{\lambda}h^{(1)} + \frac{1}{\lambda^2}h^{(2)} + .... \tag{4.21}$$

Substituting the above expansions into (4.1), and equating the coefficients of powers of $1/\lambda$, we have

$$\frac{\partial}{\partial z}\{\tilde{k}^0(1-\phi^{(0)})^2[\frac{1}{\phi^{(0)}}\phi_z^{(0)} - 1]\} = 0, \tag{4.22}$$

$$\phi_t^{(0)} = \frac{\partial}{\partial z}\{\tilde{k}^0(1-\phi^{(0)})^2\frac{1}{\phi^{(0)}}[\phi_z^{(1)} - \frac{\phi^{(1)}}{\phi^{(0)}}\phi_z^{(0)}]\}, \tag{4.23}$$

$$\phi_t^{(1)} = \frac{\partial}{\partial z}\{\tilde{k}^0(1-\phi^{(0)})^2\frac{1}{\phi^{(0)}}[\phi_z^{(2)} - \frac{\phi^{(2)}}{\phi^{(0)}}\phi_z^{(0)}]\}, ..., \tag{4.24}$$

where $\tilde{k}^0 = (\phi^{(0)}/\phi_0)^m$. The boundary conditions become

at $z = h^{(0)}$

$$\phi^{(0)} = \phi_0,$$

$$\phi^{(1)} + h^{(1)}\phi'^{(0)} = 0,$$

$$\phi^{(2)} + \frac{1}{2}h^{(2)}\phi''^{(0)} = 0, ..., \tag{4.25}$$

at $z = 0$

$$\phi_z^{(0)} = \phi^{(0)},$$

$$\phi_z^{(1)} = \phi^{(1)},$$

$$\phi_z^{(2)} = \phi^{(2)}, ..., \tag{4.26}$$

with

$$\dot{h}^{(0)} = 1 + \tilde{k}^0(1-\phi^{(0)})\frac{1}{\phi^{(0)}}[\phi_z^{(1)} - \frac{\phi^{(1)}}{\phi^{(0)}}\phi_z^{(0)}], \tag{4.27}$$

$$\dot{h}^{(1)} = \tilde{k}^0(1-\phi^{(0)})\frac{1}{\phi^{(0)}}[\phi_z^{(2)} - \frac{\phi^{(2)}}{\phi^{(0)}}\phi_z^{(0)}], .... \tag{4.28}$$

on $z = h^{(0)}$.

Integrating equation (4.22) and using boundary condition (4.26), we have

$$\tilde{k}^0(1-\phi^{(0)})^2[\frac{1}{\phi^{(0)}}\phi_z^{(0)} - 1] = 0. \tag{4.29}$$

Since $\tilde{k}^0 \neq 0$, we have

$$\frac{1}{\phi^{(0)}}\phi_z^{(0)} - 1 = 0 \text{ with } \phi^{(0)} = \phi_0 \text{ at } z = h^{(0)}. \tag{4.30}$$

Its solution is then

$$\phi^{(0)} = \phi_0 e^{-(h^{(0)}-z)}. \tag{4.31}$$

This leading order solution is essentially a steady state solution which corresponds to compaction equilibrium to which the porosity curve will tend when $t \to \infty$. This exponentially decreasing solution was obtained by Athy (1930) by fitting the observed data of Paleozoic shales from Kansas and Oklahoma. Athy's porosity curve represents compaction equilibrium attained over a very long time span. Hedberg's (1936) porosity curve for the Tertiary shales in Venezuela is similar to Athy's curve.

From equation (4.1), we notice that the perturbation method is only valid if $\lambda\tilde{k} >> 1$, i.e. $\exp\{m[\Pi - (h^{(0)} - z)]\} >> 1$ where $\Pi = (\ln\lambda)/m$. If $\lambda = 100$ and $m = 8$, then $\Pi \approx 0.58$. Therefore, the leading term solution $\phi^{(0)}$ is expected to be valid under the condition

$$z > h^{(0)} - \Pi. \tag{4.32}$$

The comparison of the solution with related numerical results is presented in Fig. 4.3. The comparison clearly shows that Athy's relation (Athy, 1930) of porosity-burial depth is only valid in the range of $0 - 0.58d$ km in such sedimentary basins where their control parameter $\lambda >> 1$. If $d = 1$ km, then the range is $0 - 580$ metres.

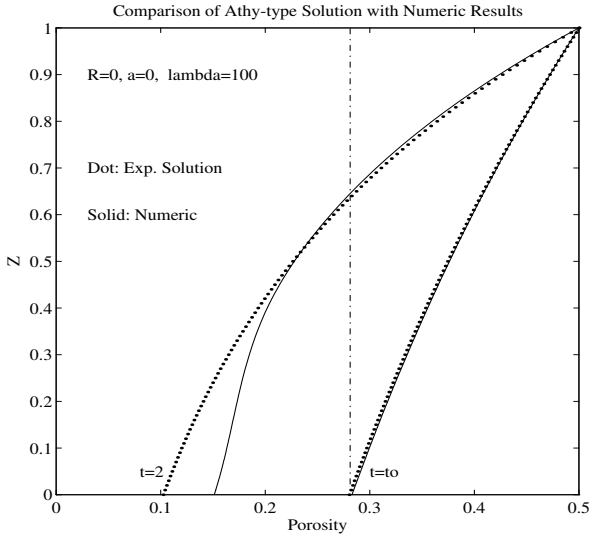


Figure 4.3 Comparison of Athy-type solutions (dashed) with numerical results (solid) for $\lambda = 100$. $Z$ is scaled height, and $t_0$ is the time given by equation (4.39).

Using the solution (4.31), equation (4.23) becomes

$$-\dot{h}^{(0)}\phi_0 e^{-(h^{(0)}-z)} = \frac{\partial}{\partial z}\{\tilde{k}^0(1-\phi^{(0)})^2\frac{1}{\phi^{(0)}}[\phi_z^{(1)} - \phi^{(1)}]\}, \tag{4.33}$$

Integrating the above equation, using boundary condition (4.26), and noticing that $\phi_z^{(0)}/\phi^{(0)} = 1$, we have

$$\phi_z^{(1)} - \phi^{(1)} - \frac{\dot{h}^{(0)}\phi_0(1-e^z)e^{-h^{(0)}}\phi^{(0)}}{\tilde{k}^0(1-\phi^{(0)})^2} = 0. \tag{4.34}$$

Using this equation, equation (4.27) and solution (4.31), we obtain a relation for $\dot{h}^{(0)}$

$$-(1-\dot{h}^{(0)})(1-\phi_0) + \dot{h}^{(0)}\phi_0(1-e^{-h^{(0)}}) = 0. \tag{4.35}$$

Integrating this equation, we have

$$h^{(0)} = (1-\phi_0)t + \phi_0[1 - e^{-h^{(0)}}]. \tag{4.36}$$

Clearly, if $t$ is large, then $\exp[-h^{(0)}] << 1$, we thus have

$$\dot{h}^{(0)} \approx 1 - \phi_0. \tag{4.37}$$

If $t$ is small, then $\exp[-h^{(0)}] \sim 1$, we have

$$\dot{h}^{(0)} \approx 1. \tag{4.38}$$

Putting $h^{(0)} = \Pi$, we can obtain an explicit expression for $t_0$ by using the above solution:

$$t_0 = \frac{\Pi + \phi_0(e^{-\Pi} - 1)}{1 - \phi_0}. \tag{4.39}$$

If $\lambda = 100$ and $m = 8$, then $\Pi \approx 0.58$, $t_0 \approx 0.71$.

The solution of equation (4.34) with boundary condition (4.25) is then

$$\phi^{(1)} = \phi_o e^z[-h^{(1)}e^{-h^{(0)}} - \chi(0, h^{(0)}) + \chi(0, z)], \tag{4.40}$$

where

$$\chi(0,z) = \phi_0 \int_0^z \frac{(1 - e^{\eta - h^{(0)}})e^{\eta - h^{(0)}}e^{-\eta}}{e^{m(\eta - h^{(0)})}(1 - \phi_0 e^{\eta - h^{(0)}})^2} d\eta. \tag{4.41}$$

By using $m >> 1$, this integral can be approximately expressed as

$$\chi(0,z) = \frac{\phi_0}{m(m-1)(1-\phi_0)^2}\{[1 - m + me^{z-h^{(0)}}]e^{m(h^{(0)}-z)-h^{(0)}} - [1 - m + me^{-h^{(0)}}]e^{(m-1)h^{(0)}}\}. \tag{4.42}$$

Substituting this integral into (4.40), we have

$$\phi^{(1)} = \phi_0 e^z\{-h^{(1)}e^{-h^{(0)}} + \frac{\phi_0}{m(m-1)(1-\phi_0)^2}[(1 - m + me^{z-h^{(0)}})e^{m(h^{(0)}-z)-h^{(0)}} - e^{-h^{(0)}}]\}, \tag{4.43}$$

By using equation (4.24), boundary condition (4.26) and solution (4.31), we can obtain a relation for $\dot{h}^{(1)}$ at $z = h^{(0)}$

$$\dot{h}^{(1)}(1 - \phi_0) = \int_0^{h^{(0)}} \phi_t^{(1)} dz. \tag{4.44}$$

Employing solution (4.43) and noticing that $e^{-(m-1)h^{(0)}} \approx 0$ when $m >> 1$, we have an approximate solution for $\dot{h}^{(1)}$

$$\dot{h}^{(1)} \approx \frac{[\dot{h}^{(0)}]^2}{m}\phi_0 e^{(m-1)h^{(0)}}. \tag{4.45}$$

From the above solution, we find that the perturbation method is only valid for sufficiently small $t$, otherwise $\dot{h}^{(1)}$ goes unboundedly.

From the above solution and the numerical results, we find that for the case of $t < t_0$, the porosity has not reduced to a value $\phi < \phi^*$, so the case $\phi < \phi^*$ with $t < t_0$ need not be considered.

### 4.2.4 Compaction of thick sediment layer ($\phi < \phi^*$ with $t > t_0$)

Note that, from the definition, $\phi^* << 1$ if $\lambda >> 1$, so that we must formally assume $m >> 1$ in order to have $\phi^*$ of order one. Thus, we now consider a limit in which $m$ is large. For convenience in the following discussion, we set

$$\phi = \phi^* e^{\frac{\psi - \ln m}{m}} \quad \text{with} \quad \phi^* = \phi_0 e^{-\frac{1}{m}\ln\lambda}. \tag{4.46}$$

Then the $\phi$ equation becomes

$$\phi^* \psi_t e^{\psi/m} = \frac{\partial}{\partial z}\{e^{\psi}(1 - \phi^* e^{\psi/m})^2[\frac{1}{m}\psi_z - 1]\}. \tag{4.47}$$

Noticing that $m >> 1$ and $\exp(\psi/m) = O(1)$, the above equation is then simplified as

$$\psi_{t'} + Ke^{\psi}\psi_z = 0, \quad K = \frac{(1-\phi^*)^2}{\phi^*} \tag{4.48}$$

with boundary conditions

$$\psi = 0 \quad \text{at} \quad z = h(t) - \Pi, \tag{4.49}$$

and

$$\psi_z = m \quad \text{at} \quad z = 0. \tag{4.50}$$

From the method of characteristics, we have

$$\dot{\psi} = 0 \quad \text{and} \quad \dot{z} = Ke^{\psi}. \tag{4.51}$$

The solution satisfying the boundary condition is then

$$\psi = \psi_b(\tau),$$

$$z = Ke^{\psi_b(\tau)}(t - \tau), \tag{4.52}$$

where $\psi_b(\tau)$ will be determined by the boundary condition at $z = 0$. From the above solution and the boundary condition (4.50), we have

$$\psi_z = \psi_b^{'}(\tau) \cdot \tau_z = m, \tag{4.53}$$

which is simply

$$\psi_b' + mKe^{\psi_b(\tau)} = 0. \tag{4.54}$$

Integrating this equation, and using that when $\tau = 0$, $\psi = 0$ and $h = \Pi$ which corresponds to the fixed time $t = t_0$, we obtain

$$\psi_b(\tau) = \ln[\frac{1}{mK(\tau - t_0) + 1}]. \tag{4.55}$$

Substituting $\tau$ from solution of (4.52) into the above solution and rearranging the equation, we have

$$\psi(z, t) = \ln[\frac{1 + mz}{mK(t - t_0) + 1}]. \tag{4.56}$$

Using (4.46), we finally have

$$\phi(z, t) = \phi^*[\frac{1 + mz}{m\frac{(1-\phi^*)^2}{\phi^*}(t - t_0) + 1} \cdot \frac{1}{m}]^{\frac{1}{m}}. \tag{4.57}$$

The fixed time $t_0$, which is given by equation (4.39), defines a lower time value under which the solution will be invalid.

When $t$ is large (i.e. $t >> t_0$, $z = O(t) >> 1$), then the solution (4.57) can be expressed approximately as

$$\phi = \phi^*(\frac{\phi^* z}{mt})^{\frac{1}{m}}. \tag{4.58}$$

Using the definition of $\phi^*$ in (4.19) in the above expression, $(1/\lambda)^{1/m} \sim (1/\lambda)^{1/(m-1)}$ as $m >> 1$, and putting $\xi = z/t$, we have

$$\phi = \phi_0(\frac{\phi_0 \xi}{m\lambda})^{\frac{1}{m-1}}. \tag{4.59}$$

This is exactly the same solution obtained by Audet & Fowler (1992, equation (5.9)) for the case of $\lambda >> 1$ and $t >> 1$.

### 4.2.5 Compaction of thick sediment layers ($\phi > \phi^*$ with $t > t_0$)

In this case, the equation (4.29) will not be valid, and a more general expression is

$$\tilde{k}^0(1-\phi^{(0)})^2[\frac{1}{\phi^{(0)}}\phi_z^{(0)} - 1] = \mathcal{F}(t), \tag{4.60}$$

where $\mathcal{F}(t)$ is a function of $t$ only. From the moving boundary condition, we have

$$\mathcal{F}(t) = (\dot{h} - 1)(1 - \phi_0). \tag{4.61}$$

This is only valid in the region with a depth less than $\Pi$ from the top boundary. In the region which includes the transition region of $\phi \approx \phi^*$, the term $\phi_t$ can not be ignored. The three terms in the $\phi$ equation must be considered at the same time. In fact, from the leading solution (4.31) in the perturbation method, we have $\phi_t \sim -\dot{h}\phi_z$.

From (4.31), we find that $\phi$ depends on $h(t) - z$ near the top, i.e. $\phi \sim \phi(h(t) - z)$. From the numerical results, we observed that $\phi$ decreases nearly exponentially with increasing depth $\eta = h(t) - z$ in the top region. This suggests a solution for $\phi$ equation in the form

$$\phi = \phi(\eta), \quad \text{with} \quad \eta = h(t) - z, \tag{4.62}$$

then the $\phi$ equation (4.1) becomes

$$\dot{h}\phi' = \lambda[(\frac{\phi}{\phi_0})^m(1-\phi)^2(\frac{1}{\phi}\phi' + 1)]', \tag{4.63}$$

where a prime means a differentiation with respect to $\eta$. The boundary conditions (on $\eta = 0$) are

$$\begin{aligned} \phi &= \phi_0, \\ \dot{h} &= 1 - \lambda(\frac{\phi}{\phi_0})^m(1-\phi)(\frac{1}{\phi}\phi' + 1). \end{aligned} \tag{4.64}$$

We can see that (2.64) will imply $\dot{h}$ =const due to (4.31) and (4.62). By integrating the above equation again and using its top boundary condition at $\eta = 0$, we have

$$\dot{h}(\phi_0 - \phi) = (1 - \dot{h})(1 - \phi_0) - \lambda(\frac{\phi}{\phi_0})^m(1-\phi)^2(\frac{1}{\phi}\phi' + 1), \tag{4.65}$$

whose solution can be written as a quadrature. The undetermined $\dot{h}$ in this solution will be determined by matching it to that in a transition layer analysed below.

The comparisons of the travelling wave solution (4.65) and solution (4.57) (dashed) with the numerical results (solid) are shown in Fig. 4.4 and Fig.4.5

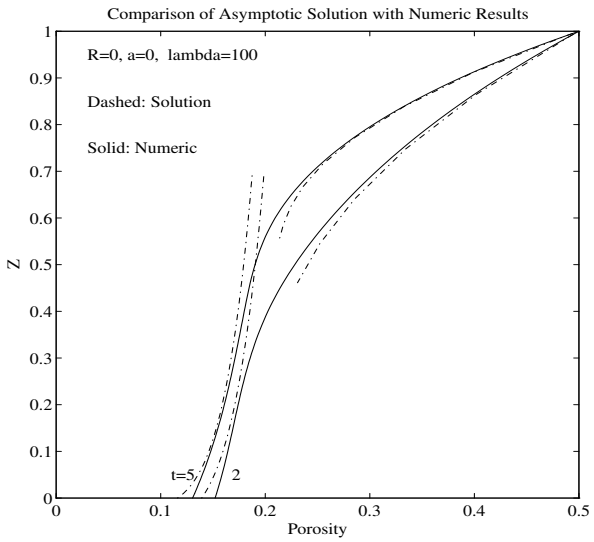


Figure 4.4 Comparison of asymptotic solutions (dashed) with numerical results (solid) at $t = 2, 5$ for $\lambda = 100$. The upper two dashed curves correspond to solution (4.65), and the lower two correspond to solution (4.57). $Z$ is scaled height. Agreement gets better as $t$ increases.

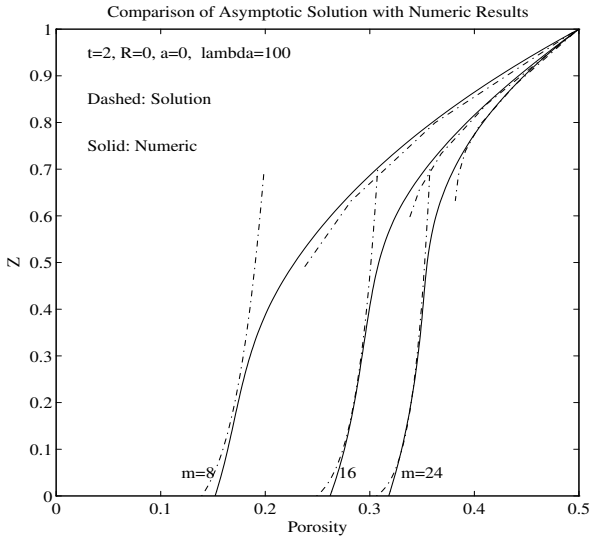


Figure 4.5 Comparison of asymptotic solutions (dashed) with numerical results (solid) with different values of $m$. The dashed curves have the same meaning as in Fig. 4.4. The agreement gets better as $m$ increases.

The porosity profile for $t = 2, 5$ is plotted in figure 4.4 with other values fixed

($a = 0$, $\lambda = 100$, $\mathcal{R} = 0$). In Fig. 4.5, different values of $m$ are compared for the same $t = 2$ with all the other values fixed as in Fig. 4.4. They clearly show that their consistency becomes better for larger times or larger $m$ even with small $t$. This is what we have expected from the condition used to derive the solutions.

### 4.2.6 Matching the solutions

In order to match the solution (4.65) to the solution (4.57), we define a transition region by adopting the transition variable $\zeta$,

$$z = h(t) - \Pi + \frac{1}{m}\zeta \quad \text{i.e.} \quad \zeta = m(h(t) - \Pi - z). \tag{4.66}$$

Rewriting the solution (4.57) in terms of the new variable with $\Psi = \psi$ as in (4.46), we have

$$\phi = \phi^* e^{\frac{\Psi - \ln m}{m}}, \tag{4.67}$$

where

$$\Psi = \ln[\frac{1 + m(h - \Pi) + \zeta}{m\frac{(1-\phi^*)^2}{\phi^*}(t - t_0) + 1}]. \tag{4.68}$$

Noticing that $m >> 1$, we have approximately, for the lower solution (4.57),

$$\Psi \approx \ln[\frac{h - \Pi}{\frac{(1-\phi^*)^2}{\phi^*}(t - t_0)}]. \tag{4.69}$$

for $1 << -\zeta << m$. Now the $\phi$ equation in the transition region can be written as

$$-m\dot{h}\phi^*[e^{\frac{\Psi - \ln m}{m}}]_\zeta = m\frac{\partial}{\partial\zeta}[\frac{1}{m}e^{\Psi}(1 - \phi^*)^2(\Psi_\zeta - 1)]. \tag{4.70}$$

Integrating this equation, we find

$$\begin{aligned} &\frac{1}{m}e^{\Psi}(1 - \phi^*)^2(\Psi_\zeta - 1) + \dot{h}\phi^* e^{\frac{\Psi - \ln m}{m}} \\ &= \dot{h}\phi^* e^{\frac{\Psi_\infty - \ln m}{m}} - \frac{1}{m}e^{\Psi_\infty}(1 - \phi^*)^2, \end{aligned} \tag{4.71}$$

where we require $\Psi \to \Psi_\infty$ as $\zeta \to -\infty$. Comparing with (4.69), we have

$$\Psi \to \ln[\frac{h - \Pi}{\frac{(1-\phi^*)^2}{\phi^*}(t - t_0)}] = \Psi_\infty, \tag{4.72}$$

or

$$\phi_\infty \approx \phi^* e^{\frac{\Psi_\infty - \ln m}{m}}. \tag{4.73}$$

Rewriting and rearranging the upper solution (4.65) in terms of the new variables $\zeta$ and $\Psi$, we have

$$\frac{1}{m}e^{\Psi}(1-\phi^*)^2(\Psi_\zeta - 1) + \dot{h}\phi^* e^{\frac{\Psi-\ln m}{m}} = -(1-\phi_0) + \dot{h}. \tag{4.74}$$

By using Van Dyke's matching rule (Van Dyke, 1964; Hinch, 1991), we expect that the $\Psi$ obtained from (4.71) and (4.74) should be the same in the matching region. From equations (4.71) and (4.74), we notice that the left hand sides of both equations are the same and independent of $\zeta$, thus we have

$$-(1-\phi_0) + \dot{h} = \dot{h}\phi^* e^{\frac{\Psi_\infty-\ln m}{m}} - \frac{1}{m}e^{\Psi_\infty}(1-\phi^*)^2. \tag{4.75}$$

using the fact that $m >> 1$, and rearranging (4.75), we finally obtain an equation for $h(t)$:

$$\dot{h} \approx \frac{1-\phi_0}{1-\phi_\infty}, \tag{4.76}$$

which determines $h(t)$. It is worth pointing out that $(\Psi - \ln m)/m$ in the second term of the left hand side of (4.74) is not accurately set to zero, since it is order of $-\frac{1}{m}\ln m$. But if we do set $(\Psi - \ln m)/m \approx 0$, then we obtain the leading order approximation for $\dot{h}$:

$$\dot{h} \approx \frac{1-\phi_0}{1-\phi^*}. \tag{4.77}$$

Clearly, the non-negligible term $(\Psi - \ln m)/m$ will provide us a more accurate approximation for $\dot{h}$.

Now we understand that the top solution breaks down as $\eta > \Pi$ while the bottom solution fails as $z > h(t) - \Pi$. We can simply construct a uniformly valid asymptotic solution (Hinch 1991) since the solution in the upper region is the same as that in the lower transition region. If we note the solution in the top region as $\phi_{\text{top}}$ and that in the bottom region $\phi_{\text{bottom}}$, the composite solution is then

$$\phi(z,t) = \phi_{\text{bottom}} + \phi_{\text{top}} - \phi_\infty. \tag{4.78}$$

From equations (4.59) and (4.73), we know that $\phi_\infty$ is time independent when $t$ is large ($t \to \infty$), therefore, $\dot{h}$ is a constant. We simply have

$$\dot{h} \approx \frac{1-\phi_0}{1-\phi_\infty} \quad \text{with} \quad \phi_\infty \approx \phi_0(\frac{\phi_0\dot{h}}{m\lambda})^{\frac{1}{m-1}}. \tag{4.79}$$

Clearly, this is exactly the equation (5.16) obtained by Audet & Fowler (1992). In this case, the solution is a travelling wave solution.

The comparison of the matched composite asymptotic solution (4.78) with numerical results (dashed lines) is shown in Fig. 4.6.

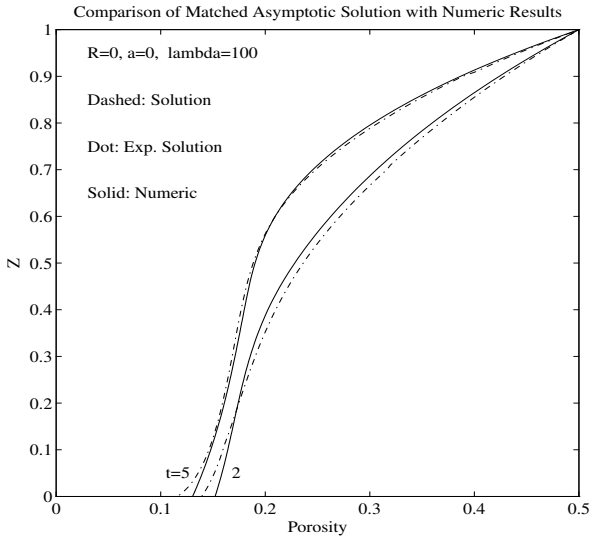


Figure 4.6 Comparison of matched asymptotic solutions (dashed) with numerical results (solid) at $t = 2$, 5 for $\lambda = 100$.

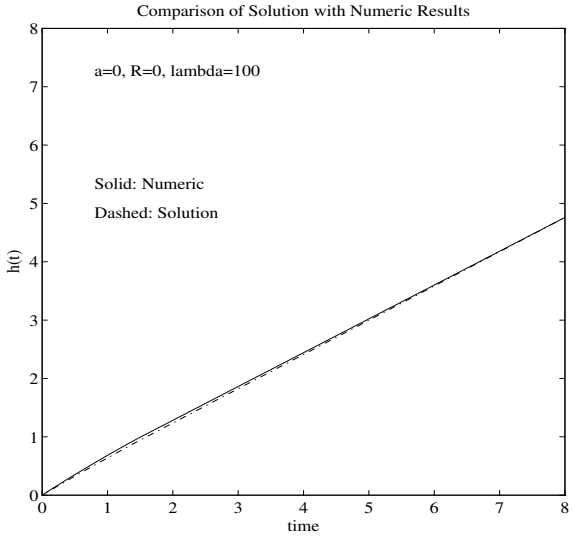


Figure 4.7 Comparison of $h(t)$ solutions (dashed) with numerical results (solid) with $\lambda = 100$.

For the case of $\lambda >> 1$ and $\phi > \phi^*$, substituting Athy's solution for $\phi$ in the top

region, we have

$$\frac{\partial p_a}{\partial z} = 0. \tag{4.80}$$

This equation with the boundary condition $p_a = 0$ at the top $z = h(t)$ gives that $p_a = 0$ at the leading order. This means excess pressure does not occur for short times or in the top region where $z > h(t) - \Pi$. This region is clearly shown in Fig. 4.8. For larger times, the solution suggests that $\phi_z << \phi$, whence

$$\frac{\partial p_a}{\partial z} \approx -(1 - \phi), \tag{4.81}$$

which shows that the excess pore pressure develops at large times even if $\lambda >> 1$.

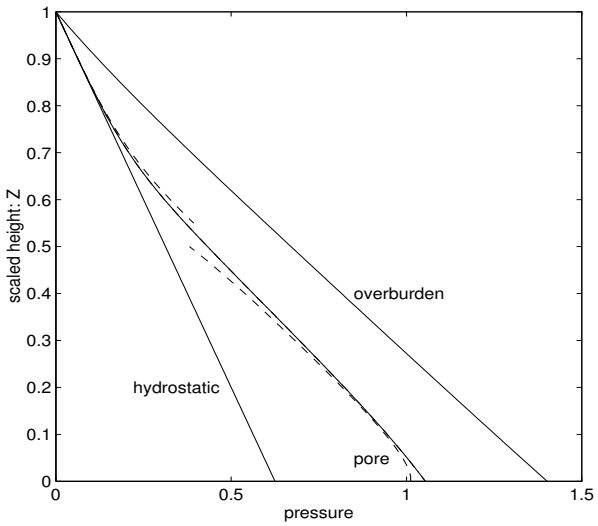


Figure 4.8 Hydrostatic, pore and overburden pressures at $t = 5$ for $\lambda = 100$. Dashed curves are computed by using (4.65) and (4.57).

The comparison of the numerical results with the pore pressure calculated from the asymptotic solutions (dashed) is shown in Fig. 4.8. The overpressure only develops in the lower region, while the pore pressure remains hydrostatic in the top region with a depth of order $\Pi$ from the surface.

## 4.3 Summary

In summary, we find that the limit $\lambda << 1$ (slow compaction) can be simply analysed by means of a boundary layer analysis at the sediment base. Essentially, sediment is added so fast that the porosity remains virgin except near the base, where compaction

occurs. The pore pressure is then essentially lithostatic, that is, excess pore pressures exist over the whole domain.

The more interesting mathematical case is when $\lambda >> 1$ (fast compaction). For sufficiently small times, the porosity profile is exponential with depth, corresponding to an equilibrium (long-time) profile. However, because of the large exponent $m$ in the permeability law $\tilde{k} = (\phi/\phi_0)^m$, we find that even if $\lambda >> 1$, the product $\lambda\tilde{k}$ may become small at sufficiently large depths. In this case, the porosity profile consists of an upper part near the surface where $\lambda\tilde{k} >> 1$ and the equilibrium is attained, and a lower part where $\lambda\tilde{k} << 1$, and the porosity is higher than equilibrium. Straightforward asymptotic methods are difficult to implement because the limit $m >> 1$ implies exponential asymptotics, but we use a hybrid method which appears to correspond accurately to numerical computations.

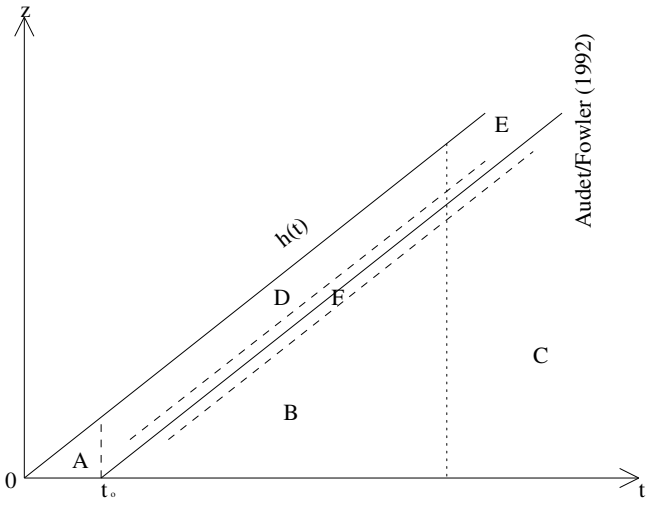


Fig. 4.9 Regions of different solutions ($\lambda >> 1$). A, D, E are the regions with $\phi > \phi^*$ while B, C are the ones with $\phi < \phi^*$. The region F between the two dashed lines is the transition region with $\phi \approx \phi^*$. Audet & Fowler's regions C, E are for large times ($t \to \infty$).

To summarise the solutions for the case of $\lambda >> 1$, we represent the solutions in their related valid regions in Fig. 4.9. The regions below $h(t)$ line labelled as A, D, E are the regions with $\phi > \phi^*$ while those labelled as B, C are the ones with $\phi < \phi^*$. The region with dashed lines on both sides is the one with $\phi \approx \phi^*$ which is the transition

region. The regions E, C on the right side of the dotted line constitutes Audet & Fowler's region (1992) which is only valid for large times ($t \to \infty$).

Correspondingly, the terms in the $\phi$ equation will play different roles in the behaviour of the solutions. The over- and under- braces label the relative terms which govern the features of the solutions in different regions.

$$\underbrace{\frac{\partial \phi}{\partial t} = \lambda \frac{\partial}{\partial z}\{\tilde{k}(1-\phi)^2[}_{\text{RegionB\&C}} \overbrace{-1 + \frac{1}{\phi}\frac{\partial \phi}{\partial z}}^{\text{RegionA,D\&E}}]\}. \tag{4.82}$$

When the left hand side $\phi_t$ is negligible, we have

$$\{\tilde{k}(1-\phi)^2[-1 + \frac{1}{\phi}\frac{\partial \phi}{\partial z}]\}_z \approx 0. \tag{4.83}$$

then we have the solutions for the top regions ($\phi > \phi^*$). If the first integral of the right hand side is zero, the Athy-type solution is obtained in region A. If the first integral is not negligible, the solution in region D is thus obtained. If $t$ is large, this solution moves into the region E of the travelling wave type solution which is given by Audet & Fowler (1992).

When the diffusion term on the right hand side is negligible, we have

$$\phi_t \approx -\lambda\{\tilde{k}(1-\phi)^2\}_z, \tag{4.84}$$

thus the solution for the bottom region ($\phi < \phi^*$) is obtained. The limit for large $t$ of this solution is exactly Audet & Fowler's solution for large times. In the region F ($\phi \approx \phi^*$), all the three terms in the $\phi$ equation must be considered. The matched composite asymptotic solutions provide a uniformly balanced solution for the whole region.

The methods presented in this paper pave the path for the analysis of compaction in sedimentary basins when more complicated loading histories are studied, and also when more realistic phenomena are included, such as diagenesis, or state-dependent rheology.

# Chapter 5

# Unloading and Variation of Sedimentation Rate

In the model we analysed in the previous chapters, the rheology of the porous medium is considered as poro-elastic, and it is equivalent to a single-valued function of the Athy's type $p_e = p_e(\phi)$ in the 1-D case. A more realistic rheological relation should include the nonlinear effect of hysteresis derived from soil tests. In addition, the sedimentation rate $\dot{m}_s$ has also been taken as a constant in the poroelastic compaction model. From the numerical simulations in chapter 3 and the analysis in chapter 4, we can see that the model does not require the sedimentation rate to be constant. In fact, the dimensionless sedimentation rate $\dot{m}_s$ can vary with time $t$ and it can also be negative, which corresponds to the case of unloading.

In this chapter, we will mainly investigate the effect of unloading and variation of the sedimentation rate by using a more realistic rheological relation. As the analysis of the model equations is very complicated, we will simply show the numerical results and give some analysis whenever possible.

## 5.1 Model Equations for Unloading and Reloading

### 5.1.1 Non-linear soil behaviour

In order to model the phenomena of unloading and reloading, we must consider the non-linear stress-strain behaviour which has been investigated in many cases.

Bethke & Corbet (1988) examined the non-linear effects associated with the long-term compaction of sedimentary basins. The one-dimensional isotropic consolidation test (Das 1983, Burland 1990) of soils accompanied by unloading/reloading sequences clearly shows that the soil behaviour is path-dependent and nonlinear as shown in Fig. 5.1. The behaviour during unloading and reloading is essentially elastic with a small amount of hysteresis. The void ratio

$$e = \phi/(1-\phi) \tag{5.1}$$

is used in this figure as the conventional way of presenting the test results.

In order to model the behaviour of soils as shown in this figure, the Cam-clay models developed by the Cambridge group, in terms of *Critical State Formulations*, are very attractive since these models are able to reproduce qualitatively a good number of the main features of the mechanical behaviour of soils such as unloading/reloading, stress path-dependence etc (Schofield & Wroth, 1968; Atkinson & Bransby, 1978, Huekel & Baldi 1990). If a more accurate reproduction of actual soil behaviour is sought, the more sophisticated models such as the Modified Cam-clay model (Roscoe & Burland, 1968) and the more modern cap model (Chen & Mizuno, 1990) should be used.

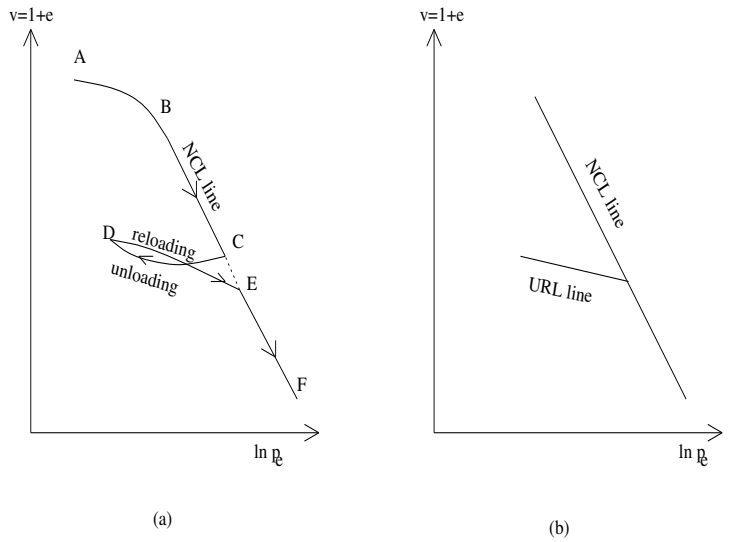


Figure 5.1 Non-linear behaviour of soil consolidation. NCL is the normal consolidation line, and URL is the unloading and reloading line.

The modified Cam-clay model is an isotropic, nonlinear elastic strain-hardening plastic model in which only volumetric strain is assumed to be partially recoverable. The consolidation curve in Fig. 5.1(a) is idealised as that shown in Fig. 5.1(b). The virgin isotropic normal consolidation line is assumed to be linear, and the unloading and reloading curves are parallel as a single straight line.

The equation for the normal consolidation line (NCL line) is given as

$$e = e_0 - C_c \ln(p_e/p_0), \tag{5.2}$$

where $C_c$ is the compression index (Das, 1983; Burland, 1990). For the unloading-reloading line (URL line), we have

$$e = e'_0 - C_s \ln(p_e/p_0), \tag{5.3}$$

which is valid when $p_e < p_e^*$, where $p_e^*$ is the maximum of previous values of $p_e$. Similarly, $C_s$ is called the swelling index. The join of the two lines corresponds to a special value $p_e^*$ of $p_e$ in the time-history of compaction, and the value $e'_0$ can be expressed in terms of $p_e^*$ as

$$e'_0 = e_0 - (C_c - C_s)\ln(p_e^*/p_0). \tag{5.4}$$

If written in dimensionless form in terms of $\tilde{p}$, then equations (5.2) and (5.3) become

$$e = e_0 - C_c \ln(\tilde{p}/\tilde{p}_0), \tag{5.5}$$

and

$$e = e_0 - (C_c - C_s)\ln(\tilde{p}^*/\tilde{p}_0) - C_s \ln(\tilde{p}/\tilde{p}_0). \tag{5.6}$$

In equations (5.5) and (5.6), we provide only one of the many possible formulations of the nonliear constitutive laws which can be derived from the modified Cam-clay model (Roscoe & Burland, 1968) and modern cap model (Chen & Mizuno, 1990). In fact, what we have used before in equation (3.1) is just another form of the formulations, and is widely used in the literature (Smith, 1971; Sharp, 1976; Das, 1983; Audet & Fowler, 1992; Wangen, 1992). Different formulations will result different forms of function $\tilde{p}(\phi)$ or $e(\tilde{p})$, but they all can reproduce the main features of the nonlinear behavior of loading/unloading. In order to compare with the results obtained in Chapter 4, we will use the modified constitutive law (5.15) similar to (3.1).

### 5.1.2 1-D model equations

From the derivation of the general model discussed before, we know that the model does not require the sedimentation rate to be constant. Nor does it require increasing loading only. Change of sedimentation rate and erosional unloading can be treated within this model, but the constitutive laws for the case of unloading should be changed.

Recalling the process of non-dimensionalization in Chapter 2, we defined a length-scale $d$ in (2.48), and scaled $z$ with $d$, $u^s$ with $\dot{m}_s$, time $t$ with $d/\dot{m}_s$, pore pressure $p$ with $(\rho_s-\rho_l)gd$, and permeability $k$ with $k_0$. Clearly, the scalings involve the sedimentation rate $\dot{m}_s$, and thus must be modified to allow the variation of the sedimentation rate and erosional unloading.

If we scale time $t$ with a time scale $\tau$ instead of $d/\dot{m}_s$, $u^s$ and $\dot{m}_s$ with $d/\tau$ instead of $\dot{m}_s$, and keep all the scalings of other quantities the same as before on Page 22, then the obtained dimensionless governing equations are the same as equations (2.51)-(2.58). The only change is to replace the $\dot{m}_s$ by $d/\tau$ in the expressions of $\lambda$, $\Lambda$ and $\mathcal{R}$. Thus (2.59)-(2.61) are replaced by

$$\lambda = \frac{k_0(\rho_s - \rho_l)g}{\mu(d/\tau)}, \quad \Lambda = \frac{K_0}{\rho_l c_l (d/\tau)d}, \quad \mathcal{R} = \frac{k_r^0 d}{(d/\tau)}. \tag{5.7}$$

Clearly, if one substitutes $\dot{m}_s = d/\tau$ back into the above expressions of $\lambda$, $\Lambda$ and $\mathcal{R}$, we do have the same expressions as (2.59)-(2.61) in the case of constant sedimentation rate. Therefore, the dimensionless model equations (2.51)-(2.58) are still suitable when sedimentation rate changes, but the real meaning of $\dot{m}_s$ is the average sedimentation rate in the relevant time history of sedimentation. In the case of constant sedimentation rate, $\dot{m}_s$ is the real constant sedimentation rate.

In order to show more efficiently the effect of the variation of sedimentation rates and erosional unloading on the porosity evolution, it is convenient to ignore diagenesis and temperature effects by setting $\mathcal{R} = 0$, $a = 0$, $\dot{b} = 0$, $\phi_l = \phi$ in equations (2.54) and (2.58), and omitting the temperature equation (2.57). By using the force balance equation (2.58) to eliminate $p$ in Darcy's law (2.56), and using the expressions (2.64)-

(2.65) for $u^s$ and $u^l$, we finally obtain a single non-linear diffusion equation

$$\frac{\partial \phi}{\partial t} = \lambda \frac{\partial}{\partial z}\{\tilde{k}(1-\phi)[-\frac{\partial \tilde{p}}{\partial z} - (1-\phi)]\}, \tag{5.8}$$

with constitutive laws

$$\tilde{p} = \tilde{p}(\phi), \quad \tilde{k} = \tilde{k}(\phi), \tag{5.9}$$

which are given below in equation (5.13)-(5.15).

**Boundary conditions**

Rewriting the definition of the effective pressure in dimensionless form, we have

$$\tilde{p} = P - p. \tag{5.10}$$

In the case of very rapid unloading (Haxby & Turcotte, 1976), $P$ decreases suddenly, but $p$ may not have enough time to respond to such a quick change, and thus remains nearly a constant, which subsequently forces the effective pressure $\tilde{p} < 0$. The whole column of the sediments will be unloaded instantaneously. The negative effective pressure implies that fracturing should occur, and the model equations will become invalid for fracturing. In reality, the unloading due to erosion at basin surface is a very slow process, and the effective pressure should be always non-negative, $\tilde{p} \geq 0$. Therefore, a reasonable boundary condition at the basin top $z = h(t)$ in the present model is to assume that the effective pressure $\tilde{p}$ always remains zero, i.e., $\tilde{p} = 0$, which eliminates the possibility of fracturing due to very quick unloading, discussed by Haxby & Turcotte (1976).

Now the boundary conditions are

$$-\frac{\partial \tilde{p}}{\partial z} - (1-\phi) = 0 \text{ at } z = 0, \tag{5.11}$$

$$\phi = \phi_0 \quad \text{at} \quad z = h,$$

$$\dot{h} = \dot{m}(t) + \lambda \tilde{k}[-\frac{\partial \tilde{p}}{\partial z} - (1-\phi)]. \tag{5.12}$$

Here, $\dot{m}$ is the dimensionless sedimentation rate which is 1 if it is constant, or $O(1)$ if time-varying. It is based on these equations that the change of sedimentation rate ($\dot{m}(t) \geq 0$, increasing loading) and erosional unloading ($\dot{m}(t) < 0$) will be treated, but the constitutive laws will change correspondingly.

### 5.1.3 A specific case

To investigate the main features for the cases of our interest and compare with the earlier results in Chapter 4, we still use the Smith type constitutive function of permeability as before,

$$\tilde{k} = (\phi_0/\phi)^m \quad \text{with} \quad m = 8. \tag{5.13}$$

But the constitutive relation (3.1)

$$\tilde{p} = \ln(\phi_0/\phi) - (\phi_0 - \phi), \tag{5.14}$$

is only valid on the increasing loading branch (NCL). On the unloading-reloading branch (URL), we use the following constitutive relation:

$$\tilde{p} = [1 - (1-\gamma)\phi_0^*]\ln[\frac{\phi_0^*\gamma}{\phi - (1-\gamma)\phi_0^*}] - (\phi_0^* - \phi) + \tilde{p}^*, \tag{5.15}$$
$$\tilde{p} \le \tilde{p}^* \quad \text{and} \quad \phi \ge \phi_0^*,$$

with

$$\phi_0^*(z,t) = \min \phi(z, \tau < t), \quad \tilde{p}^*(z,t) = \max \tilde{p}(z, \tau < t),$$
$$\tilde{p}^* = \ln(\phi_0/\phi_0^*) - (\phi_0 - \phi_0^*) \ \text{ and } \ \gamma = \frac{C_s}{C_c}, \tag{5.16}$$

where $\gamma$ is the slope ratio of the URL line to the NCL line. The normal ratio for soils is $\gamma \approx 0.1 \sim 0.25$ (Das, 1983). Clearly, equation (5.15) degenerates into equation (5.14) when $\gamma = 1$ which corresponds to the case that URL branch falls onto, as we expected, the NCL branch. In this case, the behaviour of unloading and reloading is reversible.

A relation similar to equation (5.15) was used by Wangen (1994), which can be written as

$$\phi = \phi_{\min}[1 + \alpha_e(p_{e,\max} - p_e)], \tag{5.17}$$

but Wangen's relation is only valid in the case of $\tilde{p} \approx \tilde{p}^*$ and $\phi \approx \phi_0^*$. In fact, Wangen's relation is only a special case of our relation (5.15) when $\gamma << 1$. Equation (5.15) can be written as

$$\frac{\phi - (1-\gamma)\phi_0^*}{\gamma\phi_0^*} = e^{\frac{\tilde{p}^* - \tilde{p} + (\phi - \phi_0^*)}{1-(1-\gamma)\phi_0^*}} \tag{5.18}$$

Taking $\gamma$ to be small, this implies that $\phi \approx \phi_0^*$, whence

$$\phi - \phi_0^* \approx \gamma \phi_0^* \exp \frac{\tilde{p}^* - \tilde{p}}{1 - \phi_0^*}. \tag{5.19}$$

Rearranging this equation, we finally have

$$\phi \approx \phi_0^* [1 + \frac{\gamma}{1 - \phi_0^*} (\tilde{p}^* - \tilde{p})], \tag{5.20}$$

which is similar to the equation (10) used by Wangen (1994).

The switch conditions for loading and unloading at any point following the material are

On URL branch:

$$\frac{d\tilde{p}^*}{dt_s} = 0, \quad \text{if} \quad \tilde{p} = \tilde{p}^* \quad \text{and} \quad \frac{d\tilde{p}}{dt_s} < 0,$$

$$\frac{d\tilde{p}^*}{dt_s} = 0, \quad \text{if} \quad \tilde{p} < \tilde{p}^*, \tag{5.21}$$

On NCL branch:

$$\frac{d\tilde{p}^*}{dt_s} = \frac{d\tilde{p}}{dt_s}, \quad \text{if} \quad \tilde{p} = \tilde{p}^* \quad \frac{d\tilde{p}}{dt_s} > 0, \tag{5.22}$$

where $d/dt_s = \partial/\partial t + u^s \partial/\partial z$, and $\tilde{p}^*(z^*, t) = \max \tilde{p}(z, \tau < t)$, where $z^*$ is a Lagrangian spatial coordinate which is related to $z$ by $dz/dt = u^s$ with $z = z^*$ at $t = 0$. If we use $| u^s | << 1$ as an approximation, then $z^* \approx z$, and the material derivatives in (5.21) and (5.22) can be taken to be partial time derivatives. Now we have

On URL branch:

$$\tilde{p} = \tilde{p}^* \quad \text{if} \quad \dot{\tilde{p}} < 0,$$

$$\text{or} \quad \tilde{p} < \tilde{p}^*; \tag{5.23}$$

On NCL branch:

$$\tilde{p} = \tilde{p}^* \quad \text{and} \quad \dot{\tilde{p}} \geq 0. \tag{5.24}$$

If the constitutive relations (5.14) and (5.15) are plotted in semilogarithmic coordinates, we have the curves in Fig. 5.2 which are similar to the NCL and URL lines in Fig. 5.1. This means that the Athy-type relations in the present model are suitable and reasonable in reproducing the main features of soil behaviour.

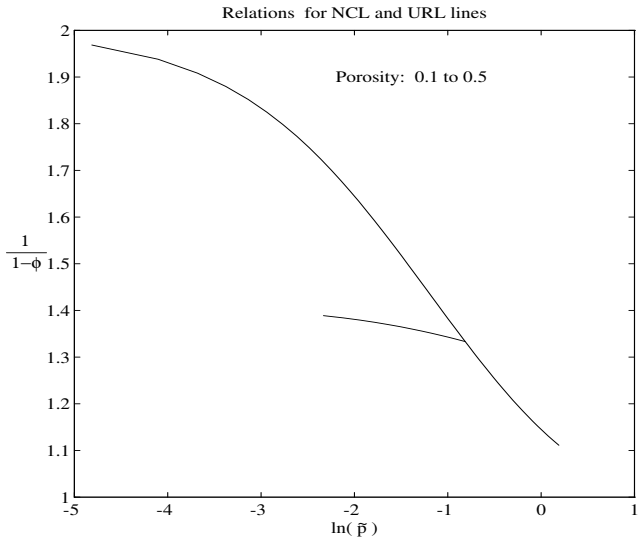


Figure 5.2 Constitutive laws plotted in semilogarithmic coordinates. The curves are similar to the NCL and URL lines as in Figure 5.1.

## 5.2 Numerical Method

The numerical method in Chapter 3 is only robust to solve the model equations when $\phi$ and its first derivatives $\phi_z$ and $\phi_t$ are continuous. But for the present case, the non-linear history-dependent property of the porosity function may imply that $\phi$ or its first derivatives are discontinuous at the interface between swelling region (where $\phi$ or $e$ increases) and compressing region (where $\phi$ or $e$ decreases). Therefore, we should first ensure that the numerical method can work well in these cases. Special modification at the interface is needed.

### 5.2.1 Finite difference implementation

For convenience in the discussion of numerical method, the general 1-D model equations can be simplified without losing its main features by leaving out the second term on the right side of the equation (5.8), so that we have

$$\frac{\partial \phi}{\partial t} = \lambda \frac{\partial}{\partial z}\{D(\phi)\frac{\partial \phi}{\partial z}\}, \tag{5.25}$$

$$D(\phi) = -\tilde{k}(1-\phi)\tilde{p}'(\phi) \tag{5.26}$$

Generally speaking, $D(\phi)$ will take different forms on the NCL [ $D^+(\phi)$] and URL [ $D^-(\phi)$] branches, and may be discontinuous at their interface.

The erosional unloading or change of sedimentation rate at the top of the basin will usually generate a series of interfaces, which separate the swelling and compressing regions, travelling at different velocities down to the bottom. The advancing interface is determined by solving a compatibility equation which is usually derived from an integral formulation of the non-linear diffusion equation while the smooth solution away from the interface is treated with a standard finite-difference method. Therefore, the integral form of the conservation law gives a contour integral formulation along the moving boundary (interface) $\Gamma_s$

$$\int_{\Gamma_s} f(z,t)\left\{\lambda[D(\phi)\phi_z]dt + [\phi]dz\right\} = 0, \tag{5.27}$$

where $f(z,t)$ is any continuously differentiable function of $z$ and $t$ that vanishes on the boundary of the solution domain. The notation [ ] means $[\phi_z] = \phi_z^+ - \phi_z^-$. Since the above relation is true for any arbitrary $f(z,t)$, the integrand must vanish, and we thus obtain

$$\dot{s}(t) = -\frac{\lambda[D(\phi)\phi_z)]}{[\phi]}. \tag{5.28}$$

This condition defines the travelling speed $\dot{s}(t)$ of the interface in terms of the values of the solution on either side.

To illustrate the modification of the finite difference formulae near the moving interface, we consider the case with a swelling region above the interface and compressing region below the interface. By using a fixed finite-difference grid, the moving interface, at any time $j\,\delta t$, will usually be located between two neighbouring grid points, say $i\,\delta z$ and $(i+1)\,\delta$. The unequal space intervals are used to modify the related finite-difference formulae near the moving interface. By using the three-point interpolation formulae of Lagrangian type (Crank 1975) with three known values $f(z_0), f(z_1), f(z_2)$ at three points $z = z_0,\ z_1,\ z_2$ respectively, we have

$$f(z) = \sum_{k=0}^{2} L_k(z) f(z_k), \tag{5.29}$$

with

$$L_k(z) = \frac{\pi_2}{(z - z_k)\pi_2'(z)}, \quad \pi_2(z) = \prod_{k=0}^{2}(z - z_k). \tag{5.30}$$

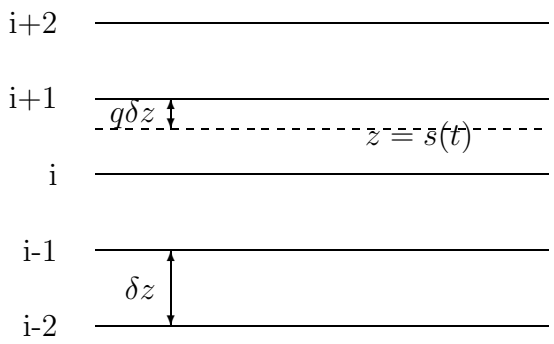


Figure 5.3 Grid lines near the moving interface $z = s(t)$.

The formulae for space derivatives are then

$$\frac{df}{dz} = \sum_{k=0}^{2} L_k' f(z_k), \quad L_k' = \sum_{l=0, l\neq k}^{2} \frac{\pi_2(z)}{(z - z_k)(z - z_l)\pi_2(z)}, \tag{5.31}$$

and

$$\frac{d^2 f}{dz^2} = \sum_{k=0}^{2} 2! f(z_k)\Big(\prod_{l=0, l\neq k}^{2} \frac{1}{x_k - x_l}\Big). \tag{5.32}$$

Applying the above formulae for the grid lines $(i-1)\,\delta z$, $i\,\delta z$ and the moving interface $z = s(t)$ (Fig. 5.3), we have (for $z < s(t)$)

$$\frac{\partial^2 \phi}{\partial z^2} = \frac{2}{(\delta z)^2}\Big(\frac{\phi_{i-1}}{2-q} - \frac{\phi_i}{1-q} + \frac{\phi_s}{(1-q)(2-q)}\Big), \quad z = i\delta z, \tag{5.33}$$

and

$$\frac{\partial \phi}{\partial z} = \frac{1}{\delta z}\Big(\frac{(1-q)\phi_{i-1}}{2-q} - \frac{(2-q)\phi_i}{1-q} + \frac{(3-2q)\phi_s}{(1-q)(2-q)}\Big), \quad z = s(t) - 0. \tag{5.34}$$

For $z > s(t)$ we have similarly

$$\frac{\partial^2 \phi}{\partial z^2} = \frac{2}{(\delta z)^2}\Big(\frac{\phi_s}{q(q+1)} - \frac{\phi_{i+1}}{q} + \frac{\phi_{i+2}}{q+1}\Big), \quad z = (i+1)\delta z, \tag{5.35}$$

and

$$\begin{aligned}\frac{\partial \phi}{\partial z} = \frac{1}{\delta z}\Big[&-\frac{(2q+1)\phi_s}{q(q+1)} + \frac{(q+1)\phi_{i+1}}{q} \\ &-\frac{q\phi_{i+2}}{q+1}\Big], \quad z = s(t) + 0.\end{aligned} \tag{5.36}$$

The above modified formulae for the space derivatives near the moving interface are used for the points $i\delta z, s(t)$ and $(i+1)\delta z$. These formulae together with the usual equal space interval formulae for other points can be applied for the whole region at any time. In addition, the switch conditions (5.23) and (5.24) are checked at every point near the interface at the beginning of each time step to make sure that the correct branch of the constitutive relation $\tilde{p}(\phi)$ is used for the numerical implementation.

### 5.2.2 A test case

To test the above finite difference formulae, it is convenient to investigate first a simplified non-linear diffusion with discontinuous diffusion coefficient. To compare the numerical results with some available analytical solution, a very special semi-infinite case (Crank 1975) is solved numerically. Written in the variable $\eta$ increasing downward with the origin at the top, the equation is

$$\frac{\partial \phi}{\partial t} = D\frac{\partial^2 \phi}{\partial \eta^2}, \tag{5.37}$$

where $D = D_1$ =constant if $\phi > \phi_s$=constant, $D = D_2$ =constant if $\phi < \phi_s$. The boundary conditions are

$$\phi(\eta = 0) = \phi_0 \quad \text{and} \quad \phi(\eta = \infty) = \phi_\infty. \tag{5.38}$$

As we mentioned before, the condition at the interface $\eta = s(t)$ is

$$D_1 \phi_\eta^{s(t)-} = D_2 \phi_\eta^{s(t)+}. \tag{5.39}$$

Crank (1975) obtained an analytical solution for this problem

$$\phi = \phi_0 + A\text{erf}\frac{\eta}{2\sqrt{D_1 t}} \quad 0 < \eta < s(t), \tag{5.40}$$

and

$$\phi = \phi_\infty + B\text{erfc}\frac{\eta}{2\sqrt{D_2 t}} \quad \eta > s(t), \quad s(t) = \alpha\sqrt{t}, \tag{5.41}$$

where $\alpha$ is determined by

$$\frac{(\phi_s - \phi_0)\sqrt{D_1}}{e^{\alpha^2/4D_1}\text{erf}\frac{\alpha}{2\sqrt{D_1}}} + \frac{(\phi_s - \phi_\infty)\sqrt{D_2}}{e^{\alpha^2/4D_2}\text{erfc}\frac{\alpha}{2\sqrt{D_2}}} = 0, \tag{5.42}$$

and

$$A = \frac{\phi_s - \phi_0}{\text{erf}\frac{\alpha}{2\sqrt{D_1}}}, \quad B = \frac{\phi_s - \phi_\infty}{\text{erfc}\frac{\alpha}{2\sqrt{D_2}}}. \tag{5.43}$$

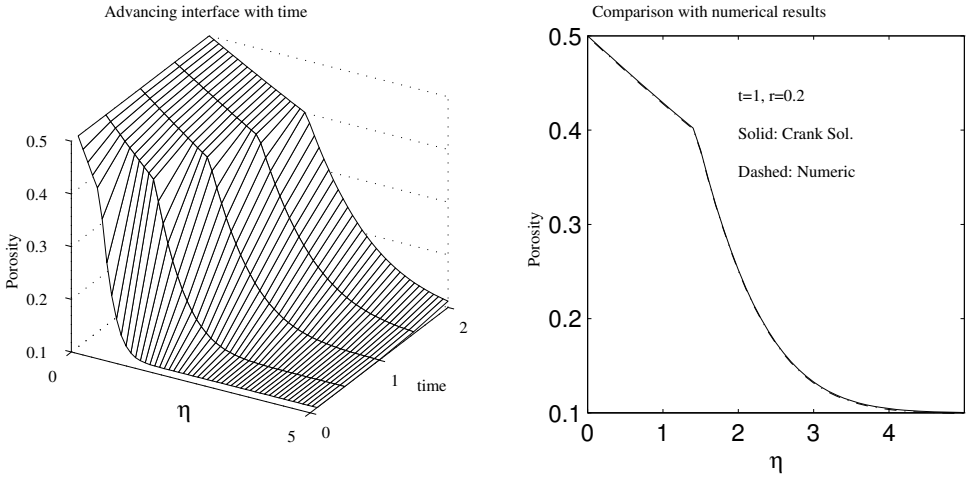


Figure 5.4 The advancing interface with time and comparison of Crank solution (solid) with numerical solutions (dashed) at $t = 1$.

Taking the values of $D_1 = 5$, $D_2 = 1$, $\phi_0 = 0.5$, $\phi_s = 0.4$, and $\phi_\infty = 0.1$, solving this problem numerically, we have the advancing interface in Fig. 5.4.

The comparison of the numerical solution with Crank's solution is shown in Fig. 5.4 which clearly shows that the numerical method is robust.

## 5.3 Irreversible unloading and reloading

By using the modified numerical formulae, we can study the case of irreversible unloading and reloading. When $calR = 0$ and $\dot{b} = 0$, equation (2.65) is equivalent to $u^s = -\phi(u^l - u^s)$. Now we can write the conditions at the interface as follows

$$[\tilde{p}] = 0 \ \text{ and } \ [\phi(u^l - u^s)] = 0 \ \text{ (i.e. } [u^s] = 0), \tag{5.44}$$

where $[\tilde{p}] = 0$ is the physical condition of continuous effective pressure, and $[\phi(u^l - u^s)] = 0$ is derived from the condition of no fluid stored (mass conservation) at the interface. The condition $[\tilde{p}] = 0$ does not necessarily imply that $[\phi] = 0$. From Fig. 5.1(b), we understand that $[\tilde{p}] = 0$ is equivalent to $[\phi] = 0$ only at the interface of *loading* and *unloading*, but it is generally equivalent to $[\phi] \neq 0$ at the interface of

*reloading* and *loading* although the jump $[\phi]$ may disappear when loading proceeds to the extent where the two branches join again. This will be also illustrated later in Fig. 5.9.

In the case of $[\phi] = 0$, $[u^s] = 0$ or $[\lambda\tilde{k}(-\frac{\partial\tilde{p}}{\partial z} - 1 + \phi] = 0$ implies $\tilde{p}_z^{NCL} = \tilde{p}_z^{URL}$. From Fig. 5.1(b) or Fig. 5.2, we have $\tilde{p}_\phi^{\rm NCL}/\tilde{p}_\phi^{\rm URL} = \gamma$ or $\phi_z^{\rm URL}/\phi_z^{\rm NCL} = \gamma$. Then, we have a jump condition at the interface

$$[\phi_z] = (1-\gamma)\phi_z^{\rm NCL} = (\frac{1}{\gamma} - 1)\phi_z^{\rm URL}, \tag{5.45}$$

where $\phi_z^{\rm NCL}$ is the value of $\phi_z$ along the NCL line while being compacted. Thus $\phi_z$ will be continuous if $\gamma = 1$. The discontinuity is a property of the irreversible compaction, which will be illustrated later in Fig. 5.7 and Fig. 5.8.

### 5.3.1 Slow compaction $\lambda << 1$

From the numerical results and discussion in Chapter 4, we understand that the behaviour of small $\lambda$ case is relatively simple. To study its main features, we use a step function of constant loading and constant unloading. The numerical results are shown in Fig. 5.5 at different times.

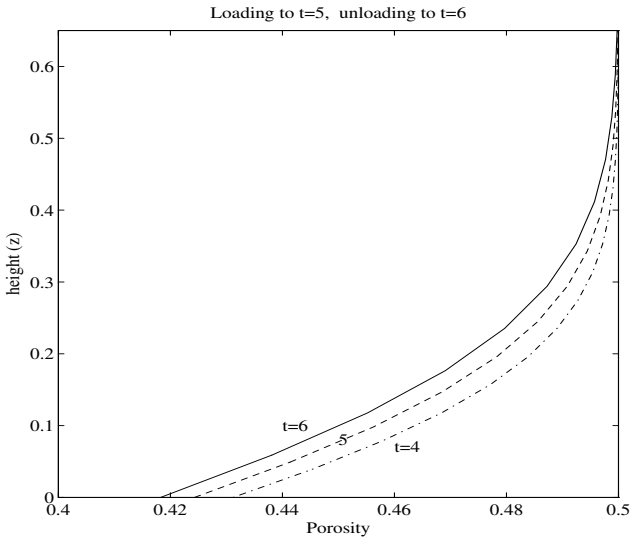


Figure 5.5 Porosity profile under constant unloading ($\lambda = 0.01$, $\gamma = 0.25$). $\dot{m} = 1$ if $t < 5$, $\dot{m} = -1$ if $5 \le t < 6$, $\dot{m} = 1$ if $6 \le t < 7$, .... Unloading begins at $t = 5$. $z$ is the height measured from the basement.

We see that the unloading at the top has very little influence on the porosity profile in the whole region. This is actually consistent with the boundary layer phenomenon near the bottom we obtained before in Chapter 4. The condition for the diffusion boundary layer remains unchanged in the case of constant unloading and cyclic loading. The porosity in the top region is $\phi = \phi_0$, which lies outside the boundary layer, that the effective pressure there is zero; thus the pore pressure $p$ is equal to the overburden pressure $P$, i.e., $p = P$, outside the boundary layer. The change in $P$ will affect the change of $p$ instantaneously, and their changes are in phase. The effective pressure is only positive within a thin boundary layer near the base where compaction proceeds very slowly. Thus the change of sedimentation rate or unloading without changing its surface porosity $\phi_0$ will not change the behaviour of the boundary layer near the bottom.

### 5.3.2 Fast compaction $\lambda >> 1$

Based on the previous discussion, we understand that it is the case of $\lambda >> 1$ that is more complicated and of more interest and importance. In order to show the main features of unloading, the following simple cases are investigated.

### 5.3.3 Constant loading, evolving to equilibrium, then constant unloading

We first investigate the system behaviour subject to unloading from the state of equilibrium. We load the system with a constant sedimentation rate to time $t = 5$, then let it evolve to its equilibrium. We then unload the system from this equilibrium state, and shift the time origin to $t = 0$ when unloading begins. The numerical results are shown in Fig. 5.6 in which the dashed curve corresponds to the equilibrium state.

It is clearly seen that the interface travels downward, and is smoothed by the diffusion effect which only becomes important on a length scale of $O(\frac{1}{m})$ or $O(0.1)$. Although the constitutive relations of effective pressure on porosity are two different functions in the unloading branch (above the interface) and compression branch (below the interface and at equilibrium in the present case), the model equation is still a single nonlinear diffusion equation whose diffusion coefficient strongly depends

on the porosity itself, which equivalently makes the model equation degenerate in such a way that the diffusive front essentially spreads with a finite speed. Thus, the influence region is mainly located in the top part of the basin.

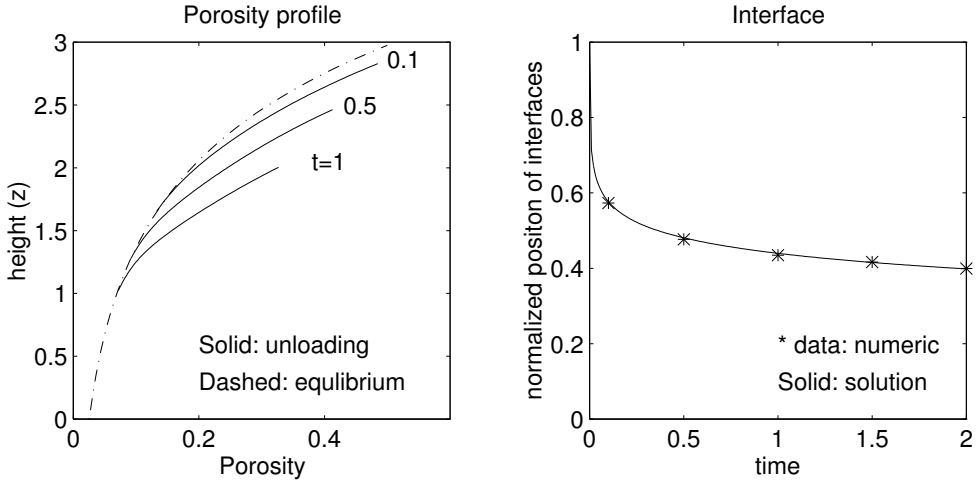


Figure 5.6 Travelling interface of unloading for the case of $\lambda = 100$, $\gamma = 0.25$. The left figure shows the travelling interface due to unloading at different times after unloading begins. The right figure gives the comparison of the solution (5.56) (solid) with numerical results (points with $*$).

To understand this phenomenon, let us make a small perturbation $\psi$, which is valid at least when $t$ is small, from the equilibrium state $\phi^e$. The equilibrium solution for the $\phi$ equation when $\lambda >> 1$ is essentially the Athy type solution

$$\phi^e = \phi_0 e^{-(h-z)}. \tag{5.46}$$

Written in terms of the (depth) variable $\eta = h - z$ with its origin at the top, this equilibrium solution is

$$\phi^e = \phi_0 e^{-\eta}. \tag{5.47}$$

Setting $\phi = \phi^e + \psi$ and using equations for equilibrium state $\dot{\phi}^e = 0$, $1/[\phi - (1-\gamma)\phi^e] \approx 1/(\gamma\phi^e)$ since $\phi \approx \phi^e$, the linearised perturbation equation for $\psi$ is

$$\frac{\partial \psi}{\partial t} = \lambda \frac{\partial}{\partial \eta}[\tilde{k}\frac{(1-\phi^e)^2}{\phi^e}\frac{\partial \psi}{\partial \eta}]. \tag{5.48}$$

Using (5.47), we find,

$$\frac{\partial \psi}{\partial t} = \Lambda \frac{\partial}{\partial \eta}[e^{-(m-1)\eta}\frac{\partial \psi}{\partial \eta}] \quad \text{with} \quad \Lambda = \lambda\frac{(1-\phi_0)^2}{\gamma\phi_0}, \tag{5.49}$$

i.e.

$$\psi_t = \Lambda e^{-(m-1)\eta}[\psi_{\eta\eta} - (m-1)\psi_\eta], \tag{5.50}$$

which is only valid when $t \leq O(\frac{1}{\lambda})$. Since $m >> 1$, we thus have approximately

$$\psi_t + \Lambda(m-1)e^{-(m-1)\eta}\psi_\eta = 0. \tag{5.51}$$

For a semi-infinite space approximation, we have the initial and boundary conditions for $\psi$

$$\psi(\eta = 0, t) = f(t) \text{ and } \psi(t = 0, \eta) = 0. \tag{5.52}$$

By using the method of characteristics, we have

$$\dot{\psi} = 0 \quad \text{and} \quad \dot{\eta} = \Lambda(m-1)e^{-(m-1)\eta}. \tag{5.53}$$

Integrating the above equations and using the initial and boundary conditions, we have

$$\psi = f(\tau) \quad \text{and} \quad \frac{1}{m-1}[e^{(m-1)\eta} - 1] = \Lambda(m-1)(t-\tau). \tag{5.54}$$

Eliminating $\tau$, we obtain the solution of (5.51)

$$\psi(\eta, t) = f[t - \frac{e^{(m-1)\eta} - 1}{\Lambda(m-1)^2}]. \tag{5.55}$$

Since the unloading begins from equilibrium state, the interface travelling downward is the interface where $\psi = 0$ or $t - (e^{(m-1)\eta} - 1)/\Lambda(m-1)^2 = 0$. From the above solution, we therefore find that the interface $s(t)$ is given by

$$s(t) = \frac{1}{m-1}\ln[\Lambda(m-1)^2 t + 1]. \tag{5.56}$$

Written in terms of $\lambda$, we have

$$s(t) \approx \frac{1}{m-1}\ln[\frac{\lambda(1-\phi_0)^2(m-1)^2}{\gamma\phi_0}t + 1]. \tag{5.57}$$

This solution implies that the interface will travel faster as $\gamma$ gets smaller. In the extreme case when $\gamma = 0$, the interface travels downward nearly instantaneously to the base of the column, and the whole region is unloaded ($s(t) \to \infty$ as $\gamma \to 0$). It is worth pointing out that $s(t)$ is actually the characteristics of equation (5.51) and thus the interface velocity $\dot{s}(t)$ is independent of unloading rate. Furthermore $\dot{s}(t)$ is

decreasing with time $t$, which implies that the unloading effect is essentially located in the top region at least for a short time after unloading begins.

The comparison of this solution with numerical results is shown in the right in Fig. 5.6. The consistency verifies the above obtained solution.

### 5.3.4 Constant loading, then constant unloading

Figure 5.7 shows the porosity profile for constant loading to $t = 5$, then constant unloading for some short times. $\lambda = 100$ and $\gamma = 0.25$ are fixed throughout the computations.

Figure 5.7 clearly shows that an interface of discontinuous $\phi_z$ will be generated at the time when increasing loading switches to erosional unloading. The travelling velocity of the interface is not a constant. The downward travelling interface of the unloading region will extend the unloading region much deeper, and finally to the whole domain. From the numerical results, we have $\phi_z^{NCL} \approx 0.126$, $\phi_z^{URL} \approx 0.032$, $[\phi_z] \approx 0.094 \approx (1-\gamma)\phi_z^{NCL}$, which confirms that the jump condition (5.45) is satisfied.

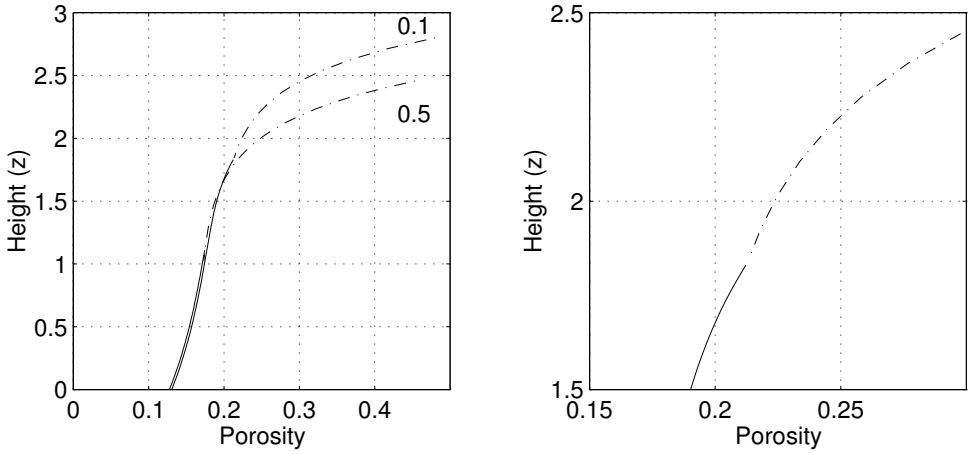


Figure 5.7 The advancing interfaces of discontinuity of $\phi_z$ with a Heaviside step function of sedimentation/erosion rate ($\dot{m}(t) = 1$ if $t < 5$, $\dot{m}(t) = -1$ if $t \geq 5$). The values of $\lambda = 100$, $\gamma = 0.25$ are used. Dashed parts shows the swelling region while the solid ones correspond to the compressing region at different times $t = 5.1$, 5.5 (or 0.1, 0.5 after unloading). The right figure is the enlarged part of the left one near the first interface.

### 5.3.5 Cyclic loading and unloading

To investigate the main features of the system under cyclic loading and unloading, a square wave function of sedimentation/erosion rates is used. Firstly, the system is constantly loaded to $t = 5$, then it goes under a *square* wave of unloading and reloading with a period $T = 1$. An interesting feature arises, a discontinuous porosity profile as shown in Fig. 5.8 (only the first cycle is shown). There exist two travelling interfaces after a cycle of loading-unloading-reloading.

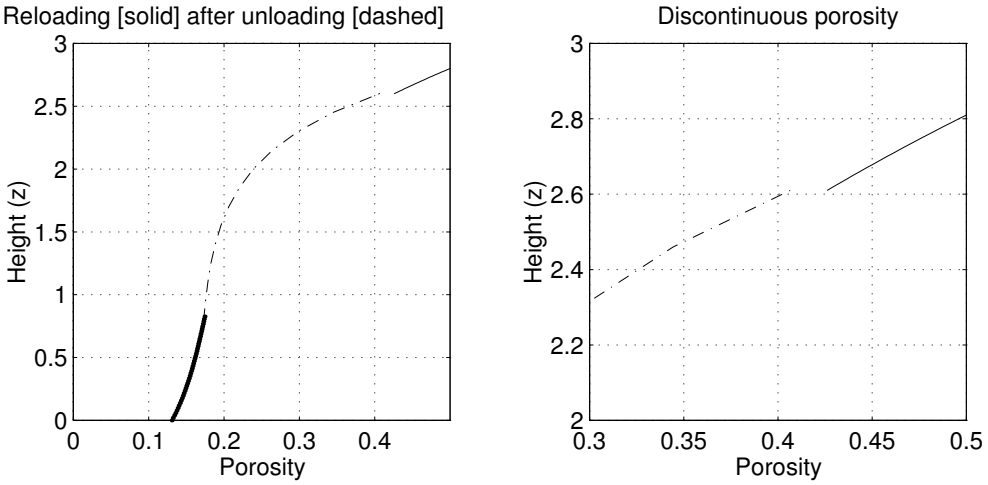


Figure 5.8 Porosity profile under cyclic unloading and reloading at time $t = 5.8$ (or 0.8 after unloading). We have used $\lambda = 100$, $\gamma = 0.2$ and $\dot{m}(t) = 1$ if $t < 5$, $\dot{m}(t) = -1$ if $5 \leq t < 5.5$, $\dot{m}(t) = 1$ if $5.5 \leq t < 6$, $\dot{m}(t) = -1$ if $6 \leq t < 6.5$ .... Solid part is in compression along NCL line, dashed part is reloaded along URL line and dotted part corresponds to swelling along URL (unloading). Discontinuous porosity occurs at the interface of newly loaded region (solid) near the top and reloaded region (dashed) in the middle.

To understand how the phenomenon of the discontinuous porosity occurs, we refer to Fig. 5.9 to aid our discussion. For some short time $t$ after reloading it is possible that the effective pressure $\tilde{p} < \tilde{p}^*$, where $\tilde{p}^*$ is the maximum value in the time-history. The new sediment added to the system will go along the NCL line, while the older previously unloading sediment will be reloaded along the URL line. The physical condition at the interface between the new and older sediments is the continuity of

the effective pressure. From Fig. 5.9, we see that the same value of effective pressure corresponds to two different porosity values if $\tilde{p} < \tilde{p}^*$. Thus a discontinuity of porosity will appear at the interface. If the loading proceeds to $\tilde{p} \geq \tilde{p}^*$, then this discontinuity will disappear.

The velocity of the interface of discontinuous porosity can be obtained by using the jump condition from the weak formulation of (5.8)

$$\dot{s}(t) = -\frac{[(1-\phi)u^s]}{[\phi]}, \tag{5.58}$$

where $u^s = -\lambda\tilde{k}[\frac{\partial\tilde{p}}{\partial z} + (1-\phi)]$.

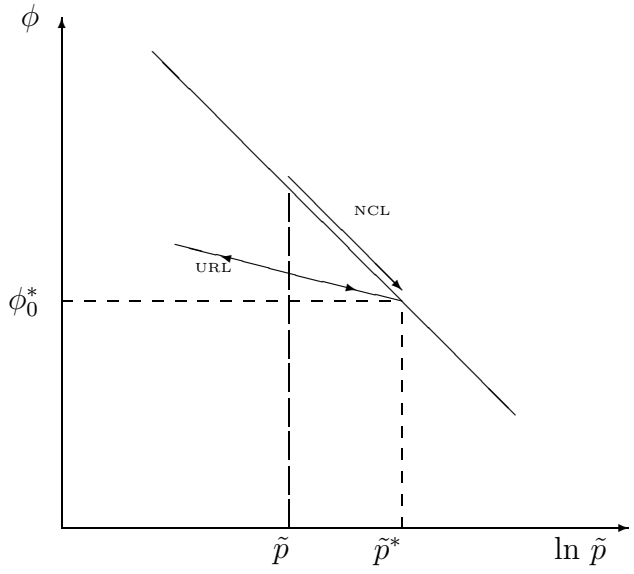


Figure 5.9 Sketch map of effective pressure versus porosity. NCL is normal consolidation line and URL is unloading-reloading line.

From the equation $\phi u^l + (1-\phi)u^s = 0$, the condition of no fluid stored at the interface implies the Darcy flow is continuous, which is equivalent to the statement $u^s$ should be continuous, i.e., $[u^s] = 0$. Then the above equation becomes

$$\dot{s}(t) = -\frac{[(1-\phi)]u^s}{[\phi]} = \frac{[\phi]}{[\phi]}u^s = u^s. \tag{5.59}$$

This means that the interface will *'fix'* on the solid matrix. But when reloading proceeds to $\tilde{p} \geq \tilde{p}^*$ then $[\phi] = 0$, the interface will move off the solid matrix and start

travelling down if effective pressure in the previously unloaded sediment below this interface has not reached its previous maximum in time-history.

## 5.4 Summary

The nonlinear compaction behaviour of unloading and loading on a basin scale has been modelled as a two-branch nonlinear diffusion equation with a switch condition (5.23) and (5.24). The constitutive relations are extended in terms of a dimensionless parameter $\gamma$ which is a slope ratio of URL line to NCL line.

In the case of slow compaction ($\lambda << 1$), the behaviour is relatively simple, and the loading/unloading at the top has very little influence on the porosity profile. The behaviour of large $\lambda$ case (fast compaction) is more complicated and of more interest. A downward travelling interface is generated whenever a switch occur between URL and NCL branches. The velocity of the travelling interface depends on the slope ratio $\gamma$ and decrease with time $t$. In the lower region, the porosity profile is essentially the same as that of constantly increasing loading.

In the case when newly loaded sediments adds at the top of unloaded sediments, a discontinuity of porosity may occur for a very short time. The new sediment added to the system will go along the NCL line, while the older previously unloading sediment will be reloaded along the URL line. The physical condition at the interface between the new and older sediments is the continuity of the effective pressure, which corresponds to two different porosity values when $\tilde{p} < \tilde{p}^*$. Thus a discontinuity of porosity may occur at the interface. If the loading proceeds to $\tilde{p} \geq \tilde{p}^*$, then this discontinuity will disappear.

# Chapter 6

# Diagenesis: First Order Model

In the previous chapters, we have mainly investigated the porosity evolution due to mechanical compaction. In this chapter, we will analyse the effects of diagenesis on the porosity evolution, and show how the model suggests radically different styles of behaviour in the distinct limits of slow ($\lambda << 1$) and fast ($\lambda >> 1$) compaction.

## 6.1 Simplified model equations

It is clearly seen that $\mathcal{R}\bar{k}_r$ always appears as a combination in the above model equations (2.51)-(2.57). It can be easily rewritten as

$$\mathcal{R}\bar{k}_r = \exp[\beta(\Theta - \Theta_c)] \quad \text{and} \quad \Theta_c = \frac{1}{\beta}\ln\frac{1}{\mathcal{R}}, \tag{6.1}$$

where the new parameter $\Theta_c$, which replaces $\mathcal{R}$, is a dimensionless critical temperature (with reference to the surface temperature). In the following discussions, we will see that the diagenesis reaction virtually takes place in a region called the *diagenetic window*, at a depth of $\sim \Theta_c$, with its thickness controlled by $\beta$.

From the typical values of model parameters (Smith 1971, Eberl & Hower 1976, Lerche 1990, Audet & Fowler 1992) $E_a = 60$ kJ/mol, $T_c = 90^o$C, $T_0 = 300$ K, we have $\beta \approx 2.3$, $\Theta_c \approx 2$, $\lambda \approx 1$ and $\mathcal{R} \approx 0.01$ for $d \sim 1\,$km. An initial porosity of $\phi_0 = 0.5$ for pore water at the top of the basin is used by other authors (Smith 1971, Sharp 1976, Bethke & Corbet 1988, Audet & Fowler 1992). Initial porosities 0.2 for montmorillonite, 0 for illite and 0.3 for quartz are used in our computations.

For the convenience of discussing the main effects of diagenesis, we can simply take $\overline{\Delta H} = 0$, $a = 0$, and $\dot{b} = 0$ in these equations without loss of generality. Based on the work of Smith (1971), Sharp (1976) and Audet & Fowler (1992), we adopt the following constitutive functions

$$\tilde{p} = \ln(\phi_0/\phi) - (\phi_0 - \phi), \tag{6.2}$$

$$\tilde{k} = (\phi/\phi_0)^m, \quad m = 8, \tag{6.3}$$

$$\hat{K} = (K_l/K_s)^{\phi-\phi_0}, \quad K_l/K_s = 0.3, \tag{6.4}$$

$$\dot{m}_s = 1, \tag{6.5}$$

We notice that $\phi_c$ can be determined if we know $\phi_i, \phi_m, \phi$ since $\phi_c+\phi_i+\phi_m+\phi = 1$. Thus the quartz equation can be eliminated. Inserting these constitutive relations, letting $\phi = \phi_l$, and using *Darcy's law* (2.56) and the *force balance equation* (2.58) to obtain $u^s, u^l$. we finally have the simplified model equations

*Equations for volume fractions*

$$\frac{\partial \phi_m}{\partial t} = -e^{\beta(\Theta-\Theta_c)}\phi_m - \lambda\frac{\partial}{\partial z}\{\tilde{k}\phi_m(1-\phi)[\frac{1}{\phi}\frac{\partial \phi}{\partial z} - 1]\}$$

$$-(\delta-1)a_1\frac{\partial(\psi\phi_m)}{\partial z}, \tag{6.6}$$

$$\frac{\partial \phi_i}{\partial t} = (1-a_1)e^{\beta(\Theta-\Theta_c)}\phi_m - \lambda\frac{\partial}{\partial z}\{\tilde{k}\phi_i(1-\phi)[\frac{1}{\phi}\frac{\partial \phi}{\partial z} - 1]\}$$

$$-(\delta-1)a_1\frac{\partial(\psi\phi_i)}{\partial z}, \tag{6.7}$$

$$\frac{\partial \phi}{\partial t} = \lambda\frac{\partial}{\partial z}\{\tilde{k}(1-\phi)^2[\frac{1}{\phi}\frac{\partial \phi}{\partial z} - 1]\}$$

$$+a_1\delta e^{\beta(\Theta-\Theta_c)}\phi_m - (\delta-1)a_1\frac{\partial[\psi(1-\phi)]}{\partial z}, \tag{6.8}$$

*Temperature equation*

$$[\alpha(1-\phi)+\phi]\frac{\partial \Theta}{\partial t} = \Lambda\frac{\partial}{\partial z}(\hat{K}\frac{\partial \Theta}{\partial z}) - a_1(\delta-\alpha)e^{\beta(\Theta-\Theta_c)}\phi_m\Theta$$

$$-(\delta-1)a_1\psi\frac{\partial \Theta}{\partial z} - (\alpha-1)\lambda\tilde{k}(1-\phi)^2[\frac{1}{\phi}\frac{\partial \phi}{\partial z} - 1]\frac{\partial \Theta}{\partial z}, \tag{6.9}$$

with *boundary conditions*

$$\frac{\partial \phi}{\partial z} - \phi = 0, \;\; \frac{\partial \Theta}{\partial z} = -\frac{1}{\hat{K}} \;\text{ at } z = 0, \tag{6.10}$$

and

$$\phi_j = \phi_{j0}, \;\; \Theta = 0,$$

$$\dot{h} = 1 + \lambda \tilde{k}(1-\phi)[\frac{1}{\phi}\frac{\partial \phi}{\partial z} - 1] + (\delta - 1)a_1 \psi \text{ at } z = h. \tag{6.11}$$

$$\psi = \int_0^z e^{\beta(\Theta - \Theta_c)} \phi_m dz, \tag{6.12}$$

where $\phi_j = \phi_i, \phi_m, \phi$; and $\phi_{c0} + \phi_{i0} + \phi_{m0} + \phi_0 = 1$.

It is based on these equations that the moving boundary problems will be solved numerically by using the predictor/corrector implicit finite-difference method presented by Meek & Norbury (1982).

## 6.2 Diagenesis with slow compaction $\lambda << 1$

From the generalized mathematical model, we notice that the temperature equation (6.9) is only weakly coupled with porosity via heat conductivity. If the heat change during diagenesis is negligible, then temperature essentially evolves in rather an independent way. Thus if $\Lambda >> 1$ the temperature distribution can be treated as a prescribed function. In order to investigate the main features of diagenesis, it is convenient to first study the case of $\lambda << 1$ (slow compaction) with nearly steady-state temperature distribution ($\Lambda >> 1$). When $\Lambda >> 1$ so that conduction is dominate, then (6.9) becomes approximately

$$\frac{\partial^2 \Theta}{\partial z^2} = 0, \tag{6.13}$$

so $\Theta$ can be written as

$$\Theta = \frac{h(t) - z}{\hat{K}}. \tag{6.14}$$

For the case of $\Lambda << 1$, temperature increases mainly in the boundary layer near the basement and is normally not high enough to switch on the diagenetic reaction. The temperature distribution is usually very close to steady state in most geological cases

of interest. Therefore, we will mainly concentrate on the case of a linear temperature distribution.

The numerical results are given in Fig. 6.1 with $a_1 = 0.15, \Theta_c = 2, t = 5$. It is clearly shown that $\phi_m$ decreases very rapidly in a region of temperature near the critical value $\Theta_c$. The excess pore, overburden and hydrostatic pressures are also given in Fig. 6.1.

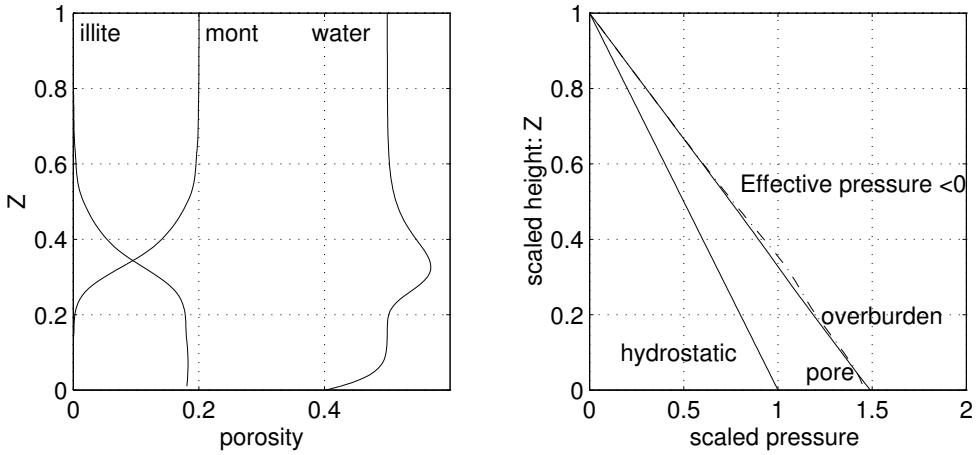


Figure 6.1 Porosity and pressure profiles with diagenesis ($\lambda = 0.01$). $Z$ is scaled height. The porosities of montmorillonite and illite are marked with 'mont' and 'illite', respectively. The negative effective pressure in the diagenetic region is physically unacceptable. *Hydraulic failure* will occur to keep effective pressure non-negative.

From the numerical results, we understand that $\phi \approx \phi_0, \phi_z \approx 0$, i.e, $u^s \approx 0$. This means the terms $\partial(\phi_m u^s)/\partial z$ in the $\phi_m$ equation, $\partial(\phi_i u^s)/\partial z$ in the $\phi_i$ equation are negligible. The temperature distribution is approximately (with $\hat{K} = 1$)

$$\Theta = h(t) - z. \tag{6.15}$$

The dimensionless parameter $a_1$ represents the effect of the water content released during montmorillite diagenesis (typically $a_1 = 0.1$). Therefore, it is reasonable to assume $a_1 << 1$ in the following analysis. The fact that $\phi \approx \phi_0$ and $\psi << 1$ in equation (6.11) for the case of small $\lambda$ suggests that $\dot{h} \approx 1$. With these approximations, the model equations can be written as

$$\frac{\partial \phi_m}{\partial t} = -e^{\beta[h(t)-z-\Theta_c]}\phi_m, \tag{6.16}$$

$$\frac{\partial \phi_i}{\partial t} + (1 - a_1)\frac{\partial \phi_m}{\partial t} = 0, \tag{6.17}$$

$$\frac{\partial \phi}{\partial t} = \lambda' \frac{\partial^2 \phi}{\partial z^2} + a_1 e^{\beta[h(t)-z-\Theta_c]}\phi_m, \tag{6.18}$$

where $\lambda' = \lambda(1-\phi_0)^2/\phi_0$. The boundary conditions are

$$\phi = \phi_0,\ \phi_m = \phi_{m0},\ \phi_i = 0, \ \text{ at } \ z = h, \tag{6.19}$$

$$\phi_z = \phi, \ \text{ at } \ z = 0. \tag{6.20}$$

The solutions for equations (6.16), (6.17) and (6.18) can be easily obtained in the approximate form

$$\phi_m = \phi_{m0}\exp\{-\frac{1}{\beta}e^{\beta[h(t)-z-\Theta_c]}\} \tag{6.21}$$

$$\phi_i = (1 - a_1)(\phi_{m0} - \phi_m), \tag{6.22}$$

$$\phi = \phi_0 - \phi_0\sqrt{4\lambda' t}\,\text{ierfc}\frac{z}{\sqrt{4\lambda' t}}$$
$$+\frac{8a_1 h}{\pi^2\lambda'}\sum_{k=1}^{\infty}\frac{1}{k^2}\{1 - e^{-\lambda' k^2\pi^2 t/4h^2}\}\cos\frac{k\pi z}{2h}\int_0^h e^{\beta[h(t)-\xi-\Theta_c]}\cos\frac{k\pi\xi}{2h}d\xi. \tag{6.23}$$

Solutions (6.21) and (6.22) will be compared with the numerical results later in Fig. 6.2. It is worth pointing out that solution (6.23) implies that $\phi > \phi_0$ in a narrow region near $z = h - \Theta_c$. This is physically unrealsitic which consequently results in an interesting phenonemenon known as *hydraulic failure*, which occurs from the diagenetic region up to the basin top (see Fig. 6.2).

## Hydraulic Failure

From Fig.6.1, we notice that the porosity $\phi$ in the diagenetic region can exceed its initial value $\phi_0$; this is physically unacceptable since the effective pressure $p_e < 0$, but in reality $p_e$ should always be nonnegative. In fact, if $p_e$ becomes negative, we expect that *hydro-fracturing* will occur to keep the effective pressure nonnegative. If we impose a condition $\tilde{p} \geq 0$, the numerical results will ensure that $\phi \leq \phi_0$. But then the permeability $\tilde{k}$ will not take the form $(\phi/\phi_0)^m$, and should be determined in another way. Hydraulic failure will behave in such a way that an increased permeability $k_{\text{frac}}$ will make the fluid drainage balance the water generation to satisfy the physical condition $\tilde{p} \geq 0$.

Since $\phi \approx \phi_0$, $\phi_t \approx 0$ in the fractured region, we have

$$u^s = -(1-\phi_0)\lambda k_{\text{frac}}. \tag{6.24}$$

Mass conservation implies that

$$(1-\phi_0)^2\lambda \frac{\partial k_{\text{frac}}}{\partial z} = a_1\delta e^{\beta[h(t)-z-\Theta_c]}\phi_m. \tag{6.25}$$

Integrating this equation from 0 to $z$, we have

$$k_{\text{frac}} = 1 + \frac{a_1\delta}{(1-\phi_0)^2\lambda}\int_0^z e^{\beta[h(t)-z-\Theta_c]}\phi_m dz. \tag{6.26}$$

By using the solution for $\phi_m$, we have

$$k_{\text{frac}} \approx 1 \quad \text{for} \quad z < h(t) - \Theta_c, \tag{6.27}$$

and

$$k_{\text{frac}} \approx 1 + \frac{a_1\delta\phi_{m0}}{(1-\phi_0)^2\lambda}\exp\{-\frac{1}{\beta}e^{\beta[h(t)-z-\Theta_c]}\} \quad \text{for} \quad z > h(t) - \Theta_c. \tag{6.28}$$

This means that hydraulic failure can only occur when $t > t_c \approx \Theta_c$.

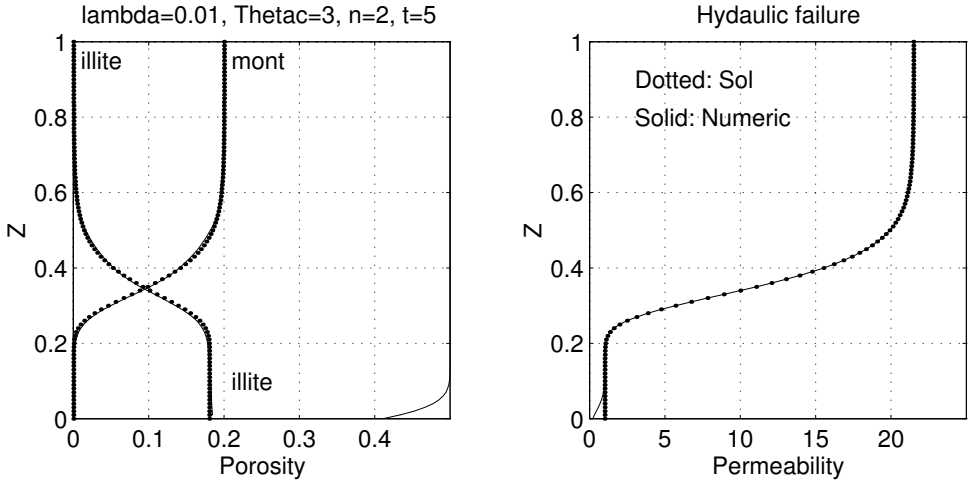


Figure 6.2 Comparison of the analytical solutions (6.21) and (6.22) with numerical results. The permeability $k_{\text{frac}}$ (6.28) (dotted) resulting from the hydraulic failure increases rapidly at the diagenetic region where porosity changes dramatically. The hydraulic failure can occur from the diagenetic region up to the basin top.

The comparison of the analytical solutions (6.21) and (6.22) with numerical results is shown in Fig. 6.2 (left figure). The permeability $k_{\text{frac}}$ (6.28) is also shown in Fig.

6.2 (right figure). The permeability $k_{\text{frac}}$ (6.28) (dotted) resulting from the hydraulic failure increases rapidly at the diagenetic region where porosity changes dramatically. It is clearly seen that the hydro-fracturing develops mainly from the diagenesis region to the top surface.

## Changing $\Theta_c$ and $\beta$

From the numerical results and the above solutions, we see that the diagenetic window is essentially controlled by the depth parameter $\Theta_c$ and the shape parameter $\beta$. Fig. 6.3 shows the effect of changing these two parameters. The numerical and the analytical solutions are virtually the same, thus we only show the analytical solutions in Fig. 6.3.

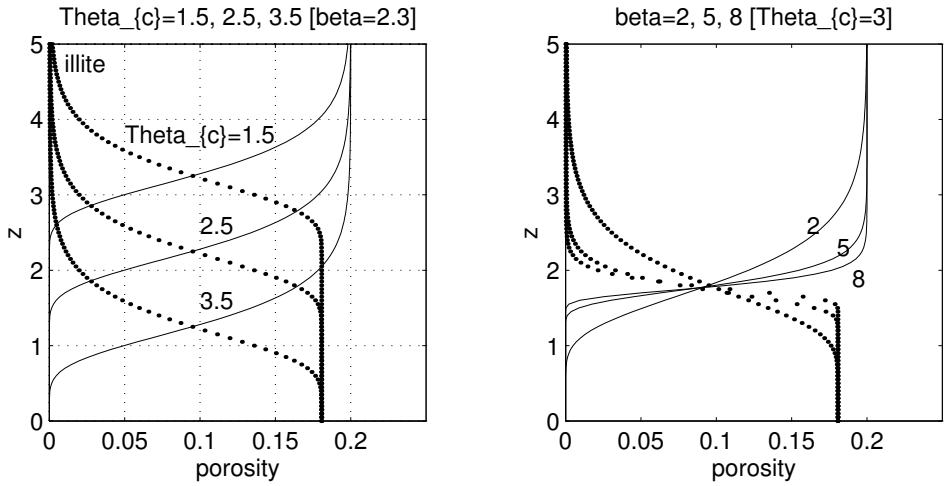


Figure 6.3 Changing $\Theta_c$ and $\beta$ in the case of $t = 5$ for $\lambda = 0.01$. The left figure shows the effect of changing $\Theta_c = 1.5,\ 2.5,\ 3.5$ which only shifts the position of the diagenetic region and does not change the shape of the porosity profile, while the right figure shows that the change of $\beta = 2,\ 5,\ 8$ will dramatically change the thickness of the diagenetic region with its central position ($\Theta_c$) fixed.

It is clearly seen that the change of $\Theta_c$ does not change the shape of the diagenetic region but does change its position, while the change of $\beta$ only affects its shape.

## 6.3 Diagenesis with fast compaction $\lambda >> 1$

In this case, the numerical results are shown in Fig. 6.4 with the values of $\mathcal{R} = 0.01$, $a_1 = 0.1$, $t = 5$ for a linear temperature distribution $\Theta = h - z$. It is worth pointing out that the curves of smectite (or montmorillonite) and illite in Fig. 6.4 correspond to their normalized volume fractions in the solid, namely, *solid volume fractions*, which remove the effect of the change of porosity $\phi$ due to compaction. The solid volume fraction is related to the real volume fraction by

$$\Phi_m = \phi_m \frac{1-\phi_0}{1-\phi} \qquad \text{or} \qquad \phi_m = \Phi_m \frac{1-\phi}{1-\phi_0}, \tag{6.29}$$

$$\Phi_i = \phi_i \frac{1-\phi_0}{1-\phi} \qquad \text{or} \qquad \phi_i = \Phi_m \frac{1-\phi}{1-\phi_0}. \tag{6.30}$$

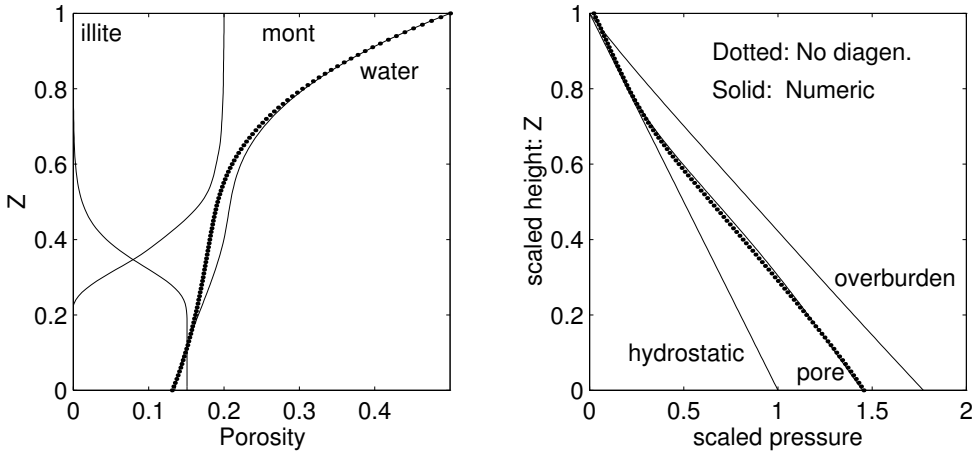


Figure 6.4 Porosity profile with diagenesis ($\lambda = 100$). $Z$ is scaled height. The solid fractions (6.29) (smectite or montmorillonite) and (6.30) (illite) are used in the left figure. The dotted curves correspond to the case of no diagenesis or $a_1 = 0$. We see that mechanical compaction is the most important factor controlling the porosity evolution and diagenesis is only of secondary importance.

We see that the top region is always nearly in equilibrium, only the middle and lower regions are dynamic. It is clearly seen that the diagenesis reaction is essentially taking place in a small region, *the diagenetic window*, which is located in the region

where the temperature is nearly at a critical temperature. This figure presents a more clear and full view of the compaction evolution during diagenesis. Pore water pressure is enhanced by the water released during diagenesis. From this figure, we understand that the mechanical compaction is the most important factor controlling the porosity evolution, the diagenesis process is also a very important factor, but it is in the secondary position.

**Analysis**

From the governing equations, we see that the $\phi_m$ and $\phi$ equations are closely coupled. Once the solutions for these two equations are obtained, then the solutions for $\phi_i$ and $\phi_c$ can be easily determined. For the convenience of analysis, we can take $\hat{K}(\phi) \approx 1$. If $\Lambda >> 1$, the temperature distribution can approximately be treated as the prescribed function $\Theta = h(t) - z$. From the numerical results, we understand that the diagenesis reaction is taking place in a narrow region below which the reaction is fully completed, and above which the reaction has not switched on. Rewriting the $\phi_m$ and $\phi$ equations (6.2) and (6.3), we have

$$\frac{\partial \phi_m}{\partial t} = -e^{\beta[h(t)-z-\Theta_c]}\phi_m - \lambda \frac{\partial}{\partial z}\{(\frac{\phi}{\phi_0})^m \phi_m (1-\phi)[\frac{1}{\phi}\frac{\partial \phi}{\partial z} - 1]\}$$
$$-(\delta - 1)a_1 \frac{\partial\{\phi_m \int_0^z \phi_m e^{\beta[h(t)-z-\Theta_c]} dz\}}{\partial z}, \tag{6.31}$$
$$\frac{\partial \phi}{\partial t} = \lambda \frac{\partial}{\partial z}\{(\frac{\phi}{\phi_0})^m (1-\phi)^2[\frac{1}{\phi}\frac{\partial \phi}{\partial z} - 1]\}$$
$$+a_1 \delta e^{\beta[h(t)-z-\Theta_c]}\phi_m - (\delta - 1)a_1 \frac{\partial\{(1-\phi)\int_0^z \phi_m e^{\beta[h(t)-z-\Theta_c]} dz\}}{\partial z}, \tag{6.32}$$

with boundary conditions

$$\frac{\partial \phi}{\partial z} - \phi = 0, \text{ at } z = 0, \tag{6.33}$$
$$\phi_m = \phi_{m0}, \quad \phi = \phi_0,$$
$$\dot{h} = 1 + \lambda(\frac{\phi}{\phi_0})^m (1-\phi)[\frac{1}{\phi}\frac{\partial \phi}{\partial z} - 1] + (\delta - 1)a_1 \int_0^z \phi_m e^{\beta[h(t)-z-\Theta_c]} dz \text{ at } z = h. \tag{6.34}$$

From the numerical results and the above governing equation, we understand that there exists a transition defined by $\phi^* = \phi_0 \exp[-\ln \lambda / m]$. In general, we have $\phi^* \sim O(1)$, which implies that $m >> 1$. As the volume fractions $\phi_m$, $\phi_i$ change dramatically

in a relatively narrow region, we will assume that $\beta >> 1$, and in fact $\beta \sim m$ (or $\beta/m = A$ with $A = O(1)$). Noticing that the typical value of $a_1$ is about 0.1, we can also assume that $a_1 \sim O(\frac{1}{m}) << 1$, which will make $ma_1 = O(1)$.

From the asymptotic analysis in the case without diagenesis (in Chapter 4) and the numerical results, we can easily find that there exist two critical times $t^*$ (defined as before) and $t_c$ corresponding to two typical basin thicknesses $h^* = \Pi$ and $h_c = \Theta_c$. Normally, $t^* < t_c$. For a short time $t < t^*$, the porosity decreases nearly exponentially with depth, which means that the compaction is essentially at equilibrium. As time increases to a critical time $t^*$, compaction becomes non-equilibrium although the diagenetic reaction has not been switched on. As the process proceeds to another critical time $t_c$, diagenesis comes into play, then we will naturally expect that the behaviours may be different in these different cases.

**Short time behaviour ($t < t^*$)**

For a thin layer or short time, we have $h - z < \Pi < \Theta_c$ and $\exp[\beta(h - z - \Theta_c)] << 1$ when $\beta >> 1$. Equations (6.31) and (6.32) become approximately

$$\frac{\partial \phi_m}{\partial t} = -\lambda \frac{\partial}{\partial z}\{(\frac{\phi}{\phi_0})^m \phi_m (1-\phi)[\frac{1}{\phi}\frac{\partial \phi}{\partial z} - 1]\}, \tag{6.35}$$

and

$$\frac{\partial \phi}{\partial t} = \lambda \frac{\partial}{\partial z}\{(\frac{\phi}{\phi_0})^m (1-\phi)^2[\frac{1}{\phi}\frac{\partial \phi}{\partial z} - 1]\}. \tag{6.36}$$

This second equation is exactly the same equation as equation (4.1) we solved in Chapter 4. As $\lambda(\phi/\phi_0)^m >> 1$ still holds, we still can get the Athy-type solution (for the leading order) by following the same perturbation procedure as discussed earlier in Chapter 4. For simplicity and clarity, we will only repeat some parts of the analysis to refresh our solution procedure. The solution for equation (6.36) is

$$\phi = \phi_0 \exp[-(h - z)], \tag{6.37}$$

As time increases, porosity $\phi$ decreases, but the dramatic decrease of $(\phi/\phi_0)^m$ if $m >> 1$ will cause the perturbation expansions only to be valid if $\lambda\tilde{k} >> 1$ or $\phi < \phi^* = \phi_0 \exp[-\frac{1}{m}\ln\lambda]$. In addition, $\exp[\beta(h - z - \Theta_c)] << 1$ if $\beta$ is relatively large.

Now if $\phi > \phi^*$, $(\phi/\phi^*)^m$ is exponentially large, and $\exp[\beta(h-z-\Theta_c)]$ is exponentially small, therefore

$$(\frac{\phi}{\phi^*})^m(1-\phi)^2(\frac{1}{\phi}\frac{\partial\phi}{\partial z}-1) \approx -(1-\phi_0)(1-\dot{h}); \tag{6.38}$$

using the boundary condition at $z = h$. We still have

$$\phi \approx \phi_0 \exp[-(h-z)], \tag{6.39}$$

whence $\phi_t \approx -\dot{h}\phi_z$, and an improved approximation (4.65) to the $\phi$ equation (4.1) therefore becomes

$$(\frac{\phi}{\phi^*})^m(1-\phi)^2(\frac{1}{\phi}\frac{\partial\phi}{\partial z}-1) \approx \dot{h}(\phi_0-\phi)-(1-\phi_0)(1-\dot{h}). \tag{6.40}$$

To obtain the solution for $\phi_m$, we change variable by defining

$$\Phi = \frac{\phi_m(1-\phi_0)}{1-\phi}, \tag{6.41}$$

which is the solid fraction of montmorillonite (or smectite). Combining this with equation (6.36), (6.35) becomes

$$(1-\phi)\frac{\partial\Phi}{\partial t}-\Phi\frac{\partial\phi}{\partial t} = -\Phi\frac{\partial\phi}{\partial t}-(\frac{\phi}{\phi^*})^m[\frac{1}{\phi}\phi_z-1]\frac{\partial\Phi}{\partial z}. \tag{6.42}$$

By using equation (6.40), we have approximately

$$\Phi_t - \frac{\dot{h}(1-\phi)-(1-\phi_0)}{(1-\phi)^3}\Phi_z = 0, \tag{6.43}$$

with a boundary condition

$$\Phi = \phi_{m0}. \tag{6.44}$$

The characteristics of equation (6.43) imply that

$$\dot{\Phi} = 0, \quad \text{or} \quad \Phi = \phi_{m0}. \tag{6.45}$$

In order to obtain the solution for $\phi_i$, we add the $\phi_i$ and $\phi_m$ equations to eliminate the source terms, so that we have

$$\frac{\partial\bar{\phi}}{\partial t}+\frac{\partial(\bar{\phi}u^s)}{\partial z} = 0 \quad \text{with} \quad \bar{\phi} = \phi_i + (1-a_1)\phi_m. \tag{6.46}$$

The same procedure applies to $\bar{\phi}$ by changing the variable $\bar{\Phi} = \bar{\phi}(1-\phi_0)/(1-\phi)$ leading to $\bar{\Phi} = (1-a_1)\phi_{m0}$.

**Transition and solution below transition layer ($t^* < t < t_c$)**

The above approximation, however, becomes invalid in the transition region when $h - z \approx \Pi$ or below the transition region and specifically we define

$$z = h - \Pi - \frac{\ln m}{m} + \frac{\xi}{m},$$

$$\phi = \phi^* \exp[\frac{1}{m}(-\ln m + \Psi)], \tag{6.47}$$

whence it follows by a matching principle that $\Psi \sim \xi$ as $\xi \to \infty$. $\Psi$ satisfies the equation

$$(-\dot{h}\Psi_\xi + \frac{1}{m}\Psi_t)\phi_\infty \exp[\frac{1}{m}(\Psi - \Psi_\infty)]$$

$$= \frac{\partial}{\partial \xi}[e^\Psi \{1 - \phi_\infty \exp[\frac{1}{m}(\Psi - \Psi_\infty)]\}^2 (\Psi_\xi - 1)], \tag{6.48}$$

or

$$-\dot{h}\phi_\infty \Psi_\xi = \frac{\partial}{\partial \xi}[e^\Psi (1 - \phi_\infty)^2 (\Psi_\xi - 1)], \tag{6.49}$$

where we define

$$\phi_\infty = \phi^* \exp[\frac{1}{m}(-\ln m + \Psi_\infty)], \tag{6.50}$$

and $\Psi_\infty$ will be defined below. As discussed before in Chapter 4, we still have

$$\dot{h} = \frac{1 - \phi_0}{1 - \phi_\infty} - \frac{(1 - \phi_\infty)^2}{m} e^{\Psi_\infty} .... \tag{6.51}$$

In terms of $z$, the equation for $\Psi$, (6.48) is then

$$\Psi_t \phi_\infty \exp[\frac{1}{m}(\Psi - \Psi_\infty)] = \frac{\partial}{\partial z}[e^\Psi \{1 - \phi_\infty \exp[\frac{1}{m}(\Psi - \Psi_\infty)]\}^2 (\frac{1}{m}\Psi_z - 1)]. \tag{6.52}$$

Using $m >> 1$ and $\exp[(\Psi - \Psi_\infty)/m] = O(1)$, the above equation becomes at leading order,

$$\phi_\infty \Psi_t + (1 - \phi_\infty)^2 e^\Psi \Psi_z = 0, \tag{6.53}$$

The initial data for (6.53) is

$$\Psi = \Psi_b(\tau) \quad \text{when} \quad z = 0, t = \tau, \tag{6.54}$$

where, if $h = \Pi + \frac{1}{m}\ln m$ at $t = t_0 \, (\approx t^*)$, then

$$\Psi_b(t_0) = 0, \tag{6.55}$$

and we choose $\Psi_b(\tau)$ in order that $\Psi_z = m$ at $z = 0$. The solution is easily found to be

$$\Psi = \ln[\frac{1+mz}{1+m\frac{(1-\phi_\infty)^2}{\phi_\infty}(t-t_0)}]. \tag{6.56}$$

This satisfies the boundary condition on $z = 0$, moreover, we see that $(\partial^2/\partial z^2)e^\Psi = 0$, so that the diffusion term in (6.52) is identically zero. Therefore (6.56) should give a uniform solution to $O(1/m)$ for $\Psi$ in $z < h - \Pi$. By matching, we still have

$$\Psi_\infty = \ln[\frac{\phi_\infty(h-\Pi)}{(1-\phi_\infty)^2(t-t_0)}] + o(1). \tag{6.57}$$

All these solutions are essentially the same as those we obtained in Chapter 4. It is worth pointing out that the solutions obtained so far are only valid for $t < t_c$ and there is no reaction involved. If the reaction comes into action, then the boundary condition (6.54) is no longer valid because the base $z = 0$ is not reachable. The boundary condition will be modified accordingly in the following subsection.

**Intermediate region** ($t > t_c$, $h - \Theta_c < z < h - \Pi$)

If diagenesis is taken into account, the improved approximation to the solution (6.40) of the $\phi$ equation should be modified to include the diagenesis term. It becomes

$$(\frac{\phi}{\phi^*})^m(1-\phi)^2(\frac{1}{\phi}\frac{\partial\phi}{\partial z} - 1) \approx \dot{h}(\phi_0 - \phi) - (1-\phi_0)[1 - \dot{h} - a_1(\delta-1)\phi_{m0}\,\dot{h}]. \tag{6.58}$$

Now the term $\exp[\beta(h - z - \Theta_c)]$ is still small in the region $z \geq h(t) - \Theta_c$, we still can expect there exists a similar transition region ($z \sim h(t) - \Pi$), and we will have the same equation as (6.53) below the transition region, but now the boundary condition is different because the base is not reachable. The boundary conditions are

$$\Psi \to \Psi_\infty \quad \text{as} \quad z \to h - \Pi, \tag{6.59}$$

$$\Psi \to \Psi_c \quad \text{as} \quad z \to h - \Theta_c, \tag{6.60}$$

where $\phi_c = \phi^* \exp[\frac{1}{m}(-\ln m + \Psi_c)]$ and $\phi_\infty = \phi^* \exp[\frac{1}{m}(-\ln m + \Psi_\infty)]$ are to be determined later. The characteristics of equation (6.53) are

$$\dot{\Psi} = 0, \quad \dot{z} = \frac{(1-\phi_\infty)^2}{\phi_\infty}e^\Psi, \tag{6.61}$$

whence

$$\Psi = \Psi_c, \quad z = \frac{(1-\phi_\infty)^2}{\phi_\infty} e^{\Psi}(t-\tau) + h(\tau) - \Theta_c, \tag{6.62}$$

which becomes, by using the boundary condition (6.59),

$$h - \Pi = \frac{(1-\phi_\infty)^2}{\phi_\infty} e^{\Psi_c}(t-\tau) + h(\tau) - \Theta_c. \tag{6.63}$$

Eliminating $\tau$, we have

$$\Psi = \Psi_c[t - \frac{(h-\Pi-z)\phi_\infty}{(1-\phi_\infty)^2(e^{\Psi_\infty} - e^{\Psi_c})}]. \tag{6.64}$$

This solution will determine $\phi_\infty$ as $z \to h - \Pi$ when $\phi_c$ (or $\Psi_c$) is known.

In order to determine $\dot{h}$, we rewrite equation (6.58) in terms of $\xi$ and $t$, and match it to equation (6.48); we thus find that

$$\dot{h} \approx \frac{1-\phi_0}{1-\phi_c} + a_1(\delta-1)\phi_{m0}(\frac{1-\phi_0}{1-\phi_c})^2 - \frac{(1-\phi_c)^2}{m} e^{\Psi_c} + ... \tag{6.65}$$

Clearly, if there is no diagenesis $\mathcal{R} = 0$ ($\Theta_c \to \infty$) or diagenesis without water release ($a_1 = 0$), the above expression will degenerate into (6.51).

### Reaction region ($t > t_c$)

In the region $z \sim h(t) - \Theta_c$, the term $\exp[\beta(h - z - \Theta_c)]$ will not be small, we can expect that there will exist another transition in this reaction region. We define

$$z = h - \Theta_c - \frac{\ln\beta}{\beta} + \frac{\zeta}{\beta},$$

$$\phi = \phi^* \exp[\frac{1}{m}(-\ln m + \Psi)]. \tag{6.66}$$

By changing variables in this way, we have $\exp[\beta(h - z - \Theta_c)] \sim \beta$ and we thus balance the terms in the governing equations (6.31) and (6.32). By using the chain rules $\partial_z = \beta\partial_\zeta$, $\partial_t = \partial_t - \beta\dot{h}\partial_\zeta$, $\Psi$ and $\phi_m$ satisfy the equations

$$\frac{1}{\beta}\Psi_t - \dot{h}\Psi_\zeta = \frac{(1-\phi_\infty^c)^2}{\phi_\infty^c}\frac{\partial}{\partial\zeta}[e^{\Psi}(\frac{\beta}{m}\Psi_\zeta - 1)] + \frac{ma_1}{\phi_\infty^c}[\delta - (\delta-1)(1-\phi_\infty^c)]e^{-\zeta}\phi_m, \tag{6.67}$$

$$\frac{1}{\beta}\frac{\partial\phi_m}{\partial t} - \dot{h}\frac{\partial\phi_m}{\partial\zeta} = \frac{(1-\phi_\infty^c)}{m}\frac{\partial(\phi_m e^{\Psi})}{\partial\zeta} - \phi_m e^{-\zeta} - (\delta-1)a_1\frac{\partial}{\partial\zeta}[\phi_m\int_{-\infty}^{\zeta}\phi_m e^{-\zeta}d\zeta], \tag{6.68}$$

where

$$\phi_\infty^c = \phi^* \exp[\frac{1}{m}(-\ln m + \Psi_\infty^c)], \tag{6.69}$$

and $\Psi^c_\infty$ will be determined later.

If we use the conditions $m \sim \beta >> 1$ and $ma_1 \sim 1$, then the above equations can be written approximately as

$$-\dot{h}\Psi_\zeta - \frac{(1-\phi^c_\infty)^2}{\phi^c_\infty}\frac{\partial}{\partial\zeta}[e^\Psi(\frac{\beta}{m}\Psi_\zeta - 1)] = \frac{ma_1}{\phi^c_\infty}[\delta - (\delta-1)(1-\phi^c_\infty)]e^{-\zeta}\phi_m, \quad (6.70)$$

$$-\dot{h}\frac{\partial\phi_m}{\partial\zeta} = -\phi_m e^{-\zeta} - (\delta-1)a_1\frac{\partial}{\partial\zeta}[\phi_m\int_{-\infty}^{\zeta}\phi_m e^{-\zeta}d\zeta], \quad (6.71)$$

where we see that the approximation of $\beta \sim m$ and $\beta \sim O(\frac{1}{m})$ are appropriate.

The far field matching conditions are

$$\phi_m \to \phi_{m0}(\frac{1-\phi^c_\infty}{1-\phi_0}), \quad \Psi \sim \Psi_c \ \text{ as } \ \zeta \to \infty, \quad (6.72)$$

$$\Psi \to \Psi^c_\infty \ \text{ as } \ \zeta \to -\infty, \quad (6.73)$$

where the factor $(1-\phi^c_\infty)/(1-\phi_0)$ is due to the effect of porosity change from $\phi_0$ to $\phi^c_\infty$. Since $a_1 << 1, \int_{-\infty}^{\zeta}\phi_m e^{-\zeta}dz = O(1)$, then the $\phi_m$ equation becomes

$$\dot{h}\frac{\partial\phi_m}{\partial\zeta} = \phi_m e^{-\zeta}. \quad (6.74)$$

Integrating this equation and using the matching condition, we have

$$\phi_m = \phi_{m0}(\frac{1-\phi^c_\infty}{1-\phi_0})\exp[-\frac{1}{\dot{h}}e^{-\zeta}]. \quad (6.75)$$

Substituting this solution into the $\Psi$ equation and integrating from $-\infty$ to $\zeta$, we have

$$[\dot{h}\Psi + \frac{(1-\phi^c_\infty)^2}{\phi^c_\infty}e^\Psi(\frac{\beta}{m}\Psi_\zeta - 1)] - B = -\frac{\dot{h}ma_1}{\phi^c_\infty}[\delta-(\delta-1)(1-\phi^c_\infty)]\phi_{m0}(\frac{1-\phi^c_\infty}{1-\phi_0})\exp[-\frac{1}{\dot{h}}e^{-\zeta}], \quad (6.76)$$

where

$$B = [\dot{h}\Psi^c_\infty - \frac{(1-\phi^c_\infty)^2}{\phi^c_\infty}e^{\Psi^c_\infty}] \quad (6.77)$$

The solution for $\Psi$ can be written in a quadrature. Clearly, when $\zeta \to \pm\infty$, we obtain the jump condition in the diagenetic region

$$[-\dot{h}\Psi + \frac{(1-\phi^c_\infty)^2}{\phi^c_\infty}e^\Psi]^\infty_{-\infty}$$

$$= \frac{\dot{h}ma_1}{\phi^c_\infty}[\delta - (\delta-1)(1-\phi^c_\infty)]\phi_{m0}(\frac{1-\phi^c_\infty}{1-\phi_0}), \quad (6.78)$$

which determines $\Psi_c$ in term of $\Psi^c_\infty$. This gives a shift in the porosity $\phi$ outside the reaction region. If we define the thickness of the reaction region as the distance that $\phi_m$ change from 90% to 10% of the initial value, then the dimensionless thickness of the reaction is about $\frac{\ln(\beta/0.1)}{\beta}$, which is clearly seen in the numerical results. In figure 6.3, we have $\ln[10\beta]/\beta \approx 1.5,\ 0.8,\ 0.5$ for $\beta = 2,\ 5,\ 8$.

### Solution below the reaction region

To obtain the solution for $\Psi^c_\infty$ as $\zeta \to -\infty$, we write the equation for $\Psi$ in terms of $z$. By using the solution (6.75), we see that the source term due to diagenesis is virtually negligible in the region $z = 0$ to $h - \Theta_c$. Then the equation for $\Psi$ becomes (at leading order)

$$\phi^c_\infty \Psi_t + (1 - \phi^c_\infty)^2 e^\Psi \Psi_z = 0. \tag{6.79}$$

Following the same procedure as before with the boundary condition $\Psi_z = m$ at the base $z = 0$, then we still obtain (6.56), and finally we have

$$\Psi^c_\infty = \ln[\frac{\phi^c_\infty (h - \Theta_c)}{(1 - \phi^c_\infty)^2 (t - t_c)}] + o(1), \tag{6.80}$$

which completes the solution procedure.

### Summary and Comparison

The solution of equation (6.32) with boundary conditions (6.33) and (6.34) consists of a near equilibrium solution (6.39) in the upper region, a transition given by (6.49), an intermediate region (6.64), a reaction region (6.78) and the solution below the reaction region (6.80).

Solution (6.80) gives $\Psi^c_\infty$ (and $\phi^c_\infty$ through (6.66)), (6.78) determines $\Psi_c$ (and $\phi_c$) in terms of $\Psi^c_\infty$, (6.64) gives $\Psi_\infty$ as $z \to h - \Pi$, and (6.65) provides an equation which determines the evolution of $h(t)$.

The comparison of the solutions (dashed) with the numerical results (solid) is shown in Fig. 6.5, Fig. 6.6 and Fig. 6.7. It is clearly seen in figure 6.6 that the agreement gets better as $\beta$ becomes larger.

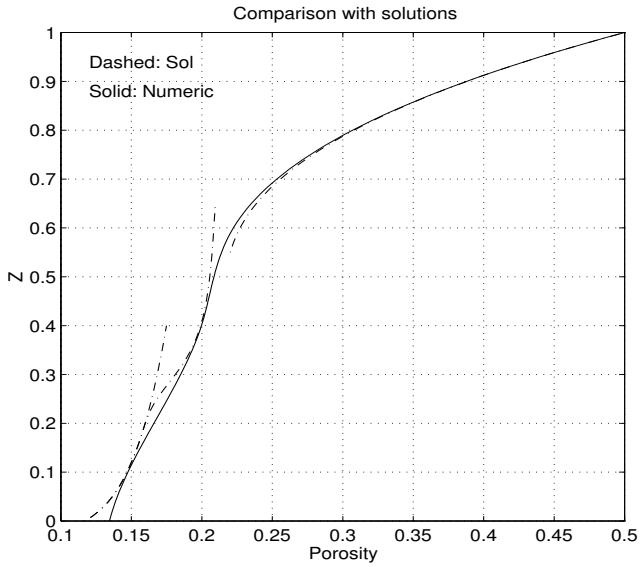


Figure 6.5 Comparison of solutions with numerical results. The values of $\lambda = 100$, $a_1 = 0.1$, $t = 5, \beta = 2.3, \Theta_c = 3$ are used. The dashed curves are calculated from solutions (6.40) (top), (6.76)(middle) and (6.80)(lower).

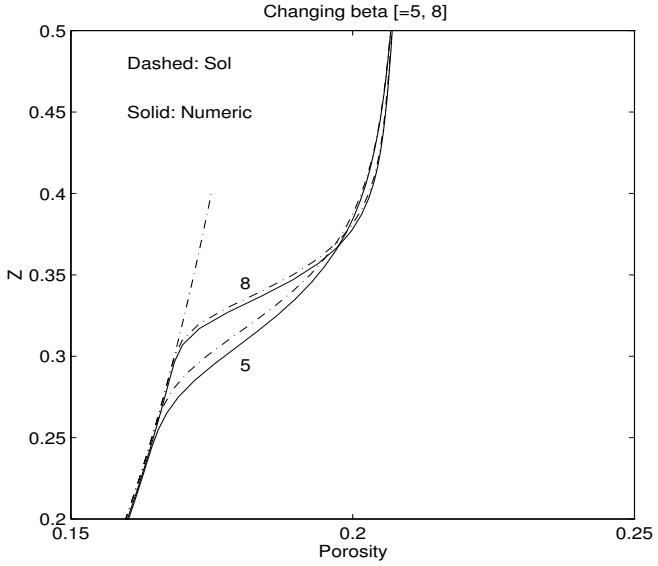


Figure 6.6 Comparison of solutions with numerical results. Parameters as for figure 6.5, but for different values of $\beta = 5$, 8. The dashed curves are calculated from solutions (6.76)(middle) and (6.80)(lower).

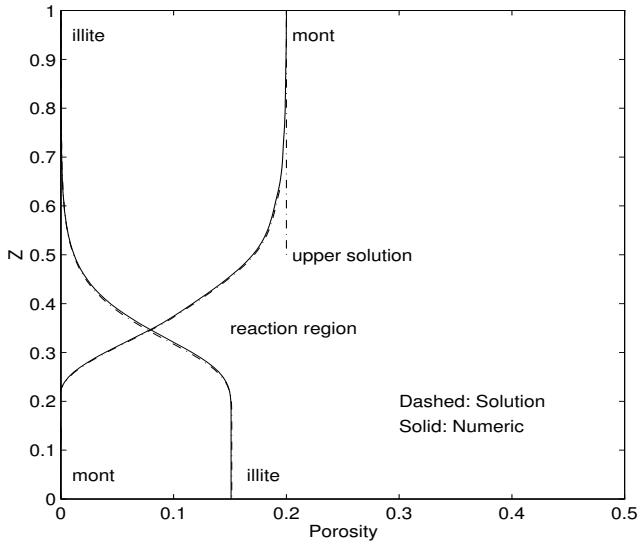


Figure 6.7 Comparison of solutions with numerical results ($\lambda = 100$, $t = 5$). The solid fractions (6.29) (smectite or montmorillonite) and (6.30)(illite) are used in this figure. The dashed curves are calculated from solutions (6.45) (top) and (6.75)(lower).

## 6.4 Application

The data analysis given by Abercrombie, Hutcheon, Bloch & Caritat (1994) from oceanic and sedimentary basins shows that burial history has significant influence on the Smectite-illite (S-I) diagenetic reaction. In a slow burial environment, the S-I reaction may begin at temperatures as low as $\sim 50^0$C, and reaches completion by $\sim 90^0$C; while in a rapid burial environment, the S-I reaction may not begin until temperatures as high as $\sim 120^0$C, and may not reach completion until $\sim 150^0$C. From these results, we understand that

- Diagenesis takes place at lower temperatures or shallower regions in the fast compaction process ($\lambda >> 1$) than in a slow compaction process ($\lambda << 1$).
- The diagenetic process is essentially constrained to a narrow region (*a diagenetic window* ) with a temperature range $\sim 30^0$C or equivalently over a depth range of $\sim$ 1km.

By using the present model and the solutions obtained so far, we can explain these phenomena. From the definitions of the parameters, we find that the depth to the centre of the reaction window; $d_c$, is

$$d_c = \frac{K_0 R T_0^2}{E_a q_0} \ln \frac{\dot{m}_s}{k_r^0 d}. \tag{6.81}$$

This clearly means that the higher the sedimentation rate, the higher the critical temperature of diagenesis, the deeper the diagenetic region, and vice versa. A change of 2 orders in sedimentation rate will cause a shift of $d_c$ by 2 (equivalently $\sim 60^0$ C) (with other parameters unchanged). In addition, the thickness of the diagenesis region $d_{\rm SI}$ is the order of $\frac{\ln(\beta/0.1)}{\beta} d$. A typical value of $\beta \approx 2.3$ gives $d_{\rm SI} \approx 1.36$km (with $d = 1$ km), or equivalently a temperature range of $\sim 40^0$C.

# Chapter 7

# Diagenesis: Dissolution and Precipitation Model

The smectite-to-illite transformation is the most important process during shale diagenesis. The mathematical model presented in the last chapter is a first-order diagenetic reaction (dehydration) model in which the geochemical compositions of pore fluid are not taken into account. The main factor included in the model is temperature. In reality, diagenesis is far more complicated and takes place via the dissolution of smectite in pore water and the subsequent precipitation of illite involving the interactions of many mineral species. This chapter's purpose is thus dedicated to extend the first-order dehydration model in Chapter 6 to a more realistic reaction-transport mathematical model with a more detailed analysis in some practical cases.

## 7.1 Introduction

Diagenesis is observed world-wide in sedimentary basins. The close spatial and temporal correlations between smectite disappearance and illite formation imply the existance of the smectite-illite reaction. Such a smectite-illite (S-I) reaction is one of the fundamental mechanisms in clastic diagenesis. The reaction has received much attention but the nature of both the illite/smectite (I/S) mixed-layer and the reaction mechanism are still under discussion, and many experiments have been carried out

to investigate the kinetic features of the S-I conversion (Eberl & Hower 1976; Bethke & Altaner, 1986; Huang, Longo & Pevear, 1993; Abercromie, Hutcheon, Bloch & Caritat, 1994).

Many authors write the overall S-I transformation with K-feldspar as the following reaction

$$\text{smectite} + \text{K-feldspar} \rightarrow \text{illite} + \text{quartz (aq)} + \text{interlayer water}. \tag{7.1}$$

One detailed example of this symbolic reaction is

$$KAlSi_3O_8(\text{K-feldspar}) + 2K_{0.3}Al_{1.9}(Si_4)O_{10}(OH)_2 \cdot 4.5H_2O\,(\text{K-smectite})$$

$$\rightleftharpoons 2K_{0.8}Al_{1.9}(Al_{0.5}Si_{3.5})O_{10}(OH)_2\,(\text{illite}) + 9H_2O\,(\text{interlayer water}) + 4SiO_2(aq), \tag{7.2}$$

as given by Abercromie, Hutcheon, Bloch & Caritat (1994).

Recently, Huang, Longo & Pevear (1993) systematically analysed experimental and field data and derived the conversion rate

$$-\frac{dS}{dt} = k(T)[K^+]S^2 \quad \text{or} \quad \frac{dI}{dt} = k(T)[K^+](1-I)^2, \tag{7.3}$$

where $S, I$ are relative fractions of smectite and illite in the I/S mixed-layer ($I+S=1$), $[K^+]$ is $K^+$ concentration in the fluid, $k(T)$ is the reaction constant depending on temperature $T$.

We see that the experimentally derived reaction rate (7.3) is second-order with respect to smectite and first-order with respect to $K^+$ concentration. This empirical relation can be easily obtained via the law of mass action for the reaction (7.2).

Potassium cation concentration has an important effect on the reaction rate. $K^+$ is mainly supplied by the dissolution of K-feldspar. The characterization of K-feldspar dissolution rate is essential for the accurate description of the overall S-I process. Experimental investigations of feldspar dissolution rates have been performed (Busenberg & Clemency, 1976; Helgeson, Murphy & AaGaard, 1984; Chou & Wollast, 1985; Hellmann, 1994; Gautier, Oelkers & Schott, 1994). Although the dissolution process of K-feldspar in natural environment is nearly at equilibrium with a temperature

range of $0 \sim 150$°C,

$$KAlSi_3O_8 + 2H_2O \rightleftharpoons K^+ + 3SiO_2(aq) + Al(OH)_4^-, \tag{7.4}$$

most of the experiments have been carried out at far from equilibrium conditions with a temperature range of $200 \sim 400$°C.

Helgeson (1968) and his coworkers (Helgeson, Garrels & MacKenzie, 1969) developed the first model to consider water-rock interaction as a system of coupled dissolution and precipitation. In their model, dissolution reactions of primary minerals (smectite, K-feldspar) are treated as irreversible processes, while partial equilibrium with respect to the secondary phases (illite, quartz) is assumed. As pointed out by Helgeson (1979) and Steefel & Cappellen (1990), the assumption of partial equilibrium is only justified where the rate of precipitation of a secondary phase is faster then the rate of dissolution. However, the precipitation of the stable insoluble minerals may be slow even on geological time scales. Therefore, the partial equilibrium may be a good approximation to natural water-rock systems.

## 7.2 Mechanisms of S-I Reaction

Extensive studies on clay diagenesis with increasing depth of burial reveals that the most systematic evolution consists of the progressive illitization of smectite minerals (Chamley, 1989).

- Firstly, such modifications usually occur at depths exceeding 2 km. In the series marked by normal geothermal gradients of about $30^o$C/km, the process develops between 2.5 and 3.5 km, and does not progress beyond a depth of 5 or 6 km. This suggests that highly expandable smectite-rich minerals change to slightly expandable illite-rich ones over a relatively narrow temperature interval (the *diagenetic window*);

- Secondly, contrary to what is often believed, diagenetic processes do not noticeably depend on the absolute age of burial series. More important than geological

age are certainly the geothermal gradient and the residence time at a diagenetically active temperature;

- Thirdly, the illitization process does significantly involve $K^+$ which is supplied by dissolved K-feldspar.

- In addition, extensive investigations also suggest that some cations like $K^+$, $Al^+$, needed for the evolution of smectite to illite, are provided through *short-distance transportation* not by *long-distance transport* processes. The dominance of such very short exchanges in shaly sediments is confirmed by high-resolution transmission electron microscopic observations (Ahn & Peacor, 1986). This means that diagenetic sediments are not significantly affected by pore-water migration, at least not since their initial compaction.

- Finally, the argillaceous deposits (in the Gulf Coast) behave essentially as a nearly closed system, pore fluid being present in small amounts compared to the solid materials, and acting possibly as a catalyst for short-distance ion transport and for local clay reconstruction at the reaction interfaces (Ahn & Peacor, 1986; Chamley, 1989), which means that the system is nearly at equilibrium.

Several mechanisms have been put forward to explain the S-I reaction process. Two main ones are *transformation* and *dissolution-precipitation*. The former mechanism suggests that the S-I reaction is a transformation process through smectite/illite mixed-phase with (a series of) reordering processes of the intermediate mixed-layer (Hower et al, 1976). An alternative modification is a solid-state transformation mechanism without mixed-layering. The latter mechanism involves the processes of smectite dissolution and illite precipitation without mixed-layering. According to high-resolution electron microscopic data, the mixed-layering mechanism appears to be questionable (Chamley 1989), but Ahn & Peacor (1986) provide a seemingly convincing example of a smectite-to-illite transformation rather than a neoformation. The first-order dehydration model in the previous chapter is essential a transformation model. The fact that diagenesis, which is still imperfectly understood, largely depends on lithology, fluid pressure, geothermal gradient and pore fluid compositions is

the main motivation for us to develop a more realistic reaction-transport dissolution-precipitation model in the present work.

## 7.3 Model Equations

The S-I transformation is composed of the following intermediate dissolution-precipitation reactions which can be written symbolically as

*Smectite dissolution*

$$M^S(\text{smectite}) \xrightarrow{r_1} [X^L] + n[H_2O], \tag{7.5}$$

*Illite precipitation*

$$[K^{+L}] + [AlO_2^{-L}-] + f[X^L] \xrightarrow{r_2} fI^S(\text{illite}) + [SiO_2^L], \tag{7.6}$$

*K-feldspar dissolution*

$$[\text{K-feldspar}] \xrightarrow{r_3} [K^{+L}] + [AlO_2^{-L}-] + s[SiO_2^L], \tag{7.7}$$

*Quartz dissolution and precipitation*

$$[SiO_2^L] \underset{r_{-4}}{\overset{r_4}{\rightleftharpoons}} [\text{quartz}], \tag{7.8}$$

where $n, s, f$ are stoichiometric coefficients and S, L denote solid and liquid phase. $[X]$ is an aqueous silica combination in the form such as $[-(Si_4)O_{10}(OH)_2]$. $[AlO_2^{-L}-]$ is only a general notation of the combination such as $[Al(OH)_4^-]$.

Let the molar rates of the above reactions be $r_1, r_2, r_3, r_4$ (for forward reaction) and $r_{-4}$ (for backward reaction), respectively. Then, the reaction-transport (by diffusion and advection) model can be written as

$$\frac{\partial [M]}{\partial t} + \nabla \cdot [\mathbf{u}^s [M]] = -r_1, \tag{7.9}$$

$$\frac{\partial (\phi [X])}{\partial t} + \nabla \cdot [\mathbf{u}^l \phi [X]] - \nabla \cdot [\phi D \nabla ([X])] = r_1 - f r_2, \tag{7.10}$$

$$\frac{\partial [I]}{\partial t} + \nabla \cdot [\mathbf{u}^s [I]] = f r_2, \tag{7.11}$$

$$\frac{\partial(\phi[K^+])}{\partial t} + \nabla \cdot [\mathbf{u}^l \phi[K^+]] - \nabla \cdot [\phi D \nabla([K^+])] = -r_2 + r_3, \tag{7.12}$$

$$\frac{\partial(\phi[Al^+])}{\partial t} + \nabla \cdot [\mathbf{u}^l \phi[Al^+]] - \nabla \cdot [\phi D \nabla([Al^+])] = -r_2 + r_3, \tag{7.13}$$

$$\frac{\partial(\phi[SiO_2])}{\partial t} + \nabla \cdot [\mathbf{u}^l \phi[SiO_2]] - \nabla \cdot [\phi D \nabla([SiO_2])] = sr_3 - r_4 + r_{-4} + r_2, \tag{7.14}$$

$$\frac{\partial[H_2O]}{\partial t} + \nabla \cdot [\mathbf{u}^l[H_2O]] = nr_1, \tag{7.15}$$

$$\frac{\partial[quartz]}{\partial t} + \nabla \cdot [\mathbf{u}^s[quartz]] = r_4 - r_{-4}, \tag{7.16}$$

$$\frac{\partial[feldspar])}{\partial t} + \nabla \cdot [\mathbf{u}^s[feldspar]] = -r_3, \tag{7.17}$$

where $[M], [I], [quartz]$ are molar concentrations, measured in units of mol $\mathrm{m}^{-3}$ of rock. $[SiO_2], [K]$... are molar concentrations in units of mol $\mathrm{m}^{-3}$ of pore water. $\phi$ is porosity.

The reaction rates $r_i, i = 1, 2, 3, 4, -4$ are generally complicated nonlinear functions of concentrations, satisfying $r_i = 0$ at equilibrium (Dewynne, Fowler & Hagan 1993). Their precise form should be determined by experiments.

### 7.3.1 Surface controlled or transport controlled

The kinetics of mineral dissolution and precipitation are strongly controlled by reaction rates which depend in a complicated way on the solution compositions and surface chemistry. A complete formulation of a quantitative dissolution/precipitation rate law is more complicated for multicomponent systems. It is usually helpful to identify one of the processes, transport or surface attachment, as the *rate-limiting step* (Berner 1978, Lasaga 1981, 1984). If the transport process is much slower than the reaction rate at the surface of the mineral, then the dissolution and precipitation are referred to as *transport-controlled*, while the opposite case is termed *surface-controlled*.

In the case of a transport-controlled process, the surface detachment and attachment are so rapid that a saturated solution adjacent to the surface is maintained. Dissolution and precipitation are then regulated by transport via diffusion and advection into the surrounding medium. The reaction rate thus depends on the flow

velocity and the degree of stirring (Nielsen, 1964). If transport is by pure diffusion without advection, then the case is termed *diffusion-controlled* (Berner 1978). In surface-controlled dissolution/precipitation, the surface process is sufficiently slow that it can not keep pace with diffusion and advection. The concentration level adjacent to the surface is essentially the same as that in the bulk solution. Flow velocity and stirring have a negligible effect on dissolution/precipitation rates. Generally speaking, surface-controlled dissolution/precipitation reaction is slower than that by transport-controlled process. The two limiting cases are determined by the final value of the surface solution compositions.

Berner (1978) found that most mineral dissolution/precipitation reactions are very close to the case of a surface-controlled process. We will see below that the rate laws derived from most experimental data are essentially surface-controlled. Therefore, the transport effect is included in the model equations but not in the reaction rates.

### 7.3.2 Nucleation and crystal growth

The precipitation process can be described in more detail as *nucleation* and *crystal growth*. If the concentration is gradually increased, exceeding the solubility with respect to a secondary solid phase, the new phase will not form until a certain degree of supersaturation has been achieved. Stable nuclei can only be formed after an activation energy barrier has been surmounted. Nucleation normally proceeds via *homogeneous* or *heterogeneous* nucleation. In most cases, however, heterogeneous nucleation is the predominant formation process in natural waters since it has a lower activation energy barrier than that in the case of homogeneous nucleation. Just as a catalyst reduces the activation energy of chemical reaction, foreign solids may catalyze the nucleation process by reducing the energy barrier. Phase changes in natural aqueous systems are almost always initiated by heterogeneous solid substrates, as pointed out by Stumm (1992).

The free energy of heterogeneous nucleation $\Delta G_i$ can be generally written as

$$\Delta G_i = RT\ln\frac{Q}{K_{eq}} + \Delta G_{\text{surf}}(\bar{\gamma}), \tag{7.18}$$

where $K_{eq}$ is the equilibrium constant for the reaction, and $Q$ is the reaction quotient for the same reaction. $Q/K_{eq}$ represents the solution saturation state (Steefel & Cappellen, 1990; Stumm 1992). $\bar{\gamma}$ is the interfacial free energy. For homogeneous nucleation, $\Delta G_{\text{surf}} = \bar{\gamma}_{\text{CW}} A$. In the case of heterogeneous nucleation, this term should be modified because the nucleus is now formed in part contact with the solution and in part with the surface of the solid substrate (Cappellen, 1991; Stumm, 1992). More generally, we have

$$\Delta G_{\text{surf}} = \bar{\gamma}_{\text{CW}} A_{\text{CW}} + (\bar{\gamma}_{\text{CS}} - \bar{\gamma}_{\text{SW}}) A_{\text{CS}}, \tag{7.19}$$

where the suffixes CW, CS, SW refer to cluster-water, cluster-substrate and substrate-water, respectively. If $\bar{\gamma}_{\text{SW}} >> \bar{\gamma}_{\text{CW}}$, the precipitate tends to form a structurally continuous coating on the substrate grain. In this case, the interfacial energy may even possibly become negative and the activation barrier vanishes. These considerations show that the interfacial energy is of importance in determining the thermodynamics and kinetics of the nucleation process.

### 7.3.3 Rate laws for dissolution and precipitation

Most dissolution/precipitation experiments are carried out under far from equilibrium conditions. However, such laboratory data are not directly applicable to field observations. Unfortunately, the discrepancies between field estimates and laboratory measurements of reaction rates are as large as up to four orders of magnitude. One possibility of explaining this difference lies in the fact that not all of the potentially available surface in natural systems actually participates in reactions with pore fluids. A common implicit assumption in modelling interface-controlled kinetics is that the rate is linearly dependent on surface area of which is poorly estimated in spite of its vital importance for a better understanding of the reaction mechanism. Coating of mineral surfaces by secondary mineral precipitation and associated occlusion of natural surfaces may account for the apparent lesser reactivity of natural mineral surfaces relative to their laboratory conterparts. However, the extensive etching widely observed on some silicate-mineral surfaces indicates all portions of the primary mineral surface are accessible to pore fluids in spite of secondary precipitation, militating

against an extensive surface-covering role for coating (Velbel, 1993). Lasaga (1981, 1984) and Aagaard & Helgeson (1983) try to bridge the gap and extend the laboratory kinetic data into a general rate law that is applicable to natural situations.

In the case of interest to us, smectite dissolution will normally proceed with respect to the nearly amorphous silica solubility $2 \times 10^{-3}$ (M) or 120 ppm at 25$^o$C. Quartz precipitates with respect to quartz solubility $1 \times 10^{-4}$ (M) or 6 ppm. Illite precipitation goes with respect to a solubility $c_{eq}^{illite}$ between the upper limit of amorphous silica solubility $c_{eq}^{amorph}$ and the lower limit of quartz $c_{eq}^{quartz}$ according to the thermodynamic and kinetic constraints and the activity calculations by Aagaard & Helgeson (1982, 1983).

According to the earlier works by Rimstidt & Barnes 1980, Lasaga 1981, 1984, Ortoleva, Merino & Sen, 1987 and Huang, Longo & Pevear, 1993, we can generally write the reaction rates as

$$r_i = k_i A_i f_i(a_j) g(\Delta G_i), \quad i = 1, 2, 3, 4, -4, \tag{7.20}$$

where $k_i, i = 1, 2, 3, 4, -4$ are rate constants which are functions of temperature $T$. $A_i, ...$ is the specific reactive surface area ($m^2/m^3$) of the mineral (smectite, illite, K-feldspar and quartz), $f_i(a_j)$ is a function of the activities $a_j$ of the $j$th primary species in solution, which is usually assumed to be of the form

$$f_i(a_j) = \prod_j a_j^{n_{ij}}, \tag{7.21}$$

where $n_j$ is the stoichiometric coefficient. $g(\Delta G_i)$ accounts for the important variation of the rate with the deviation from equilibrium ($\Delta G_i = 0$). Lasaga et al (1994) write this function as the following form

$$\begin{aligned} g(\Delta G_i) &= (1 - \exp(\Delta G_i / RT))_+ \quad \text{(dissolution)}, \\ g(\Delta G_i) &= (\exp(\Delta G_i / RT) - 1)_+ \quad \text{(precipitation)}, \end{aligned} \tag{7.22}$$

where $(\phi)_+ = max\{0, \phi\}$, $\Delta G_i$ is the Gibbs Free Energy of the reaction. $\Delta G_i \leq 0$ is for undersaturation, while $\Delta G_i \geq 0$ for supersaturation. Note that this equation satisfies $g(0) = 0$. At constant temperature and surface area, it follows from this

equation that the dissolution rate will be essentially constant at far from equilibrium condition ($\Delta G_i << 0$). Normally, for a single species dissolution and precipitation, $\Delta G_i = RT \ln(c/c_{eq})$, then we have

$$g(\Delta G_i) = (1 - S)_+ \quad \text{(dissolution)},$$

$$g(\Delta G_i) = (S - 1)_+ \quad \text{(precipitation)}, \tag{7.23}$$

where $S = c/c_{eq}$ is the saturation ratio, and $c_{eq}$ is the concentration at solubility equilibrium. The present ability to predict reaction rates as a function of saturation state is still limited. A further consideration is the possibility of fully nonlinear rate laws. Rate laws with a functional dependence on $\Delta G_i$ of the form

$$g(\Delta G_i) = (1 - \exp(\Delta G_i/RT))^{n_i}, \tag{7.24}$$

have been applied most commonly to precipitation kinetics ($n_i = 2$).

The temperature dependence of $k_i$ follows the Arrhenius law

$$k_i = \nu_i e^{-E_i/RT} \quad (i = 1, 2, 3, 4, -4), \tag{7.25}$$

where $E_i$ is the activation energy, $\nu_i$ is the frequency factor and $R$ is the gas constant. $A_i$ is a function of the volume fraction of the mineral. For uniformly packed spherical particles with an averaged radius $\bar{r}_i$, we have $A_i = 3\phi_i/\bar{r}_i$ or $A_i \propto \phi_i$.

For convenience in the following discussion, we can rewrite the rate laws as

$$r_i = k_i^{eff} \exp(-E_i/RT)\ \hat{r}_i, \tag{7.26}$$

where $k_i^{eff}$ has the unit of $\mathrm{s}^{-1}$. $r_i$ absorbs all the other terms (noting that $A_i \propto \phi_i$) and has the same units as molar concentration. If $r_i$ is written in terms of volume fractions, then we have

$$\hat{r}_i = \frac{\text{density}}{\text{molar weight}} \tilde{r}_i, \tag{7.27}$$

where $\tilde{r}_i$ is dimensionless. The term (density)/(molar weight) can be written as $\rho_m/M_m, i = 1, 2$ and $\rho_{Si}/M_{Si}, i = 3, 4, -4$.

## 7.4 Non-dimensionalization

Let $\phi_m, \phi_i, \phi_f, \phi_q$ be volume fractions of smectite, illite, feldspar and quartz, respectively. $c_X$, $c_{Si}$ and $c_K$ are the solubility limits of $[X]$, $[SiO_2]$ and $[K^+]$,respectively

By using the relations between molar concentrations and volume fractions

$$[M] = \frac{\rho_m \phi_m}{M_m}, \ [I] = \frac{\rho_i \phi_i}{M_i}, \ [quartz] = \frac{\rho_{Si} \phi_q}{M_{Si}}, \ [H_2O] = \frac{\rho_w \phi}{M_w}, \ [feldspar] = \frac{\rho_f \phi_f}{M_f},$$

$$[X] = \frac{\rho_X \phi_X}{M_X}, \ [SiO_2] = \frac{\rho_{Si} \phi_{Si}}{M_{Si}}, \ [K] = \frac{\rho_K \phi_K}{M_K}, \ [Al] = \frac{\rho_{Al} \phi_{Al}}{M_{Al}}, \tag{7.28}$$

we can write the governing equations in terms of volume fractions

$$\frac{\partial \phi_m}{\partial t} + \nabla \cdot (\mathbf{u}^s \phi_m) = -r_1 \frac{M_m}{\rho_m}, \tag{7.29}$$

$$\frac{\partial \phi_X}{\partial t} + \nabla \cdot (\mathbf{u}^l \phi_X) - \nabla \cdot [D(\phi) \nabla \phi_X] = (r_1 - f r_2) \frac{M_X}{\rho_X}, \tag{7.30}$$

$$\frac{\partial \phi_i}{\partial t} + \nabla \cdot (\mathbf{u}^s \phi_i) = f r_2 \frac{M_i}{\rho_i}, \tag{7.31}$$

$$\frac{\partial \phi_K}{\partial t} + \nabla \cdot (\mathbf{u}^l \phi_K) - \nabla \cdot [D(\phi) \nabla \phi_K] = (-r_2 + r_3) \frac{M_K}{\rho_K}, \tag{7.32}$$

$$\frac{\partial \phi_{Al}}{\partial t} + \nabla \cdot (\mathbf{u}^l \phi_{Al}) - \nabla \cdot [D(\phi) \nabla \phi_{Al}] = (-r_2 + r_3) \frac{M_{Al}}{\rho_{Al}}, \tag{7.33}$$

$$\frac{\partial \phi_{Si}}{\partial t} + \nabla \cdot (\mathbf{u}^l \phi_{Si}) - \nabla \cdot [D(\phi) \nabla \phi_{Si}] = (s r_3 - r_4 + r_{-4} + r_2) \frac{M_{Si}}{\rho_{Si}}, \tag{7.34}$$

$$\frac{\partial \phi}{\partial t} + \nabla \cdot (\mathbf{u}^l \phi) = (n r_1 - n_1 r_3) \frac{M_w}{\rho_w}, \tag{7.35}$$

$$\frac{\partial \phi_q}{\partial t} + \nabla \cdot (\mathbf{u}^s \phi_q) = (r_4 - r_{-4}) \frac{M_q}{\rho_q}, \tag{7.36}$$

$$\frac{\partial \phi_f}{\partial t} + \nabla \cdot (\mathbf{u}^s \phi_f) = -r_3 \frac{M_f}{\rho_f}, \tag{7.37}$$

where $D(\phi)$ is a known function of $\phi$.

If we scale $u^s, u^l$ with $\dot{m}_s$, $z$ with $d$, $t$ with $d/\dot{m}_s$, $\phi_X$ with $\bar{\phi}_X$, $\phi_{Si}$ with $\bar{\phi}_{Si}$, $\phi_K$ with $\bar{\phi}_K$, $k_i^{eff}$ with $k_i^{(0)eff}$

$$k_i^{eff} = k_i^{(0)eff} \bar{k}_i, \quad i = 1, 2, 3, 4, -4, \tag{7.38}$$

where $\bar{\phi}_X, \bar{\phi}_{Si}, \bar{\phi}_K, \bar{\phi}_{Al}$ are the volume fractions corresponding to the solubility limits of $[X], [SiO_2], [K^+], [Al^+]$. As before, $T$ is rescaled as $\Theta = (T - T_0)K_0/q_0 d$ which is

the dimensionless temperature with reference to the surface temperature $T_0$. Then the governing equations become (without diffusion)

$$\frac{\partial \phi_m}{\partial t} + \nabla \cdot (\mathbf{u}^s \phi_m) = -\mathcal{R}_1 \bar{k}_1 \tilde{r}_1, \tag{7.39}$$

$$\frac{\partial \phi_X}{\partial t} + \nabla \cdot (\mathbf{u}^l \phi_X) = \frac{a_1}{\bar{\phi}_X}[\mathcal{R}_1 \bar{k}_1 \tilde{r}_1 - f\mathcal{R}_2 \bar{k}_2 \tilde{r}_2], \tag{7.40}$$

$$\frac{\partial \phi_i}{\partial t} + \nabla \cdot (\mathbf{u}^s \phi_i) = f\mathcal{R}_2 \bar{k}_2 a_2 \tilde{r}_2, \tag{7.41}$$

$$\frac{\partial \phi_K}{\partial t} + \nabla \cdot (\mathbf{u}^l \phi_K) = \frac{1}{\bar{\phi}_K}[-a_3 \mathcal{R}_2 \bar{k}_2 \tilde{r}_2 + a_4 \mathcal{R}_3 \bar{k}_3 \tilde{r}_3], \tag{7.42}$$

$$\frac{\partial \phi_{Al}}{\partial t} + \nabla \cdot (\mathbf{u}^l \phi_{Al}) = \frac{a_5}{\bar{\phi}_{Al}}[-a_3 \mathcal{R}_2 \bar{k}_2 \tilde{r}_2 + a_4 \mathcal{R}_3 \bar{k}_3 \tilde{r}_3], \tag{7.43}$$

$$\frac{\partial \phi_{Si}}{\partial t} + \nabla \cdot (\mathbf{u}^l \phi_{Si}) = \frac{1}{\bar{\phi}_{Si}}[s\mathcal{R}_3 \bar{k}_3 \tilde{r}_3 - \mathcal{R}_4 \bar{k}_4 \tilde{r}_4 + \mathcal{R}_{-4} \bar{k}_{-4} \tilde{r}_{-4} + \frac{a_3}{a_4} \mathcal{R}_2 \bar{k}_2 \tilde{r}_2], \tag{7.44}$$

$$\frac{\partial \phi}{\partial t} + \nabla \cdot (\mathbf{u}^l \phi) = a_6 \mathcal{R}_1 \bar{k}_1 \tilde{r}_1, \tag{7.45}$$

$$\frac{\partial \phi_q}{\partial t} + \nabla \cdot (\mathbf{u}^s \phi_q) = a_7[\mathcal{R}_4 \bar{k}_4 \tilde{r}_4 - \mathcal{R}_{-4} \bar{k}_{-4} \tilde{r}_{-4}], \tag{7.46}$$

$$\frac{\partial \phi_f}{\partial t} + \nabla \cdot (\mathbf{u}^s \phi_f) = -a_8 \mathcal{R}_3 \bar{k}_3 \tilde{r}_3, \tag{7.47}$$

where

$$\mathcal{R}_i = \frac{k_i^{(0)eff} d}{\dot{m}_s}, \quad i = 1, 2, 3, 4, -4, \tag{7.48}$$

$$\bar{k}_i = e^{\beta_i \Theta} \quad \text{with} \quad \beta_i = \frac{E_i q_0 d}{K_0 R T_0^2}. \tag{7.49}$$

$$a_1 = \frac{\rho_m M_X}{\rho_X M_m}, \ \ a_2 = \frac{\rho_m M_i}{\rho_i M_m}, \ \ a_3 = \frac{\rho_m M_K}{\rho_K M_m}, \ \ a_4 = \frac{\rho_{Si} M_K}{\rho_K M_{Si}},$$
$$a_5 = \frac{\rho_K M_{Al}}{\rho_{Al} M_K}, \ \ a_6 = \frac{n\rho_m M_w}{\rho_w M_m}, \ \ a_7 = \frac{\rho_{Si} M_q}{\rho_q M_{Si}}, \ \ a_8 = \frac{\rho_{Si} M_f}{\rho_f M_{Si}}. \tag{7.50}$$

We see that this present model is essentially controlled by ten dimensionless parameters $\mathcal{R}_i$ and $\beta_i, i = 1, 2, 3, 4, -4$. $a_i = O(1)$. According to Rimstidt & Barnes (1980), Aagaard & Helgeson (1982,1983) and Stumm (1992), $\bar{\phi}_X \sim 12 \times 10^{-5}$(amorphous), $\bar{\phi}_{Si} \sim 6 \times 10^{-6}$(quartz). i.e. $\bar{\phi}_X, \bar{\phi}_K, \bar{\phi}_{Si}, \bar{\phi}_{Al} << 1$. These conditions suggest that the reactions for the aqueous species are very fast, and thus the pseudo-steady state approximation is valid.

## 7.5 Two-step Case and Dehydration Model

In order to investigate the main features of the dissolution-precipitation process and verify the validity of the first-order dehydration model discussed in chapter 2 and chapter 6, we will now simplify the whole model into a two-step case of one-step dissolution and one-step precipitation. With these simplifications, we can analyse in more detail the effect of transport and reaction rate and find out the controlling mechanism of the processes. We will also see that how the dehydration model can be derived from this two-step model.

In the two-step case without potassium/aluminium/silica activities, $\bar{k}_4 = \bar{k}_{-4} = \bar{k}_3 = 0$, $\phi_K = 1$ (at equilibrium), $f = 1$. This corresponds to the following reaction mechanism

*Smectite dissolution*

$$M^S(\text{smectite}) \xrightarrow{r_1} [X^L] + n[H_2O], \tag{7.51}$$

*Illite precipitation*

$$[X^L] \xrightarrow{r_2} I^S(\text{illite}). \tag{7.52}$$

It is clearly seen that $\mathcal{R}_i\bar{k}_i$ always appear as combinations in the model equations. This combination can be easily rewritten as

$$\mathcal{R}_i\bar{k}_i = \exp[\beta_i(\Theta - \Theta_{c,i})] \quad \text{and} \quad \Theta_{c,i} = \frac{1}{\beta_i}\ln\frac{1}{\mathcal{R}_i}, \tag{7.53}$$

and

$$\mathcal{R}_i = \frac{k_i^{(0)eff}d}{\dot{m}_s}, \quad i = 1, 2 \tag{7.54}$$

where the new parameter $\Theta_{c,i}$, which is equivalent to $\mathcal{R}_i$, is a dimensionless critical temperature (with reference to the surface temperature $\Theta_0$).

The above model equations can be rewritten as the following one-dimensional model (without transport)

$$\frac{\partial\phi_m}{\partial t} = -\mathcal{R}_1\bar{k}_1\tilde{r}_1, \tag{7.55}$$

$$\frac{\partial\phi_X}{\partial t} = \frac{(1-a_0)}{\epsilon}[\mathcal{R}_1\bar{k}_1\tilde{r}_1 - \mathcal{R}_2\bar{k}_2\tilde{r}_2], \tag{7.56}$$

$$\frac{\partial\phi_i}{\partial t} = \mathcal{R}_2(1-a_0)\bar{k}_2\tilde{r}_2, \tag{7.57}$$

$$\frac{\partial \phi}{\partial t} = a_0 \delta \mathcal{R}_1 \bar{k}_1 \tilde{r}_1, \tag{7.58}$$

with

$$a_0 = \frac{n M_w}{M_i} \text{ and } \delta = \frac{\rho_s}{\rho_l}. \tag{7.59}$$

where we have used the approximation $M_X = M_i$, $M_m = M_i + nM_w$, $\rho_m = \rho_i = \rho_X = \rho_s$, $\rho_w = \rho_l$, and $\epsilon = \bar{\phi}_X << 1$. We notice that the first two equations (7.55) and (7.56) are decoupled from the other two equations (7.57) and (7.58). The total mass conservation implies that $\phi_m + \phi_i + \phi/\delta + \epsilon\phi_X = 1$.

For typical parameters $k_1^{(0)eff} \sim 1 \times 10^{-16}\,\mathrm{s}^{-1}$ (Swoboda-Colberg & Brever, 1993), $k_2^{(0)eff} \sim 0.2 \times 10^{-16}\,\mathrm{s}^{-1}$ (Small, 1993), $d \sim 1000\,\mathrm{m}$, $\dot{m}_s \sim 0.5 \times 10^{-11}\,\mathrm{m\,s}^{-1}$, $\mathcal{R}_1 \approx 0.02$, $\mathcal{R}_2 \approx 0.004$. Here we have used Swoboda-Colberg & Brever's results (1993) that dissolution/precipitation rates measured in the field appear to be a factor of $\sim 200-400$ slower than that of the same minerals measured in the laboratory. $E_1 \sim 60-80\,\mathrm{k\,J\,mol}^{-1}$ (dissolution) (Eberl & Hower, 1976; Lasaga 1984), $E_2 \sim 90-110\,\mathrm{kJ\,mol}^{-1}$ (precipitation) (Small, 1993) ($E_2 > E_1$) correspond to $\beta_1 \sim 2.3 - 2.8, \beta_2 \approx 2.9 - 3.5$ and $\Theta_{c,1} \approx 2 < \Theta_{c,2} \approx 2.15$.

### 7.5.1 Degeneration to the dehydration model

Now we will show that how the present two-step model can degenerate into a first-order dehydration model and thus verify the validity of first-order model we have discussed in chapter 2 and chapter 6.

Since $\epsilon << 1$, the steady-state approximation for $[X]$ can be used. Thus we have

$$\mathcal{R}_1 \bar{k}_1 \tilde{r}_1 - \mathcal{R}_2 \bar{k}_2 \tilde{r}_2 \approx 0. \tag{7.60}$$

If we assume $\bar{k}_1 = \bar{k}_2 = \bar{k}_r$ ($\mathcal{R}_2 = \mathcal{R}_1 = \mathcal{R}$), and use the following rate functions

$$\tilde{r}_2 = \tilde{r}_1 = \phi_m, \tag{7.61}$$

then we obtain (with transport)

$$\frac{\partial \phi_m}{\partial t} + \frac{\partial (u^s \phi_m)}{\partial z} = -\mathcal{R} \bar{k}_r \phi_m, \tag{7.62}$$

$$\frac{\partial \phi_i}{\partial t} + \frac{\partial (u^s \phi_i)}{\partial z} = \mathcal{R}(1 - a_0) \bar{k}_r \phi_m, \tag{7.63}$$

$$\frac{\partial \phi}{\partial t} + \frac{\partial (u^l \phi)}{\partial z} = a_0 \delta \mathcal{R} \bar{k}_r \phi_m. \tag{7.64}$$

These equations are exactly the equations (equations (6.2)-(6.4) with $a_0 = a_1$) we discussed before in the one-step dehydration diagenetic model. Therefore, the same solution procedures will give the same results as those in Chapter 6. This first-order approach is consistent with the previous attempts (Eberl & Hower, 1976; Bethke & Altaner, 1986), and can represent adequately complex reactions with a rate-limiting reaction step (Lasaga, 1981; Velde & Vasseur, 1992).

### 7.5.2 Effect of transport

From the above subsection, we see that the assumptions ($\bar{k}_1 = \bar{k}_2, \tilde{r}_2 = \tilde{r}_1 = \phi_m$) are very specific. To be more realistic, we use the following rate functions

$$\tilde{r}_1 = \phi_m (\phi_s - \phi_X)_+, \quad \tilde{r}_2 = (\phi_X - \phi_s)_+, \tag{7.65}$$

where $\phi_s = \phi_s(\Theta)$ is the solubility (of $[X]$) which is a known function of temperature or equivalently a function of time $t$ and depth $z$. $\phi_s(z = h(t)) = 1$. $\phi_s$ usually increases as $\Theta$ increases.

The first two model equations with transport are

$$\frac{\partial \phi_m}{\partial t} + \frac{\partial (u^s \phi_m)}{\partial z} = -\mathcal{R}_1 \bar{k}_1 \phi_m (\phi_s - \phi_X)_+, \tag{7.66}$$

$$\frac{\partial \phi_X}{\partial t} + \frac{\partial (u^l \phi_X)}{\partial z} - \frac{1}{Pe} \frac{\partial}{\partial z} (\tilde{D} \frac{\partial \phi_X}{\partial z}) = \frac{1 - a_0}{\epsilon} [\mathcal{R}_1 \bar{k}_1 \phi_m (\phi_s - \phi_X)_+ - \mathcal{R}_2 \bar{k}_2 (\phi_X - \phi_s)_+], \tag{7.67}$$

where

$$Pe = \frac{\dot{m}_s d \tau_D^2}{D_0} \tag{7.68}$$

is the Peclet number. $D_0$ is the diffusion coefficient, and $\tau_D^2$ is the tortuosity. For the typical values of $\dot{m}_s \sim 0.5^{-11}$m s$^{-1}$, $d \sim 1000$ m, $D_0 \sim 10^{-9}$ m$^2$ s$^{-1}$, $\tau_D^2 \sim 3$, $Pe \approx 15$.

#### Reaction without transport

In this case, the equations for $\phi_m$, $\phi_X$ become

$$\dot{\phi}_m = -\mathcal{R}_1 \bar{k}_1 \phi_m (\phi_s - \phi_X)_+, \tag{7.69}$$

$$\dot{\phi}_X = \frac{1-a_0}{\epsilon}[\mathcal{R}_1\bar{k}_1\phi_m(\phi_s-\phi_X)_+ - \mathcal{R}_2\bar{k}_2(\phi_X-\phi_s)_+]. \tag{7.70}$$

Since $\epsilon << 1$, the above equations are similar to the model equations for enzyme kinetics. Therefore, Michaelis-Menten's pseudo-steady state approximation applies. In other words, the reaction for $\phi_X$ is so fast it is more or less in equilibrium at all times. Mathematically, we have

$$\mathcal{R}_1\bar{k}_1\phi_m(\phi_s-\phi_X)_+ \approx \mathcal{R}_2\bar{k}_2(\phi_X-\phi_s)_+, \tag{7.71}$$

which holds exactly only if $\phi_X = \phi_s$. Thus, we can simply look for a perturbation

$$\phi_X = \phi_s + \epsilon\phi_X^{(1)} + .... \tag{7.72}$$

Subsistituting into equations (7.69) and (7.70), we have

$$\dot{\phi}_m = -\mathcal{R}_1\bar{k}_1\epsilon\phi_m(-\phi_X^{(1)})_+, \tag{7.73}$$

$$\dot{\phi}_s = (1-a_0)[\mathcal{R}_1\bar{k}_1\phi_m(-\phi_X^{(1)})_+ - \mathcal{R}_2\bar{k}_2(\phi_X^{(1)})_+]. \tag{7.74}$$

We can easily see that if $\phi_X^{(1)} < 0$, then

$$\dot{\phi}_m + \frac{\epsilon}{1-a_0}\dot{\phi}_s = 0, \tag{7.75}$$

which implies $\dot{\phi}_m \approx 0$; If $\phi_X^{(1)} > 0$, then

$$\dot{\phi}_m = 0, \quad \phi_X^{(1)} = -\frac{\dot{\phi}_s}{(1-a_0)\mathcal{R}_2\bar{k}_2} = O(1). \tag{7.76}$$

This argument also suggests that $\dot{\phi}_m \approx 0$. That is to say, the reaction for $\phi_m$ will proceed extremely slowly.

In order to model the ongoing reaction, we obviously have two choices to make modifications. One choice is to consider the effect of transport by advection and diffusion. The other is to modify the rate laws.

#### Effect of compactional flow

Firstly, let us consider the effect of transport by purely compactional flow. From the compaction analysis in the earlier chapters, we understand that $u^l \approx 0, \partial u^l/\partial z \approx 0$ for the case $\lambda << 1$ (slow compaction). Naturally, the effect of compactional flow

is negligible for the reaction. For the cases of $\lambda = O(1)$ and $\lambda >> 1$, we have $u^l = O(1)$, $\partial u^l/\partial z = O(1)$, then $\partial(\phi_X u^l)/\partial z = O(1)$. Therefore, Michaelis-Menten's approximation is still valid for $\phi_X$, which means we still have $\phi_X \approx \phi_s$. In other words we say that the effect of compactional flow is also negligible for the transport of species $[X]$. Smectite moves (at the speed of $u^s$) with the other solids in the matrix, and its reaction rate is nearly zero.

The effect of transport is only possibly important only if $\partial(\phi_X u^l)/\partial z >> 1$. This implies that the compactional flux should be extremely high. An extremely high compactional flux is very rare in natural sedimentation environments and can only possibly be generated under very special conditions. In fact, Bjorlykke & Egeberg (1993) studied the transport of silica in quartz cementation and concluded that the advective transport is not noticeably important in sedimentary basins.

Therefore, the effect of advective transport is negligible in normal sedimentary basins.

**Effect of diffusion**

Since the effect of advective transport is not important, we can simply neglect the advection terms in the model equations, and we have

$$\dot{\phi}_m = -\mathcal{R}_1 \bar{k}_1 \phi_m (\phi_s - \phi_X)_+, \tag{7.77}$$

$$\frac{\partial \phi_X}{\partial t} - \frac{1}{Pe}\frac{\partial^2 \phi_X}{\partial z^2} = \frac{1-a_0}{\epsilon}[\mathcal{R}_1 \bar{k}_1 \phi_m (\phi_s - \phi_X)_+ - \mathcal{R}_2 \bar{k}_2 (\phi_X - \phi_s)_+], \tag{7.78}$$

where we have assumed that $\tilde{D} = 1$. We can easily see that if $Pe >> 1$, then the diffusion is naturally negligible. In the case $Pe = O(1)$, Michaelis-Menten's hypothesis still applies, thus we have $\phi_X \approx \phi_s$. The effect of transport by diffusion is still not important.

Diffusion will possibly be important when $Pe = \dot{m}_s d/D_0 << 1$. This can be true either in a very slow sedimentation environment (small $\dot{m}_s$) or in fast diffusion process (large $D_0$) or in short-distance exchanges (small $d$). To be more precise, as seen from equation (7.78), $Pe = O(\epsilon)$ or $Pe << \epsilon$.

In the case of $Pe << \epsilon$ (i.e. $Pe/\epsilon << 1$), equation (7.78) implies

$$\frac{\partial^2 \phi_X}{\partial z^2} \approx 0, \tag{7.79}$$

which means $\phi_X$ is a linear function of $z$. In a pseudo-steady state, the slope is determined by mass conservation. If long-distance diffusion dominates the transport process, then smectite dissolves in the lower region and illite precipitates in the upper region. Therefore, illite should exist even at the top region near the surface, but this is contrary to the field observations (illite is rarely found within a depth of $1 \sim 2$ km). This contradiction suggests that only very short-distance diffusion is important in natural systems as is suggested by Ahn & Peacor (1986).

### 7.5.3 Dissolution controlled or precipitation controlled

We have seen in the previous discussion that the effect of transport on the reaction is negligible. In order to modify the model to mimic the more realistic dissolution-precipitation mechanism, we can assume that the solubility of smectite (dissolution) is different from that of illite (precipitation) ($\theta \approx 6/120$), and we use the following rate functions

$$\tilde{r}_1 = \phi_m(1-\phi_X)_+, \quad \tilde{r}_2 = (\phi_X - \theta)_+, \quad \theta = \frac{c_{eq}^{illite}}{c_{eq}^{amorph}} \quad (0 < \theta < 1), \tag{7.80}$$

then the first two equations (7.66) and (7.67) become

$$\dot{\phi}_m = -\mathcal{R}_1 \bar{k}_1 \phi_m \{1-\phi_X\}_+, \tag{7.81}$$

$$\epsilon \dot{\phi} = (1-a_0)[\mathcal{R}_1 \bar{k}_1 \phi_m \{1-\phi_X\}_+ - \mathcal{R}_2 \bar{k}_2 \{\phi_X - \theta\}_+], \tag{7.82}$$

$$\mathcal{R}_1 \bar{k}_1 = e^{\beta_1(\Theta - \Theta_{c,1})}, \quad \mathcal{R}_2 \bar{k}_2 = e^{\beta_2(\Theta - \Theta_{c,2})}, \tag{7.83}$$

with initial conditons

$$\phi_m = \phi_m^0 \text{ and } \phi_X = \phi_X^0. \tag{7.84}$$

Since $\epsilon << 1$, the above equations are similar to the model equations for enzyme dynamics, then Michaelis-Menten's pseudo-steady state approximation is valid. This fast asymptotics implies $\mathcal{R}_1 \bar{k}_1 \tilde{r}_1 \approx \mathcal{R}_2 \bar{k}_2 \tilde{r}_2$. That is

$$\phi_m(1-\phi_X)_+ = A(\phi_X - \theta)_+ \quad \text{with} \quad A = \frac{\mathcal{R}_2 \bar{k}_2}{\mathcal{R}_1 \bar{k}_1} = e^{(\beta_2-\beta_1)\Theta + (\beta_1 \Theta_{c,1} - \beta_2 \Theta_{c,2})}. \tag{7.85}$$

Solving this equation for $\phi_X$, we can easily obtain

$$\phi_m(1-\phi_X)_+ = \frac{\phi_m A(1-\theta)}{\phi_m + A},$$

$$(\phi_X - \theta)_+ = \frac{\phi_m(1-\theta)}{\phi_m + A}. \tag{7.86}$$

Substituting these two expressions into the $\phi_m$, $\phi_i$ equations, we have

$$\dot{\phi}_m = -e^{\beta_1(\Theta-\Theta_{c,1})}\frac{\phi_m A(1-\theta)}{\phi_m + A}, \tag{7.87}$$

$$\dot{\phi}_i = (1-a_0)e^{\beta_2(\Theta-\Theta_{c,2})}\frac{\phi_m(1-\theta)}{\phi_m + A} = (1-a_0)fe^{\beta_1(\Theta-\Theta_{c,1})}\frac{\phi_m A(1-\theta)}{\phi_m + A}. \tag{7.88}$$

Adding these two equations (7.87) and (7.88), we have

$$\dot{\phi}_i + (1-a_0)\dot{\phi}_m = 0 \quad \text{or} \quad \phi_i = (1-a_0)(\phi_m^0 - \phi_m). \tag{7.89}$$

Therefore, we only need to solve the first equation (7.87), but it is a nonlinear equation whose solution can only be written down implicitly as a quadrature although its numerical solution is easily calculated. If $A$ is independent of $t$, then we can write down the solution explicitly. From a geological point of view, we are more interested in the following specific cases.

### Equal reaction rates

If dissolution and precipitation have the same reaction rates with the same activation energy ($\beta_1 = \beta_2$, $\Theta_{c,1} = \Theta_{c,2}$), then $A = 1$. If the further simplifications $\theta << 1$, $\phi_m << 1$ are used, then we have approximately

$$\dot{\phi}_m = -e^{\beta_1(\Theta-\Theta_{c,1})}\phi_m,$$

$$\dot{\phi}_i = (1-a_0)e^{\beta_2(\Theta-\Theta_{c,2})}\phi_m, \tag{7.90}$$

which is the case we discussed before in the dehydration model. We see that the dehydration model is a very special case of the dissolution-precipitation model with equal reaction rates and very low illite solubility and small volume fraction of smectite involved in the transformation process.

### Dissolution controlled

When dissolution is the rate limiting process, this is equivalently to two special cases: 1) $\beta_1 > \beta_2\,(E_1 > E_2)$ with $\Theta_{c,1} \approx \Theta_{c,2} \approx \Theta_c$; or 2) $\Theta_{c,1} > \Theta_{c,2}\,(\mathcal{R}_1 < \mathcal{R}_2)$ with $\beta_1 \approx \beta_2 \approx \beta$.

**1)** $\beta_1 > \beta_2 \quad (\Theta_{c,1} \approx \Theta_{c,2} \approx \Theta_c)$

In this case, $A << 1$ since $\Theta_c = O(1)$, we then have approximately

$$\phi_m(1-\phi_X)_+ = A(1-\theta),$$
$$(\phi_X - \theta)_+ = (1-\theta). \tag{7.91}$$

The equations become

$$\dot{\phi}_m = -e^{\beta_2\Theta - \beta_1\Theta_c}(1-\theta). \tag{7.92}$$

With a linear temperature approximation $\Theta = h(t) - z$, the solution can be easily obtained.

$$\phi_m = \phi_m^0 \exp[-\frac{1-\theta}{\beta_2\dot{h}(t)\phi_m^0}e^{\beta_2[h(t)-z]-\beta_1\Theta_c}], \tag{7.93}$$

Here we have used the approximation $\exp(-\beta_1\Theta_c) << 1$. This solution is obtained from an approximation from the original equation (7.55) rather than directly from (7.92) since equation (7.92) is only valid in the top part of the region, but the solutions we obtained here hold approximately in the entire region. The purpose of writing down equation (7.92) is just to show that the reaction rate is nearly independent of $\phi_m$ in its region of validity. We can see that dissolution-precipitation will not be switched on until a higher critical temperature ($\Theta^* = \beta_1\Theta_c/\beta_2 > \Theta_c$) is achieved.

**2)** $\Theta_{c,1} > \Theta_{c,2} \quad (\beta_1 \approx \beta_2 \approx \beta)$

In this case, $A >> 1$, we have approximately

$$\phi_m(1-\phi_X)_+ = \phi_m(1-\theta),$$
$$(\phi_X - \theta)_+ = \frac{\phi_m(1-\theta)}{A}. \tag{7.94}$$

The equations become

$$\dot{\phi}_m = -e^{\beta(\Theta-\Theta_{c,1})}\phi_m(1-\theta). \tag{7.95}$$

Its solution can be written explicitly if a linear approximation $\Theta = h(t) - z$ for temperature is assumed.

$$\phi_m = \phi_m^0 \exp[-\frac{(1-\theta)}{\beta \dot{h}(t)} e^{\beta(h-z-\Theta_{c,1})}]. \tag{7.96}$$

Similarly, the dissolution and precipitation are simultaneously switched on at the higher critical temperature $\Theta_{c,1}$.

### Precipitation controlled

When precipitation is the rate limiting process, this is equivalently to 1) $\beta_1 < \beta_2$ ($E_1 < E_2$) with $\Theta_{c,1} \approx \Theta_{c,2} \approx \Theta_c$; or 2) $\Theta_{c,1} < \Theta_{c,2}$ ($\mathcal{R}_1 > \mathcal{R}_2$) with $\beta_1 \approx \beta_2 \approx \beta$.

In the former case, $A >> 1$. With a similar discussion as in the *dissolution controlled* case, we have

$$\dot{\phi}_m = -e^{(\beta_1 \Theta - \beta_2 \Theta_c)} \phi_m (1-\theta), \tag{7.97}$$

and its solution (for $\Theta = h(t) - z$) is

$$\phi_m = \phi_m^0 \exp[-\frac{(1-\theta)}{\beta \dot{h}(t) \phi_m^0} e^{\beta_1(h-z) - \beta_2 \Theta_c}]. \tag{7.98}$$

Similarly, the precipitation increases rapidly at a higher critical temperature $\Theta^{*'} = \beta_2 \Theta_c / \beta_1 > \Theta_c$.

In the latter case, $A << 1$. We similarly have

$$\dot{\phi}_m = -e^{\beta(\Theta - \Theta_{c,2})} (1-\theta), \tag{7.99}$$

with

$$\phi_m = \phi_m^0 \exp[-\frac{(1-\theta)}{\beta \dot{h}(t)} e^{\beta(h-z-\Theta_{c,2})}]. \tag{7.100}$$

As easily seen, precipitation suddenly increases after temperature is above the higher critical temperature $\Theta_{c,2}$.

### Equal solubility

If smectite and illite have the same solubilities, then $\theta = 1$. We can clearly see that all the above discussed processes reach equilibrium very quickly. The transformation ceases within a very short time. From a thermodynamic and kinetic point of

view, smectite is equivalent to illite. This is what we have discussed in the previous subsection. Fortunately, this impractical case is not of geological interest.

**Effect of transport**

The above results for the dissolution-precipitation model with $\theta < 1$ do not include the effect of transport. If we include the terms of transport, we have

$$\frac{\partial \phi_m}{\partial t} + \frac{\partial (u^s \phi_m)}{\partial z} = -\mathcal{R}_1 \bar{k}_1 \phi_m \{1 - \phi_X\}_+, \tag{7.101}$$

$$\frac{\partial \phi_X}{\partial t} + \frac{\partial (u^l \phi_X)}{\partial z} - \frac{1}{Pe}\frac{\partial}{\partial z}(\tilde{D}\frac{\partial \phi_X}{\partial z}) = \frac{1 - a_0}{\epsilon}[\mathcal{R}_1 \bar{k}_1 \phi_m \{1 - \phi_X\}_+ - \mathcal{R}_2 \bar{k}_2 \{\phi_X - \theta\}_+]. \tag{7.102}$$

If $Pe = O(1)$, then the Michaelis-Menten approximation is still valid. From the second equation, we can still have equation (7.85). Thus, the transport of $[X]$ does not change $\phi_X$ noticeably, and the advective term of $\phi_m$ will only change, increasing rather than decreasing, $\phi_m$ when the solid matrix moves down but will not change the reaction rate. The effect of transport on the reaction rate is, therefore, negligible.

## 7.6 Effect of $K^+$ and $Al^+$ Activities

Up to now, we have not investigated the interaction of $[K^+]$ from K-feldspar. For convenience in discussing $[K^+]$ influence without $Al^+$, the quartz dissolution and precipitation processes are not included at the moment. Then the related governing equations become (without transport )

$$\dot{\phi}_m = -\mathcal{R}_1 \bar{k}_1 \tilde{r}_1, \tag{7.103}$$

$$\dot{\phi}_X = \frac{a_1}{\epsilon}[\mathcal{R}_1 \bar{k}_1 \tilde{r}_1 - f\mathcal{R}_2 \bar{k}_2 \tilde{r}_2], \tag{7.104}$$

$$\dot{\phi}_i = f\mathcal{R}_2 \bar{k}_2 a_2 \tilde{r}_2, \tag{7.105}$$

$$\dot{\phi}_K = \frac{1}{\epsilon_K}[-a_3 \mathcal{R}_2 \bar{k}_2 \tilde{r}_2 + a_4 \mathcal{R}_3 \bar{k}_3 \tilde{r}_3], \tag{7.106}$$

$$\dot{\phi}_f = -a_8 \mathcal{R}_3 \bar{k}_3 \tilde{r}_3, \tag{7.107}$$

where $\epsilon = \bar{\phi}_X$, $\epsilon_K = \bar{\phi}_K$ are the equilibrium solubilities. According to Lasaga (1981, 1984), Ortoleva (1992) and Steefel & Cappellen (1990), we use the following functions for the rate laws

$$\tilde{r}_1 = \phi_m(1 - \phi_X), \tag{7.108}$$

$$\tilde{r}_2 = \phi_K \phi_X^n - \theta^n \kappa, \tag{7.109}$$

$$\tilde{r}_3 = \phi_f(\kappa - \phi_K), \tag{7.110}$$

where $n$ is a constant which is usually 1 or 2. $\kappa = O(1)$ is the K-feldspar solubility ratio with respect to some reference solubility (e.g. amorphous silica).

The fast aqueous reaction approximation ($\epsilon << 1$, $\epsilon_K << 1$) from equations (7.104) and (7.106) suggests that

$$\phi_m(1 - \phi_X) = A(\phi_K \phi_X^n - \theta^n \kappa), \tag{7.111}$$

$$\phi_K \phi_X^n - \theta^n \kappa = B\phi_f(\kappa - \phi_K), \tag{7.112}$$

with

$$A = \frac{f\mathcal{R}_2 \bar{k}_2}{\mathcal{R}_1 \bar{k}_1}, \quad B = \frac{a_4 \mathcal{R}_3 \bar{k}_3}{a_3 \mathcal{R}_2 \bar{k}_2}. \tag{7.113}$$

We see that the above two algebraic equations can be solved for $\phi_X$ and $\phi_K$ in terms of $A$ and $B$. To understand the $[K^+]$ influence more clearly, we are more interested in two extreme cases: $B >> 1$ if K-feldspar dissolves very rapidly while $B << 1$ if it dissolves very slowly. In the following discussions, without loss of generality, we can take $A = O(1)$ if smectite dissolution and illite precipitation reactions proceed at the nearly same rate.

### 7.6.1 K-feldspar dissolution controlled

In this case, $B << 1$. By solving $\phi_X$, $\phi_K$ from equations (7.111) and (7.112), the governing equations become approximately

$$\dot{\phi}_m = -\mathcal{R}_1 \bar{k}_1 \phi_f AB\kappa, \tag{7.114}$$

$$\dot{\phi}_i = f\mathcal{R}_2 \bar{k}_2 a_2 \phi_f B\kappa, \tag{7.115}$$

$$\dot{\phi}_f = -a_8 \mathcal{R}_3 \bar{k}_3 \phi_f (1 - B\phi_f - \theta^n)\kappa, \quad n = 1, 2. \tag{7.116}$$

We see that the dissolution rate of K-feldspar is nearly a constant ($B << 1$), but smectite dissolution and illite precipitation are very slow as they are controlled by the K-feldspar dissolution.

### 7.6.2 Fast K-feldspar reaction

In this case, $B >> 1$. From equation (7.112), we have

$$\phi_K \approx \kappa. \tag{7.117}$$

From equation (7.111), we can easily obtain

$$\phi_X = \theta + (1 - \theta)\frac{\phi_m}{A\kappa + \phi_m} \quad \text{for} \quad n = 1;$$

$$\phi_X = \frac{\sqrt{(\phi_m + 2A\theta\kappa)^2 + 4A\kappa\phi_m(1-\theta)} - \phi_m}{2A\kappa} \quad \text{for} \quad n = 2. \tag{7.118}$$

Substituting these relations into the governing equations for $\phi_m$, $\phi_i$, $\phi_f$, we have (for $n = 1$)

$$\dot{\phi}_m = -\mathcal{R}_1 \bar{k}_1 \phi_m (1 - \theta)\frac{A\kappa}{A\kappa + \phi_m}, \tag{7.119}$$

$$\dot{\phi}_i = f\mathcal{R}_2 \bar{k}_2 \phi_m a_2 (1 - \theta)\frac{\kappa}{A\kappa + \phi_m} = a_2 \mathcal{R}_1 \bar{k}_1 \phi_m (1 - \theta)\frac{A\kappa}{A\kappa + \phi_m}, \tag{7.120}$$

$$\dot{\phi}_f \approx 0. \tag{7.121}$$

By comparing with equations (7.87) and (7.88), we see that the above equations are identical to equations (7.87) and (7.88) if we replace $A$ with $A\kappa$. Following similar procedures, we will have all the results as before. Therefore, the two-step model is a very good approximation for the case of fast K-feldspar dissolution and $[K^+]$ concentration remains nearly at equilibrium solubility. The equations are not much different for the case of $n = 2$.

### 7.6.3 $Al^+$ activity

From the model formulations, it is clearly seen that $Al^+$ always appears with $K^+$. Both cations have similar roles. In other words, they are mathematically equivalent

and satisfy similar equations though their chemical roles are different. This means that we can always take these two cations as a single combination $[K^+ - Al^+]$. Therefore, the effect of $Al^+$ is essentially the same as $K^+$ and their combination $[K^+ - Al^+]$. Similar mathematical argument will give similar results as before if we replace $\phi_K, \bar{\phi}_K$ by $\phi_{Al}, \bar{\phi}_{Al}$.

## 7.7 Quartz Precipitation

### 7.7.1 Quartz precipitation controlled

To include the process of quartz precipitation from the excess silica released by K-feldspar dissolution, we still use the same rate laws for $\tilde{r}_1$ and $\tilde{r}_2$, but we use

$$\tilde{r}_3 = \phi_f(\kappa\theta_{Si} - \phi_K\phi_{Si}), \tag{7.122}$$

$$\tilde{r}_4 = \phi_{Si} - \theta_{Si}, \tag{7.123}$$

where $\theta_{Si} < 1$ is the ratio of quartz solubility to amorphous silica solubility. Here, we have ignored the dissolution process of quartz ($\tilde{r}_{-4} = 0$) or can take $\tilde{r}_4$ as the net rate of quartz precipitation and dissolution. In addition to the model equations in the subsection with $K^+$ activity, we still have (without transport)

$$\dot{\phi}_{Si} = \frac{1}{\epsilon_{Si}}[s\mathcal{R}_3\bar{k}_3\tilde{r}_3 - \mathcal{R}_4\bar{k}_4\tilde{r}_4 + \frac{a_3}{a_4}\mathcal{R}_2\bar{k}_2\tilde{r}_2], \tag{7.124}$$

where $\epsilon_{Si} = \bar{\phi}_{Si} << 1$ is the equilibrium solubility for quartz. The Michaelis-Menten pseudo-steady steady approximation for $\phi_K$ and $\phi_{Si}$ implies that

$$s\mathcal{R}_3\bar{k}_3\tilde{r}_3 + \frac{a_3}{a_4}\mathcal{R}_2\bar{k}_2\tilde{r}_2 \approx \mathcal{R}_4\bar{k}_4\tilde{r}_4, \tag{7.125}$$

$$a_4\mathcal{R}_3\bar{k}_3\tilde{r}_3 \approx a_3\mathcal{R}_2\bar{k}_2\tilde{r}_2. \tag{7.126}$$

Eliminating $\tilde{r}_2$, we have

$$\phi_f(\kappa\theta_{Si} - \phi_K\phi_{Si}) \approx C(\phi_{Si} - \theta_{Si}) \quad \text{with} \quad C = \frac{\mathcal{R}_4\bar{k}_4}{(s+1)\mathcal{R}_3\bar{k}_3}, \tag{7.127}$$

or

$$\tilde{r}_3 = \phi_f(\kappa\theta_{Si} - \phi_K\phi_{Si}) = \frac{C\phi_f\theta_{Si}(\kappa - \phi_K)}{C + \phi_f\phi_K}. \tag{7.128}$$

It is clearly seen that if quartz precipitation is very fast ($C >> 1$), then $\phi_{Si} \approx \theta_{Si}$, the rate law of K-feldspar dissolution is $\tilde{r}_3 \approx \phi_f \theta_{Si}(\kappa - \phi_K)$, we can then have all the similar results as before as in the cases of slow or fast K-feldspar dissolutions. On the other hand, if quartz precipitation is very slow ($C << 1$), then K-feldspar dissolution rate is $\tilde{r}_3 \approx C\theta_{Si}(\kappa/\phi_K - 1)$ which is clearly controlled by the rate of quartz precipitation. This is essentially similar to the case of slow K-feldspar dissolution. In the top region where the temperature is relatively low, the rate of quartz precipitation is very slow. If the temperature increases to some critical value during continuous burial, then the rate of quartz precipitation increases dramatically, and this in turn switches on K-feldspar dissolution to provide enough $K^+$ for illite precipitation, and the process of smectite dissolution and illite precipitation will proceed until the reaction is completed. This reaction series is in line with the recent work by Abercromie, Hutcheon, Bloch & Caritat (1994).

### 7.7.2 Production of quartz

The precipitation of extra silica as quartz will have an important effect on porosity modifications and reservoir impairments. The calculation of the amount of quartz production is obviously needed. For convenience, we neglect the effect of transport. By using the full model equations and the pseudo-steady state approximations for $\phi_X, \phi_{Si}, \phi_K$, we can easily obtain the relations among $\tilde{r}_2, \tilde{r}_3, \tilde{r}_4$, then we can relate $\dot{\phi}_q$ with $\dot{\phi}_m$ or $\dot{\phi}_i$. We have

$$\dot{\phi}_q = -\frac{s+1}{f}\bar{a}_1\dot{\phi}_m, \tag{7.129}$$

and

$$\dot{\phi}_q = \frac{s+1}{fa_2}\bar{a}_1\dot{\phi}_i, \tag{7.130}$$

where

$$\bar{a}_1 = \frac{a_7 a_3}{a_4} = \frac{\rho_m M_q}{\rho_q M_m}. \tag{7.131}$$

From the first equation (7.129), we have

$$\phi_q = \frac{s+1}{f}\bar{a}_1(\phi_m^0 - \phi_m). \tag{7.132}$$

Similarly, we can have the expression for amount of K-feldspar consumed

$$\dot{\phi}_f = \frac{1}{f}\bar{a}_2\dot{\phi}_m, \quad \bar{a}_2 = \frac{a_8 a_3}{a_4} = \frac{\rho_m M_f}{\rho_f M_m}, \tag{7.133}$$

or

$$\phi_f^{\text{consumed}} = -\frac{1}{f}\bar{a}_2(\phi_m^0 - \phi_m). \tag{7.134}$$

With the values of $M_m = 367$, $M_q = 60$, $s = 3$, $f = 2, \rho_m/\rho_q \approx 1, \phi_m^0 = 0.2$ (20%), then $\phi_q \approx 0.065$ ( or 6.5%), $\phi_f^{\text{consumed}} \approx -0.075$ (or $-$ 7.5%) after the completion of the S-I reaction. Such a large amount of quartz may have important effect on reservoir quality.

## 7.8 Summary

From the above discussions, we see that the reaction-transport dissolution- precipitation model of diagenesis can reproduce many essential features of the smectite-to-illite process if the appropriate reaction rate laws are used based on the known physics and chemistry from experimental studies. The detailed investigation of the two-step model shows that smectite-to-illite reaction occurs within a narrow region, *diagenetic window*, at a depth nearly $\Theta_c$, and the reaction processes do not noticeably depend on the absolute age of the burial series. More important than geological age is the temperature distribution. Long-distance mass transport is negligible in the progress of the whole diagenetic process. In addition, we see that the first-order dehydration model of diagenesis is a good approximation in the sense of describing the extent of progress of the overall smectite-to-illite transformation without much concern for its detailed geochemical features. All the results in the case of dehydration model are already presented in Chapter 6.

The full investigations of the whole model in different possible cases reveal that $K^+$, $Al^+$ cations provided from the dissolution of K-feldspar are very important in controlling the progress of the diagenetic reaction. The similarities between the present model and Michaelis-Menten's theory of enzyme kinetics suggest that these cations play a role partially like a catalyst during diagenesis. In the case of fast K-feldspar dissolution, the two-step model is a very good approximation in describing

the whole process. In the case of slow K-feldspar dissolution, the whole process is controlled by the rate of K-feldspar dissolution. If there is not enough K-feldspar available, then diagenesis can not be completed and may cease in the intermediate stage.

Quartz activity is also a very important factor in controlling the progress of the diagenetic reactions. The case of fast quartz precipitation shows no noticeable difference from those of slow or fast K-feldspar dissolutions. But slow quartz precipitation will hinder the diagenetic process. In the shallow region, the temperature is relative low, the rate of quartz precipitation is extremely slow. As burial continues, the temperature increases, and the rate of quartz precipitation increases dramatically at some critical value of temperature, and this in turn switches on K-feldspar dissolution to provide $K^+$ for illite precipitation, thus the process of smectite dissolution and illite precipitation will proceed until the reaction is completed. The amount of quartz product during diagenesis will possibly have an important effect on reservoir quality.

# Chapter 8

# Pressure Solution Creep and Viscous Compaction

The diagenetic modelling in the previous chapter is a transport-reaction model whose reaction rate laws do not include the effect of intergranular stress. Obviously, a more realistic model should reflect the complexity of the stressed rock system. *Pressure solution/dissolution* has been considered as an important process in deformation and porosity change during compaction and diagenesis in sedimentary rocks (Angevine & Turcotte, 1983; Tada & Siever 1989). Pressure solution refers to a process by which grains dissolve at intergranular contacts under nonhydrostatic stress and reprecipitate in pore spaces, thus resulting in compaction. The solubility of minerals increases with increasing effective stress at grain contacts. Pressure dissolution at grain contacts is therefore a compactional response of the sediment during burial in an attempt to increase the grain contact area so as to distribute the effective stress over a larger surface. The typical forms of pressure solution are intergranular pressure solution (IPS) which occurs at individual grain contacts (Tada & Siever 1989) and free face pressure solution (FFPS) which occurs at the face in contact with the pore fluid (Ortoleva 1994), but most studies have concentrated on the former one (IPS). In spite of its geological importance, the mechanism leading to pressure solution is still poorly understood.

## 8.1 Mechanism of Pressure Solution

Angevine and Turcotte (1983) presented a wonderful theoretical model to study the role of pressure solution in the porosity reduction of quartz arenites and the effects of grain size, sedimentation rate, and the thermal gradient. Augevine & Turcotte's work was later extended by Birchwood and Turcotte (1994) to give a unified approach to geopressuring, low-permeability zone formation, and secondary porosity generation in sedimentary basins. A comprehensive review on models of pressure solution was given by Tada & Siever (1989). Birchwood & Turcotte (1994) presented more recently a brief review on this research subject.

Extensive studies from petrographic, field and experimental evidence suggest that pressure solution is a very complicated process controlled by many factors (Augevine & Turcotte, 1983; Tada & Siever 1989; Birchwood & Turcotte, 1994).

- The main factors controlling pressure solution are temperature, pressure, time, grain size and geometry, grain mineralogy, cementation, and solution chemistry. These factors do not seem to be simple controlling factors, and may interact with each other. The rate generally increases with increase of temperature or effective pressure and decrease of grain size.

- Pressure solution usually involves three successive steps: pressure-enhanced dissolution, diffusive transfer and reprecipitation. The rate of pressure solution is thus controlled by the slowest of the three steps, *diffusion-controlled* or *reaction-controlled*. Most of the existing models of pressure solution assume that diffusive transport is the rate-limiting step (Weyl, 1959; Coble, 1963; Rutter, 1976; Augevine & Turcotte, 1983).

- The driving force for pressure solution is possibly the gradient of chemical potential, existing between dissolution and reprecipitation areas, which depends mainly on the difference of normal stress, elastic, plastic and surface energies. De Boer (1977) has shown that the effect of elastic strains on the gradient of chemical potential is negligible.

- Pressure solution can start at depths as shallow as 900m in sandstones (Wilson & Sibley, 1978) but occurs more commonly at depths of $1 \sim 2$ km.

- Pressure solution is an effective compaction mechanism as well as a source of cementing material, especially in sandstones and carbonate packstones. Mass transport and redistribution during pressure solution may possibly occur over the order of km (Tada & Siever 1989).

- Pressure solution is probably a combination of plastic deformation and free-face pressure solution within and at the edge of the grain contacts (Tada & Siever 1989). Mass transfer may be carried out by grain boundary diffusion (locally) or by bulk diffusion (regionally), depending on the distance of mass transfer. Gratier (1984) proposed various pressure solution creep laws for these cases. Drewers & Ortoleva (1990) considered pressure solution as a diffusion-reaction creep mechanism.

In spite of all these extensive studies, the operating mechanism of pressure solution and the role of plastic versus elastic strain energy as a driving force are still under discussion. According to Mullis (1992), two main mechanisms of pressure solution are possible. One mechanism assumes that increased solubility at the grain boundary sets up a concentration gradient resulting in mass transfer by diffusion into the pore spaces. The diffusive transfer could occur by thin water film diffusion adsorbed to the grain boundary (Weyl, 1959; Rutter, 1976; Augevine & Turcotte, 1983), or by bulk diffusion or through fluid 'island channels' (Raj & Chyung, 1981). An alternative mechanism is the undercutting model which supposes that the increased solubility at the grain contacts results in preferential dissolution at the rim of grain contacts leading to undercutting and brittle failure (Bathurst, 1958) or plastic deformation (Pharr & Ashby, 1983; Tada, Maliva & Siever, 1987; Pytte & Reynolds, 1989).

Many experiments have been carried out to investigate the mechanism of pressure solution, but no evidence has been found for grain undercutting though neither is direct evidence for adsorbed thin water films convincing. It is worth pointing out that the theory of (adsorbed thin) water film diffusion (WFD) is theoretically favoured by

the concept of very high disjoining pressure ($\sim$ 270 MPa) of removing a monolayer from a thin film (De Boer, 1977; Rutter, 1976; Tada, Maliva & Siever, 1987; Mullis, 1992). However, some controversy still exists about which of the two mechanisms is more appropriate, as they produce the same creep rate in the simplest case of diffusion-controlled creep; the only difference lies in the interpretation and values of parameters such as the effective grain-boundary diffusion coefficient.

## 8.2 Mathematical Model

For the convenience of investigating the effect of pure pressure solution, we will begin by neglecting diagenetic reactions such as the smectite-to-illite transformation and will assume a single species only such as quartz. Extensions will then be made to reactive multiple species during diagenesis. From the discussion in the previous subsection, we will also assume that the dissolution-diffusion-precipitation process only occurs *locally* on a grain scale. Based on the existing models of pressure solution (Weyl, 1959; Rutter, 1976; Angevine & Turcotte, 1983; Nielsen, 1986; Mullis, 1991) and models of compaction (Fowler, 1990; Stevenson & Scott 1991; Audet & Fowler, 1992; Birchwood & Turcotte, 1994), the present model is written as

*Conservation of mass*

$$\frac{\partial}{\partial t}(1-\phi) + \nabla \cdot [(1-\phi)\mathbf{u}^s] = 0, \tag{8.1}$$

$$\frac{\partial \phi}{\partial t} + \nabla \cdot (\phi \mathbf{u}^l) = 0, \tag{8.2}$$

*Darcy's law*

$$\phi(\mathbf{u}^l - \mathbf{u}^s) = -\frac{k}{\mu}(\nabla p^l + \rho_l g \mathbf{j}), \tag{8.3}$$

*Force balance*

$$\nabla \cdot \boldsymbol{\sigma^e} \ - \nabla[(1-a)p^l] - \rho g \mathbf{j} = \mathbf{0}, \tag{8.4}$$

where $\xi$ is bulk viscosity, $\boldsymbol{\sigma_e}$ is the effective stress, $p_e$ is the effective pressure, $\mathbf{j}$ is the unit vector pointing vertically upwards, $k$ is the matrix permeability, $\mu$ is the liquid viscosity and $p^l$ is the pore pressure.

A rheological relation and a *constitutive law* are needed to complete this model. If an Athy-type law is used to relate effective pressure $p_e$ with porosity $\phi$, we will again return to the model we have analyzed in the earlier chapters. To emphasise the features of pressure solution creep, a different type of constitutive law is expected.

### 8.2.1 Constitutive creep laws

There are generally two ways to make mathematical formulations of *creep laws* for pressure solution. One way is to derive creep rate in terms of concentrations, grain size and geometry (usually spherical or cylindrical packings), effective stress, grain boundary diffusion. Most models fall into this category (Weyl, 1959; Paterson, 1973; Rutter, 1976; Angevine & Turcotte, 1983; Mullis, 1991, 1992; Shimizu, 1995; Lehner, 1995; Schneider et al, 1996). This allows us to include the detailed reaction-transport process in a simplified relation between strain rate and effective stress although further simplifications are usually assumed such as steady-state dissolution and *local* reprecipitation along the grain boundary. An alternative method of formulation is simply to assume a viscous law, as is done, for example, in modelling magma transport (McKenzie, 1984; Fowler, 1990). The latter treatment does not describe the details of the pore scale dynamics. The connection between these two kinds of formulations can be easily seen from the *constitutive law* used in the formulations.

In the formulations of the first kind, the Weyl-Rutter *creep law* is widely used (Weyl, 1959; Rutter, 1976; Angevine & Turcotte, 1983)

$$\dot{e} = \frac{A_k c_0 \, w D_{gb}}{\rho_s \bar{d}^3} \sigma, \tag{8.5}$$

where $\sigma$ is the effective normal stress across the grain contacts, $A_k$ is a constant, $c_0$ is the equilibrium concentration (of quartz) in pore fluid, $\rho$, $\bar{d}$ are the density and (averaged) grain diameter (of quartz). $D_{gb}$ is the diffusivity of the solute in water along grain boundaries with a thickness $w$. This relation holds for the case of steady-state diffusion and no grain-boundary sliding.

The relation between porosity $\phi$ and volume strain $e$ depends the grain geometry and packing texture. Weyl (1959) and Augevine & Turcotte (1983) used the following

relation

$$e = 1 - (\frac{\pi}{6(1-\phi)})^{1/3}, \tag{8.6}$$

for regularly 3-D spherical packing, while Schutjens (1991) used

$$e = \frac{\phi_0 - \phi}{1-\phi}, \tag{8.7}$$

in explaining the experimental compaction of quartz. $D_{gb}$ also varies with temperature $T$. In fact, Augevine & Turcotte (1983) wrote $D_{gb}(T)$ as

$$D_{gb}(T) = D_{gb} e^{-\frac{H_{cd}}{RT}}, \tag{8.8}$$

where $H_{cd}$ is the effective activation energy with a value of $3 \sim 6$ kJ/mole or even much lower (Angevine & Turcotte, 1983; Nakashima, 1995; Shimizu, 1995). From the values of the diffusion coefficient used by Paterson (1995) in quartz-water and rocksalt-water systems at 300, 600, 1200 K, we get an estimate value of $H_{cd} \approx 0.65$ kcal/mole. Rutter (1976) and Angevine & Turcotte (1983) pointed out that these values are only estimations.

In the classical formulations, the following constitutive laws are often used (Roberts & Tabor, 1971; Paterson, 1973; Mullis, 1991)

$$c = c_0 \exp(-\frac{\nu\sigma}{RT}) \quad \text{and} \quad w = w_0 \exp(-\frac{\sigma}{\sigma_0}), \tag{8.9}$$

where $w_0$, $\sigma_0$ are constants depending on the properties of the thin film, and $\nu$ is the molar volume (of quartz). These constitutive laws, though experimentally based, are essentially theoretical simplifications as in the case of Athy's law $p_e = p_e(\phi)$.

In addition, the diffusion coefficient $D_{gb}$ also depends on the porosity $\phi$. According to Archie (1942) and Paterson (1995), we have the following Archie's law

$$D_{gb} = (\frac{\phi}{\phi_0})^n D_0, \tag{8.10}$$

where $D_0$ is the diffusion coefficient at the initial porosity $\phi_0$, and $n$ is the exponent in Archie's law. The value of $n$ has been determined empirically to be 1.3 for uncemented sand-like granular media and 2 for a wide range of cemented rocks (Paterson, 1995).

Experimental studies show that $A_k$ in the creep law (8.5) is not a constant and depends on temperature $T$ (Raj & Chyung, 1981; Augevine & Turcotte, 1983; Spiers

& Schutjens, 1990; Dewers & Hajash, 1995). To incoorporate this, (8.5) is usually modified as

$$\dot{e} = A(\phi, T)\sigma, \quad \text{with} \quad A(\phi, T) = \frac{A_\alpha c_0\, w D_{gb}}{RT\bar{d}^3} \tag{8.11}$$

where $R$ is the gas constant, and $A_\alpha = \alpha\nu_m^2/\nu_{H_2O}$. $\alpha$ is a factor depending on the grain geometry and stress distribution. $\nu_m$ is the molar volume (of quartz) and $\nu_{H_2O}$ is the molar volume of water. The constitutive relation (8.11) is originally for the one-dimensional case. We can extend it to a more general form by writing

$$\sigma = \frac{RT\bar{d}^3}{A_\alpha c_0\, w D_{gb}} \dot{e}_{kk}. \tag{8.12}$$

Note that $p_e = -\sigma$ and $\dot{e}_{kk} = \nabla \cdot \mathbf{u^s}$. With this, (8.12) becomes

$$p_e = -\frac{RT\bar{d}^3}{A_\alpha c_0\, w D_{gb}} \nabla.\mathbf{u}^s, \tag{8.13}$$

which is equivalent to the following *compaction law*

$$p_e = -\xi \nabla.\mathbf{u}^s. \tag{8.14}$$

This was first used by Birchwood and Turcotte (1994) to study pressure solution in sedimentary basins by presenting a unified approach to geopressuring, low permeability zone formation and secondary porosity generation. The compaction law is analogous to dislocation creep controlled viscous compaction laws used in studies of magma transport in the Earth's mantle (McKenzie 1984, Fowler 1990).

Another way of formulating constitutive laws for *pressure solution creep* is to consider it as a viscous compaction mechanism. The creeping process under effective pressure $p_e$ can be formulated as

$$\frac{d(1-\phi)}{dt_s} = K(\phi, T) p_e, \tag{8.15}$$

where $d/dt$ is the material derivative $\partial/\partial t + \mathbf{u^s} \cdot \nabla$, following the solid matrix. Rewriting the equation (8.1) of mass conservation

$$\frac{d(1-\phi)}{dt_s} = -(1-\phi)\nabla.\mathbf{u}^s, \tag{8.16}$$

then (8.15) becomes

$$p_e = -\frac{1-\phi}{K(\phi, T)} \nabla.\mathbf{u}^s, \tag{8.17}$$

which is equivalent to (8.13). Therefore, we can say that the two kinds of formulations can be unified as a single creep law such as (8.14).

### 8.2.2 Derivation of creep law

The approach of deriving the law of pressure solution creep depends on the underlying mechanism. The classical theoretical consideration used by Weyl (1959) and Rutter (1976) assumed a grain-boundary diffusion film of constant thickness and diffusivity, while others used the concept of a roughened, fluid-invaded non-equilibrium contact structure (Raj, 1982; Lehner, 1990; Spier & Schutjens, 1990; Lehner, 1995). Shimizu (1995) presented a kinetic approach extending Coble's classical treatment of grain boundary diffusion creep (Coble, 1963) by including the kinetics of quartz dissolution/ precipitation reaction. Shimuzu's (1995) derivation is instructive although the boundary conditions used in his 1-D diffusion model are questionable. This 1-D approximation is only valid for a *closed system* when the thickness $w$ of the water film is small with respect to the grain diameter ($d$).

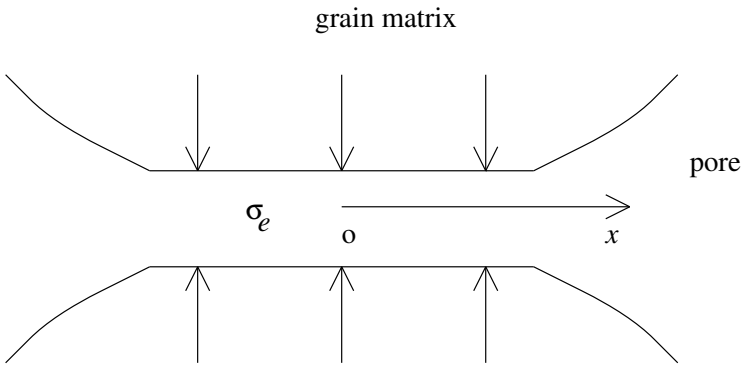


Figure 8.1 Water film diffusion model of pressure solution creep in which dissolution occurs in the contact region and reprecipitation takes place along grain boundaries in pore space. $\sigma^e$ is the *effective normal stress*.

Existing pressure solution creep laws can produce some typical features such as pressure and grain-size dependence of creep rate, but have essentially remained re-

stricted to macroscopically *closed systems*, with negligible long-distance transport in the pore fluid, and they are somewhat biased toward grain-boundary diffusion-controlled pressure solution creep. This shortcoming of the creep laws eliminates the effect of solution transfer over large distances. The consequence is that the coupling effects between solute transport and pressure solution deformation under possible *open system* conditions encountered during sediment diagenesis or metamorphism have received limited attention (Dewers & Ortoleva, 1990; Lehner, 1995). Augevine & Turcotte (1983) pointed out that future quantitative modelling of sediment diagenesis should incorporate temporal variations in subsidence rates, spatial variations in lithology, and heat flow (Turcotte & Schubert, 1982). Lehner (1995) investigated, for the first time, the creep law of pressure solution in *open* fluid-rock systems by recasting the classical Weyl-Rutter model of intergranular pressure solution in terms of a (linear) phenomenological creep rate law. However, Lehner (1995) left an open question concerning the validity of the postulated simple creep law due to the uncertainty of the assumed phenomenological rate constant $K^{gb}$, and suggested that a new generation of diagenetic models should describe an *open system* including the effect of composition, fluid pressure, temperature as well as solid stress state.

Now let us consider the intergranular contact region as a disk with a radius $r = L$. Let $J(r)$ be the radial component of solute mass flux, $\dot{e}$ be the average strain rate, and $v$ is the uniform shortening velocity of the upper grain relative to the lower grain due to the pressure solution creep. The kinetic relation between $v$ and $\dot{e}$ is (Lehner, 1995)

$$v = \dot{e}\bar{d}. \tag{8.18}$$

For simplicity, we assume that the film thickness $w$ is constant and the diffusion is near steady-state as Rutter (1976) and Lehner (1995) did. Mass conservation gives

$$2\pi r J(r) + \rho_s \pi r^2 v = 0, \tag{8.19}$$

where the flux $J(r)$ obeys *Fick's Law*

$$J(r) = -D_{gb} w \frac{dc}{dr}. \tag{8.20}$$

The steady-state solution of concentration $c(r)$ for the boundary condition $c_r = 0$ at $r = 0$, $c = c_0$ at $r = L$ is

$$c(r) = c_0 - \frac{\rho_s v}{4D_{gb}w}(L^2 - r^2). \tag{8.21}$$

The parabolic change of concentration $c(r)$ implies that the stress $\sigma(r)$ should be heterogeneously distributed in the contact region. From the relation (8.9), we have

$$\sigma^e(r) = -\frac{RT}{\nu_m}\ln\frac{c(r)}{c_0}, \tag{8.22}$$

where we have used the condition $\sigma^e(r) = 0$ at $r = L$. Let $\sigma$ be the averaged effective stress, then

$$\pi L^2\sigma = \int_0^L 2\pi\sigma^e(r)rdr. \tag{8.23}$$

Combining (8.22) and (8.23), we have

$$\sigma = -\frac{2RT}{\nu_m L^2}\int_0^L r\ln[1 - \frac{\rho_s\dot{e}\bar{d}}{4c_0D_{gb}w}(L^2 - r^2)]dr. \tag{8.24}$$

Using (8.18) and integrating by parts, we have

$$\sigma = -\frac{RT}{\nu_m}[(1 - \frac{1}{BL^2})\ln(1 - BL^2) - 1], \tag{8.25}$$

where

$$B = \frac{\rho_s\dot{e}\bar{d}}{4c_0D_{gb}w}. \tag{8.26}$$

By defining a critical effective stress $\sigma_c$ (and equivalently a critical creep rate $\dot{e}_c$ ) when $BL^2 = 1$

$$\sigma_c = \frac{RT}{\nu_m}, \quad \dot{e}_c = \frac{4c_0D_{gb}w}{\rho_s L^2\bar{d}}, \tag{8.27}$$

(8.25) can be rewritten as

$$\frac{\sigma}{\sigma_c} = [1 - (1 - \frac{\dot{e}_c}{\dot{e}})\ln(1 - \frac{\dot{e}}{\dot{e}_c})]. \tag{8.28}$$

A typical value of $\sigma_c$ is about 95 MPa with values of $T \sim 300$ K, $R \sim 8.31$ J mol$^{-1}$ K$^{-1}$, and $\nu_m \sim 2.6 \times 10^{-5}$ m$^3$ mol$^{-1}$.

Clearly, if $|\sigma| \ll \sigma_c$, we have

$$\dot{e} = \frac{4\nu_m c_0 D_{gb}w}{RT\rho_s\bar{d}L^2}\sigma = \frac{16\nu_m c_0 D_{gb}w}{RT\rho_s\bar{d}^3}\sigma, \tag{8.29}$$

which is exactly the creep law (8.11). Here we have used $L = \bar{d}/2$. A different choice of $L = O(\bar{d})$ will only introduce an additional shape factor into the above relation. Under upper-crustal stress conditions $\sigma < 100$ MPa (Zoback et al, 1993), the above approximation is valid as we expected. At higher stress states, we can use $|\sigma| \gg \sigma_c$, then (8.28) becomes

$$\dot{e} = \frac{4c_0 D_{gb} w}{\rho_s \bar{d} L^2}[1 - e^{-\frac{\nu_m \sigma}{RT}}]. \tag{8.30}$$

Let $L^2 = 4\bar{d}^2/\alpha_s$, and $\alpha_s = O(1)$ is a shape factor. The above relation (8.30) becomes

$$\dot{e} = \frac{\alpha_s c_0 D_{gb} w}{\rho_s \bar{d}^3}[1 - e^{-\frac{\nu_m \sigma}{RT}}], \tag{8.31}$$

which is consistent with Dewers and Hajash's empirical law derived from a quartz compaction experiment (Dewers & Hajash, 1995; Siese & Spiers, 1997). It is worth pointing out that the creep law (8.31) degenerates into (8.29) when $\nu_m \sigma / RT \ll 1$, but it may be inaccurate when $|\sigma| \sim \sigma_c$.

### 8.2.3 Equation of motion

For an *open system*, we expect that a source term will be introduced into the macroscopic equation of mass conservation. Now the porous medium consists of two phases, the solid matrix (quartz) and the pore fluid (dissolved silica and water). Let $\phi_m$ be the volume fraction of the solid, $c_{Si}$ and $c_w$ be molar concentrations of the dissolved solid species and water in the *pore fluid*, respectively, $r_m$ be the rate of mass dissolved by *pressure solution*, and $r_+$ and $r_-$ be the rates of dissolution and precipitation (of quartz) on *free surfaces* of grains where the effective pressure $\sigma^e = 0$. The equations of mass conservation now become

*Conservation of mass*

$$\frac{\partial \phi_m}{\partial t} + \nabla.[\phi_m \mathbf{u}^s] = (-r_m - r_+ + r_-)\frac{M_m}{\rho_m}, \tag{8.32}$$

$$\frac{\partial \phi c_w}{\partial t} + \nabla.(\phi c_w \mathbf{u}^l) = 0, \tag{8.33}$$

$$\frac{\partial \phi c_{Si}}{\partial t} - \nabla.(D\phi \nabla c_{Si} - \mathbf{u}^l \phi c_{Si}) = r_m + r_+ - r_-, \tag{8.34}$$

$$\phi_m + \phi = 1. \tag{8.35}$$

In the above equations, we have used volume fractions ($\phi_m$ and $\phi$) together with molar concentrations ($c_{Si}$ and $c_w$). For convenience in the following non-dimensionlization and analysis, we will rewrite the above equations solely in terms of volume fractions $\phi_{Si}$ (of the dissolved solid species) and $\phi_w$ (of water) to replace the molar concentrations ($c_{Si}$ and $c_w$). Clearly, $\phi = \phi_{Si} + \phi_w$ is the porosity and $\phi_m = 1 - \phi$. Thus, we have

*Conservation of mass*

$$\frac{\partial(1-\phi)}{\partial t} + \nabla.[(1-\phi)\mathbf{u}^s] = (-r_m - r_+ + r_-)\frac{M_m}{\rho_m}, \tag{8.36}$$

$$\frac{\partial(\phi - \phi_{Si})}{\partial t} + \nabla.[(\phi - \phi_{Si})\mathbf{u}^l] = 0, \tag{8.37}$$

$$\frac{\partial \phi_{Si}}{\partial t} - \nabla.(D\nabla\phi_{Si} - \mathbf{u}^l\phi_{Si}) = (r_m + r_+ - r_-)\frac{M_{Si}}{\rho_l}, \tag{8.38}$$

where $M_m$ and $M_{Si}$ are the molar weights of the solid and the disolved solid species, respectively. $\rho_m$ and $\rho_l$ are the densities of the solid and the pore fluid, respectively. $D$ is the diffusion coefficient in the pore fluid. If the process is only pressure-enhanced and there is no free surface reaction involved, then we have only one source term $r_m$.

The source term $r_m$ is

$$r_m = N\rho_s v\pi L^2 = N\rho_s \dot{e}\bar{d}L^2, \tag{8.39}$$

where $N$ is the number of grains per unit volume. Substituting (8.29), we have

$$r_m = \frac{4\pi\nu_m c_0 D_{gb} w}{RT} N\sigma. \tag{8.40}$$

For 3-D packed spherical grains, $N = A_0/\bar{d}^3$, we finally obtain

$$r_m = \frac{4A_0\pi\nu_m c_0 D_{gb} w}{RT\bar{d}^3}\sigma, \tag{8.41}$$

where $A_0 = O(1)$ is a shape factor which is 1 for cube-shaped grain packing and $6/\pi$ for spherical grain packing.

From the kinetic theory of the quartz-water system (Rimstidt & Barnes, 1980; Paterson, 1995), quartz pressure solution is described approximately by the reaction

$$\mathrm{SiO_2(solid)} \ + \ 2\mathrm{H_2O}(aq) \rightleftharpoons \mathrm{H_4SiO_4}(aq). \tag{8.42}$$

The free surface dissolution rate $r_+$ and precipitation rate $r_-$ depend on the temperature, pore pressure $p$ and the concentrations.

$$r_+ = k_+(T,p)\ a_{SiO_2}\ a_{H_2O}^2, \tag{8.43}$$

$$r_- = k_-(T,p)\ \ a_{H_4SiO_4}, \tag{8.44}$$

where $a$ is activity. For free surface dissolution and precipitation in dilute solutions, we may assume

$$a_{H_2O} \approx 1,\ \ a_{SiO_2} \approx 1,\ \ a_{H_4SiO_4} \approx \phi_{Si}. \tag{8.45}$$

Under the natural conditions of sedimentation, the dissolution rate constant $k_+$ and precipitation rate constant $k_-$ change with temperature $T$. Based on Rimstidt and Barnes' (1980) theory, we have $k_+ \sim 2.0 \times 10^{-9}\,\mathrm{mol\,m^2\,s^{-1}}$ (at 300 K) to $59 \times 10^{-6}\,\mathrm{mol\,m^2\,s^{-1}}$ (at 600 K); $k_- \sim 1.5 \times 10^{-4}\,\mathrm{mol\,m^2\,s^{-1}}$ (at 300 K) to $8.0 \times 10^{-4}\,\mathrm{mol\,m^2\,s^{-1}}$ (at 600 K).

### 8.2.4 Compaction relation

Now the total strain rate $\dot{\varepsilon}_{ij}$

$$\dot{\varepsilon}_{ij} = \frac{1}{2}(\frac{\partial u_i^s}{\partial x_j} + \frac{\partial u_j^s}{\partial x_i}), \tag{8.46}$$

in the sediments is considered to be partly elastic $\dot{\varepsilon}_{ij}^e$ and partly viscous $\dot{\varepsilon}_{ij}^v$

$$\dot{\varepsilon}_{ij} = \dot{\varepsilon}_{ij}^e + \dot{\varepsilon}_{ij}^v, \tag{8.47}$$

whose Maxwell formulations are in the following form

$$\nabla.\mathbf{u}^s = \frac{1}{(1-\phi)p_e'(\phi)}\frac{dp_e}{dt_s}(\text{elastic}) - \gamma(\phi,T)p_e(\text{viscous}), \tag{8.48}$$

or

$$\dot{\varepsilon}_{kk} = g(\phi)\frac{d\sigma_{kk}^e}{dt_s} - \gamma(\phi,T)\sigma_{kk}^e, \tag{8.49}$$

where $g(\phi)$ is a known function of $\phi$. We also have used equations (8.16), (8.14) and Athy-type law $p_e = p_e(\phi)$, $p_e'(\phi) < 0$.

$$\gamma(\phi,T) = (\frac{\phi}{\phi_0})^n \frac{\alpha\nu_m c_0 D_0 w}{RT_0\rho_s\bar{d}^3}(1 - \frac{T-T_0}{T_0})e^{(T-T_0)\frac{H_{cd}}{RT_0^2}}. \tag{8.50}$$

where $T_0$ is the surface temperature at the top of basin. $H_{cd}$ is an effective activation energy (Augevine & Turcotte, 1983). For convenience in the following discussion, we will prescribe the temperature distribution.

In principle, we can write a generalized Jaumann-type relation in a corotational frame of reference for (8.49) by considering the coordinate objectivity (Fowler & Noon 1995; Khan & Huang 1995). For simplicity and clarity in the following analysis of the effect of pressure solution creep, now we will mainly focus on the purely viscous compaction and use the following compaction relation

$$p_e = -\xi \nabla . \mathbf{u}^s, \tag{8.51}$$

which was first used by Birchwood & Turcotte (1994) to present a unified approach to geopressuring, low permeability zone formation and secondary porosity generation due to pressure solution in sedimentary basins.

## 8.3 1-D model and Non-dimensionalization

### 8.3.1 1-D model

For simplicity, we let $a = 0$ and $\sigma = \sigma_3^e$ be the averaged effective stress ($z-$component). The 1-D model equations then become

$$\frac{\partial(1-\phi)}{\partial t} + \frac{\partial[(1-\phi)u^s]}{\partial z} = (-r_m - r_+ + r_-)\frac{M_m}{\rho_m}, \tag{8.52}$$

$$\frac{\partial(\phi - \phi_{Si})}{\partial t} + \frac{\partial[(\phi - \phi_{Si})u^l]}{\partial z} = 0, \tag{8.53}$$

$$\frac{\partial \phi_{Si}}{\partial t} - \frac{\partial}{\partial z}(D\frac{\partial \phi_{Si}}{\partial z} - u^l \phi_{Si}) = (r_m + r_+ - r_-)\frac{M_{Si}}{\rho_l}, \tag{8.54}$$

$$\phi(u^l - u^s) = -\frac{k}{\mu}(\frac{\partial p}{\partial z} + \rho_l g), \tag{8.55}$$

$$\frac{\partial \sigma}{\partial z} - [\rho_s(1-\phi) + \rho_l \phi]g = 0, \tag{8.56}$$

$$\frac{\partial u^s}{\partial z} = \gamma(\phi, T)\sigma. \tag{8.57}$$

where $\gamma(\phi, T)$ is a function of porosity $\phi$ and temperature $T$.

Now we have 6 equations for 6 unknown variables: two for porosity $\phi$ and $\phi_{Si}$, two for velocities $u^s$, $u^l$, two for effective stress $\sigma$ and pore water pressure $p$. The boundary conditions are

$$\sigma = 0,\ p = 0,\ \phi = \phi_0,\ \phi_{Si} = \bar{\phi}_{Si},\ \text{at}\ z = h(t), \tag{8.58}$$

$$u^s = 0,\quad u^l = 0 \quad \text{at}\ z = b, \tag{8.59}$$

$$\dot{h}(t) = \dot{m}_s + u^s. \tag{8.60}$$

### 8.3.2 Non-dimensionalization

We scale the effective pressure $-\sigma$ with $(\rho_s - \rho_l)gd$

$$-\sigma = (\rho_s - \rho_l)gd\tilde{p}, \tag{8.61}$$

so that $\tilde{p} = O(1)$). We will define the length scale $d$ by equation (8.72). We also scale pore pressure $p$ with $(\rho_s - \rho_l)gd$, permeability $k$ with $k_0$, time $t$ with $d/\dot{m}_s$, $z$ with $d$, $k_+$ with $k_+^0$, $k_-$ with $k_-^0$, $\phi_{Si}$ with $\bar{\phi}_{Si}$ and putting

$$T = T_0 + \frac{q_0 d}{K_0}\Theta, \tag{8.62}$$

then the dimensionless model becomes

*Conservation of mass*

$$\frac{\partial(1-\phi)}{\partial t} + \frac{\partial[(1-\phi)u^s]}{\partial z} = -A\Gamma\tilde{\gamma}\tilde{p} - a_1(\mathcal{R}_+\tilde{r}_+ - \mathcal{R}_-\tilde{r}_-), \tag{8.63}$$

$$\frac{\partial(\phi - \epsilon\phi_{Si})}{\partial t} + \frac{\partial[(\phi - \epsilon\phi_{Si})u^l]}{\partial z} = 0, \tag{8.64}$$

$$\frac{\partial\phi_{Si}}{\partial t} - \frac{1}{Pe}\frac{\partial}{\partial z}(\tilde{D}\frac{\partial\phi_{Si}}{\partial z} - u^l\phi_{Si}) = \frac{1}{\epsilon a_1}[A\Gamma\tilde{\gamma}\tilde{p} + a_1(\mathcal{R}_+\tilde{r}_+ - \mathcal{R}_-\tilde{r}_-)], \tag{8.65}$$

*Darcy's law*

$$\phi(u^l - u^s) = -\lambda\tilde{k}(\frac{\partial p}{\partial z} + r), \tag{8.66}$$

*Force balance*

$$\frac{\partial}{\partial z}(-\tilde{p} - p) - (1 + r) + \phi = 0, \tag{8.67}$$

*compaction relation*

$$\frac{\partial u^s}{\partial z} = -\Gamma\tilde{\gamma}\tilde{p}, \tag{8.68}$$

where

$$\lambda = \frac{k_0(\rho_s - \rho_l)g}{\mu\dot{m}_s}, \quad \Gamma = \frac{\alpha\nu_m c_0 D_0 w(\rho_s - \rho_l)gd^2}{RT_0\rho_s\bar{d}^3\dot{m}_s}, \tag{8.69}$$

$$\tilde{\gamma} = (\frac{\phi}{\phi_0})^n(1-\beta_1\Theta)e^{\beta_m\Theta}, \quad \tilde{k} = (\frac{\phi}{\phi_0})^m, \quad \tilde{D} = e^{\beta_m\Theta},$$

$$\beta_m = \frac{H_{cd}q_0 d}{RK_0T_0^2}, \quad \beta_1 = \frac{q_0 d}{K_0T_0}, \quad A = \frac{4\pi A_0}{\alpha}, \quad a_1 = \frac{M_m\rho_l}{\rho_m M_{Si}}, \tag{8.70}$$

$$\mathcal{R}_+ = \frac{k_+^0 d}{\dot{m}_s}, \quad \mathcal{R}_- = \frac{k_-^0 d}{\dot{m}_s}, \quad Pe = \frac{\dot{m}_s d\tau_D^2}{D_0}, \quad r = \frac{\rho_l}{\rho_s - \rho_l},$$

$$\tilde{r}_+ = e^{\beta_+\Theta}(1-\phi),\ \tilde{r}_- = e^{\beta_-\Theta}\phi_{Si},\ \beta_+ = \frac{E_+ q_0 d}{K_0RT_0^2},\ \beta_- = \frac{E_- q_0 d}{K_0RT_0^2}, \tag{8.71}$$

and $\epsilon = \bar{\phi}_{Si} \sim 6\times10^{-6} \ll 1$ is the quartz solubility in the pore fluid. Now we can define a length scale $d$ by setting $\Gamma = 1$

$$d = \sqrt{\frac{RT_0\rho_s\bar{d}^3\dot{m}_s}{\alpha\nu_m c_0 D_0 w(\rho_s - \rho_l)g}}, \tag{8.72}$$

The related boundary conditions become

$$\tilde{p} = 0,\ \ \phi = \phi_0,\ \ \phi_{Si} = \phi_{Si}^0,\ \ \text{at}\ \ z = h(t), \tag{8.73}$$

$$u^s = u^l = 0, \quad \text{at}\ \ z = 0, \tag{8.74}$$

$$\dot{h}(t) = \dot{m}_s + u^s. \tag{8.75}$$

### 8.3.3 Values of parameters

By using the typical values of $\rho_l \sim 10^3\,\mathrm{kg\,m^{-3}}$, $\rho_s \sim 2.5\times10^3\,\mathrm{kg\,m^{-3}}$, $k_0 \sim 10^{-18}\mathrm{m}^2$, $\mu \sim 10^{-3}\,\mathrm{N\,s\,m^2}$, $\bar{d} \sim 10^{-4}\,\mathrm{m}$, $R \sim 8.31\,\mathrm{J\,mol^{-1}\,K^{-1}}$, $\nu_m \sim 2\times10^{-5}\,\mathrm{m^3\,mol^{-1}}$, $\alpha \sim 16$, $H_{cd} \sim 3\,\mathrm{kcal\,mol^{-1}}$, $T_0 \sim 300\,\mathrm{K}$, $c_0 \sim 10^{-4}\,\mathrm{M}$, $w_0 D_{gb} \sim 1\times10^{-19}\,\mathrm{m^3\,s^{-1}}$ (Rutter, 1976; Gratz, 1991; Birchwood & Turcotte, 1994; H. Ockendon & J. R. Ockendon, 1995), $G_0 \sim 1\times10^{-7}\,\mathrm{Pa}$, $\nu \sim 0.2$, $d \sim 900m\,\mathrm{m}$, $\dot{m}_s \sim 10^{-11}\,\mathrm{m\,s^{-1}}$, $k_+^0 \sim 10^{-15}\,\mathrm{mol\,m^2\,s^{-1}}$, $k_-^0 \sim 5\times10^{-15}\,\mathrm{mol\,m^2\,s^{-1}}$, $E_+ \sim 51.4\,\mathrm{kJ\,mol^{-1}}$, $E_- \sim 34.3\,\mathrm{kJ\,mol^{-1}}$, then we have

$$\lambda \approx 1, \qquad \Gamma \approx 1, \qquad Pe \approx 30, \qquad r \approx 0.6, \tag{8.76}$$

$$\beta_m \approx 0.2, \qquad \beta_1 \approx 0.1, \qquad m = 8, \qquad n = 2, \qquad a_1 \approx 0.4, \tag{8.77}$$

$$\mathcal{R}_+ \approx 0.1, \qquad \mathcal{R}_- \approx 0.5, \qquad \beta_+ \approx 1.5, \qquad \beta_- \approx 1, \qquad A \approx 0.8, \tag{8.78}$$

where we have used $M_m = M_{Si}$ and $|q_0/K_0| = 30^o$ C/km (thermal gradient).

### 8.3.4 Effect of transport

Because $\epsilon \ll 1$, the pseudo-steady state theory applies, this means that

$$A\Gamma\tilde{\gamma}\tilde{p} + a_1(\mathcal{R}_+\tilde{r}_+ - \mathcal{R}_-\tilde{r}_-) = O(\epsilon) \approx 0, \tag{8.79}$$

which is an algebraic equation for $\phi_{Si}$ in terms of $\tilde{p}$, $\Theta$ and $\phi$, i.e. $\phi_{Si} = \phi_{Si}(\tilde{p}, \Theta, \phi)$.

Adding the first three equations (of mass conservation), we have

$$\frac{\partial[u^s + \phi(u^l - u^s)]}{\partial z} = \frac{\epsilon}{Pe}\frac{\partial}{\partial z}(\tilde{D}\frac{\partial \phi_{Si}}{\partial z}) + (\frac{1}{a_1} - 1)O(\epsilon), \tag{8.80}$$

which implies that the effect of diffusion is only significant in a characteristic diffusion length $d_D$

$$d_D = \sqrt{\frac{\epsilon}{Pe}}d, \tag{8.81}$$

which is approximately 0.4 m. The diffusion length $d_D \ll d$ shows that reprecipitation essentially occurs *locally*, and the effect of long-distance transport is negligible in the natural sedimentation environment. Furthermore, $\epsilon \ll 1$ implies that $\phi - \epsilon\phi_{Si} \approx \phi$. The *locality* of reprecipitation of the dissolved species by pressure solution enables us to model the process by using the reduced equations

$$\frac{\partial(1-\phi)}{\partial t} + \frac{\partial[(1-\phi)u^s]}{\partial z} = 0, \tag{8.82}$$

$$\frac{\partial \phi}{\partial t} + \frac{\partial(\phi u^l)}{\partial z} = 0, \tag{8.83}$$

Adding these two equations and integrating, we have $u^s = -\phi(u^l - u^s)$ in a barycentric frame. Solving pore fluid pressure $p$ from the force balance equation, and substituting into Darcy's law, then we have only three coupled governing equations left in the model. They are

$$\frac{\partial(1-\phi)}{\partial t} + \frac{\partial[(1-\phi)u^s]}{\partial z} = 0, \tag{8.84}$$

$$u^s = -\lambda\tilde{k}[\frac{\partial\tilde{p}}{\partial z} + (1-\phi)]. \tag{8.85}$$

$$\frac{\partial u^s}{\partial z} = -\Gamma\tilde{\gamma}\tilde{p}, \tag{8.86}$$

which are essentially the equations given by Birchwood & Turcotte (1994). The related boundary conditions become

$$\tilde{p} = 0, \;\; \phi = \phi_0, \;\; \text{at} \;\; z = h(t), \tag{8.87}$$

$$u^s = 0, \quad \text{at} \;\; z = 0, \tag{8.88}$$

$$\dot{h}(t) = \dot{m}_s - \lambda\tilde{k}[\frac{\partial\tilde{p}}{\partial z} + (1-\phi)]. \tag{8.89}$$

## 8.4 Viscous Compaction

If we put $\Xi = 1/\Gamma$, $\tilde{\xi}\tilde{f} = 1/\tilde{\gamma}$, then the governing equations become

$$\frac{\partial(1-\phi)}{\partial t} + \frac{\partial[(1-\phi)u^s]}{\partial z} = 0, \tag{8.90}$$

$$u^s = -\lambda\tilde{k}[\frac{\partial\tilde{p}}{\partial z} + (1-\phi)]. \tag{8.91}$$

$$\tilde{p} = -\Xi\tilde{\xi}\tilde{f}\frac{\partial u^s}{\partial z}, \tag{8.92}$$

where $\tilde{\xi}$ is porosity-dependent and $\tilde{f}$ is temperature-dependent. i.e.

$$\tilde{\xi} = (\frac{\phi}{\phi_0})^{-n}, \tag{8.93}$$

$$\tilde{f} = (1 + \beta_1\Theta)e^{-\beta_m\Theta}. \tag{8.94}$$

Eliminating $\tilde{p}$, the governing equations become

$$\frac{\partial\phi}{\partial t} = \frac{\partial[(1-\phi)u^s]}{\partial z}, \tag{8.95}$$

$$u^s = \lambda\tilde{k}[\Xi\frac{\partial}{\partial z}(\tilde{\xi}\tilde{f}\frac{\partial u^s}{\partial z}) - (1-\phi)]. \tag{8.96}$$

Now the boundary conditions are

$$\frac{\partial u^s}{\partial z} = 0, \;\; \phi = \phi_0, \;\; \text{at} \;\; z = h(t), \tag{8.97}$$

$$u^s = 0, \quad \text{at} \;\; z = b, \tag{8.98}$$

$$\dot{h}(t) = \dot{m}_s + u^s. \tag{8.99}$$

This problem is very difficult to analyse. In the rest of this chapter, we will mainly solve it numerically and give some asymptotic analysis when it is possible to do so.

## 8.5 Numerical Results and Analysis of Viscous Compaction

From the governing equations and their boundary conditions, we understand that the physical model suggests that $\lambda$, $\Xi$, $\tilde{k}$, $\tilde{f}$ are all positive, $\phi \geq 0$, $\tilde{p} \geq 0$ and $u^s \leq 0$. The non-negativeness of $\tilde{p}$ implies

$$\frac{\partial u^s}{\partial z} \leq 0, \tag{8.100}$$

which means $u^s$ monotonically decreases as $z$ increases. Thus, $u^s$ reaches its minimum $u_0 = u^s(z = h)$ at $z = h$ and its maximum $u^s = 0$ at $z = 0$.

It is seen that the coupling of the temperature $\Theta$ with $\phi$, $u^s$ in the governing equations appears in the form $(1 + \beta_1\Theta)\exp(-\beta_m\Theta)$ which complicates the analysis. In order to separate the effect of temperature change from that of viscous compaction with a constant temperature distribution, and to compare with the existing results, we will mainly discuss viscous compaction without temperature change ($\beta_m = \beta_1 = 0$ or $\tilde{f} = 1$). These simplifications are in fact reasonable since $\beta_m \approx 0.2 \ll 1$ and $\beta_1 \approx 0.1 \ll 1$.

### 8.5.1 Slow compaction $\lambda << 1$ with $\Xi = O(1)$

The numerical results for the case of small $\lambda$ is shown in Fig. 8.2. A boundary layer clearly occurs at the basement.

For the case of $\lambda << 1$, we can expect that $u^s = O(\lambda) << 1$ since $\tilde{k} = O(1)$, this implies that $\dot{\phi} = O(\lambda)$ or $\phi \approx \phi_0$ and thus $\tilde{k} \approx 1$, $\tilde{\xi} \approx 1$ which are in line with the numerical results. With these simplifications, the model equations become approximately

$$\phi_t = (1 - \phi_0)u^s_z, \tag{8.101}$$

$$\lambda\Xi u^s_{zz} - u^s = \lambda(1 - \phi_0). \tag{8.102}$$

The outer solutions are $\phi = \phi_0$, $u^s = -\lambda(1 - \phi_0)$, and there is a boundary layer at the base, for which the effective boundary conditions can be written as

$$u^s_z \to 0, \quad \phi \to \phi_0, \quad \text{as} \quad z \to \infty, \tag{8.103}$$

$$u^s = 0, \quad \text{at} \quad z = 0. \tag{8.104}$$

The solution for equation (8.102) can be easily written as

$$u^s = \lambda(1-\phi_0)[e^{-\frac{z}{\sqrt{\lambda\Xi}}} - 1]. \tag{8.105}$$

Substituting this solution into (8.101), the solution for $\phi$ is approximately

$$\phi = \phi_0 - (1-\phi_0)^2\sqrt{\frac{\lambda}{\Xi}}te^{-\frac{z}{\sqrt{\lambda\Xi}}}, \tag{8.106}$$

and

$$\dot{h} \approx 1 - \lambda(1-\phi_0). \tag{8.107}$$

We see that a boundary layer is developed at the base with a thickness of the order of $\sqrt{\lambda\Xi}$. The comparison with numerical results shows good agreement (Fig. 8.2).

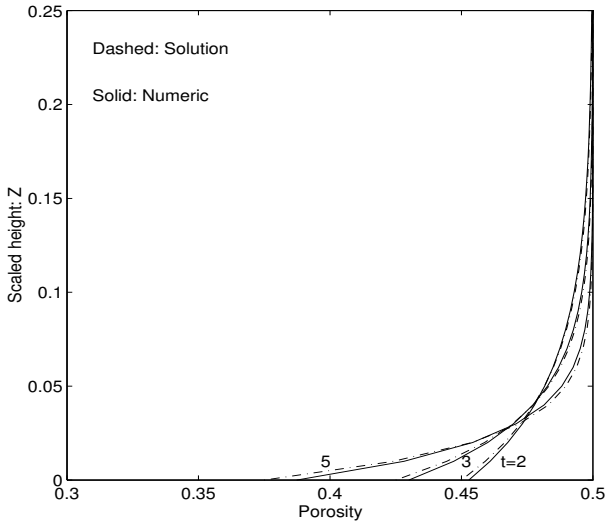


Figure 8.2 Comparison of solutions (as dashed curves) in the boundary layer with numerical results (as solid curves) in the case of slow creep ($\lambda \ll 1$) for $t = 2, 3, 5$. $Z$ is the scaled height $z/h(t)$.

### 8.5.2 Fast compaction $\lambda >> 1$ with $\Xi = O(1)$

#### Numerical Solutions

The numerical solutions for $\lambda = 100$ at different times ($t = 1, 2, 3, 5, 8$) are shown in Figures 8.3-5.

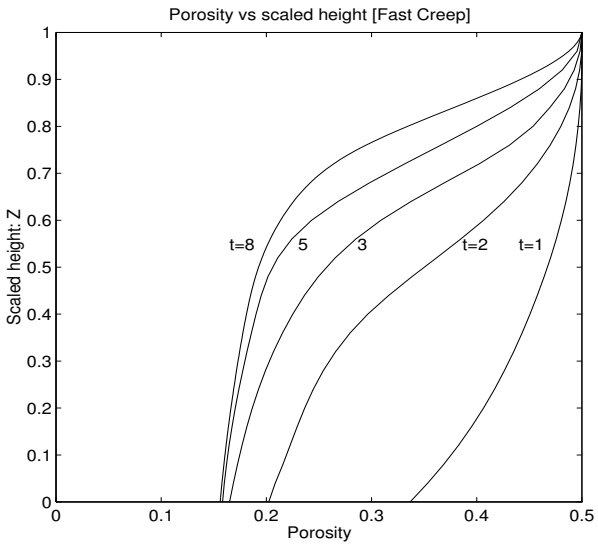


Figure 8.3 Porosity profile versus scaled height $Z = z/h(t)$ at different times ($t = 1, 2, 3, 5, 8$).

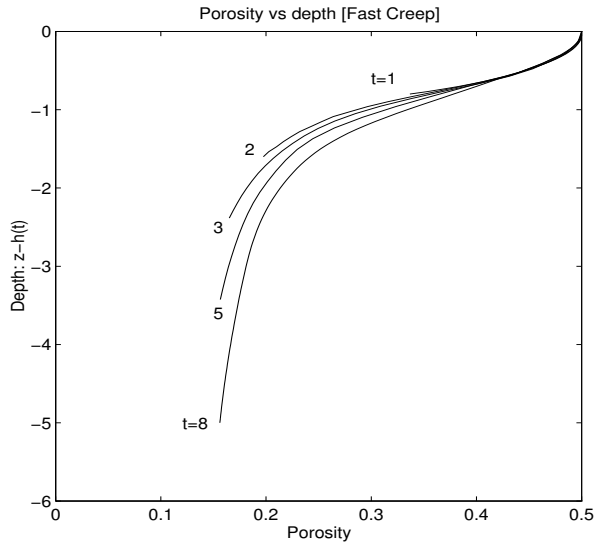


Figure 8.4 Porosity profile versus depth $z - h(t)$ at different times ($t = 1, 2, 3, 5, 8$)

From Fig. 8.3 and Fig. 8.4, we can clearly see that the porosity profile is nearly in a parabolic shape in the region near the top, and moves as time $t$ increases, which suggests that there exists a travelling wave solution in the top region (Fig. 8.4). On the other hand, the solutions at longer times suggest a different feature below the transition region where the compaction becomes permeability-controlled as the porosity decreases so that $\lambda\tilde{k} << 1$.

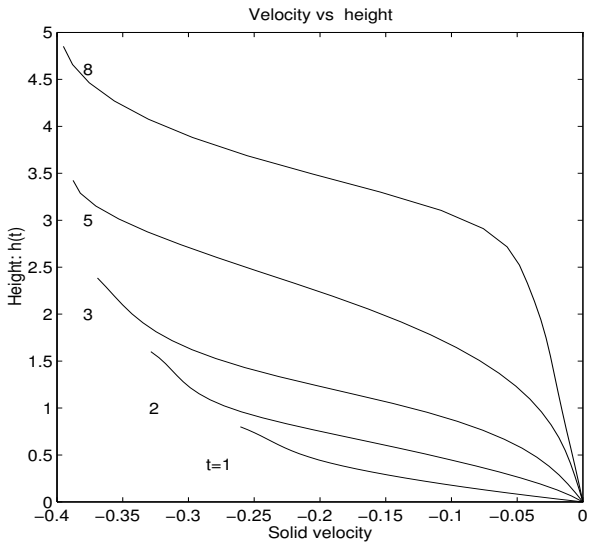


Figure 8.5 Velocity profile versus height $h(t)$ at different times ($t = 1, 2, 3, 5, 8$).

Figure 8.5 shows the velocity profile at different times, and this profile suggests that the velocity at the top tends to be a constant as $t$ increases. In other words, this means that $\dot{h} = \dot{m}_s + u^s$ becomes nearly constant.

### Poro-elastic compaction versus viscous creep

To study the behaviour of creeping compaction, it is helpful to compare numerical solutions with the counterparts for poro-elastic compaction. Figure 8.6 shows such a comparison with values of $\lambda = 100$ and $t = 5$.

It is clearly seen that poro-elastic compaction behaves differently from viscous compaction in the top region in that the former decreases more rapidly than the latter, but they behave in a similar way in the lower region. This is because the high permeability near the top will enable poro-elastic compaction to proceed rapidly, leading to a nearly exponentially decreasing porosity profile in the top region, but the low effective pressure near the surface will only make viscous creep proceed slowly, resulting in a nearly parabolic profile of porosity evolution at the top region. On the other hand, the porosity decreases to values lower than the critical value $\phi^*$ below the transition region, where the permeability is low enough (i.e. $\lambda\tilde{k} \ll 1$) to retard the compaction or creep process, so that both processes essentially become *permeability-*

*controlled*, resulting in a similar profile in the lower region.

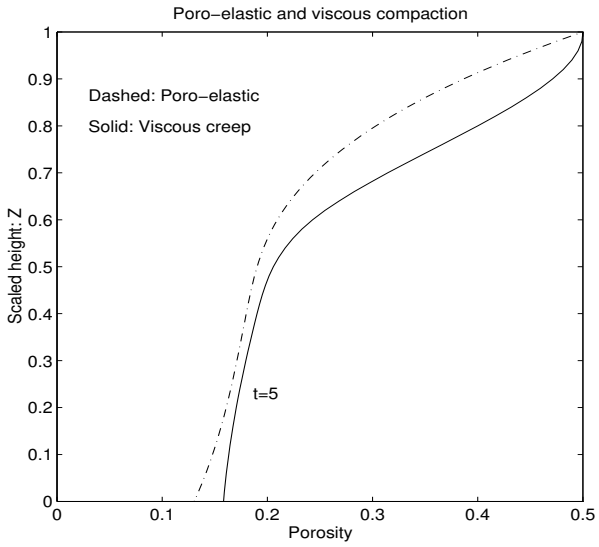


Figure 8.6 Comparison of poro-elastic compaction (dashed) with viscous compaction (solid) for $\lambda = 100$) at $t = 5$. Here we have choosed the parameter values in equation (8.72) in such a way that the length scale defined by (8.72) is equal to the length scale defined by (2.48) in the poroelastic compaction. We then can make the comparison with the same length scale. The choice of other combination of the parameter values in (8.72) will make the two curves look very different in this figure.

### 8.5.3 Analysis for $\lambda >> 1$

From the governing equations (8.95) and (8.96), we see that $\lambda\tilde{k}$ appears always as a combination. Because $\tilde{k}$ decreases dramatically as $\phi$ decreases, we can expect that the value of $\phi$ when $\lambda\tilde{k} = 1$, or

$$\phi = \phi^* = \phi_0 e^{-\frac{\ln\lambda}{m}}, \tag{8.108}$$

will define a transition as in chapter 4.

Since $\lambda\tilde{k} >> 1$ holds in the top region, then we have

$$1 - \phi \approx \Xi\frac{\partial}{\partial z}(\tilde{\xi}\frac{\partial u^s}{\partial z}). \tag{8.109}$$

Substituting this into equation (8.90) and interchanging $t$ and $z$ in differentiations,

we have

$$\frac{\partial}{\partial z}[\frac{\partial}{\partial t}(\tilde{\xi}\frac{\partial u^s}{\partial z}) + u^s\frac{\partial}{\partial z}(\tilde{\xi}\frac{\partial u^s}{\partial z})] = 0. \tag{8.110}$$

Rewriting the boundary condition $u^s_z = 0$ at the top by multiplying by $\tilde{\xi}$ and differentiating with respect to $t$, we have

$$\frac{\partial}{\partial t}(\tilde{\xi}\frac{\partial u^s}{\partial z}) + \dot{h}\frac{\partial}{\partial z}(\tilde{\xi}\frac{\partial u^s}{\partial z}) = 0. \tag{8.111}$$

Using this relation and integrating equation (8.110), we obtain

$$\frac{\partial}{\partial t}(\tilde{\xi}\frac{\partial u^s}{\partial z}) + u^s\frac{\partial}{\partial z}(\tilde{\xi}\frac{\partial u^s}{\partial z}) = -\frac{\dot{m}_s(1-\phi_0)}{\Xi}. \tag{8.112}$$

Let $p = \tilde{p}$, $u = u^s$, and for simplicity choose $\tilde{\xi} = 1$, then we have the following equations

$$p_t + up_z = \dot{m}_s(1-\phi_0), \tag{8.113}$$

$$p = -\Xi u_z. \tag{8.114}$$

The boundary conditions are

$$p = 0 \quad \text{at} \quad z = h(t), \tag{8.115}$$

and

$$u = 0 \quad \text{at} \quad z = 0. \tag{8.116}$$

The characteristics of (8.113) are

$$\dot{z} = u \quad \text{and} \quad \dot{p} = \dot{m}_s(1-\phi_0), \tag{8.117}$$

The boundary condition (8.115) can be written as

$$t = \tau, \;\; z = h(\tau), \;\; p = 0. \tag{8.118}$$

By integration, we have

$$p = \dot{m}_s(1-\phi_0)(t-\tau), \tag{8.119}$$

$$z = \int_\tau^t u(s,\tau)ds + h(\tau), \tag{8.120}$$

and

$$h = -\int_\tau^{t_b(\tau)} u(s,\tau)ds, \tag{8.121}$$

where $t_b(\tau)$ is the time $t$ at the basement $z = 0$.

Changing variables from $(t, z)$ to $(t', \tau)$ (in fact, $t' = t$), we get

$$u_z = \frac{1}{z_\tau} u_\tau \quad \text{and} \quad z_\tau = \dot{m}_s + \int_\tau^t u_\tau(s, \tau) ds. \tag{8.122}$$

Now we rewrite equation (8.114) as

$$\frac{\dot{m}_s(1-\phi_0)}{\Xi}(t-\tau) = \frac{-u_\tau}{\dot{m}_s + \int_\tau^t u_\tau(s,\tau)ds}, \tag{8.123}$$

whose integration leads to

$$\frac{\dot{m}_s(1-\phi_0)}{2\Xi}(t-\tau)^2 = -\ln[\frac{\dot{m}_s + \int_\tau^t u_\tau(s,\tau)ds}{\dot{m}_s}], \tag{8.124}$$

or

$$\int_\tau^t u_\tau(s,\tau)ds = \dot{m}_s[e^{-\frac{\dot{m}_s(1-\phi_0)}{2\Xi}(t-\tau)^2} - 1], \tag{8.125}$$

Differentiating with respect to $t$, then integrating $u_\tau$ with respect to $\tau$, and noticing that $f_t(t-\tau) = -f_\tau(t-\tau)$, we obtain

$$u = \dot{h} - \dot{m}_s e^{-\frac{\dot{m}_s(1-\phi_0)}{2\Xi}(t-\tau)^2}. \tag{8.126}$$

Using the boundary condition $u = 0$ at $z = 0$, we get an expression for $\dot{h}$:

$$0 = \dot{m}_s[1 - e^{-\frac{\dot{m}_s(1-\phi_0)}{2\Xi}(t_b(\tau)-\tau)^2}] + (\dot{h} - \dot{m}_s), \tag{8.127}$$

that is

$$\dot{h} = \dot{m}_s e^{-\frac{\dot{m}_s(1-\phi_0)}{2\Xi}(t_b(\tau)-\tau)^2}. \tag{8.128}$$

Substituting the solution (8.126) into equation (8.120), we have

$$-\int_\tau^t \{\dot{m}_s[1 - e^{-\frac{\dot{m}_s(1-\phi_0)}{2\Xi}(t-\tau)^2}] + (\dot{h}(t) - \dot{m}_s)\}dt = h(\tau) - z, \tag{8.129}$$

Changing variable $t = \tau + \sqrt{\frac{2\Xi}{\dot{m}_s(1-\phi_0)}}v$, the above equation becomes

$$\dot{m}_s\sqrt{\frac{2\Xi}{\dot{m}_s(1-\phi_0)}}\int_0^{\sqrt{\frac{\dot{m}_s(1-\phi_0)}{2\Xi}}(t-\tau)} e^{-v^2}dv - [h(t) - h(\tau)] = h(\tau) - z. \tag{8.130}$$

or

$$h(t) - z = \sqrt{\frac{\Xi\dot{m}_s\pi}{2(1-\phi_0)}}\,\mathrm{erf}[\sqrt{\frac{\dot{m}_s(1-\phi_0)}{2\Xi}}(t-\tau)]. \tag{8.131}$$

Here, we see that $h - z \to \sqrt{\frac{\Xi\dot{m}_s\pi}{2(1-\phi_0)}}$ as $t - \tau \to \infty$.

It is clearly seen that $u^s$ and $p$ are only functions of $h(t) - z$, which implies that $\phi$ is also a function of $h - z$. The equation of conservation of mass then becomes

$$\dot{h}\phi' + [(1-\phi)u]' = 0. \tag{8.132}$$

Integrating this equation (8.132) and using the boundary conditions at $z = h$, we have

$$\dot{h}\phi + (1-\phi)u^s = \dot{h}\phi_0 + (1-\phi_0)(\dot{h} - \dot{m}_s), \tag{8.133}$$

or

$$(1-\phi)(\dot{h} - u) = \dot{m}_s(1-\phi_0), \tag{8.134}$$

Substituting solution (8.126) into this equation, we have

$$\phi = 1 - (1-\phi_0)e^{\frac{\dot{m}_s(1-\phi_0)}{2\Xi}(t-\tau)^2}. \tag{8.135}$$

To find the solution for $h(t)$, we rewrite equation (8.128) in terms of $s_b = t_b - \tau$ as

$$\dot{h} = \dot{m}_s e^{-\frac{\dot{m}_s(1-\phi_0)}{2\Xi}s_b^2}. \tag{8.136}$$

When $z = 0$, equation (8.131) becomes

$$h(t) = \sqrt{\frac{\Xi\dot{m}_s\pi}{2(1-\phi_0)}}\,\mathrm{erf}[\sqrt{\frac{\dot{m}_s(1-\phi_0)}{2\Xi}}s_b]. \tag{8.137}$$

Differentiating this equation with respect to $s_b$, we have

$$\frac{dh}{ds_b} = \dot{m}_s e^{-\frac{\dot{m}_s(1-\phi_0)}{2\Xi}s_b^2}. \tag{8.138}$$

Combining this with equation (8.136) implies that

$$\frac{ds_b}{dt} = 1, \tag{8.139}$$

which means $s_b = t$ by using the initial condition $s_b = 0$ when $t = 0$. Now we have

$$h(t) = \sqrt{\frac{\Xi\dot{m}_s\pi}{2(1-\phi_0)}}\,\mathrm{erf}[\sqrt{\frac{\dot{m}_s(1-\phi_0)}{2\Xi}}t]. \tag{8.140}$$

From these solutions, we can calculate the time $t^*$ when the porosity decreases to the typical transition value of $\phi^*$,

$$t^* = \sqrt{\frac{2\Xi}{\dot{m}_s(1-\phi_0)}\ln(\frac{1-\phi^*}{1-\phi_0})}, \tag{8.141}$$

and $h(t^*) = \Pi_0$,

$$\Pi_0 = \sqrt{\frac{\Xi \dot{m}_s \pi}{2(1-\phi_0)}} \mathrm{erf}(\sqrt{\ln(\frac{1-\phi^*}{1-\phi^0})}). \tag{8.142}$$

The typical value of $\dot{h}$ at the transition is

$$\dot{h} = \dot{m}_s \frac{1-\phi_0}{1-\phi^*}. \tag{8.143}$$

The values of solid velocity $u^*$ and effective pressure $p^*$ at the transition are respectively

$$u^* = \dot{h} - \frac{\dot{m}_s(1-\phi_0)}{1-\phi^*}, \tag{8.144}$$

and

$$p^* = \dot{m}_s(1-\phi_0)\sqrt{\frac{2\Xi}{\dot{m}_s(1-\phi_0)} \ln(\frac{1-\phi^*}{1-\phi_0})}. \tag{8.145}$$

It is clearly seen that the above solutions are only valid in the top region with a depth of $\Pi_0$. Below this region, the approximation is invalid, and we may expect a transition region which joins the regions where $\phi > \phi^*$ and $\phi < \phi^*$.

In the outer region just above this transition layer as $h - z \to \Pi_0$, we can write the solutions approximately as

$$\begin{aligned} \phi &\sim \phi^* + \phi^{*'}(z - h + \Pi_0), \\ u &\sim u^* - \frac{p^*}{\Xi}(z - h + \Pi_0), \\ p &\sim p^* - (1-\phi^*)(z - h + \Pi_)), \end{aligned} \tag{8.146}$$

where we have used $u_z = -p/\Xi$ and $p_z = -(1-\phi)$. $\phi^{*'}$ is a constant which is now determined. Using $\phi(h - \Pi_0, t) = \phi^*$ and mass conservation, we have

$$\phi_t + \phi_z \dot{h} = 0 \quad \text{at} \quad z = h - \Pi, \tag{8.147}$$

and

$$\phi_t = (1-\phi^*)u_z - u^*\phi_z \quad \text{at} \quad z = h - \Pi. \tag{8.148}$$

Combining these equations, we get

$$\phi_z \dot{h} + (1-\phi^*)u_z - u^*\phi_z = 0, \tag{8.149}$$

or

$$\phi_z = \frac{p^*(1-\phi^*)}{\Xi(\dot{h} - u^*)} \quad \text{at} \quad z = h - \Pi, \tag{8.150}$$

from which we can write $\phi^{*'}$ as

$$\phi^{*'} = \frac{p^*(1-\phi^*)}{\Xi \dot{m}_s}. \tag{8.151}$$

## Transition Layer

In the transition layer, we define $\gamma = \frac{\phi^{*'}}{\phi^*} = \frac{p^*(1-\phi^*)}{\Xi \dot{m}_s \phi^*}$, and put

$$z = h - \Pi_0 + B + \frac{\eta}{m}, \quad B << 1, \tag{8.152}$$

thus $\phi \sim \phi^* + \phi^{*'}(B + \frac{\eta}{m}) \sim \phi^* \exp[\gamma(B + \frac{\eta}{m})]$. Therefore, we define

$$\phi = \phi^* \exp[C + \frac{\Psi}{m}], \quad \text{and} \quad C = \gamma B, \tag{8.153}$$

whence it follows by a matching principle that $\Psi \sim \gamma\eta$ as $\eta \to \infty$.

Based on $u \sim u^* - \frac{p^*}{\Xi}(B + \frac{\eta}{m})$, we anticipate that $u^* - \frac{p^* B}{\Xi} \sim \frac{1}{m}$. Therefore, we put $u = \frac{W}{m}$, and we have

$$W \sim m(u^* - \frac{p^* B}{\Xi}) - \frac{p^*}{\Xi}\eta = W^* - \frac{p^*}{\Xi}\eta, \quad W^* = m(u^* - \frac{p^* B}{\Xi}), \tag{8.154}$$

as $\eta \to \infty$.

Using the relations $\partial_z = m\partial_\eta$, $\partial_t = \partial_t - m\dot{h}\partial_\eta$, the governing equations become

$$-\phi^* e^{C+\frac{\Psi}{m}}[\frac{1}{m}\Psi_t - \dot{h}\Psi_\eta] + (1 - \phi^* e^{C+\frac{\Psi}{m}})W_\eta - \frac{W}{m}\phi^* e^{C+\frac{\Psi}{m}}\Psi_\eta = 0, \tag{8.155}$$

$$\frac{W}{m} = -e^{mC+\Psi}[m\tilde{p}_\eta + (1 - \phi^* e^{C+\frac{\Psi}{m}})], \tag{8.156}$$

$$\tilde{p} = -\Xi W_\eta. \tag{8.157}$$

By choosing $C = -\frac{2}{m}\ln m$ to balance the terms in the above equations, we have the leading order approximations

$$\dot{h}\phi^*\Psi_\eta + (1-\phi^*)W_\eta = 0, \tag{8.158}$$

$$W = -e^{\Psi} p_\eta, \tag{8.159}$$

$$p = -\Xi W_\eta. \tag{8.160}$$

These equations are subject to the matching conditions

$$\Psi \sim \gamma\eta, \quad p \sim p^*, \quad W \sim W^* - \frac{p^*}{\Xi}\eta, \quad \text{as} \quad \eta \to \infty. \tag{8.161}$$

The last two equations give

$$W = \Xi W_{\eta\eta} e^{\Psi}. \tag{8.162}$$

Integrating the first equation and using the matching conditions, we have

$$\dot{h}\phi^*\Psi + (1-\phi^*)W = (1-\phi^*)(W^* - \frac{p^*}{\Xi}\eta) + \dot{h}\phi^*\gamma\eta = (1-\phi^*)W^*, \tag{8.163}$$

where we have used $\gamma = \frac{p^*(1-\phi_0)}{\Xi \dot{m}_s \phi^*} \approx \frac{p^*(1-\phi^*)}{\Xi\phi^*\dot{h}}$ and $u^* << 1$. Thus we have

$$W = W^* - \frac{\dot{h}\phi^*}{1-\phi^*}\Psi. \tag{8.164}$$

Combining this equation with (8.162), we finally have

$$\Xi\Psi_{\eta\eta} = (\Psi - \frac{(1-\phi^*)W^*}{\dot{h}\phi^*})e^{-\Psi}. \tag{8.165}$$

This is of the form of a nonlinear oscillator $\Xi\Psi_{\eta\eta} + V'(\Psi) = 0$ with the potential

$$V'(\Psi) = (K - \Psi)e^{-\Psi} \quad \text{and} \quad K = \frac{(1-\phi^*)W^*}{\dot{h}\phi^*}, \tag{8.166}$$

or

$$V = [\Psi - (K-1)]e^{-\Psi}, \tag{8.167}$$

which reaches its maximum at $\Psi = K$. The only trajectory which can match to a solution in $\eta < 0$ is the one with $\Psi \to K$ as $\eta \to -\infty$. Therefore, we define

$$\Psi_\infty = K = \frac{(1-\phi^*)W^*}{\dot{h}\phi^*}, \tag{8.168}$$

and we require $\Psi \to \Psi_\infty$ as $\eta \to -\infty$.

Now rewriting equation (8.165) in terms of $\Psi$ and $\eta$, we have

$$\Xi\Psi_{\eta\eta} + V'(\Psi) = 0, \tag{8.169}$$

with a matching condition $\Psi_\eta \sim \gamma$ as $\eta \to \infty$. Integrating this equation, we have

$$\frac{1}{2}\Psi_\eta^2 + V(\Psi) = \frac{1}{2}\Xi\gamma^2, \tag{8.170}$$

which is an energy equation. We also require $\Psi_\eta = 0$ when $V = K$, that is

$$\frac{1}{2}\Xi\gamma^2 = e^{-\Psi_\infty}. \tag{8.171}$$

This relation determines $\Psi_\infty$. Once we have $\Psi_\infty$, we can determine $W^*$ from (8.168). That is

$$W^* = \frac{\dot{h}\phi^*\Psi_\infty}{1-\phi^*}. \tag{8.172}$$

Combining (8.144) and (8.154), we have

$$\dot{h} = \dot{m}_s(\frac{1-\phi_0}{1-\phi^*}) - \frac{2p^*}{m\Xi\gamma}\ln m + \frac{W^*}{m}. \tag{8.173}$$

Substituting the expressions for $p^*$, $W^*$, we finally have

$$\dot{h} \approx \frac{\dot{m}_s(\frac{1-\phi_0}{1-\phi^*}) - \frac{2(1-\phi_0)\ln m}{m\Xi^2\dot{m}_s\phi^*}}{1-\frac{\phi^*\Psi_\infty}{m(1-\phi^*)}}, \tag{8.174}$$

which determines $\dot{h}$ and is valid for $t > t^*$ or $h > \Pi_0$. It is clearly seen that the leading order approximation of (8.174) is constant with (8.143) when $t = t^*$.

**Solution below the transition layer**

From the transition layer, we have $W, p \to 0$, $\Psi \to \Psi_\infty$ as $\eta \to -\infty$. Now going back to $z$ rather than $\eta$ and substituting $\eta = m[z - h - \Pi_0 - B]$ into the equations (8.155)-(8.157), we have

$$-\phi^* e^{C+\Psi/m}\Psi_t + (1-\phi^* e^{C+\Psi/m})W_z - \frac{W}{m}\phi^* e^{C+\Psi/m}\Psi_t = 0,$$

$$\frac{W}{m} = -\frac{1}{m^2}e^{\Psi}[p_z + (1-\phi^* e^{C+\Psi/m})]$$

$$p = -\frac{1}{m}\Xi W_z. \tag{8.175}$$

In order to balance the second and the third equations, we suppose that

$$W = \frac{1}{m}\hat{W}, \quad p = \frac{1}{m^2}\hat{p}, \quad \Psi = \Psi_\infty + \frac{1}{m}\hat{\Psi}. \tag{8.176}$$

Now the governing equations become approximately

$$-\phi^*\hat{\Psi}_t + (1-\phi^*)\hat{W}_z = 0,$$

$$\hat{W} = -e^{\Psi_\infty}(1-\phi^*),$$

$$\hat{p} = -\Xi\hat{W}_z. \tag{8.177}$$

By using the boundary conditions $\hat{W}$, $\hat{p}$, $\hat{\Psi} \to 0$ as $z \to h - \Pi_0 - \frac{2}{\gamma m} \ln m$, we can easily write the solutions for these three equations as

$$\hat{p} = \hat{\Psi} = 0, \quad \hat{W} = -e^{\Psi_\infty}(1 - \phi^*). \tag{8.178}$$

The fact that the constant $\hat{W}$ does not satisfy the boundary condition $\hat{W} = 0$ at the base $z = 0$ suggests that there should exist a boundary layer near the base although its thickness is only of the order of $O(\frac{1}{m})$.

**Boundary layer at $z = 0$**

In the boundary layer at $z = 0$, $\Psi \approx \Psi_\infty$, then we have approximately

$$u^s = (\frac{\phi_\infty}{\phi^*})^m[\Xi u^s_{zz} - (1 - \phi_\infty)], \quad \text{and} \quad \phi_\infty = \phi^* \exp[-\frac{2 \ln m}{m} + \frac{\Psi_\infty}{m}], \tag{8.179}$$

with a boundary condition

$$u^s = 0 \quad \text{at} \quad z = 0. \tag{8.180}$$

The outer solution is $u^s = -(\frac{\phi_\infty}{\phi^*})^m(1 - \phi_\infty)$, which implies a far field condition $u_z \to 0$ as $z \to \infty$. The solution is

$$u^s = (\frac{\phi_\infty}{\phi^*})^m(1 - \phi_\infty)[e^{-\frac{z}{\sqrt{(\frac{\phi_\infty}{\phi^*})^m \Xi}}} - 1]. \tag{8.181}$$

This completes the solution procedure.

**Comparisons**

The comparison of the solutions in the lower and upper regions (dashed) with numerical results is shown in Fig. 8.7 for the case of $\lambda = 100$ and $t = 5$. Figure 8.8 shows the comparison for the basin thickness $h(t)$. A reasonably good agreement verifies the validity of the solution procedure.

We see clearly that in the case of fast compaction ($\lambda >> 1$), compaction occurs throughout the basin, and the basic equilibrium solution near the surface is a near parabolic profile of porosity. However, as depth increases, the permeability has decreased sufficiently, and there is a narrower transition region which marks the sharp variation of permeability with porosity. More generally, we might therefore expect

that in a marine environment where stratigraphic layers cause sudden changes in permeability, that clay layers with small permeability may be associated with the formation of abnormally high pressures.

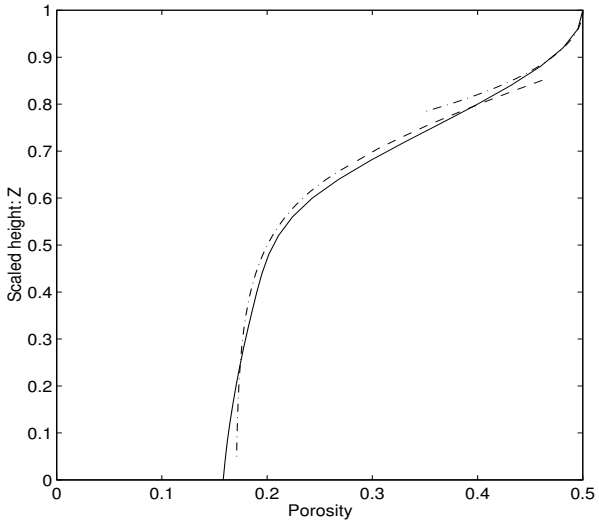


Figure 8.7 Comparison of travelling wave solution (8.135), and transition solution (8.170) (dashed) with the numerical results (solid) for $\lambda = 100$) at $t = 5$.

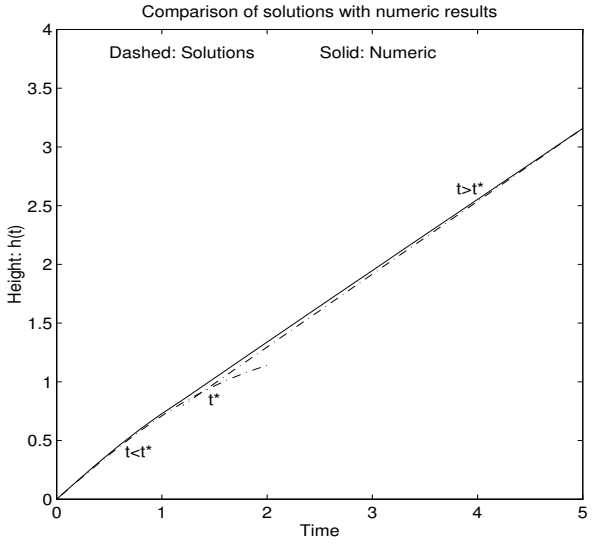


Figure 8.8 Comparison of short time solution (8.128) and large time solution (8.174) (dashed) with the numerical results (solid) for $\lambda = 100$) at $t \leq 5$. The two dashed curves joins at $t = t^*$ (or $h = \Pi_0$), and there is a jump $[\dot{h}]^{t^*+}_{t^*-} = O(\frac{\ln m}{m})$ which is relatively small.

### 8.5.4 Summary

For a model of sedimentary basin formation which incorporates viscous compaction due to pressure solution, we have been able to derive approximate solutions in the distinct limits of slow compaction ($\lambda \ll 1$) and fast compaction ($\lambda \gg 1$). When $\lambda \ll 1$, compaction is limited to a basal boundary layer of thickness $O(\sqrt{\lambda})$ (8.106). This result is similar to that which occurs for elastic compaction, and is equivalent to results obtained in viscous compaction in the asthenosphere (McKenzie 1984).

When $\lambda \gg 1$, compaction occurs throughout the basin, and the basic equilibrium solution (which we may call normally pressured, since the pore pressure increases hydrostatically) which applies near the surface is a near parabolic profile of porosity as a function of depth.

$$\phi \approx \phi_0 - \frac{(1-\phi_0)^2}{2\Xi \dot{m}_s}(h-z)^2, \tag{8.182}$$

this compares with the equilibrium elastic profile, which is exponentially decreasing with depth. However, this normally pressured solution is only valid to a depth $\Pi_0$, given by (8.142), and approximately

$$\Pi_0 \approx \left\{ \frac{2\Xi \dot{m}_s}{(1-\phi_0)} \ln\left(\frac{1-\phi^*}{1-\phi_0}\right) \right\}^{1/2}. \tag{8.183}$$

At this depth, the permeability has decreased sufficiently, and there is a narrower transition region which marks the sharp variation of permeability with porosity. Notice also that even if the permeability exponent is not large, so that $\phi^*$ is small ($\phi^* = \phi_0 \exp[-\frac{1}{m}\ln\lambda]$), nevertheless (8.183) implies that the critical depth is still finite. Thus the switch from normally pressured to abnormally pressured is predicted to occur in any case in a marine environment where stratigraphic layers cause sudden changes in permeability and the subsequent formation of abnormally high pressures.

At greater depths still, cementation begins to occur. As the grain boundaries begin to become cemented, pressure solution will decrease, and it can be expected that the rheology reverts to an elastic one; from the point of view of the sediments, compaction will cease and the medium will become virtually rigid, with pore pressure being controlled purely by Darcy flow. Incorporation of these and other processes such as diagenesis will form the substance of future developments.

# Chapter 9

# Conclusions

Conventional studies have treated compaction and diagenesis separately, and the experimentally derived nonlinear behaviour of soils is generally studied numerically and has never been investigated on a basin scale. One main novelty of the current research work, based on previous work (chapters 1-2), is to model compaction, thermal history (chapters 2-4), unloading (chapter 5), diagenetic (smectite-illite) reactions (chapters 6-7) and pressure solution creep (chapter 8) *simultaneously* in a compacting 3-D frame. Another novelty is that the nonlinear sediment behaviour including phenomena such as hysteresis is treated for the first time on a basin scale, and the basinwide response to the unloading from surface erosion is also investigated (chapter 5). The coupled partial differential equations with a free boundary are solved numerically, and analytical solutions are obtained for some geologically interesting cases such as rapid and slow sedimentations, diagenesis in the temperature range of hydrocarbon generations and basinal response to sediment erosion at the surface in a nearly equilibrium state. The well known Athy's law, derived from field data, can be easily obtained from our analytical solutions.

Based on the pseudo-steady state approximations, the transport-reaction model equations of compaction and diagenesis can be simply written in dimensionless form as

$$\frac{\partial(1-\phi)}{\partial t} + \frac{\partial[(1-\phi)u^s]}{\partial z} = 0, \quad \text{(Mass conservation)} \tag{9.1}$$

$$u^s = -\lambda\tilde{k}[\frac{\partial\tilde{p}}{\partial z} + (1-\phi)]. \quad \text{(Darcy's law)} \tag{9.2}$$

A *constitutive* relation is needed to complete this model. In the case of poro-elastic compaction, we use an Athy-type relation $\tilde{p} = \tilde{p}(\phi)$ (chapter 4); while in the case of viscous compaction due to pressure solution creep only, we choose $\tilde{p} = -\Xi(\frac{\phi}{\phi_0})^{-n}\frac{\partial u^s}{\partial z}$ (chapter 8). These two different rheological relations result in two quite different behaviours of porosity evolution. In the simpler poro-elastic case, we have a single non-linear diffusion equation for porosity $\phi$

$$\frac{\partial\phi}{\partial t} = \lambda\frac{\partial}{\partial z}\{\tilde{k}(1-\phi)^2[\frac{1}{\phi}\frac{\partial\phi}{\partial z} - 1]\} \tag{9.3}$$

$$\tilde{k} = (\phi/\phi_0)^m, \quad m = 8, \tag{9.4}$$

with a moving boundary described by

$$\dot{h} = 1 + \lambda\tilde{k}(1-\phi)[\frac{1}{\phi}\frac{\partial\phi}{\partial z} - 1], \tag{9.5}$$

and boundary conditions

$$\phi_z - \phi = 0 \text{ at } z = 0, \tag{9.6}$$

$$\phi = \phi_0 \text{ at } z = h, \tag{9.7}$$

The analysis in Chapter 4, which was further elaborated by Fowler & Yang (1997), showed that the limit $\lambda << 1$ (slow compaction) can be simply analysed by means of a boundary layer analysis at the sediment base. The more interesting mathematical case is when $\lambda >> 1$ (fast compaction). For sufficiently small times, the porosity profile is exponential with depth, corresponding to an equilibrium (long-time) profile. However, because of the large exponent $m$ in the permeability law $\tilde{k} = (\phi/\phi_0)^m$, we find that even if $\lambda >> 1$, the product $\lambda\tilde{k}$ may become small at sufficiently large depths. In this case, the porosity profile consists of an upper part near the surface where $\lambda\tilde{k} >> 1$ and the equilibrium is attained, and a lower part where $\lambda\tilde{k} << 1$, and the porosity is higher than equilibrium. Straightforward asymptotic methods are difficult to implement because the limit $m >> 1$ implies exponential asymptotics, but we use a hybrid method which appears to correspond accurately to numerical computations.

For the case of viscous compaction due to pressure solution creep, the equations can be simplified as, by taking $n = 0$,

$$-\frac{\partial \phi}{\partial t} + \frac{\partial}{\partial z}\left[(1-\phi)u\right] = 0,$$

$$u = -\lambda \tilde{k}\left[\frac{\partial p}{\partial z} + 1 - \phi\right],$$

$$p = -\Xi \frac{\partial u}{\partial z}, \tag{9.8}$$

whose boundary conditions are that

$$u = 0 \quad \text{on} \quad z = 0,$$

$$p = 0, \ \phi = \phi_0, \ \dot{h} = \dot{m}_s + u \quad \text{at} \quad z = h(t). \tag{9.9}$$

The analysis in Chapter 8, which was given in more detail by Fowler & Yang (1998), showed that for $\lambda \ll 1$, compaction is limited to a basal boundary layer of thickness $O(\sqrt{\lambda})$. This result is similar to that which occurs for elastic compaction, and is equivalent to results obtained in viscous compaction (McKenzie, 1984; Birchwood & Turcotte, 1994).

When $\lambda \gg 1$, compaction occurs throughout the basin, and the basic equilibrium solution (which we may call normally pressured, since the pore pressure increases hydrostatically) which applies near the surface is a near parabolic profile of porosity

$$\phi \approx \phi_0 - \frac{(1-\phi_0)^2}{2\Xi \dot{m}_s}(h-z)^2; \tag{9.10}$$

this compares with the equilibrium elastic profile, which is exponentially decreasing with depth.

However, this normally pressured solution is only valid to a depth $\Pi_0$, given by (8.142), and approximately

$$\Pi_0 \approx \left\{\frac{2\Xi \dot{m}_s}{(1-\phi_0)} \ln\left(\frac{1-\phi^*}{1-\phi_0}\right)\right\}^{1/2}. \tag{9.11}$$

At this depth, the permeability has decreased sufficiently that the hydrostatic balance no longer applies, and there is a narrower transition region in which the effective pressure drops to near zero, and the porosity profile changes shape. This transition

region marks a (relatively sudden) switch from a normally pressured environment to one with high pore pressures, and is caused by the sharp variation of permeability with porosity. Notice also that even if the permeability exponent is not large, so that $\phi^*$ is small ($\phi^* = \phi_0 \exp[-\frac{1}{m}\ln\lambda]$), nevertheless (9.11) implies that the critical depth is still finite. Thus the switch from normally pressured to abnormally pressured is predicted to occur in any case. More generally, we might therefore expect that in a marine environment where stratigraphic layers cause sudden changes in permeability, that clay layers with small permeability may be associated with the formation of abnormally high pressures.

## 9.1 Main Conclusions

A general mathematical model of compaction and diagenesis is presented in this work. The coupled non-linear diffusion equations have been solved numerically and several asymptotic solutions are given for the cases of geological importance. Asymptotic analysis and numerical simulations showed that

- The processes of diagenesis, temperature and porosity evolution for continuously compacting sediments are characterised and controlled by three dimensionless parameters $\lambda$, $\Lambda$, $\mathcal{R}$ which relate the sedimentation rate, permeability, heat conductivity, viscosity, diagenetic reaction rate and heat flux.

- The present model clearly degenerates to that of Audet & Fowler (1992) by setting $a = 0$, $\bar{k}_r = 0$ and omitting the temperature equation, or equivalently leaving out the parameters $\Lambda$ and $\mathcal{R}$ by setting them to zero.

- The parameter $\lambda = 1$ defines a transition between slow sedimentation and fast sedimentation. Here, the fast and slow are only meaningful relative to the time scale for the compaction process. $\lambda >> 1$ corresponds to the case of slow sedimentation or high permeability and $\lambda << 1$ corresponds to that of fast sedimentation or low permeability. The parameter $\lambda$ governs the mechanism of the excess pressure development of the sedimentary basins. High sedimentation rate may cause excess pressures even in basins with moderate permeability.

- The effect of variation of sedimentation rates and unloading are investigated by solving two sets of equations with a switching condition derived from critical state soil mechanics. A very interesting phenomenon arises in the case of constant unloading. A downward travelling interface separates the unloading region from the loading region. If the system is reloaded, a discontinuous porosity may occur. A literature survey suggests that this is the first attempt to investigate unloading on a basin scale.

- The parameter $\Lambda$ also defines a transition in a quite similar manner. $\Lambda << 1$ shows that the temperature solution is dominated by the fast moving boundary effect of the basin due to fast sedimentation, while $\Lambda >> 1$ shows that the sedimentation rate has an negligible influence on the temperature development. In the realistic geological environment, it is usually $\Lambda >> 1$, which means that the time scale of thermal conduction is much shorter than the time scale of compaction, thus temperature evolution is essentially independent of the compaction process as the coupling is very weak.

- The parameter $\mathcal{R}$, which may be defined in terms of a critical temperature $\Theta_c$, controls the speed of diagenesis and its characteristic effect on compaction. This study reveals that mechanical compaction, which is controlled by the strata permeability and sedimentation rate, is the most important geological factor in porosity reduction and the formation of overpressure. The chemical compaction controlled by the diagenesis is of secondary importance in the whole mechanism. The first-order dehydration model of diagenesis is a good approximation in the sense of only describing the extent of progress of the overall smectite-to-illite transformation without much care of its detailed geochemical features.

- Diagenesis has been successfully modelled as a dissolution-precipitation reaction model which can reproduce many essential features of the smectite-to-illite process if the appropriate reaction rate laws are used based on the known physics and chemistry from experimental studies.

- Pressure solution is an effective compaction mechanism as well as a source of

cementing material, especially in sandstones and carbonate packstones. Pressure solution is successfully modelled as a viscous compaction creep model. Athy's law is replaced by a viscous rheology, and the present model extends earlier work.

## 9.2 Future Work

Based on our current research work, the main further research objectives are

- *Application* to practical sedimentary basins. Our new models will be tested by real field data, and modifications will be added to the models in order to make more realistic modelling. We aim at making reasonable predictions of overpressuring before drilling and identification of its precursors by using *in situ* data; and modelling hydrocarbon generation and migration to predict reservoir quality. We also aim at applying the present diagenetic reaction model to other clay minerals such as quartz production, and geochemical weathering processes in the near surface environment.

- *Extensions* to formulations of new rate laws of natural water-rock systems. One unsolved problem in the studies of water-rock interactions is that the laboratory data are not directly applicable to field observations. The discrepancies between field estimates and laboratory measurements of reaction rates are as large as up to four orders of magnitude (Swoboda-Colberg & Drever, 1993; Bitzer, 1996). Therefore, we intend to aim at extending our present models to formulate more realistic rate laws of water-rock systems in the field.

- *Development* to model the nonlinear sediment creep behaviour. Biot theory in soil mechanics prescribes a relation between porosity (volume fraction of pore space in total volume) and effective pressure (overburden pressure minus pore pressure). It is valid for small strains and usually in the one-dimensional case. It is not true for large strains. We therefore intend to aim at developing a fully nonlinear soil mechanic model to correct the drawbacks of the present Biot theory and to reproduce much of the experimentally derived nonlinear features of sediments.

An eventual aim of the model development will be the production of a code which can solve the compaction problem which includes most of the known physics and chemistry, in a three-dimensional environment.

# Bibliography


Aagaard, P. & Helgeson, H., 1983. Activity/composition relations among silicates and aqueous solutions: II. chemical and thermodynamic consequences of ideal mixing of atoms on homological sites in montmorillonites, illites, and mixed-layer clays, *Clays & Clay Minerals*, **31**, 207-217.

Abercrombie, H. J, Hutcheon, I. E., Bloch, J. D. & Caritat, P., 1994. Silica activity and the smectite-illite reaction, *Geology*, **22**, 539-542.

Ahn, J. H. & Peacor, D. R., 1986. Transmission electron microscopic study of diagenetic chlorite in Gulf Coast argillaceous sediments, *Clays Clay Min.*, **34**, 165-179.

Angevine, C. L. & Turcotte, D. L., 1983. Porosity reducation by pressure solution: A theorectical model for quartz arenites, *Geol. Soc. Am. Bull.*, **94**, 1129-1134.

Atkinson, J. H. & Bransby, P.L., 1978. The mechanics of soil: an introduction to critical state soil mechanics, McGraw-Hill, London, 375pp.

Audet, D.M. & Fowler, A.C., 1992. A mathematical model for compaction in sedimentary basins, *Geophys. J. Int.*, **110**, 577-590.

Audet, D. M. & McConnell, J. D. C., 1992. Forward modelling of porosity and pore pressure evolution in sedimentary basins, *Basin Research*, **4**, 147-162.

Baccar, M. B. & Fritz, B., 1993. Geochemical modelling of sandstone diagenesis and its consequences on the evolution of porosity, *Appl. Geochem.*, **8**, 285-295.

Bear, J. & Bachmat, Y., 1990. *Introduction to modeling of transport phenomena in porous media*, Kluwer Academic, London.

Berner, R. A., 1978. Rate control of mineral dissolution under earth surface conditions, *Am. J. Sci.*, **278**, 1235-1252.

Bethke, C.M., 1985. A numerical model of compaction-driven groundwater flow and heat transfer and its application to the paleohydrology of intracratonic sedimentary basins, *J. Geophys. Res.*, **90**, 6817-6828.

Bethke, C.M. & Corbet, F., 1988. Linear and nonlinear solutions for one-dimensional compaction flow in sedimentary basins, *Water Res. Res.*, **24**, 461-467.

Biot, M.A., 1941. General theory of three-dimensional consolidation, *J. Appl. Phys.*, **12**, 155-164.

Birchwood, R. A. & Turcotte, D. L., 1994. A unified approach to geopressuring, low-permeability zone formation, and secondary porosity generation in sedimentary basins, *J. Geophys. Res.*, **99**, 20051-20058.

Bird, R.B., Armstrong, R.C. & Hassager, O., 1977. Dynamics of polymeric liquids, Vol.1, John Willy & Son press.

Bishop, R.S., 1979. Calculated compaction states of thick abnormally pressured shales, *Am. Ass. Petrol. Geol. Bull.*, **63**, 918-933.

Bitzer, K. 1996. Modeling consolidation and fluid flow in sedimentary basins, *Computers & Geosciences*, **22**, 467-478.

Bjorlykke, K. & Egeberg, P. K., 1993. Quartz cementation in sedimentary basins, *Am. Ass. Petrol. Geol. Bull.*, **77**, 1538-1548.

Bredehoeft, J.D. & Hanshaw, B.B., 1968. On the maintenancce of anomalous fluid pressure: I. Thick sedimentary sequences, *Geol. Soc. Am. Bull.,***79**, 1097-1106.

Burland, J. B., 1990. On the compressibility and shear strength of natural clays, *Geotechnique*, **40**, 329-378.

Busenberg, E. & Clememcy, C. V., 1976. The dissolution kinetics of feldspar at 25$^o$C and 1 atm $CO_2$ partial pressure, *Geochim. Cosmochim. Acta.*, **40**, 41-50.

Carslaw, H.S. & Jaeger, J.C. 1959. Conduction of heat in solids, 2nd ed. Oxford University Press.

Casey, W. H., Banfield, J. F., Westrich, H. R. & Mclaughlin, L., 1993. What do dissolutin experiments tell us about natural weathering, *Chemical Geology*, **105**, 1-15.

Chamley, H., 1989. *Clay Sedimentology*, Springer-Verlag.

Chen, W. F. & Mizuno, E., 1990. Nonlinear analysis in soil mechanics: theory and implementation, Elsevier, Armsterdam, 661pp.

Chou, L. & Wallast, R., 1985. Steady-state kinetics and dissolution mechanisms of albite, *Amer. J. Sci.*, **285**, 963-993.

Coble, R.L., 1963. A model for boundary diffusion controlled polycrystalline materials, *J. Appl. Phys.*, **34**, 1679-82.

Crank, J., 1975. The mathematics of diffusion, 2nd, Oxford University Press.

Das, B. M., 1983.*Advanced soil mechanics*, MicGraw-Hill, New York.

De Boer, R. B., 1977. On the thermodynamics of pressure solution— interaction between chemical and mechanical forces, *Geochim. Cosmochim. Acta.*, **41**, 249-256.

Deming,, D., Nunn, J. A. & Evans, D. G., 1990. Thermal effects of compaction-driven groundwater flow from overthrust belts, *J. Geophys. Res.*, **95**, 6669-6683.

Dewers, T. & Ortoleva, P., 1990. A coupled reaction/transport/mechancial model for intergranular pressure solution, stylolites, and differential compaction and cementation in clean sandstones, *Geochim. Cosmochim. Acta.*, **54**, 1609-25.

Dewers, T. & Hajash, A., 1995. Rate laws for water-assisted compaction and stress-induced water-rock interaction in sandstones, *J. Geophys. Res.*, B**100**, 13093-112.

Dewynne, J. N., Fowler, A. C. & Hagan, P.S., 1993. Multiple reaction fronts in the oxidation-reduction of iron-rich uranium ores, *SIAM J. Appl. Math.*, 971-989.

Drew, D. A., 1983. Mathematical modelling of two-phase flow, *A. Rev. Fluid Mech.*, **15**, 261-291.

Eberl, D. & Hower, J., 1976. Kinetics of illite formation, *Geol. Soc. Am. Bull.*, **87**, 1326-1330.

Fowler, A. C., 1984. On the transport of moister in polythermal glaciers, *Geophys. Astrophys. Fluid Dyn.*, **29**, 99-140.

Fowler, A. C., 1985. A mathematical model of magma transport in the asthenosphere, *Geophys. Astrophys. Fluid Dyn.*, **33**, 63-96.

Fowler, A.C., 1990. A compaction model for melt transport in the Earth's asthenosphere. Part I: the basic model, in *Magma Transport and Storage*, ed. Ryan, M.P., John Wiley, pp. 3-14.

Fowler, A.C. & Yang, X. S., 1997. Fast and slow compaction in sedimentary basins, *SIAM J. Appl. Math.*, (in press).

Fowler, A.C. & Yang, X. S., 1998. Pressure solution and viscous compaction in sedimentary basins, *J. Geophys. Res.*, (submitted).

Fowler, A.C. & Noon, C. G., 1995. Mathematical models of compaction, consolidation, and regional groundwater flow, *Geophys. J. Int.*, (submitted).

Freed, R.L. & Peacor, D. R., 1989. Geopressured shale and sealing effect of smectite to illite transition, *AAPG Bulletin*, **73**, 1223-1232.

Gautier, J.M., Oelkers, E.H. & Schott, J., 1994. Experimental study of K-feldspar dissolution rates as a function of chemical affinity at 150$^o$C and pH 9, *Geochim. Cosmochim. Acta*, **58**, 4549-4560.

Gibson, R.E., 1958. The progress of consolidation in a clay layer increasing in thickness with time, *Geotechnique*, **8**, 171-182.

Gibson, R. E., England, G. L. & Hussey, M. J. L., 1967. The theory of one-dimensional consolidation of saturated clays, I. finite non-linear consolidation of thin homogeneous layers, *Can. Geotech. J.*, **17**, 261-273.

Gibson, R. E., Schiffman, R. L. & Cargill, K. W., 1981. The theory of one-dimensional consolidation of saturated clays, II. finite non-linear consolidation of thick homogeneous layers, *Can. Geotech. J.*, **18**, 280-293.

Gratier, J. P. & Guiguet, R., 1986. Experimental pressure solution- deposition on quartz grains: the crucial effect of the nature of the fluid, *J. Struct. Geolo.*, **8**, 845-856.

Gratz, A. J., 1991. Solution-transfer compaction of quartzites—Progress toward a rate law, *Geology*, **19**, 901-904.

Hanshaw, B.B.& Bredehoeft, J.D., 1968. On the maintenancce of anomalous fluid pressure: II. Source layer at depth, *Geolo. Soc. Am. Bull.,***79**, 1107-1122.

Haxby, W. F.& Turcotte, D. L., 1976. Stresses induced by the addition or removal of overburden and associated thermal effects, *Geology*, **4**, No. 3, 181-184.

Hedberg, H.D., 1936. Gravitational compaction of clays and shales, *Am. J. Sci.*, **184**, 241-287.

Helgeson, H. C., 1968. Evaluation of irreversible reactions in geochemicalpreocess involving minerals and aqueous solutions-I. Thermodynamic relations, *Geochim. Cosmochim. Acta*, **32**, 853-857.

Helgeson, H. C., Murphy, W. M. & Aagaard, P., 1984. Thermodynamics and kinetic constraints on reaction rates among minerals and aqueous solutions, II. Rate constants, effective surface area, and the hydrolysis of feldspar, *Geochim. Cosmochim. Acta.*, **48**, 2405-2432.

Hinch, E.J., 1991. *Perturbation Methods*, Cambridge University Press.

Hower, J., Eslinger, E. V., Hower, M. E. & Perry, E. A., 1976. Mechanism of burial meramorphism of argillaceous sediment: 1. Mineralogical and chemical evidence,

*Geol. Soc. Am. Bull.*, **87**, 725-737.

Huang, W. L., Longo, J. M. & Pevear, 1993. An experimentally derived kinetic model for smectite-to-illite conversion and its use as a geothermometer, *Calys & Clay Minerals*, **41**, 162-177.

Huekel, T. & Baldi, G., 1990. Thermoplasticity of saturated clays: experimental constitutive study, *J. Geotech. Eng.* , **116**, 1778-1792.

Hunt, J.M., 1990. Generation and migration of petroleum from abnormally pressured fluid compartments, *AAPG Bull.*, **74**, 1-12.

Keith, L.A. & Rimstidt, J. D., 1985. A numerical compaction model of overpressuring in shales, *Math. Geol.*, **17**, 115-135.

Kearey, P. & Allen, P. A., 1993. The Encyclopedia of the solid earth sciences, Blackwell Scientific.

Khan, A. S. & Huang, S. J., 1995. Continuum theory of plasticity, Wiley-Interscience.

Kumpel, H. J., 1991. Poroelasticity: parameters reviewed, *Geophys. J. Int.*,**105**, 783-799.

Lahann, R.W. & Roberson, H. E., 1980. Dissolution of silica from montnorillonite: effect of solution chemistry, *Geochim. Cosmochim. Acta*, **44**, 1937-1943.

Lambe, T.W. & Whitman, R.V., 1979. Soil Mechanics, SI version, John Wiley & Sons, New York, 553 pp.

Lasaga, A. C., 1981. Rate laws of chemical reactions, In: Kinetics of geochemical processes, *Reviews in Mineralogy*, 1-66.

Lasaga, A. C., 1984. Chemical kinetics of water-rock interactions, *J. Geophys. Res.*,**89**, 4009-4025.

Lasaga, A. C., Soler, J. M., Ganor, J., Burch, T. E. & Nagy K. L., 1994. Chemical weathering rate laws and global geochemical cycles, *Geochim. Cosmochim. Acta*, **58**, 2361-2386.

Lehner, F. K., 1995. A model for intergranular pressure solution in open systems, *Tectonophysics*, **245**, 153-170.

Lerche, I. 1990. Basin analysis: quantitative methods, Vol. I, Academic Press, San Diego, California.

Lewis, C.R. & Rose, S.C., 1970. A theory relating high tempreture and overpressures, *J. Pet. Technol.* , January, pp 11-16.

Luo, X. & Vasseur, G., 1992. Contribution of compaction and aquathermal pressuring to geopressure and the influence of environmental conditions, *AAPG bulletin*, **76**, 1550-1559.

Luo, X. & Vasseur, G., 1993. Contribution of compaction and aquathermal pressuring to geopressure and the influence of environmental conditions: Reply, *AAPG bulletin*, **77**, 2011-2014.

McDonald, D.A. & Surdam, R. C., 1984. Clastic diagenesis, *Am. Assoc. Petrol Geol. Mem.* , **37**, 43pp.

McKenzie, D. P., 1984. The generation and compaction of partial meltss, *J. Petrol.*, **25**, 713-765.

Meek, P.C. & Norbury, J., 1982. Two-stage, two level finite difference schemes for no-linear parabolic equations, *IMA J. Num. Anal.*, **2**, 335-356.

Miller, T. W. & Luk, C. H., 1993. Contribution of compaction and aquathermal pressuring to geopressure and the influence of environmental conditions: Discussion, *AAPG bulletin*, **77**, 2006-2010.

Mullis, A. M., 1991. The role of silica precipitation kinetics in determining the rate of quartz pressure solution, *J. Geophys. Res.*, **96**, 10007.

Mullis, A. M., 1992. Determination of the rate-limiting mechanism for quartz pressure dissolution, *Geochim. Cosmocgim. Acta*, **57**, 1499-1503.

Murray, J. D., 1989. *Mathematical Biology*, Springer-Verlag.

Neuzil, C. E. & Pollock, P. W., 1983. Erosional unloading and fluid pressures in hydraulically *tight* rocks, *J. Geology*, **91**, 179-193.

Nielsen, A. E., 1964. *The Kinetics of Precipitation*, MacMillan.

Nielsen, A. E., 1986. Mechanisms and rate laws in electrolyte crystal growth from aqueous solution, In *Geochemical Processes at Mineral Surfaces*, eds. J. A. Davis & K. F. Hayes, ACS *Symp. Ser.*, **323**, 600-614.

Ockendon, H. & Ockendon, J. R., 1995. *Viscous Flow*, Cambridge University Press.

Ortoleva, P., 1994. *Geochemical self-organization*, Oxford University Press.

Ortoleva, P., Merino, E., Moore, C. H. &Chadam, J., 1987. Geochemical self-organization I:feedback mechanism and modelling approach, *Am. J. Sci.*, **287**, 979-1007.

Patterson, M. S., 1973. Nonhydrostatic thermodynamics and its geological applications, *Rev. Geophys. Space Phys.*, **11**, 355-389.

Pearson, M. J. & Small, J. S., 1988. Illite-smectite diagenesis and palaeotemperatures in North Sea Quaternary to Mesozoic shale sequences, *Clay Mineral*, **23**, 109-132.

Perkins, E.H., Kharaka, Y.K., Gunter, W. D. & DeBraal, J. D., 1990. Geochemical modelling of water-rock interaction using SOLMINEQ.88. In *Chemical modelling of Aqueous Systems II*, (eds. D. C. Melchior & R. L. Bassett, American Chemical Society, pp.117-127.

Pharr, G. M. & Ashby, M. F., 1983. On creep enhanced by a liquid phase, *Acta. Metall.*, **31**, 129-138.

Pytte, A. M. & Reynolds, R. C., 1989. The thermal transformation of smectite to illite: in *Thermal History of Sedimentary Basins*, N. D. Naeser & T. H. McCuuloh, eds., Springer-Verlag, New York, pp.113-140.

Raj, R. & Chyung, C. K., 1981. Solution precipitation creep in glass ceramics, *Acta. Metall.*, **29**, 159-166.

Rice, J. R. & Cleary, M. P., 1976. Some basic stress-diffussion solutions for fluid-saturated elastic porous media with compressible constitents, *Rev. Geophys. Space Phys.*, **14**, 227-241.

Rieke, H.H. & Chilingarian, C.V., 1974. Compaction of argillaceous sediments, Elsevier, Armsterdam, 474pp.

Rimstidt, J. D. & Barnes, H. L., 1980. The kinetics of silica-water reactions, *Geochim. Cosmochim. Acta*, **44**, 1683-1699.

Roscoe, K. H. & Burland, J. B., 1968. On the generalized stress-strain behavior of *wet* clay, in *Engineering Plasticity*, edited by Heyman, J. & Leckie, F. A., Cambridge University Press, 535-609.

Rutter, E. H., 1976. The kinetics of rock deformation by pressure solution, *Philos. Trans. R. Soc. London Ser.***A 283**, 203-219.

Rutter, E. H., 1976. Pressure solution in nature, theory and experiment, *J. Geol. Soc. London*, **140**, 725-740.

Sass, B. M., Rosenberg, P. E. & Kittrick, J. A., 1987. The stability of illite/smectite during diagenesis: An experimental study, *Geochim. Cosmochim. Acta*, **51**, 2103-2115.

Schneider, F., Potdevin, J. L., Wolf, S. & Faille, I., 1996. Mechanical and chemical compaction model for sedimentary basin simulators, *Tectonophysics*, **263**, 307-317.

Schofield, A. N. & Wroth, C. P., 1986.*Critical State Soil Mechanics*, McGraw-Hill, New York.

Scholz, C. H., Leger, A. & Karner, S. L., 1995. Experimental diagenesis: exploratory results, *Geophys. Res. Lett.*, **22**, 719-722.

Scott. D. R. & Stevenson, D. J., 1984. Magma solitions, *Geophys. Res. Lett.*, **11**, 1161-1164.

Sharp, J. M., 1976. Momentum and energy balance equations for compacting sediments, *Math. Geol.*, **8**, 305-332.

Sharp, J.M., 1983. Permeability controls on aquathermal pressuring, *Am. Ass. Petrol. Geol. Bull.*, **67**, 2057-2061.

Sharp, J.M. & Domenico, P.A., 1976. Energy transport in thick sequences of compacting sediments, *Geol. Soc. Am. Bull.*, **87**, 390.

Siese, M. & Spiers, C. J., 1997. Uniaxial compaction creep of wet gypsum aggregates, *J. Geophys. Res.*, B**102**, 875-891.

Skempton, A.W., 1960. Effective stress in soils, concrete and rocks, in *Pore Pressure and Sucction in Soils*, Butterworths, London.

Shi, Y. & Wang, C. Y., 1986. Pore pressure generation in sedimentary basin, overloading versus aquathermal, *J. Geophys. Res.*, **91**, 2153-2162.

Shimuzu, I., 1995. Kinetics of pressure solution creep in quartz: theorectical considerations, *Tectonophysics*, **245**, 121-134.

Smith, G. D., 1985. *Numerical Solutions of Partial Differential Equations: Finite Differerence Methods*, 3rd ed., Clarendon Press, Oxford.

Smith, J.E., 1971. The dynamics of shale compaction and evolution in pore-fluid pressures, *Math. Geol.*, **3**, 239-263.

Steefel, C. I. & Cappellen, P. V., 1990. A new kinetic approach to modelling water-rock interaction: The role of nucleation, precursors, and Ostwald ripening, *Geochim. Cosmochim. Acta*, **54**, 2657-2677.

Steefel, C. L. & Lasaga, A. C., 1994. A coupled model for transport of multiple chemical species and kinetic precipitation/dissolution reactions with application to reactive flow in single phase hydrothermal systems, *Am. J. Sci.*, **294**, 529.

Stevenson, D. J. & Scott, D. R., 1991. Mechanics of fluid-rock systems, *Ann. Rev. Fluid Mech.*, **23**, 305-339.

Stumm, W., 1992. *Chemistry of the Solid-Water Interface: Processes at the mineral-water and particle-water interface in natural systems*, Wiley Interscience.

Swoboda-Colberg, N. G. & Drever, J. I., 1993. Mineral dissolution rates in plot-scale field and laboratory experiments, *Chemical Geology*, **105**, 51-69.

Tada, R., Maliva, R. & Siever, R., 1987. A new mechanism for pressure solution in porous quartzose sandstone, *Geochim. Cosmochim. Acta.*, **51**, 2295-2301.

Tada, R. & Siever, R., 1989. Pressure solution during diagenesis, *Ann. Rev. Earth Planet. Sci.*, **17**, 89-118.

Terzaghi, K., 1943. *Theorectical Soil Mechanics*, New York, Wiley, 510pp.

Turcotte, D. L. & Schubert, G., 1982. *Geodynamics: Application of Continuum Physics to Geological Problems*, 1st. ed., John Wiley, New York.

Van Dyke, M., 1964. *Perturbation Methods in Fluid Mechenics*, Academic Press, Annotated version (1975) Parabolic Press.

Velde, B. & Vasseur, G., 1992. Estimation of the diagenetic smectite illite transformation in time-temperature space, *Amer. Mineral.*, **77**, 967-976.

Wang, H. F., 1993. Quasi-static poroelastic parameters in rock and their geophysical applications, *PAGEOPH*, **141**, 269-286.

Wangen, M., 1992. Pressure and temperature evolution in sedimentary basins, *Geophys. J. Int.*, **110**, 601-613.

Weller, J. M., 1959. Compaction of sediments, *Bull. Am. Ass. Petrol. Geol.* , **43**, 273-310.

Weyl, P. K., 1959. Pressure solution and force of crystallization— a phonomenological theory, *J. Geophys. Res.*, **64**, 2001-2025.

Wilson, T.V. & Sibley, D. F., 1978. Pressure solution and porosity reduction in shallow buried quartz arenite, *Am. Assoc. Pet. Geolo. Bull.*, **62**, 2329-2334.

Wolery, T. J., 1979. Calculation of chemical equilibrium between aqueous solutions and minerals: The EQ3/EQ6 software package, UCRL-52658.

Zoback, M.D., Apel, R., Baumgartner, J., Brudy, M., Emmermann, R., Engeser, B., Fuchs, K., Kessels, W., Rischmuller, H, Rummel, F. & Vernik, L., 1993. Upper-crustal strength inferred from stress measurements to 6km depth in the KTB borehole, *Nature*, **365**, 633-635.